Majorana bound states in topological insulators and nanowires

INAUGURALDISSERTATION

zur

Erlangung der Würde eines Doktors der Philosophie

vorgelegt der

Philosophisch-Naturwissenschaftlichen Fakultät

der Universität Basel

von

Constantin Schrade
aus Sindelfingen, Deutschland

Basel, 2017

Originaldokument gespeichert auf dem Dokumentenserver der Universität Basel
edoc.unibas.ch

Dieses Werk ist unter dem Vertrag „Creative Commons Namensnennung-Keine kommerzielle Nutzung-Keine Bearbeitung 2.5 Schweiz“ lizenziert. Die vollständige Lizenz kann unter
creativecommons.org/licences/by-nc-nd/2.5/ch
eingesehen werden.

Genehmigt von der Philosophisch-Naturwissenschaftlichen Fakultät auf Antrag von

Prof. Dr. Daniel Loss

Prof. Dr. Reinhold Egger

Basel, den 20. Juni 2017

Prof. Dr. Martin Spiess
Dekan

Namensnennung-Keine kommerzielle Nutzung-Keine Bearbeitung 2.5 Schweiz

---

Sie dürfen:

das Werk vervielfältigen, verbreiten und öffentlich zugänglich machen

Zu den folgenden Bedingungen:

Namensnennung. Sie müssen den Namen des Autors/Rechteinhabers in der von ihm festgelegten Weise nennen (wodurch aber nicht der Eindruck entstehen darf, Sie oder die Nutzung des Werkes durch Sie würden entlohnt).

Keine kommerzielle Nutzung. Dieses Werk darf nicht für kommerzielle Zwecke verwendet werden.

Keine Bearbeitung. Dieses Werk darf nicht bearbeitet oder in anderer Weise verändert werden.

- Im Falle einer Verbreitung müssen Sie anderen die Lizenzbedingungen, unter welche dieses Werk fällt, mitteilen. Am Einfachsten ist es, einen Link auf diese Seite einzubinden.
- Jede der vorgenannten Bedingungen kann aufgehoben werden, sofern Sie die Einwilligung des Rechteinhabers dazu erhalten.
- Diese Lizenz lässt die Urheberpersönlichkeitsrechte unberührt.

Die gesetzlichen Schranken des Urheberrechts bleiben hiervon unberührt.

Die Commons Deed ist eine Zusammenfassung des Lizenzvertrags in allgemeinverständlicher Sprache: http://creativecommons.org/licenses/by-nc-nd/2.5/ch/legalcode.de

Haftungsausschluss:
Die Commons Deed ist kein Lizenzvertrag. Sie ist lediglich ein Referenztext, der den zugrundeliegenden Lizenzvertrag übersichtlich und in allgemeinverständlicher Sprache wiedergibt. Die Deed selbst entfaltet keine juristische Wirkung und erscheint im eigentlichen Lizenzvertrag nicht. Creative Commons ist keine Rechtsanwaltsgesellschaft und leistet keine Rechtsberatung. Die Weitergabe und Verlinkung des Commons Deeds führt zu keinem Mandatsverhältnis.

Quelle: http://creativecommons.org/licenses/by-nc-nd/2.5/ch/ Datum: 3.4.2009

Acknowledgments

It is my greatest pleasure to thank my supervisor Prof. Daniel Loss for providing me with the opportunity to work as a Ph.D. student in his group, and I am feeling extraordinarily fortunate to have had the chance to work with him on so many different research topics. While there are of course an abundance of reasons that will most likely never cease to amaze me about Daniel, here I want to name the three things that were of most value to me:

First, despite being one of the world-leading researchers in his many fields of expertise, Daniel has remained a very approachable supervisor, which made it very enjoyable to interact and discuss with him. The door to his office was always open so that I could stop by, sometimes in the late evening, to share an idea or talk about a project.

The second quality of Daniel from which I greatly benefitted for the full four years of Ph.D. studies is his exceptional taste for problems that are important and that truly matter for the field. This allowed me to work with him on some of the most cutting-edge questions and over time it helped me to learn on how to identify these important questions myself.

Finally, I am also very grateful for Daniel's great support during my application for the SNF fellowship and for all the advice he has given to me in this context for a future career in science.

Furthermore, I am also very thankful to Prof. Reinhold Egger for accepting to co-referee my thesis and for taking the time to come to Basel for my Ph.D. examination.

Also, I would like to thank my collaborators, Prof. Jelena Klinovaja, Alexander Zyuzin, Silas Hoffman, Manisha Thakurathi and Christopher Reeg, for sharing their knowledge and expertise with me. It was a privilege to work with all of you.

My thanks also go to all my colleagues of the Condensed Matter Theory section in Basel for a joyful time with many lively discussions and conversations over the past four years. In particular, my thanks go to Samuel Aldana, Ehud Amitai, Pavel Aseev, Prof. Christoph Bruder, Daniel Becker, Denis Chevallier, Olesia Dmytruk, Kevin van Hoogdalem, Adrian Hutter, Christoph Klöffel, Martin Koppenhöfer, Viktoriia Kornich, Axel U. J. Lode, Niels Loerch, Franziska Maier, Tobias Meng, Kouki Nakata, Simon Nigg, Andreas Nunnenkamp, Christoph Orth, Christina Psaroudaki, Diego Rainis, Marko Rancic, Hugo Ribeiro, Arijit Saha, Thomas Schmidt, Tibor Sekera, Marcel Serina, Grégory Strübi, Pawel Szumniak, Rakesh Tiwari, Luka Trifunovic, Stefan Walter, James Wootton, Yanick Volpez, and Robert Zielke.

Last but not least, I want to thank my family and my friends for their endless support and encouragements. Most importantly, my deepest gratitude goes to my parents, Dagmar and Richard Schrade, as well as my grandparents, Anna and Josef Heider, who shaped my personality and made me who I am. Also, I want to thank my relatives, Ingrid and Lothar Heider, for all the support that they have given me throughout the years. Moreover, I want to thank my best friend, Konrad Grosser, for the endless conversations that were spurring my intellectual curiosity about so many different topics and for being almost like a brother to me. Finally, my thanks also go to all my other friends. Most importantly to Felix Stang, Samuel Trautwein, Stephan Tornier, Lilly Fan, Sahika Karabudak, Szymon Hennel and Markus Rexroth for all their help and support.

Summary

Quantum computers outperform classical computers by achieving exponential increases in calculation speed for certain types of problems and for that reason have great potential to revolutionize computing. Compared to their classical counterparts the elementary units of information in a quantum computer are not the classical bits, zero and one, but rather the so-called quantum bits (or qubits) which most generally are quantum mechanical superpositions of the zero and one state. Unfortunately, the quantum bits are highly sensitive to the effects of environmental noise and consequently storing the quantum information in a robust manner represents a major challenge. Historically, it was Kitaev in 2001 who first proposed that this problem can be circumvented by using Majorana bound states as the building block for robust, so-called topologically protected, qubits [1]. Subsequently, it was Fu et al. in 2008 who proposed the first realistic setup for generating Majorana bound states, namely topological insulator-superconductor heterostructures where the Majorana bound states can emerge within vortex cores [2]. Moreover, in 2010 Lutchyn et al. [3] as well as Oreg et al. [4] put forward that Majorana bound states can also appear at the ends of semiconductor Rashba nanowires which are proximity-coupled to an s-wave superconductor and subject to a magnetic field. Finally, in 2013 Klinovaja et al. [5] found that Majorana bound states can arise in chains of magnetic atoms that are deposited on a superconducting substrate. Within the last years these theoretical proposals have all been implemented experimentally and the first signatures for Majorana bound states, such as zero-bias conductance peak measurements, were reported [6–12]. However, despite these encouraging experimental results, there still exists a broad range of open questions and hurdles. In this thesis, we address some of the most important experimental challenges and present new theoretical solutions.

In the first part of this thesis, we introduce two new platforms for generating Majorana bound states based on proximity-induced π Josephson

junctions in topological insulators and crossed-Andreev pairing between semiconductor Rashba nanowires. Unlike the current experimental setups, the proposed schemes require either low magnetic fields or no magnetic fields at all. The latter characteristic constitutes a compelling improvement over current experimental setups for two reasons: (1) The detrimental effects of the magnetic fields on the superconductivity are either reduced or completely avoided. (2) In current experimental schemes the proximity-induced superconducting gap, which assures the topological protection of the Majorana qubits, is well-defined only at low magnetic fields ("hard gap"). At strong magnetic fields, a finite subgap conductance arises ("soft gap") and destroys the topological protection [13–17]. Hence, with regards to future experiments on quantum information procession with Majorana bound states, a setup operated at lower magnetic field is highly desirable.

In the second part of this thesis, we propose a new method for detecting Majorana bound states based on quantum dot φ_0 Josephson junctions. Here, we are motivated by the search for new, more conclusive indicators for Majorana bound states which is one of the most urgent challenges following the experimental results mentioned above. In fact, the recent zero-bias conductance peak measurements only constitute a sufficient, but not a necessary condition for the emergence of Majorana bound states. That is to say, the zero-bias conductance peaks can be explained by a multitude of different physical effects which are completely unrelated to the presence or absence of Majorana bound states [18–23]. Interestingly, in the case of quantum dot φ_0 Josephson junctions, the required ingredients largely overlap with those necessary to obtain Majorana bound states in Rashba nanowire systems [24–26]. This motivated us to compare both the trivial superconducting and the topologically superconducting regimes of quantum dot φ_0 Josephson junction and work out qualitative differences that can serve as new indicators for Majorana bound states.

In the final part of the thesis, we put forward a scalable scheme for quantum computation based on both Majorana bound state qubits and conventional spin qubits. The motivation for this part is three-fold: (1) The topological Majorana qubits are not universal for quantum computation. That is to say, not every logical quantum gate necessary to perform a quantum computation can be executed using Majorana braiding alone. For that reason, we couple the Majorana qubit to another type of qubit, namely the spin qubit, which can supplement the logical quantum gates that cannot be carried out on the Majorana qubits. (2) Spin and Majorana qubits are complementary with regards to their strengths and weaknesses. For example, unlike spin qubits, the Majorana qubits are intrinsically robust against unwanted perturbations and noise. At the same time spin qubits allow for significantly faster operations times compared to Majorana qubits. The hybrid spin-Majorana qubit which we develop in this chapter allows us to combine the best features of both worlds. (3) To utilize the full power of a quantum computer, it is not enough to consider a single qubit alone. What we need is a collection of many qubits making up a so-called surface code architecture on which many operations can run in parallel. We thus show how to construct a scalable network of the spin-Majorana hybrid qubits that can readily be experimentally implemented based on recent breakthroughs in the lithographic fabrication of Majorana nanowires in InAs/Al heterostructures [27].

Contents

Contents ix

1 Introduction 1
1.1 Majorana bound states 2
1.2 Josephson junctions 7

I New platforms for topological superconductivity

2 Proximity-induced π Josephson Junctions in Topological Insulators 17
2.1 Introduction 18
2.2 Josephson junction models 19
2.3 Proximity-induced π Josephson junctions 20
2.4 Kramers pairs of Majorana fermions 23
2.5 Conclusions 26
2.A Energy spectrum 26
2.B Wavefunctions of the Majorana fermions 27

3 Low-field Topological Threshold in Majorana Double Nanowires 32
3.1 Introduction 33
3.2 Model 35
3.3 Topological phase diagram 36
3.4 Localization lengths 38
3.5 Stability analysis 39
3.6 Conclusions 41
3.A Microscopic model of the proximity effect 42
3.B Energy spectrum in the strong spin-orbit interaction regime 47
3.C Majorana bound state wavefunctions in the strong spin-orbit interaction regime 51
3.D Interwire tunneling 54

3.E Numerical results 56

II New probes for topological superconductivity

4 Detecting Topological Superconductivity with φ_0 Josephson Junctions 62
4.1 Introduction 63
4.2 Josephson junction models 64
4.3 Detecting topological superconductivity. 67
4.4 Experimental proposal 69
4.5 Conclusions 72
4.A A Quantum dot with spin orbit interaction in a Zeeman field 72
4.B An s-wave Superconductor φ_0 Josephson junction 77
4.C A Topological Superconductor φ_0 Josephson junction . . . 85
4.D Critical angle 89
4.E Critical currents 91

III Spin-Majorana hybrid qubits and scalability

5 Universal Quantum Computation with Hybrid Spin-Majorana Qubits 96
5.1 Introduction 97
5.2 Setup 99
5.3 Effective Hamiltonian 100
5.4 Quantum gates 102
5.5 MaSH network 104
5.6 Outlook and conclusions 106
5.A Effective Hamiltonian 108
5.B Full exchange Hamiltonian 115
5.C Hybrid CNOT gate 117
5.D Effective interaction between Majorana fermion qubits . . 118
5.E Inner-outer Majorana basis 119

Bibliography 121

CHAPTER 1

Introduction

In this Introduction, we give an overview of the most relevant concepts for the subsequent chapters of this thesis.

In the first section, we provide an introduction to Majorana bound states and their non-Abelian braiding statistics [28–30]; a feature that sets them apart from regular fermionic or bosonic particles. We then discuss the semiconductor Rashba nanowire subject to a magnetic field and proximity-coupled to an s-wave superconductor as one of the simplest systems where Majorana bound states are predicted to appear [3, 4, 31]. Additionally, we point out that the magnetic field required for this particular setup is not a necessary ingredient for Majorana bound states. In fact, we discuss that a Kramers pair of Majorana bound states emerges in the absence of magnetic fields for a system of two semiconductor Rashba nanowires coupled by the same s-wave superconductor [32]. This point is especially relevant with regards to future experiments because the magnetic field acts detrimental on the superconductivity.

In the second section of the Introduction, we provide an overview of several Josephson junctions. This overview covers the superconductor / normal-metal / superconductor junction [33–36], the π Josephson junction realized by coupling two superconductors via a layer with magnetic impurities [37,38] or a quantum dot in the Coulomb blockade regime [39] and the topological superconductor Josephson junction with Majorana bound states [1, 40]. We do not discuss the φ_0 Josephson junction within this overview as a thorough discussion is contained in the fourth chapter of this thesis.

1.1 Majorana bound states

In condensed matter physics Majorana bound states (MBSs) are zero-energy quasiparticles that arise at the zero-dimensional boundaries of certain one-dimensional [3–5, 31] or two-dimensional [2, 28] superconducting system; specific examples for those types of systems will be discussed below. In general, a MBS quasiparticle is of the form

$$\gamma_n = \int \mathrm{d}x \, \left[\phi_{n\tau\sigma}(x)\Psi_{\tau\sigma}(x) + \phi^*_{n\tau\sigma}(x)\Psi^\dagger_{\tau\sigma}(x)\right], \tag{1.1}$$

where $\Psi^\dagger_{\tau\sigma}(x)$ $[\Psi_{\tau\sigma}(x)]$ creates [destroys] an electron at position x with spin $\sigma/2 = \pm 1/2$ and some additional quantum numbers τ. In particular, Eq. (1.1) implies that a MBS is its own antiparticle, $\gamma_n^\dagger = \gamma_n$. Moreover, n is an index labelling different MBSs in the same system. In addition to Eq. (1.1), we also require that

$$\sum_{\tau,\sigma} \int \mathrm{d}x \, [\phi_{n\tau\sigma}(x)\phi^*_{m\tau\sigma}(x) + \phi^*_{m\tau\sigma}(x)\phi_{n\tau\sigma}(x)] = 2\delta_{nm}, \tag{1.2}$$

which implies that the Majorana bound states satisfy the algebra

$$\{\gamma_n, \gamma_m\} = 2\delta_{nm}. \tag{1.3}$$

Here, the curly brackets denote the anti-commutator. The total number of MBSs in a system is always even. That is to say, $n = 1...2N$ for some integer N. This allows us to combine two MBSs to a conventional fermion defined by

$$C_j = (\gamma_{2j-1} + i\gamma_{2j})/2, \tag{1.4}$$

where $j = 1...N$. The choice of combination of the MBSs is arbitrary meaning that any two fermionic states realized by two different pairings of the MBSs are related by a unitary transformation.

The reason why MBSs are interesting, is because of their non-Abelian braiding statistics. The latter feature means that the quantum state of the system changes by a unitary transformation when two MBSs are exchanged. Interestingly, this unitary transformation is not proportional to the identity matrix and only depends on the topology of the exchange path, *i.e.*, not on the microscopic details. Following the standard references [28, 30], the operation B_i of exchanging the MBSs γ_i and γ_{i+1} is given by

$$B_i(\gamma_j) = \begin{cases} \gamma_{j+1} & \text{if } i = j \\ -\gamma_{j-1} & \text{if } i = j-1 \ . \\ \gamma_j & \text{else} \end{cases} \tag{1.5}$$

From a physical perspective, the minus sign for the case $i = j - 1$ is most easily understood for MBSs that are localized in vortex cores of a two-dimensional spinless p-wave superconductor, see [28] for more details. In this case, when encircling a vortex the superconducting order parameter acquires a phase of 2π. This implies that the electron operators, and likewise the MBS operators, acquire a phase of π, *i.e.*, a minus sign. The action of the braiding operation B_i on the fermionic states is given by the representation $\tau(B_i)$ which satisfies

$$\tau(B_i)\gamma_j\tau(B_i)^{-1} = B_i(\gamma_j). \tag{1.6}$$

A solution to this equation is given by the unitary operator

$$\tau(B_i) = (1 + \gamma_{i+1}\gamma_i)/\sqrt{2}. \tag{1.7}$$

For applications in quantum information processing these unitary braiding matrices are used to construct the logical gates that act on MBS qubit which in a system of four MBSs is defined in either the even or odd total fermion parity subspace, see the fifth chapter for more details.

Conventional Majorana bound states

Having established the key characteristics of MBSs, we now examine a particular system where MBSs arise, namely the semiconductor Rashba nanowire (NW) proximity-coupled to an s-wave superconductor (SC) and subject to a magnetic field, see also Fig. 1.1(a). We will closely follow the standard references [3, 4, 31]. The Hamiltonian of the setup is given by $H = \int \mathrm{d}x\ \Psi^\dagger(x)\mathcal{H}(x)\Psi(x)/2$ with the Hamiltonian density

$$\mathcal{H}(x) = \left(-\frac{\hbar^2\partial_x^2}{2m} - \mu\right)\eta_z - \alpha\hat{k}\sigma_z + \Delta_Z\eta_z\sigma_x - \Delta_d\eta_y\sigma_y \tag{1.8}$$

and the electron spinor $\Psi^\dagger = (\Psi^\dagger_1, \Psi^\dagger_{\bar{1}}, \Psi_1, \Psi_{\bar{1}})$ where $\Psi^\dagger_\sigma(x)$ $[\Psi_\sigma(x)]$ creates [annihilates] an electron with spin $\sigma/2 = \pm 1/2$ and effective mass m at position x in the NW. The Pauli matrices $\eta_{x,y,z}$ and $\sigma_{x,y,z}$ act in particle-hole and spin-space, respectively. Furthermore, μ is the NW chemical

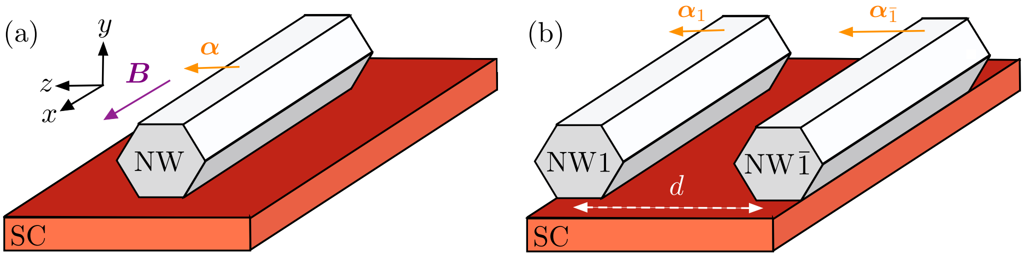

Figure 1.1: (a) A single Rashba NWs (gray) is aligned along the x direction and proximity-coupled to an s-wave SC (red) and subject to a magnetic field **B** along the x-axis. The Rashba SOI $\boldsymbol{\alpha}$ points along the z axis. The wire chemical potential μ is tuned inside the energy gap opened by the magnetic field in the normal state and subsequently set to zero. The system exhibits a topological phase hosting a MBS at each end of the NW individually provided that the Zeeman splitting Δ_Z due to the magnetic field exceeds the strength of the proximity-induced pairing Δ_d, $\Delta_Z > \Delta_d$. (b) Same as in (a) but with two Rashba NWs labeled by an index $\tau = 1, \bar{1}$ and in the absence of a magnetic field **B**. The Rashba SOI in the τ-wire is given by $\boldsymbol{\alpha}_\tau$. The SC induces both direct pairing in the NWs (Δ_d) as well as the crossed-Andreev pairing (Δ_c). When the crossed-Andreev pairing exceeds the direct pairing a Kramers pair of MBSs arises at each end of the setup, $\Delta_c > \Delta_d$.

potential which is tuned inside the gap opened by the magnetic field and then set to zero, α is the strength the Rashba spin-orbit interaction (SOI) which points along the z direction, Δ_Z is the Zeeman splitting due to the magnetic field in the x direction, and Δ_d is the proximity-induced superconducting gap in the NW. The bulk spectrum of the Hamiltonian in Eq. (1.8) is given by

$$E_\pm^2(k) = \left(\frac{\hbar^2 k^2}{2m}\right)^2 + (\alpha k)^2 + \Delta_Z^2 + \Delta_d^2 \pm 2\sqrt{\Delta_Z^2 \Delta_d^2 + \left(\frac{\hbar^2 k^2}{2m}\right)^2 (\Delta_Z^2 + [\alpha k]^2)}. \tag{1.9}$$

Assuming $\Delta_d > 0$, the spectrum exhibits a gapless point only at $k = 0$ provided $\Delta_Z = \Delta_d$. This point marks a so-called topological phase transition; that is to say for

$$\Delta_Z > \Delta_d \tag{1.10}$$

the wire is in a topological phase and hosts a single MBS on each end. In the opposite case, $\Delta_Z < \Delta_d$, the wire is in a trivial phase and no MBSs emerge. The latter statement can be shown explicitly by calculating the MBS wavefunctions which take on the form of Eq. (1.1). They correspond to the zero-energy solutions of the Hamiltonian in Eq. (1.8) for a semi-infinite wire. In the limit of strong SOI, $E_{so} \gg \Delta_d, \Delta_Z$ with $E_{so} = m\alpha^2/\hbar^2$ the wire SOI energy, we find that the total localization length of the MBS wavefunction is given by

$$\xi = \max\{\frac{\hbar v_F}{\Delta_Z - \Delta_d}, \frac{\hbar v_F}{\Delta_d}\}, \qquad \text{(strong SOI)} \tag{1.11}$$

where the Fermi velocity is given by $v_F = \alpha/\hbar$. Moreover, $\hbar v_F/(\Delta_Z - \Delta_d)$ corresponds to the localization due to the interior branches of the spectrum at $k = 0$, while $\hbar v_F/\Delta_d$ corresponds to the localization length due to exterior branches at $k = \pm 2m\alpha/\hbar^2$. In the opposite limit of weak SOI, $E_{so} \ll \Delta_d, \Delta_Z$, and close to the topological phase transition, $\hbar^2|\Delta_Z - \Delta_d|/2m\alpha^2 \ll 1$, the total localization length of the MBS wavefunction is given by

$$\xi = \max\{\frac{\hbar v_F}{\Delta_Z - \Delta_d}, \frac{\hbar v'_F}{\Delta'_d}\} \qquad \text{(weak SOI)} \tag{1.12}$$

with the Fermi velocity $v'_F \approx \sqrt{2\Delta_Z/m}$ and renormalized pairing strength $\Delta'_d = (\sqrt{2m}\alpha\Delta_d)/\hbar\sqrt{\Delta_Z}$. Here, the effects of the SOI close to $k = 0$ can be neglected in the vicinity to the topological phase transition, *i.e.*, that the corresponding eigenstates are unchanged to first order in the SOI. Consequently, the localization length due the interior branches at $k = 0$ is identical for weak and strong SOI, $\hbar v_F/(\Delta_Z - \Delta_d)$. However, the localization length due to the exterior branches at $k = \pm\sqrt{2\Delta_Z m}/\hbar$ is modified to $\hbar v'_F/\Delta'_d$.

Kramers pairs of Majorana bound states

In the last section, we have reviewed the model of a single semiconductor Rashba NW which is subject to a magnetic field and coupled to an s-wave SC. We have seen that this model hosts a MBS at both ends of the wire individually provided that the Zeeman splitting exceeds the proximity-induced pairing. However, from the viewpoint of experiments, the magnetic field acts detrimentally on the superconductor, and so one might wonder if MBSs can also arise in the absence of magnetic fields, *i.e.*, in time-reversal symmetric systems. This is indeed the case. In systems that preserve time-reversal symmetry a so-called Kramers pair of MBSs can emerge at the interface between trivial and topological phases. The two MBSs $\gamma_1, \gamma_{\bar{1}}$ which make up the Kramers pair are related by the time-reversal symmetry $\mathcal{T}$ according to

$$\mathcal{T}\gamma_1\mathcal{T}^{-1} = \gamma_{\bar{1}} \quad , \quad \mathcal{T}\gamma_{\bar{1}}\mathcal{T}^{-1} = -\gamma_1. \tag{1.13}$$

Here, the operation of time-reversal symmetry is defined by its action on the local electron operators of the system, $\mathcal{T}\Psi_{\tau 1}(x)\mathcal{T}^{-1} = \Psi_{\tau\bar{1}}(x)$ and $\mathcal{T}\Psi_{\tau\bar{1}}(x)\mathcal{T}^{-1} = -\Psi_{\tau 1}(x)$ as well as by the requirement that $\mathcal{T}i\mathcal{T}^{-1} = -i$.

We will now outline a particular setup in which Kramers pairs of MBSs can emerge. We closely follow the reference [32]. The setup consists of two semiconductor NWs which are proximity-coupled to the same s-wave SC, see also Fig. 1.1(b). Compared to the setup in the last section, a Cooper pair from the SC can now not only tunnel into each NW separately, but it can also split up and induce a pairing between the two wires referred to as crossed-Andreev pairing. The Hamiltonian is given by $H = \int \mathrm{d}x\ \Psi^\dagger(x)\mathcal{H}(x)\Psi(x)/2$ with the Hamiltonian density

$$\begin{aligned}\mathcal{H}(x) = &\left(-\frac{\hbar^2\partial_x^2}{2m} - \mu_1\right)\left(\frac{1+\tau_z}{2}\right)\eta_z + \left(-\frac{\hbar^2\partial_x^2}{2m} - \mu_{\bar{1}}\right)\left(\frac{1-\tau_z}{2}\right)\eta_z \\ &- \alpha_1\hat{k}\left(\frac{1+\tau_z}{2}\right)\sigma_z - \alpha_{\bar{1}}\hat{k}\left(\frac{1-\tau_z}{2}\right)\sigma_z \\ &- \Delta_c\tau_x\eta_y\sigma_y - \Delta_d\eta_y\sigma_y.\end{aligned} \tag{1.14}$$

and the electron spinor $\Psi = (\Psi_{11}, \Psi_{1\bar{1}}, \Psi^\dagger_{11}, \Psi^\dagger_{1\bar{1}}, \Psi_{\bar{1}1}, \Psi_{\bar{1}\bar{1}}, \Psi^\dagger_{\bar{1}1}, \Psi^\dagger_{\bar{1}\bar{1}})$. Here, $\Psi^\dagger_{\tau\sigma}(x)$ $[\Psi_{\tau\sigma}(x)]$ creates [annihilates] an electron with mass m and spin $\sigma/2 = \pm 1/2$ in wire $\tau = 1, \bar{1}$. The Pauli matrices $\tau_{x,y,z}$, $\eta_{x,y,z}$, and $\sigma_{x,y,z}$ act in wire, particle-hole and spin-space, respectively. Moreover, $\alpha_\tau > 0$ is the strength of the SOI in wire τ, Δ_d is the strength of the proximity-induced direct pairing in the NWs, and Δ_c is the strength of the proximity-induced crossed Andreev pairing. Lastly, μ_τ are the chemical potentials of the wires, which are tuned to the crossing points of the spin-polarized bands of the Rashba spectrum in the normal state and then set to zero. As in the previous example we determine the bulk spectrum of our model and the corresponding gapless points. We find that for $|E_{so,1} - E_{so,\bar{1}}| \gg \Delta_d, \Delta_c$ with $E_{so,\tau} = m\alpha_\tau^2/\hbar^2$ the spectrum is gapless at $k = 0$ provided $\Delta_c = \Delta_d$. There are no gap closing points at finite momentum. From an explicit calculation of the MBS wavefunctions corresponding to the zero-energy solutions of the Hamiltonian in Eq. (1.14), we find that the system exhibits a topological phase provided

$$\Delta_c > \Delta_d. \tag{1.15}$$

In the opposite regime, $\Delta_c < \Delta_d$, the system is in a trivial phase with no MBS. We notice that the crossed Andreev pairing has taken over the role of the magnetic field used in the previous setup. However, because the system is time-reversal symmetric, in the topological phase instead of a single MBS, a Kramers pair of MBSs emerges. The localization length of the Kramers pair of MBS will be provided in the context of a more general setup in the third chapter of this thesis.

1.2 Josephson junctions

When two superconductors (SCs) are coupled by a tunneling contact a supercurrent, induced by the phase-coherent transport of Cooper pairs across the junction, can flow and provide information on the superconducting phase difference φ between the SC grains. The supercurrent in such a so-called Josephson junction (JJ) is always 2π periodic provided that the SC grains are topologically trivial. This is because a shift in the superconducting phase by 2π does not alter the physical state of the junction. Following closely the reference [41], the supercurrent can be expanded as a Fourier series,

$$I(\varphi) = \sum_{n\geq 1} \left[I_n \sin(n\varphi) + J_n \cos(n\varphi) \right], \tag{1.16}$$

with real coefficients I_n and J_n in units of current. We note that Eq. (1.16) is commonly referred to as the current-phase relation of the JJ. Importantly, when the SC grains are topologically non-trivial, the supercurrent exhibits an additional 4π periodic component to Eq. (1.16) which is not due to Cooper pair tunneling but due to the single-electron tunneling of non-local fermions formed by the MBSs. The free energy of a JJ, or Josephson energy for short, is given by

$$E_J(\varphi) = \frac{\hbar}{2e} \int_0^{\varphi} \mathrm{d}\chi \, I(\chi). \tag{1.17}$$

It corresponds to the potential energy that a JJ accumulates due to a flowing supercurrent. Moreover, if φ^* is the superconducting phase difference

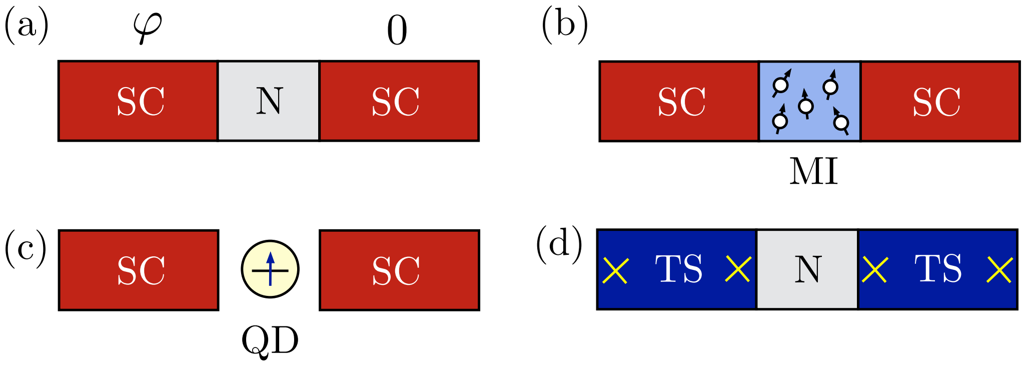

Figure 1.2: Four types of JJs (a) A conventional JJ of two s-wave SCs (red) and a normal conductor (N, gray). The ground state of the junction occurs at the superconducting phase difference $\varphi = 0$. (b) A JJ of two s-wave SC and a magnetic insulator (MI, light blue). The ground state of the junction occurs at $\varphi = \pi$, thus building up a so-called π Josephson junction. (c) JJ of two s-wave SC and a singly-occupied quantum dot (yellow). The ground state of the junction is again given by $\varphi = \pi$. (d) A JJ of two topological superconductors (TSs, blue). The MBSs which emerge at opposite ends of the TSs are depicted as yellow crosses. Unlike the previous cases, the lowest order contribution to the Josephson is not 2π periodic, but 4π periodic in the superconducting phase difference.

such that $\max_\varphi \{|I(\varphi)|\} = |I(\varphi^*)|$, then the so-called critical current of the JJ is defined by

$$I_c = I(\varphi^*). \tag{1.18}$$

In this section, we discuss various examples of JJs, both topological and non-topological, that are motivational for the setups which we will examine in the later chapters of this thesis. Here, our central focus will be on examples with $J_n = 0$, so that the supercurrent vanishes when the phase difference between the SC grains is zero. When $J_n \neq 0$ the supercurrent is offset by a finite phase φ_0, and for that reason, such a JJ is also referred to as φ_0 Josephson junction. A detailed example of such as JJ for both the topologically trivial and non-trivial case will be thoroughly studied in the fourth chapter of this thesis.

Conventional Josephson junctions

We begin with a discussion of conventional Josephson junctions which are characterized by a minimal Josephson energy for $\varphi = 0$,

$$\min_\varphi \{E_J(\varphi)\} \overset{!}{=} E_J(\varphi = 0). \tag{1.19}$$

Alternatively, the critical current of the JJ for $0 < \varphi < \pi$ is positive, $I_c > 0$. We closely follow the references [36, 41].

The first example of a conventional JJ are two weakly-coupled conventional s-wave SC close to their critical temperature T_c [33]. For the case of short junction, $d \ll \xi$ with d the extent of junction region between the SCs and ξ the superconducting coherence length, the current phase relation is determined from the Ginzburg-Landau equations and takes on a sinusoidal form,

$$I(\varphi) = I_c \sin(\varphi) \quad \text{with} \quad I_c = \frac{\pi \Delta_1 \Delta_{\bar{1}}}{4eR_N k_B T}, \tag{1.20}$$

where $\Delta_\tau > 0$ with $\tau = 1, \bar{1}$ are the pairing strengths of the two SCs and R_N is the normal-state resistance of the junction. The Josephson energy is given by

$$E_J(\varphi) = \frac{\hbar I_c}{2e}[1 - \cos(\varphi)], \tag{1.21}$$

and thus takes on the form of a washboard potential. We remark that the findings of Eq. (1.20) and Eq. (1.21) are very general, in the sense that they are for example not dependent of the electron mean free path in the junction region, and thus apply to a multitude of conventional JJs close to their critical temperature T_c.

The second example of a conventional JJ is the SC-Normal metal-SC junction [34, 35]. The setup is shown in Fig. 1.2(a) and described by the Hamiltonian

$$\begin{aligned} H = &\sum_\sigma \int \mathrm{d}^3\mathbf{r}\ \Psi_\sigma^\dagger(\mathbf{r}) \left(-\frac{\hbar^2}{2m}\nabla^2 - \mu\right) \Psi_\sigma(\mathbf{r}) \\ &+ \int \mathrm{d}^3\mathbf{r}\ \left[\Delta(\mathbf{r})\Psi_1^\dagger(\mathbf{r})\Psi_{\bar{1}}^\dagger(\mathbf{r}) + \Delta^*(\mathbf{r})\Psi_{\bar{1}}(\mathbf{r})\Psi_1(\mathbf{r})\right], \end{aligned} \tag{1.22}$$

where the superconducting order parameter is given by

$$\Delta(\mathbf{r}) = \begin{cases} \Delta e^{i\varphi/2} & \text{if } x > d/2 \\ 0 & \text{if } d/2 > x > -d/2 \\ \Delta e^{-i\varphi/2} & \text{if } x < -d/2 \end{cases} . \tag{1.23}$$

Morover, $\Psi^\dagger_\sigma(\mathbf{r})$ $[\Psi_\sigma(\mathbf{r})]$ creates [annihilates] an electron with mass m and spin $\sigma/2 = \pm 1/2$ at position $\mathbf{r}$ in the JJ. Additionally, $\Delta > 0$ denotes the pairing strength, φ is the superconducting phase difference and μ is the chemical potential across the junction. In writing down Eq. (1.23) we have assumed that the superconducting order parameter in the normal metal decreases at length scales which are shorter than the superconducting coherence length. The Hamiltonian in Eq. (1.22) can be diagonalized using a standard Bogoliubov transformation of the form,

$$\begin{aligned} \Psi^\dagger_\uparrow(\mathbf{r}) &= \sum_n \left[\gamma^\dagger_{n\uparrow} u^*_n(\mathbf{r}) - \gamma_{n\downarrow} v_n(\mathbf{r})\right] \\ \Psi^\dagger_\downarrow(\mathbf{r}) &= \sum_n \left[\gamma^\dagger_{n\downarrow} u^*_n(\mathbf{r}) + \gamma_{n\uparrow} v_n(\mathbf{r})\right] , \end{aligned} \tag{1.24}$$

where $\gamma_{n\sigma}$ denotes a quasiparticle with pseudospin $\sigma/2 = \pm 1/2$ and energy E_n. For simplicity, we assume that there are no potentials or spatial variations of the superconducting order parameter on length scales that are comparable to the Fermi wavelength of the electrons. This implies that the quasiparticle momentum is a good quantum number and of the order of the Fermi momentum of the electrons. The wavefunctions $u_n(\mathbf{r})$ and $v_n(\mathbf{r})$ are then determined so that

$$H = E_0 + \sum_{n,\sigma} E_n \gamma^\dagger_{n\sigma} \gamma_{n\sigma}. \tag{1.25}$$

The spectrum E_0, E_n is found by requiring that the wavefunctions $u_n(\mathbf{r})$ and $v_n(\mathbf{r})$ are continuous across the SC-normal metal interfaces. It can be subdivided into a continuous part with energies $|E| > \Delta$ and a discrete part with energies $|E| \leq \Delta$ corresponding to so-called Andreev bound states, which are localized in the junction region. Here, we examine the case of a short junction, $d \ll \xi$. In this limit, only Andreev bound states contribute to the Josephson current [36]. Their spectrum is found to be

$$E(\varphi) = \pm \Delta \cos(\varphi/2). \tag{1.26}$$

We are now in the position to compute the Josephson current given by,

$$I(\varphi) = \frac{2e}{\hbar}\partial_\varphi F, \tag{1.27}$$

where $F = -\ln(Z)/\beta$ is the Free energy, $Z = \mathrm{tr}(e^{-\beta H})$ is the partition function and $\beta = 1/k_B T$. We find that

$$I(\varphi) = \frac{eN\Delta\sin(\varphi/2)}{\hbar}\tanh\left(\frac{\Delta\cos(\varphi/2)}{2k_B T}\right), \tag{1.28}$$

where N denotes the number of conduction channels. We observe that at zero temperature the supercurrent is only carried by the ground state. Hence the supercurrent given in Eq. (1.28) exhibits a jump at $\varphi = \pi$ which signals that the energy branch of the ground state switches from $-\Delta\cos(\varphi/2)$ to $+\Delta\cos(\varphi/2)$.

π Josephson junctions

In this section, we introduce π Josephson Junctions (πJJs) which, unlike the conventional Josephson junctions that were discussed in the previous section, are characterized by a minimum of the Josephson energy that occurs for $\varphi = \pi$ and not $\varphi = 0$,

$$\min_\varphi \{E_J(\varphi)\} \overset{!}{=} E_J(\varphi = \pi). \tag{1.29}$$

Alternatively, the critical current of the JJ for $0 < \varphi < \pi$ is negative, $I_c < 0$. In the following, we will discuss two physical realizations of πJJ which are most relevant for the results of this thesis:

First, we address the realizations of a πJJ in a junction of two conventional s-wave SCs and an intermediate insulating layer doped with magnetic impurities, see also Fig. 1.2(b). We closely follow the reference [38]. The Hamiltonian of the system is given by $H = H_1 + H_{\bar{1}} + H_T$. Here, H_τ describes the superconducting lead $\tau = 1, \bar{1}$ and is given by

$$H_\tau = \sum_{\mathbf{k}}\sum_{\sigma}\frac{\hbar^2\mathbf{k}^2}{2m}\Psi^\dagger_{\tau\sigma}(\mathbf{k})\Psi_{\tau\sigma}(\mathbf{k}) + \sum_{\mathbf{k}}\left(\Delta e^{i\varphi_\tau}\Psi^\dagger_{\tau 1}(\mathbf{k})\Psi_{\tau\bar{1}}(-\mathbf{k}) + \text{H.c.}\right), \tag{1.30}$$

where $\Psi^\dagger_{\tau\sigma}(\mathbf{k})$ [$\Psi_{\tau\sigma}(\mathbf{k})$] creates [annihilates] an electron with spin $\sigma/2 = \pm 1/2$, mass m, and momentum $\mathbf{k}$ in the superconductor τ. Furthermore,

$\Delta > 0$ is the pairing strength and φ_τ is the superconducting phase of the superconductor τ. Without loss of generality, we set $\varphi_1 = \varphi$ and $\varphi_{\bar{1}} = 0$. The tunneling Hamiltonian coupling the two SCs is given by

$$H_T = \sum_n \sum_{\mathbf{k},\mathbf{k}'} \sum_{\sigma,\sigma'} \Psi^\dagger_{1\sigma}(\mathbf{k}) \left[t_{\mathbf{k}\mathbf{k}'} + u_{\mathbf{k}\mathbf{k}',n} \boldsymbol{\sigma} \cdot \mathbf{S}_n\right]_{\sigma\sigma'} \Psi_{\bar{1}\sigma'}(\mathbf{k}') + \text{H.c.}, \qquad (1.31)$$

where $t_{\mathbf{k}\mathbf{k}'}$ is the momentum-dependent amplitude for normal tunneling across the junction and $u_{\mathbf{k}\mathbf{k}',n}$ is the momentum-dependent amplitude for tunneling via the localized spin $\mathbf{S}_n$ at site n in the insulating layer. The conduction electron spin is given by $\boldsymbol{\sigma}$. To second order in the tunneling amplitudes, we find that the zero-temperature Josephson current is given by

$$I(\varphi) = (I_{c,0} - I_{c,s}) \sin(\varphi), \qquad (1.32)$$

with the critical current due to normal tunneling $I_{c,0}$ and the critical current via tunneling through the localized impurities $I_{c,s}$ given by,

$$I_{c,0} = 2e\pi^2\nu_F^2 \Delta t^2/\hbar\ , \ \ I_{c,s} = 2e\pi^2\nu_F^2 \Delta \left[\sum_n S(S+1)u_n^2\right]/\hbar. \qquad (1.33)$$

Here, ν_F is the normal state density of states at the Fermi level and S is the magnitude of the impurity spin. Moreover, t^2 and u_n^2 denote the mean values of $|t_{\mathbf{k}\mathbf{k}'}|^2$ and $|u_{\mathbf{k}\mathbf{k}'}|^2$ over the Fermi surface. From Eq. (1.32) we conclude that our system forms a πJJ for the case when tunneling via the magnetic impurities dominates over normal tunneling, $I_{c,s} > I_{c,0}$.

Second, we discuss the realization of a πJJ in a setup of two conventional $s-$wave SCs coupled by a single-level Quantum dot (QD) in the Coulomb blockade regime, see also Fig. 1.2(c). We follow the reference [39]. The Hamiltonian of the system takes the form $H = H_1 + H_{\bar{1}} + H_D + H_T$, where $H_D = \epsilon_0 n_0 + U(n_0)^2$ is the Hamiltonian of the single level QD with occupation number $n_0 = 0, 1, 2$. Furthermore, $\epsilon_0 < 0$ denotes the QD energy level and U is the Coulomb energy on the QD. The tunneling Hamiltonian H_T is given

$$H_T = \sum_\tau \sum_{\mathbf{k}} \sum_\sigma t_{\tau\mathbf{k}} \Psi^\dagger_{\tau\sigma}(\mathbf{k}) d_\sigma + \text{H.c.}, \qquad (1.34)$$

where $d^\dagger_\sigma$ $[d_\sigma]$ denotes the spin $\sigma/2 = \pm 1/2$ electron creation [annihilation] operator on the QD, and $t_{\tau\mathbf{k}}$ is the momentum-dependent amplitude for the tunneling between the superconductor τ and the QD. In the

Coulomb blockade regime, $U + 2\epsilon_0 \gg -\epsilon_0 > 0$, the ground states of the QD are singly-occupied, $n_0 = 1$, and to second order in the tunneling amplitudes we find that the zero-temperature Josephson current is given by

$$I(\varphi) = -\frac{2e}{\hbar} \sum_{\mathbf{k},\mathbf{k}'} \frac{(t_{1\mathbf{k}} t_{\bar{1}\mathbf{k}'})^2 \left[(u_{1\mathbf{k}} v_{\bar{1}\mathbf{k}'})^2 + (u_{\bar{1}\mathbf{k}'} v_{1\mathbf{k}})^2 \right]}{(E_{1\mathbf{k}} - \epsilon_0)(E_{\bar{1}\mathbf{k}'} - \epsilon_0)(E_{1\mathbf{k}} + E_{\bar{1}\mathbf{k}'})} \sin(\varphi). \tag{1.35}$$

Here, $E_\tau = \sqrt{\xi_{\tau\mathbf{k}} + \Delta^2}$ and $\xi_{\tau\mathbf{k}}$ are the quasiparticle and normal state dispersion in the superconductor τ, respectively. Furthermore, $u_{\tau\mathbf{k}} = (1/\sqrt{2})\sqrt{1 + \xi_{\tau\mathbf{k}}/E_{\tau\mathbf{k}}}$ and $v_{\tau\mathbf{k}} = (1/\sqrt{2})\sqrt{1 - \xi_{\tau\mathbf{k}}/E_{\tau,\mathbf{k}}}$ are the superconducting coherence factors. From Eq. (1.35), we see that the critical current in the setup is always negative and hence the setup realizes indeed a πJJ. This result is to be expected from our considerations for the previous model, because the transfer of a Cooper pair always requires a spin-flip on the QD, which fully suppresses the normal tunneling contribution to the Josephson current.

In the second chapter of this thesis, we will consider a variation of the two models presented above where one of the SCs is replaced by a topological insulator. We will see that the remaining SC still proximity-induces a SC order parameter with opposite sign in the helical edge states of the topological insulator turning the system into a so-called proximity-induced πJJ.

Topological superconductor Josephson junctions

In the previous sections, we have seen multiple examples of JJs between conventional s-wave SCs which all exhibit a Josephson current that is 2π periodic in the phase difference between the superconducting leads. In this section, we discuss the JJ between topological superconductors (TSs) which features an additional contribution to the Josephson current that is 4π periodic in the superconducting phase difference, see also Fig. 1.2(d). This change in the periodicity in the Josephson current is considered to be a hallmark feature of topological superconductivity. In our discussion we will follow the reference [40].

To begin, we provide an intuition on the change in periodicity based on a perturbation theory picture: In a conventional SC JJ, the Josephson current is mediated by Cooper pair tunneling. To lowest order, the latter constitutes a second-order tunneling process in the sense that it takes two virtual electron tunneling events within a sequence of intermediate states to transfer a Cooper pair across the junction. In each of the two tunneling events, the electron which tunnels picks up a phase factor of $e^{i\varphi/2}$ with φ the superconducting phase difference. Thus, in total, a Cooper pair consisting of two electrons acquires a phase factor of $e^{i\varphi}$ leading to a contribution $\propto \sin(\varphi)$ to the Josephson current. Compared to that, in a TS JJ the two MBS which are closest to the junction hybridize and allow for the tunneling of single electrons across the junction. To lowest order, this constitutes a first-order tunneling process in which the electron picks up solely a phase factor of $e^{i\varphi/2}$ yielding a contribution $\propto \sin(\varphi/2)$ to the Josephson current.

To make this intuitive picture more rigorous, we now derive the additional 4π periodic contribution to the Josephson current within the simplest example of two TS realized by spinless p-wave SCs. First, the tight-binding Hamiltonian of a single, one-dimensional, spinless p-wave SC labeled by an index $\tau = 1, \bar{1}$ is given by

$$H_\tau = -\frac{1}{2}\sum_{i=0}^{N-1}\Big(t_\tau c^\dagger_{\tau,i+1}c_{\tau,i} + \Delta_\tau c^\dagger_{\tau,i+1}c^\dagger_{\tau,i} + \mu_\tau c^\dagger_{\tau,i}c_{\tau,i} + \text{H.c.}\Big). \tag{1.36}$$

Here, $c_{\tau,i}$ [$c^\dagger_{\tau,i}$] denotes the electron annihilation [creation] operator in the topological superconductor τ at site i. Moreover, $t_\tau > 0$ denotes the tunneling amplitude, $\Delta_\tau > 0$ the superconducting gap and μ_τ the chemical potential in the topological superconductor τ, respectively. The total number of lattice sites is given by N. The tunneling Hamiltonian which couples the two TS is given by

$$H_\Gamma = \Gamma e^{i\varphi/2}c^\dagger_{1,N}c_{\bar{1},0} + \text{H.c.}, \tag{1.37}$$

where $\Gamma > 0$ is the tunnel coupling strength and the the superconducting phase difference φ was absorbed into the tunneling Hamiltonian via a gauge transformation. The total Hamiltonian of the TS JJ is then given by $H = H_1 + H_{\bar{1}} + H_\Gamma$. For simplicity, we set $\mu_\tau = 0$ and $\Delta \equiv \Delta_\tau = t_\tau$ and rewrite Eq. (1.36) in terms of Majorana operators, $c_{\tau,i} = (\gamma_{\tau,i} + i\gamma'_{\tau,i})/2$. This yields

$$H_\tau = -\frac{i\Delta}{2}\sum_{i=0}^{N-1}\gamma'_{\tau,i}\gamma_{\tau,i+1} \tag{1.38}$$

We see that the MBS at sites $\gamma'_{\tau,N}$ and $\gamma_{\tau,0}$ commute with the Hamiltonian. The corresponding complex fermion operators $C_{\tau,i} = (\gamma_{\tau,0} + i\gamma'_{\tau,N})/2$ thus span the zero-energy ground state subspace of the Hamiltonian H_τ. Assuming that $\Gamma \ll \Delta$, we project the full Hamiltonian H onto the ground state subspace of $H_L + H_R$. It then takes the form

$$H = \frac{i\Gamma}{2} \cos\left(\varphi/2\right) \gamma'_{1,N}\gamma_{\bar{1},0} = \Gamma \cos\left(\varphi/2\right) \left(C_I^\dagger C_I - \frac{1}{2}\right) \tag{1.39}$$

with $C_I = (\gamma_{R,0} + i\gamma'_{L,N})/2$. The zero-temperature Josephson current $I(\varphi) = 2e\partial_\varphi E_{\mathrm{GS}}/\hbar$ with E_{GS} the ground state energy of H is thus for a fixed occupation number $C_I^\dagger C_I = 0, 1$ given by

$$I(\varphi) = \pm \frac{e\Gamma}{\hbar} \sin(\varphi/2) \tag{1.40}$$

where $+$ $(-)$ refers to the case $C_I^\dagger C_I = 1$ ($C_I^\dagger C_I = 0$). This is our final result. We see that, unlike in the case of a conventional SC JJ, the Josephson current in the TS JJ also exhibits a 4π periodic component.

Finally, we emphasize that in general the Josephson current in the TS JJ exhibits also a 2π periodic component corresponding to the transport of finite-energy quasiparticles and it is a major experimental challenge to decouple the 4π periodic Josephson current due to Majorana bound states from the conventional 2π periodic component.

Part I

New platforms for topological superconductivity

CHAPTER 2

Proximity-induced π Josephson Junctions in Topological Insulators

Adapted from:
Constantin Schrade, A. A. Zyuzin, Jelena Klinovaja, and Daniel Loss
"Proximity-induced π Josephson Junctions in Topological Insulators and Kramers Pairs of Majorana Fermions",
Phys. Rev. Lett. **115**, 237001 (2015)

We study two microscopic models of topological insulators in contact with an s-wave superconductor. In the first model the superconductor and the topological insulator are tunnel coupled via a layer of randomly distributed scalar and of randomly oriented spin impurities. Here, we demonstrate that spin-flip tunneling dominates over spin-conserving one. In the second model the tunnel coupling is realized by a spatially non-uniform array of single-level quantum dots with randomly oriented spins. We find that the tunnel region forms a π-junction where the effective order parameter changes sign. Due to the random spin orientation effectively both models exhibit time-reversal symmetry. The proposed π-junctions support topological superconductivity without magnetic fields and can be used to generate and manipulate Kramers pairs of Majorana fermions by gates.

2.1 Introduction

When two s-wave superconductors (SCs) are brought into contact via an insulator doped with magnetic impurities, it was shown by theory [37, 38] and experiment [42] that spin-flip tunneling can induce an equilibrium ground state with a relative phase difference of π between the superconducting order parameters, building up a so-called π Josephson junction (πJJ). It was predicted [43] and experimentally confirmed [44] that a πJJ can be generated by replacing the layer of magnetic impurities by a ferromagnetic metal. A πJJ can also arise when two SCs are tunnel-coupled through an intermediate resonant state in the presence of strong Coulomb interactions [39], as observed in a system of two SCs coupled by a quantum dot (QD) occupied by a single electron [45]. In recent experiments [46–48] it was demonstrated that superconductivity can also be proximity-induced in the helical edge states of a topological insulator (TI) material [49–57] via coupling to an external s-wave SC. These experimental advances have also stimulated the theoretical interest in Josephson junctions based on TIs [58–61]. Motivated by the existence of ordinary πJJs an important and immediate question is: Are there microscopic mechanisms allowing one to induce a superconducting order parameter in the helical edge states of the TI that is of *opposite* relative sign compared to the one of the external s-wave SC, ideally without breaking time-reversal invariance (TRI)? In this work we answer this question in the affirmative.

We propose two setups involving TIs in which such a π-junction is shown to emerge. In the first setup the tunnel coupling is realized by a thin insulating layer of scalar and magnetic impurities with randomly oriented spins and random spatial distribution. We demonstrate that spin-flip tunneling dominates over normal tunneling. In the second setup the tunnel coupling is realized by a spatially non-uniform array of single-level QDs, each of which is occupied by a single spin with random orientation. Critically, the random orientation of spins preserves TRI in an effective description. We note that both setups can be realized by combining the already existing experiments on proximity-inducing superconductivity solely in the edge states of a TI [46–48] and the experiments on πJJs in SC-magnetic insulator-SC [42] and SC-QD-SC devices [45]. We note that the same setup could be assembled in the framework of strip of stripes models [62–68] based on an array of coupled one-dimensional channels with spin-orbit interaction [67]. As a striking consequence we find that the proposed models for proximity-induced πJJs in a TI provide an alternative approach to engineer Kramers pairs of Majorana fermions (MFs) [32, 69–78] easily movable by gates. Remarkably, no magnetic fields are needed. More precisely we consider two TI samples that form a proximity-induced πJJs with respect to one another and allow for tunneling between them in the finite space region, at the ends of which the MFs emerge.

2.2 Josephson junction models

In the first model we consider a bulk s-wave SC connected by a tunnel contact to the edge of a 2D TI, see Fig. 2.1(a). The Hamiltonian of the system is given by

$$\mathrm{H}_1 = \mathrm{H}_{\mathrm{BCS}} + \mathrm{H}_{\mathrm{TI}} + \frac{1}{2}\int \mathrm{d}\mathbf{r}\,\mathrm{d}x\ \left[\Psi^\dagger(\mathbf{r})\cdot \bar{\mathrm{T}}_1(\mathbf{r},x)\Phi(x) + \mathrm{H.c.}\right], \tag{2.1}$$

with the tunneling matrix $\bar{\mathrm{T}}_1(\mathbf{r},x) = \mathrm{T}_1(\mathbf{r},x)(1+\tau^z)/2 - \mathrm{T}_1^*(\mathbf{r},x)(1-\tau^z)/2$. Here, $\mathrm{H}_{\mathrm{BCS}} = (1/2)\int \mathrm{d}\mathbf{r}\ \Psi^\dagger(\mathbf{r})\cdot[-(\hbar^2\partial_{\mathbf{r}}^2/2m+\mu)\tau^z - \Delta_{sc}\sigma^y\tau^y]\Psi(\mathbf{r}) +$ H.c. is the BCS Hamiltonian of the SC, μ being the chemical potential in the SC and m being the electron mass, and $\mathrm{H}_{\mathrm{TI}} = (1/2)\int \mathrm{d}x\ [\Phi^\dagger(x)\cdot(-i\hbar v_F\sigma^z\partial_x)\Phi(x) + \mathrm{H.c.}]$ is the Hamiltonian of the TI edge with the Fermi velocity v_F. Without loss of generality, we assume that the superconducting order parameter Δ_{sc} is positive. The electron Nambu operator in the SC (TI) is given by $\Psi(\mathbf{r}) = (\Psi_\uparrow(\mathbf{r}), \Psi_\downarrow(\mathbf{r}), \Psi_\uparrow^\dagger(\mathbf{r}), \Psi_\downarrow^\dagger(\mathbf{r}))$ $[\Phi(x) = (\mathrm{R}(x), \mathrm{L}(x), \mathrm{R}^\dagger(x), \mathrm{L}^\dagger(x))]$. The Pauli matrices τ^a (σ^a) with $a = x, y, z$ act in particle-hole (spin) space The slowly-varying spin-up right (spin-down left) mover fields $\mathrm{R}(x)$ $[\mathrm{L}(x)]$ are defined around the Fermi points $\pm k_F$ which in turn are determined by the position of the chemical potential μ_{TI} in the TI defined with respect to the Dirac point. The last term in Eq. (2.1) describes the tunneling between points $\mathbf{r}$ of the SC and points x on the edge of the TI. The interface between the SC and the TI is assumed to be rough such that the thinnest regions of the interface give the highest probability for electrons to tunnel between the SC and the TI and there can be several impurities at the vicinity of the point contact. We model these thinnest regions located at points x_ℓ by point contacts. The tunnel contact between the SC and the TI is doped with randomly distributed scalar and magnetic impurities with randomly oriented spins $\mathbf{S}_{\ell,k} = (S_{\ell,k}^x, S_{\ell,k}^y, S_{\ell,k}^z)$. Here $\mathbf{S}_{\ell,k}$ is the operator of the k-th localized spin close to the point contact x_ℓ on the TI sample. The tunneling occurs via the virtual states of the scalar and magnetic impurities with the amplitude given by

$$\mathrm{T}_1(\mathbf{r}, x) = \delta(\mathbf{r} - x\,\mathbf{e_x}) \sum_{\ell,k} \delta(x - x_\ell) \left[t_k + \sum_{a=x,y,z} u_k^a \sigma^a S_{\ell,k}^a \right]. \tag{2.2}$$

Here, $\mathrm{e_x}$ is a unit vector pointing along the TI edge. The normal (spin-flip) tunneling is parametrized by a complex amplitude t_k (u_k^a) with scalar impurities contributing to the amplitude t_k only.

In the second model we consider a bulk s-wave SC coupled to a 2D TI via a spatially non-uniform array of single-level QDs, see Fig. 2.1(b). The Hamiltonian of the system is given by

$$\begin{aligned} \mathrm{H}_2 &= \mathrm{H_{BCS}} + \mathrm{H_{TI}} + \mathrm{H_D} \\ &+ \frac{1}{2} \sum_j \left[t_{j,1}\, D_j^\dagger \cdot \tau^z \Psi(\mathbf{r}_j) + t_{j,2}\, D_j^\dagger \cdot \tau^z \Phi(x_j) + \mathrm{H.c.} \right]. \end{aligned} \tag{2.3}$$

Here, $\mathrm{H_D} = (1/2) \sum_j (-\epsilon_j\, D_j^\dagger \cdot \tau^z D_j + U_j\, n_{j,\uparrow} n_{j,\downarrow}) + \mathrm{H.c.}$ is the Hamiltonian of an array of single-level QDs at energies $\epsilon_j > 0$ and with amplitudes U_j of the Coulomb interaction on the QDs and $D_j = (D_{j,\uparrow}, D_{j,\downarrow}, D_{j,\uparrow}^\dagger, D_{j,\downarrow}^\dagger)$ is the Nambu operator on the jth QD. The occupation number operators for electrons with the spin σ on the jth QD are given by $n_{j,\sigma} = D_{j,\sigma}^\dagger D_{j,\sigma}$. Tunneling occurs at points $\mathbf{r}_j$ and x_j on the SC and the TI, respectively, and is described by tunneling amplitudes $t_{j,1}$ and $t_{j,2}$.

2.3 Proximity-induced π Josephson junctions

We first discuss the model shown in Fig. 2.1(a) and described by Eqs. (2.1) and (2.2). We neglect the inverse proximity effect due to magnetic impurities. By integrating out the degrees of freedom of the SC and including contributions up to second order in the tunneling amplitudes we see that the equation of motion for the Green's function $g(x, x')$ of the TI in frequency space is given by

$$g^{-1}(x) \cdot g(x, x') = \delta(x - x') + \int \mathrm{d}x_1 \Sigma(x, x_1) \cdot g(x_1, x') \tag{2.4}$$

with $g^{-1}(x) = i\omega + i\hbar v_F \sigma^z \partial_x$ and ω the fermionic Matsubara frequency. In leading order, the electron self-energy in the TI is given by

$$\Sigma(x, x_1) = \int \mathrm{d}^3 r\; \mathrm{d}^3 r'\; \mathrm{T}_1^\dagger(\mathbf{r}, x) \cdot G(\mathbf{r} - \mathbf{r}') \cdot \mathrm{T}_1(\mathbf{r}', x_1). \tag{2.5}$$

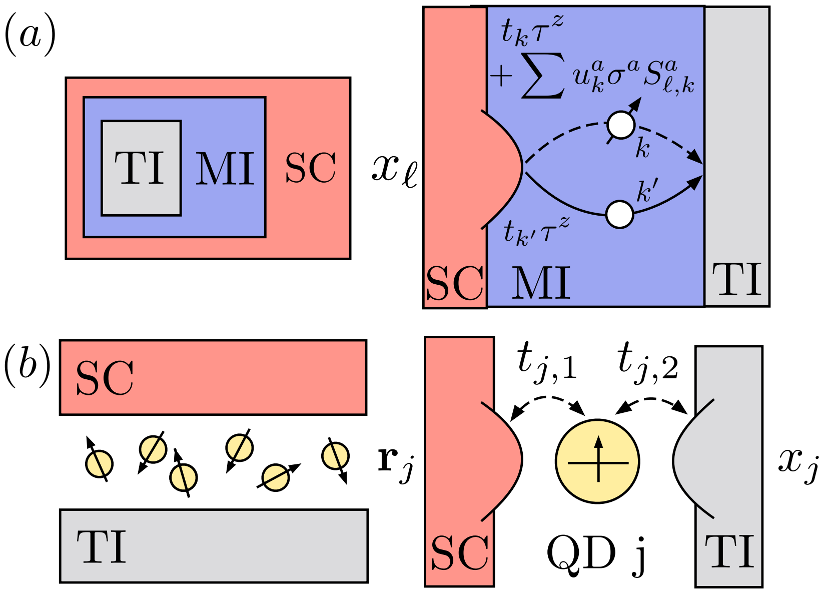

Figure 2.1: Setups to generate a proximity-induced Josephson π-junction in topological insulators (TIs). a) An s-wave SC (red) couples to a TI (grey) via an insulator doped with magnetic and scalar impurities (MI, magnetic insulator, blue). If the spin-flip tunneling rates are larger than the normal tunneling rates superconducting gaps with opposite sign are induced in the TI samples. b) Top view. Instead of the MI the SC is coupled to the TI via a spatially non-uniform array of single-level QDs in the Coulomb blockade regime. The array of QDs is occupied with randomly oriented electron spins.

Here, $G(\mathbf{r}-\mathbf{r}')$ denotes the Green's function of the bare clean homogeneous three-dimensional SC defined by $G^{-1}(\mathbf{r})\cdot G(\mathbf{r}-\mathbf{r}')=\delta(\mathbf{r}-\mathbf{r}')$ with $G^{-1}(\mathbf{r})=i\omega+(\hbar^2\partial_{\mathbf{r}}^2/2m+\mu)\tau^z-\Delta_{sc}\sigma^y\tau^y$. At vanishing relative distance a solution to this equation is given

$$G(\boldsymbol{r}=0)=\frac{-\pi\nu}{\sqrt{\omega^2+\Delta_{sc}^2}}\left[\Delta_{sc}\sigma^y\tau^y+i\omega\right], \tag{2.6}$$

with $\nu=\frac{mp_F}{2\pi^2}$ the normal-state density of states per spin and p_F the Fermi momentum in the SC. We adopt several assumptions to simplify Eq. (2.5). First, the distribution of impurities is assumed to be almost continuous and hence sums over impurities at discrete positions are replaced by integrals over impurity densities. Second, terms that are linear in the Pauli matrices σ^a vanish after averaging over the random orientation of the spins $\mathbf{S}_{\ell,k}$. Third, at some fixed x_ℓ tunneling contributions from points $x_{\ell'}$ for $\ell' \neq \ell$ can be neglected. The contribution of these terms to the effective Hamiltonian can be incorporated in the chemical potential [79]. These assumptions imply that

$$\int \mathrm{d}x_1 \Sigma(x, x_1) \cdot g(x_1, x') \approx -\Big[i\omega(\Gamma + \Gamma_S) \\ -\Delta_{sc}(\Gamma - \Gamma_S)\sigma^y \tau^y \Big] \cdot \frac{g(x, x')}{\sqrt{\omega^2 + \Delta_{sc}^2}}, \tag{2.7}$$

with the scattering rates

$$\Gamma = \pi \nu n_0 |\sum_k t_k|^2, \tag{2.8}$$

$$\Gamma_S = \pi \nu n_S S(S+1) \sum_{k,a} |u_k^a|^2 /3. \tag{2.9}$$

Here, n_0 is the concentration of point contacts that allow for spin-conserved tunneling, while n_S is the concentration of point contacts that allow for spin-flip tunneling. Impurity spins are non-interacting, *i.e.* $\langle \mathbf{S}_{\ell,k} \mathbf{S}_{\ell',k'} \rangle = S(S+1)\delta_{\ell\ell'}\delta_{kk'}$, with $\langle ... \rangle$ meaning the average over random spin directions and S being the magnitude of the impurity spin. In particular, the average vanishes for different impurity spins. This implies that in the expression for the scattering rate Γ_S terms $\propto u_k^a u_{k'}^a$ with $k \neq k'$ vanish as well. The Ruderman-Kittel-Kasuya-Yosida (RKKY) interactions between impurity spins are also neglected for two reasons: First, their amplitude is by orders of magnitude smaller than spin-flip scattering rates [80]. Second, the low temperature ground state of the MI is a spin-glass, not a ferromagnet. This is because the sign of the RKKY interactions is random due to the non-uniform spin distribution. Also the exchange couplings are highly anisotropic when mediated by spin-momentum locked TI surface states. In the spin-glass the average expectation value of spin is zero, *i.e.* on average TRI is preserved. Similarly, the Van Vleck interaction recently considered for TIs [81,82] is also neglected assuming a sufficiently large seperation between the magnetic impurities. The effective order parameter in the TI for $\omega \ll \Delta_{sc}, \Gamma, \Gamma_S$ is given by

$$\Delta_{\Gamma,\Gamma_S} \approx \Gamma - \Gamma_S. \tag{2.10}$$

Interestingly, if $\Gamma_S > \Gamma$ the effective order parameter can become negative. Such a situation naturally emerges if the tunnel contact contains a large number of magnetic and scalar impurities. At a particular point x_ℓ the electron tunneling amplitude via some magnetic impurity k is $t_k + \sum_a u_k^a \sigma^a S_{\ell,k}^a$ and $t_{k'}$ for some scalar impurity k'. We assume that $|t_k| \approx |t_{k'}|$, while generally their phases are random. Thus, for many impurities the normal tunneling contributions in Eq. (2.8) destructively interfere, so that $\sum_k t_k \approx 0$. As a result, $\Gamma_S > \Gamma$ can be realized and Δ_{Γ,Γ_S} becomes negative.

Next we discuss the model of an s-wave SC coupled to a 2D TI via an array of QDs, as depicted in Fig. 2.1(b) and described by Eq. (2.3). We will work in the Coulomb blockade regime. Thus, we assume singly occupied QDs with the electron spin on the QDs being randomly oriented. In the limit of small tunneling amplitudes that couple the SC and the TI to the QD we use a Schrieffer-Wolff transformation [83] to map the Hamiltonian H_2 as given in Eq. (2.3) onto a Hamiltonian H_1 of the form as given in Eq. (2.1) with $t_k \equiv 0$. The physical interpretation is that due to the large Coulomb interactions on the QDs only spin-flip tunneling of electrons through the dots is allowed [39]. From the discussion of the first model we can conclude again that $\Gamma_S > 0$, while $\Gamma \approx 0$. Thus, we see that in both models we obtain a proximity-induced πJJ in the tunneling region.

2.4 Kramers pairs of Majorana fermions

In a TI coupled to an s-wave SC magnetic fields was used to induce MFs [2], however, they acts detrimental on superconductivity. In the absence of magnetic fields, Kramers pairs of MFs can emerge as was shown for unconventional SCs [69–73] as well as nanowires [32, 74–76, 84] and TIs [77, 78, 85] in proximity to conventional SCs. In particular, Kramers pairs of MFs appear due to πJJs in nanowires [73–75] or in 3D TI films [78]. Here, we make use of the πJJ models introduced above and propose two setups (labeled by $N = 1, 2$) that host Kramers pairs of MFs based on two 2D TIs, which, as a major advantage, can easily be moved by tuning a tunnel barrier.

We consider two TIs labeled by $n = 1, 2$. In the first (second) setup, edge states are of opposite (same) helicity and the chemical potentials are tuned to be opposite (to be the same) with $\mu_1 = -\mu_2$ ($\mu_1 = \mu_2$), as illustrated in Fig. 2.2b (Fig. 2.2c). Both TIs are brought into proximity to an s-wave SC. In the the first TI, the tunnel contact is doped with scalar and magnetic impurities with randomly oriented spins or, equivalently, an array of QDs with randomly oriented spins is used. As shown above, a π-junction emerges and the proximity-induced order parameter in the first TI acquires the opposite sign to the bulk SC, $-\Delta_1 < 0$. The tunnel contact between the SC and the second TI does not contain a spin-flip source. Thus, the corresponding order parameter is of the same sign as in the SC, $\Delta_2 > 0$. The induced superconductivity in the nth TI of the Nth setup is described by the Hamiltonian

$$H_{sc,n}^{(N)} = (-1)^{(N-1)(n-1)} \frac{\Delta_n}{2} \int \mathrm{d}x \left[\mathrm{L}_n^\dagger \mathrm{R}_n^\dagger - \mathrm{R}_n^\dagger \mathrm{L}_n^\dagger + \mathrm{H.c.} \right] \tag{2.11}$$

in the basis $\Phi_n(x) = (\mathrm{R}_n(x), \mathrm{L}_n(x), \mathrm{R}_n^\dagger(x), \mathrm{L}_n^\dagger(x))$. For the first (second) TI of the first setup we have introduced slowly-varying spin-up (spin-down) right-mover $\mathrm{R}_1(x)$ $[\mathrm{R}_2(x)]$ and spin-down (spin-up) left-mover $\mathrm{L}_1(x)$ $[\mathrm{L}_2(x)]$ fields defined around the Fermi points $\pm k_F$. In the second setup $\mathrm{R}_2(x)$ $[\mathrm{L}_2(x)]$ is the spin up (spin down) mode, see Fig. 2.2.

The two TIs are coupled via a tunnel barrier placed in the region $0 \leqslant x \leqslant L$ as shown in Fig. 2.2(a) Neglecting the fast-oscillating terms [31], we find that the tunneling Hamiltonian in the first setup is given by

$$\mathrm{H}_t^{(1)} = \frac{t}{2} \int_0^L \mathrm{d}x [e^{i\phi} \left(\mathrm{R}_2^\dagger \mathrm{L}_1 - \mathrm{L}_1 \mathrm{R}_2^\dagger \right) + e^{-i\phi} \left(\mathrm{L}_2^\dagger \mathrm{R}_1 - \mathrm{R}_1 \mathrm{L}_2^\dagger \right) + \mathrm{H.c.}], \tag{2.12}$$

while in the second setup by

$$\mathrm{H}_t^{(2)} = \frac{t}{2} \int_0^L \mathrm{d}x [e^{i\phi} \left(\mathrm{R}_2^\dagger \mathrm{R}_1 - \mathrm{R}_1 \mathrm{R}_2^\dagger \right) + e^{-i\phi} \left(\mathrm{L}_2^\dagger \mathrm{L}_1 - \mathrm{L}_1 \mathrm{L}_2^\dagger \right) + \mathrm{H.c.}]. \tag{2.13}$$

Here, t (ϕ) is the tunneling amplitude (phase) between two TIs. The total Hamiltonian is $H^{(N)} = \sum_n (H_{TI,n} + H_{sc,n}^{(N)}) + \mathrm{H}_t^{(N)}$, where the kinetic part $H_{TI,n} \equiv H_{TI}$ is identical for both TIs and was introduced in Eq. (2.1). The tunneling phase can be removed from the total Hamiltonian by a suitable gauge transformation [111]. In both setups, we find that a topological phase transition accompanied by the bulk gap closing and reopening occurs at the point

$$t = \sqrt{\Delta_1 \Delta_2}. \tag{2.14}$$

In the second setup, there is an additional constraint $\Delta_1 \neq \Delta_2$. If $t > \sqrt{\Delta_1 \Delta_2}$, there is one Kramers pair of MFs localized at the interfaces at $x = 0$ and one at $x = L$ [31]. The localization lengths are inversely proportional to the opened gaps [111]. Thus, in regions with no tunnel coupling between the TIs the localization lengths are the superconducting

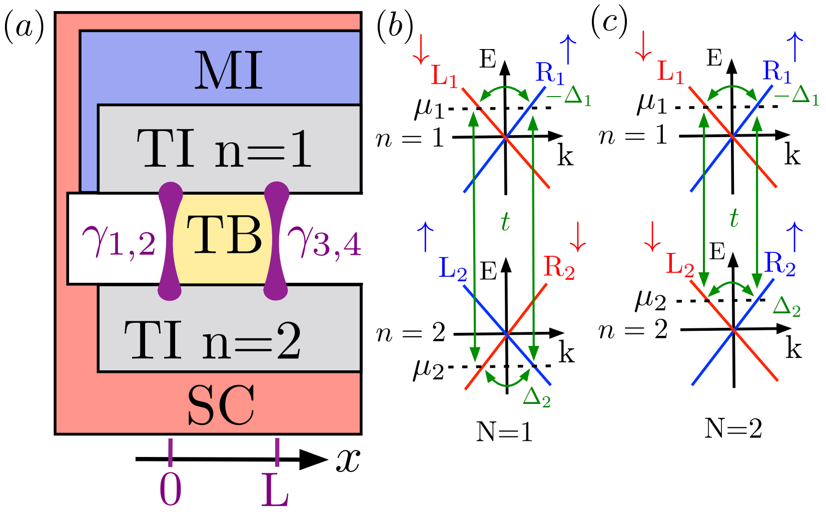

Figure 2.2: (a) Setup hosting Kramers pairs of MFs. Two TIs (grey rectangles) are placed on top of an underlying s-wave SC (red) such that proximity superconductivity is induced in both TIs. Importantly, the first TI is coupled through a magnetic insulator (MI, blue) resulting in the πJJ. The tunnel barrier (TB, yellow) between the edges of two TIs extends from $x = 0$ to $x = L$. One Kramers pair of MFs $\gamma_{1,2}$ [$\gamma_{3,4}$] (purple) is localized at the $x = 0$ [$x = L$] end of the TB and can be manipulated by tuning the length L of the TB. The spectrum of two pairs of TI edge modes is considered in (b) for the first setup and in (c) for the second setup. (b) Edge modes of the same TI are coupled by proximity-induced pairing amplitudes $-\Delta_1 < 0$ and $\Delta_2 > 0$, *resp.* The chemical potentials are opposite for the two TIs, $\mu_1 = -\mu_2$. The helicities of the edge states are opposite (indicated by the coloring in red and blue). The tunneling (t) couples a right-moving state in the first TI to a left-moving state in the second TI, and vice versa. (c) The two TIs have the same chemical potential, $\mu_1 = \mu_2$, and the same helicities. The tunneling (t) couples a right-[left-] moving state in the first TI to a right-[left-] moving state in the second TI.

coherence lengths $\xi_n = \hbar v_F/\Delta_n$, while in regions with $t > \sqrt{\Delta_1\Delta_2}$ they are given by

$$\xi^{(1)} = 2\hbar v_F/(\sqrt{(\Delta_1-\Delta_2)^2+4t^2}-\Delta_1-\Delta_2) \tag{2.15}$$

$$\xi^{(2)}_{\pm} = \frac{2\hbar v_F}{|\Delta_1-\Delta_2| \pm \Re\sqrt{(\Delta_1+\Delta_2)^2-4t^2}}. \tag{2.16}$$

Superscript (1) [(2)] corresponds to first [second] setup and $\Re$ means the real part of a complex number. In both setups we assume that L is much longer than the localization lengths $\xi^{(1)}_{\text{max}} \equiv \max\{\xi_1, \xi_2, \xi^{(1)}\}$ ($\xi^{(2)}_{\text{max}} = \max\{\xi_2, \xi^{(2)}_{-}\}$ for $\Delta_1 > \Delta_2$ and $\xi^{(2)}_{\text{max}} = \max\{\xi_1, \xi^{(2)}_{-}\}$ for $\Delta_1 < \Delta_2$). Hence the wavefunctions of the MFs localized at the two different interfaces do not overlap. If L is comparable or shorter than the localization length of the MFs they hybridize into two fermionic states whose energies are nonzero in general [1,87,88]. In a InAs/GaSb (HgTe/CdTe) TI the localization length is of the order of 0.5 μm (5 μm) [111]. Finally, we emphasize that if the relative sign of the proximity induced gaps is the same there exists no topological phase, see [111] for illustrative phase diagrams.

2.5 Conclusions

We propose two setups to realize a proximity-induced πJJ in a TI in the presence of TRI. Both setups rely on the tunnel coupling of a TI sample to an s-wave bulk SC either via a layer of randomly distributed scalar and magnetic impurities with randomly oriented spins or via a spatially nonuniform array of QDs each of which is occupied by a randomly oriented spin. In either case spin-flip tunneling dominates over normal tunneling and a π-junction emerges. The randomly oriented spins ensure that there is effectively no breaking of TRI. Such proximity-induced π-junctions can be used to generate and manipulate Kramers pairs of MFs in edge states of tunnel-coupled TIs.

2.A Energy spectrum

We find that the bulk spectrum of the Hamiltonian $H^{(1)}$ from the main text is given by

$$E_{1,s,\pm}(k) = s\left[(\hbar v_F k)^2 + \left(\Delta_+ \pm \sqrt{\Delta_-^2 + t^2}\right)^2\right]^{1/2}, \tag{2.17}$$

where k is the momentum in the TI, and $s = \pm 1$. Similarly the bulk spectrum of the Hamiltonian $H^{(2)}$ from the main text is given by

$$E_{2,s,\pm}(k) = s\left[(\hbar v_F k)^2 + \Delta_+^2 + \Delta_-^2 + t^2 \pm 2\sqrt{W(k)}\right]^{1/2} \tag{2.18}$$

with $W(k) = (\hbar v_F k)^2 t^2 + \Delta_+^2(\Delta_-^2 + t^2)$. Here, we also introduced the notations $\Delta_\pm = (\Delta_1 \pm \Delta_2)/2$. Both spectra $E_{1,s,\pm}(k)$ and $E_{2,s,\pm}(k)$ are twofold degenerate as expected for time-reversal invariant systems.

We find that the spectrum is gapless at $k = 0$ if

$$t = \sqrt{\Delta_1 \Delta_2}, \tag{2.19}$$

and is gapped otherwise. Here, for setup $N = 2$ we need the additional condition that $\Delta_1 \neq \Delta_2$. Also the spectral gap for the setup $N = 2$ closes at some finite momentum if $t > \Delta_1 = \Delta_2$. We now assume that $\Delta_1 \neq \Delta_2$ and confirm that Eq. (2.19) defines a topological phase transition. This means that there should be MFs localized at the boundary between two space regions with $t > \sqrt{\Delta_1 \Delta_2}$ and $t < \sqrt{\Delta_1 \Delta_2}$.

2.B Wavefunctions of the Majorana fermions

The operator defining a MF, which is a zero-energy bound state, is generally given by $\gamma_j^{(N)} \equiv (\gamma_j^{(N)})^\dagger = \sum_{n=1,2} \int \mathrm{d}x \; \psi_{n,j}^{(N)}(x) \cdot \Phi_n(x)$ with the wavefunction (vector)

$$(\psi_{n,j}^{(N)})^T(x) = \begin{pmatrix} f_{n,j}^{(N)}(x) \\ g_{n,j}^{(N)}(x) \\ (f_{n,j}^{(N)})^*(x) \\ (g_{n,j}^{(N)})^*(x) \end{pmatrix} \tag{2.20}$$

for some complex-valued functions $f_{n,j}^{(N)}(x)$ and $g_{n,j}^{(N)}(x)$. The index $j = 1, 2$ distinguishes between two MFs belonging to the same Kramers pair. The form of these functions is different for different setups.

Without loss of generality, we focus below on the left interfaces at which the tunneling amplitude jumps from $t = 0$ at $x < 0$ to $t = t_0 > \sqrt{\Delta_1 \Delta_2}$ for $x > 0$.

First setup.

We find that for the first setup the interface hosts a Kramers pair of MFs given by

$$\begin{gathered} -if_{n,1}^{(1)} = (g_{n,1}^{(1)})^* = \begin{cases} \left(\delta_{n1} \frac{\sqrt{\Delta_-^2 + t_0^2} - \Delta_-}{t_0} e^{ik_F x} + \delta_{n2} e^{-ik_F x}\right) e^{\frac{i\phi}{2}} e^{-x/\xi^{(1)}} & \text{if } x > 0 \\ \left(\delta_{n1} \frac{\sqrt{\Delta_-^2 + t_0^2} - \Delta_-}{t_0} e^{ik_F x} e^{x/\xi_1} + \delta_{n2} e^{-ik_F x} e^{x/\xi_2}\right) e^{\frac{i\phi}{2}} & \text{if } x < 0 \end{cases}, \\ f_{n,2}^{(1)} = (-1)^n (g_{n,1}^{(1)})^*, \quad g_{n,2}^{(1)} = (-1)^{n-1} (f_{n,1}^{(1)})^* \end{gathered} \tag{2.21}$$

with the localization lengths given by

$$\begin{aligned}\xi^{(1)} &= \hbar v_F / (\sqrt{\Delta_-^2 + t_0^2} - \Delta_+) \\ \xi_n &= \hbar v_F / \Delta_n .\end{aligned} \tag{2.22}$$

In Fig. S2.3(a) the localization length $\xi^{(1)}$ is plotted for different valus of t_0 in color scale versus Δ_1 and Δ_2. Note that the solutions for given N are orthogonal, $\psi_{n,1}^{(N)} \cdot (\psi_{n,2}^{(N)})^T = 0$, thus forming a Kramers pair. The localization length of the MF is given by $\xi_{\text{max}}^{(1)} = \max\{\xi^{(1)}, \xi_1, \xi_2\}$ and is plotted in Fig. S2.3(b).

Second setup.

The interface at $x = 0$ of the second setup also hosts a Kramers pair of MFs. For $\Delta_- > 0$ the Kramers pair of MFs is given by

$$\begin{aligned}
f_{n,1}^{(2)} &= e^{ik_F x} \\
&\times \begin{cases}
\left[i\delta_{n2} \left(\frac{\Delta_+ - \sqrt{\Delta_+^2 - t_0^2}}{2\sqrt{\Delta_+^2 - t_0^2}} e^{-x/\xi_+^{(2)}} - \frac{\Delta_+ + \sqrt{\Delta_+^2 - t_0^2}}{2\sqrt{\Delta_+^2 - t_0^2}} e^{-x/\xi_-^{(2)}} \right) e^{i\frac{\phi}{2}} \right. & \text{if } x \geq 0,\ \Delta_+ > t_0 \\
\quad \left. - \frac{\delta_{n1} (e^{-x/\xi_-^{(2)}} - e^{-x/\xi_+^{(2)}}) t_0 e^{-i\frac{\phi}{2}}}{2\sqrt{\Delta_+^2 - t_0^2}} \right] & \\
-\left[\delta_{n1} \frac{t_0 x}{\hbar v_F} e^{-i\frac{\phi}{2}} + i\delta_{n2} (1 + \frac{t_0 x}{\hbar v_F}) e^{i\frac{\phi}{2}} \right] e^{-x/\xi_\pm^{(2)}} & \text{if } x \geq 0,\ \Delta_+ = t_0 \\
-\left[\delta_{n1} \frac{t_0 \sin(k^{(2)} x)}{\sqrt{t_0^2 - \Delta_+^2}} e^{-i\frac{\phi}{2}} \right. & \text{if } x \geq 0,\ \Delta_+ < t_0 \\
\quad \left. + i\delta_{n2} \left(\frac{\Delta_+ \sin(k^{(2)} x)}{\sqrt{t_0^2 - \Delta_+^2}} + \cos(k^{(2)} x) \right) e^{i\frac{\phi}{2}} \right] e^{-x/\xi_\pm^{(2)}} & \\
-i\delta_{n2}\, e^{i\frac{\phi}{2}} e^{x/\xi_2} & \text{if } x < 0
\end{cases} \\
g_{n,1}^{(2)} &= i(f_{n,1}^{(2)})^*, \quad f_{n,2}^{(2)} = -(g_{n,1}^{(2)})^*, \quad g_{n,2}^{(2)} = (f_{n,1}^{(2)})^*,
\end{aligned} \tag{2.23}$$

while for $\Delta_- < 0$ it is given by

$$
\begin{aligned}
f^{(2)}_{n,1} &= e^{ik_F x} \\
&\times \begin{cases}
\Bigg[-\delta_{n1} \left(\frac{\Delta_+ - \sqrt{\Delta_+^2 - t_0^2}}{2\sqrt{\Delta_+^2 - t_0^2}} e^{-x/\xi_+^{(2)}} - \frac{\Delta_+ + \sqrt{\Delta_+^2 - t_0^2}}{2\sqrt{\Delta_+^2 - t_0^2}} e^{-x/\xi_-^{(2)}} \right) e^{-i\frac{\phi}{2}} & \text{if } x \geq 0,\ \Delta_+ > t_0 \\
\quad + \frac{i\delta_{n2} \left(e^{-x/\xi_+^{(2)}} - e^{-x/\xi_-^{(2)}} \right) t_0 e^{i\frac{\phi}{2}}}{2\sqrt{\Delta_+^2 - t_0^2}} \Bigg] & \\
\left[\delta_{n1} (1 + \frac{t_0 x}{\hbar v_F}) e^{-i\frac{\phi}{2}} - i\delta_{n2}\ \frac{t_0 x}{\hbar v_F}\ e^{i\frac{\phi}{2}} \right] e^{-x/\xi_\pm^{(2)}} & \text{if } x \geq 0,\ \Delta_+ = t_0 \\
\Bigg[-i\delta_{n2} \frac{t_0 \sin(k^{(2)} x)}{\sqrt{t_0^2 - \Delta_+^2}} e^{i\frac{\phi}{2}} & \text{if } x \geq 0,\ \Delta_+ < t_0 \\
\quad + \delta_{n1} \left(\frac{\Delta_+ \sin(k^{(2)} x)}{\sqrt{t_0^2 - \Delta_+^2}} + \cos(k^{(2)} x) \right) e^{-i\frac{\phi}{2}} \Bigg] e^{-x/\xi_\pm^{(2)}} & \\
\delta_{n1}\ e^{-i\frac{\phi}{2}} e^{x/\xi_1} & \text{if } x < 0
\end{cases} \\
g^{(2)}_{n,1} &= i(f^{(2)}_{n,1})^*, \quad f^{(2)}_{n,2} = -(g^{(2)}_{n,1})^*, \quad g^{(2)}_{n,2} = (f^{(2)}_{n,1})^*.
\end{aligned}
\tag{2.24}
$$

Again, the two wavefunctions for given N are orthogonal and thus forming a Kramers pair. We have defined the wavenumber

$$
k^{(2)} = \sqrt{|\Delta_+^2 - t_0^2|/\hbar v_F} \tag{2.25}
$$

and the localization lengths

$$
\xi_\pm^{(2)} = \frac{\hbar v_F}{|\Delta_-| \pm \Re\sqrt{\Delta_+^2 - t_0^2}}\,. \tag{2.26}
$$

For different values of t_0 the localization lengths $\xi_\pm^{(2)}$ are displayed in Fig. S2.3(c) and (d) in a color scale plot as a function of Δ_1 and Δ_2. For $t_0 \leq \Delta_+$ the spectral gap closes at zero momentum while for $t_0 > \Delta_+$ it closes at some finite momentum. For $\Delta_- > 0$ ($\Delta_- < 0$) the localization length of the MF is given by $\xi^{(2)}_{\text{max}} = \max\{\xi_2, \xi_-^{(2)}\}$ ($\xi^{(2)}_{\text{max}} = \max\{\xi_1, \xi_-^{(2)}\}$) and is plotted in Fig. S2.3(e). The fast-oscillating factors have explicitly been restored in the wavefunctions. We see that for $\Delta_1 = \Delta_2$ the MF wavefunction is delocalized. In the limit when $L \gg \xi^{(N)}_{\text{max}}$ the interfaces at $x = 0$ and $x = L$ can be considered as independent and a calculation of the MF wavefunctions at $x = L$ can be performed analogously. We assume that the induced gaps are given by $\Delta_1 = 0.1$ meV, $\Delta_2 = 0.2$ meV, and the tunnel coupling is set to $t = 0.2$ meV. In a InAs/GaSb (HgTe/CdTe) TI the Fermi velocity is given by $v_F = 4.6 \times 10^4$ m s^{-1} [47] (5.5×10^5 m s^{-1} [50]). This gives an estimate of the localization length of the order of 0.5 μm (5 μm).

Finally for setup N the tunneling phase ϕ can be absorbed into a redefinition of the electron operators by the gauge transformations

$$\begin{aligned} \mathrm{R}_n &\mapsto \exp\left((-1)^{n(N-1)}\frac{i\phi}{2}\right)\mathrm{R}_n \\ \mathrm{L}_n &\mapsto \exp\left(-(-1)^{n(N-1)}\frac{i\phi}{2}\right)\mathrm{L}_n. \end{aligned} \tag{2.27}$$

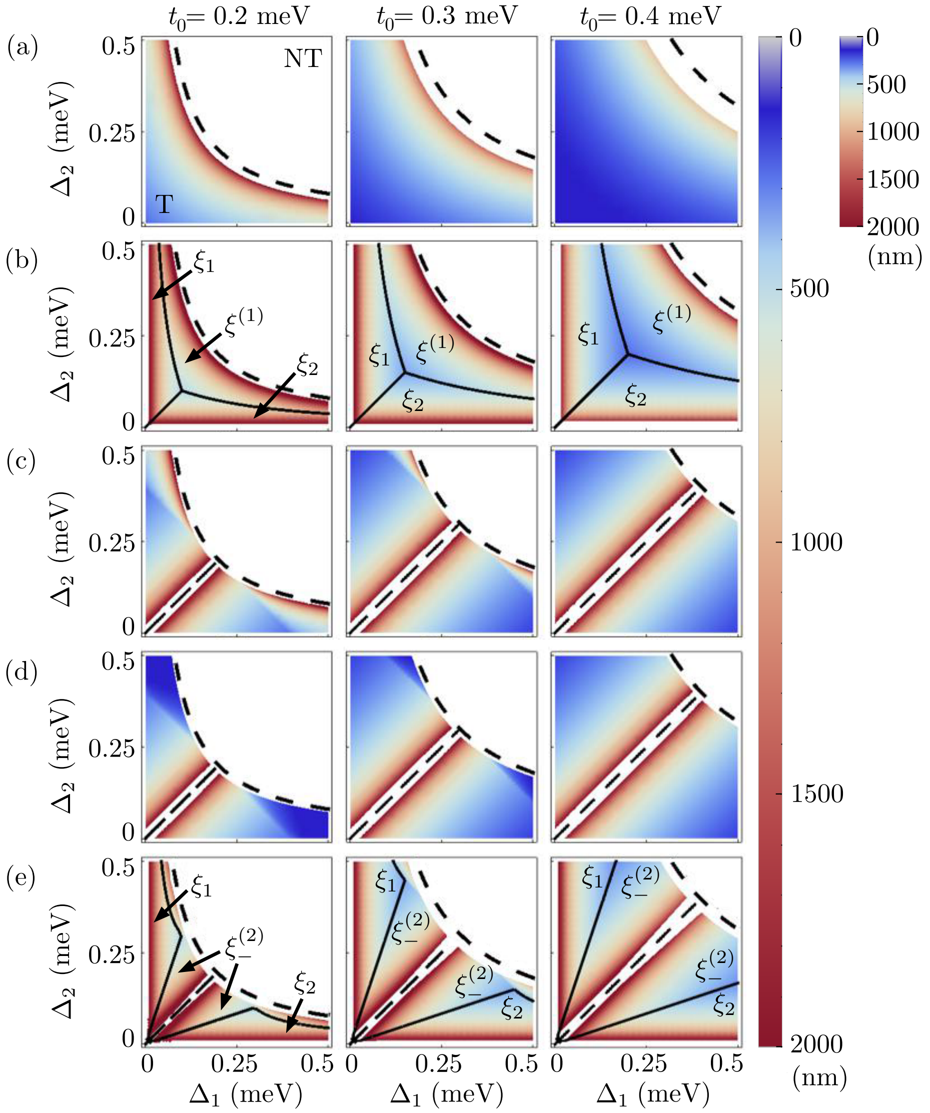

Figure 2.3: (a) Phase diagrams and color scale plots of the localization length $\xi^{(1)}$ for $x > 0$ of the Kramers pair of MFs in the first setup as a function of the superconducting gap parameters $\Delta_{1,2}$ and the tunneling amplitude t_0. Here, $\xi^{(1)}$ increases from blue, through yellow, to red; $v_F = 4.6 \times 10^4 \text{ m s}^{-1}$ in an InAs/GaSb TI [47]. The curve $t_0 = \sqrt{\Delta_1 \Delta_2}$ (dashed) seperates the topological phase (T, colored) and the non-topological phase (NT, uncolored). At the phase boundary the localization length $\xi^{(1)}$ is divergent. For $x < 0$ the localization lengths are given by the superconducting coherence lengths $\xi_{1,2} = \hbar v_F/\Delta_{1,2}$. (b) Same as in (a) but for $\xi^{(1)}_{\text{max}} \equiv \max\{\xi_1, \xi_2, \xi^{(1)}\}$. The curves $\xi_{1,2} = \xi^{(1)}$ and $\xi_1 = \xi_2$ (solid) seperate regions where $\xi^{(1)}_{\text{max}}$ is given respectively by ξ_1, ξ_2 or $\xi^{(1)}$. (c) Same as in (a) but for the localization length $\xi_-^{(2)}$ for $x > 0$ in the second setup. Along the line $\Delta_1 = \Delta_2$ (dashed) the localization lengths $\xi_\pm^{(2)}$ are divergent. (d) Same as in (c) but for the localization length $\xi_+^{(2)}$. (e) Same as in (d) but for $\xi^{(2)}_{\text{max}} = \max\{\xi_2, \xi_-^{(2)}\}$ if $\Delta_1 > \Delta_2$ and $\xi^{(2)}_{\text{max}} = \max\{\xi_1, \xi_-^{(2)}\}$ if $\Delta_1 < \Delta_2$. The curves $\xi_{1,2} = \xi_-^{(2)}$ (solid) seperate regions where $\xi^{(2)}_{\text{max}}$ is given respectively by ξ_1, ξ_2 or $\xi_-^{(2)}$.

CHAPTER 3

Low-field Topological Threshold in Majorana Double Nanowires

Adapted from:
Constantin Schrade, Manisha Thakurathi, Christopher Reeg, Silas Hoffman,
Jelena Klinovaja, and Daniel Loss
"Low-field Topological Threshold in Majorana Double Nanowires",
Phys. Rev. B **96**, 035306 (2017)

A hard proximity-induced superconducting gap has recently been observed in semiconductor nanowire systems at low magnetic fields. However, in the topological regime at high magnetic fields, a soft gap emerges and represents a fundamental obstacle to topologically protected quantum information processing with Majorana bound states. Here we show that in a setup of double Rashba nanowires that are coupled to an s-wave superconductor and subjected to an external magnetic field along the wires, the topological threshold can be significantly reduced by the destructive interference of direct and crossed-Andreev pairing in this setup, precisely down to the magnetic field regime in which current experimental technology allows for a hard superconducting gap. We also show that the resulting Majorana bound states exhibit sufficiently short localization lengths, which makes them ideal candidates for future braiding experiments.

3.1 Introduction

Majorana bound states (MBSs) form the building blocks of a topologically protected qubit. Over the last years, the first generation of Majorana devices were fabricated based on conventional s-wave superconductors (SCs) exposed to strong magnetic fields and proximity-coupled to a nanowire (NW) with Rashba spin-orbit interaction (SOI) [3,4,6–9] or chains of magnetic atoms placed on a superconducting substrate [5,10–12,89–91]. These devices provided first experimental signatures of MBSs in the form of zero-bias conductance peaks [6–12]. Today, the most important open challenge is to perform manipulations on the MBSs which should ultimately allow for the confirmation of their non-Abelian braiding statistics. For this purpose, NW devices appear particularly promising as they provide a simple means of moving MBSs by the use of local gates [29]. Unfortunately, despite the plethora of experimental breakthroughs, a long-standing [92, 93] and still unresolved [94, 95] obstacle to NW-based braiding experiments is that the proximity-induced superconducting gap in the NW is well-defined only for weak magnetic fields in the trivial regime ("hard gap"). For strong magnetic fields in the topological regime, a finite subgap conductance emerges ("soft gap") which destroys the topological protection [13–17].

Here we show that in a double NW setup the topological threshold can be reduced to the low magnetic field regime in which current experimental technology allows for a hard superconducting gap. More concretely, we consider two parallel Rashba NWs that are proximity-coupled to an s-wave SC and subjected to a magnetic field along the NWs, see Fig. 2.1(a). The SC induces both direct and crossed-Andreev pairing. We demonstrate that this double NW setup exhibits a new, previously overlooked Majorana phase that emerges at low magnetic fields. Specifically, for any finite crossed-Andreev pairing strength, we show that the system can host a single MBS at each end even when the Zeeman splitting is smaller than the strength of induced direct pairing. Notably, this phase can be realized if the direct pairing strength exceeds that of crossed-Andreev pairing, which is always the case in the absence of strong electron-electron interactions [32,77,96–101]. In the limit when direct and crossed-Andreev pairing strengths are equal, we find that even an infinitesimal magnetic field can drive the system into the proposed topological phase. Interestingly, we also find that these MBSs exhibit a sufficiently short localization length, making them ideal for experiments on quantum information processing. Our theoretical proposal can

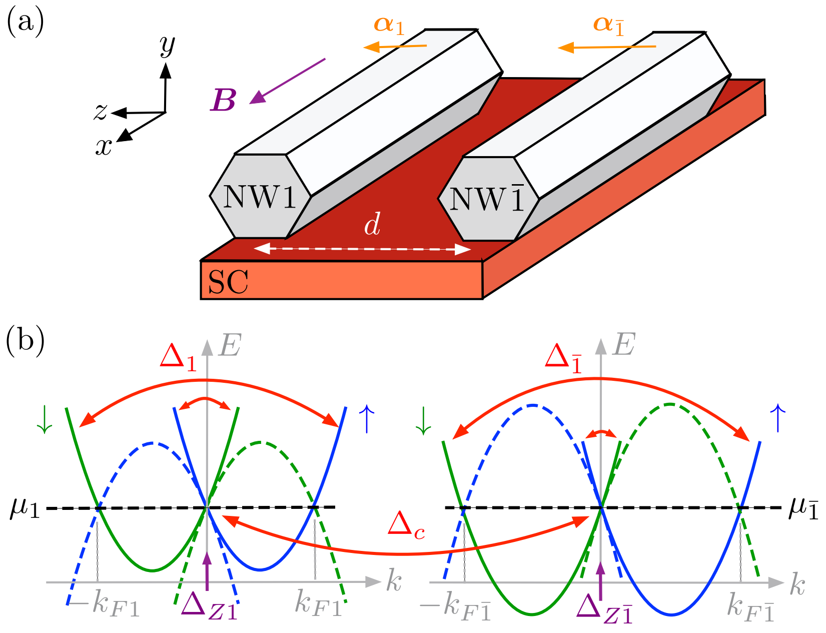
(a)
y
z
x
$\boldsymbol{B}$
$\boldsymbol{\alpha}_1$
$\boldsymbol{\alpha}_{\bar{1}}$
NW1
NW$\bar{1}$
d
SC
(b)
Δ_1
E
$\downarrow$
$\uparrow$
μ_1
$-k_{F1}$
Δ_{Z1}
k_{F1}
k
Δ_c
$\Delta_{\bar{1}}$
E
$\downarrow$
$\uparrow$
$\mu_{\bar{1}}$
$-k_{F\bar{1}}$
$\Delta_{Z\bar{1}}$
$k_{F\bar{1}}$
k

Figure 3.1: (a) Two Rashba NWs (grey) labeled by $\tau = 1, \bar{1}$ are aligned along the x direction and proximity-coupled to an s-wave SC (red). Their separation in the z-direction is given by d. Both NWs are subjected to a magnetic field $\boldsymbol{B}$ which points along the x-axis. The Rashba SOI field $\boldsymbol{\alpha}_\tau$ in the τ-wire points along the z-axis. (b) Energy spectrum in the limit of strong SOI, $E_{so,\tau} \gg \Delta_{Z\tau}, \Delta_\tau, \Delta_c$, with solid (dashed) lines corresponding to electron (hole) bands. The chemical potential μ_τ is tuned to the crossing point of spin-up (blue) and spin-down (green) bands in both NWs. The proximity-induced superconductivity generates a coupling between states with opposite momenta and spins belonging to the same NW (with strength Δ_τ) or to different NWs (with strength Δ_c). For $|E_{so,1} - E_{so,\bar{1}}| \gg \Delta_c$, the crossed-Andreev pairing potential Δ_c couples only the interior branches of the spectrum at $k = 0$. Also, the magnetic field couples states of opposite spins at $k = 0$ in each NW (with strength $\Delta_{Z\tau}$).

readily be realized and scaled to a larger qubit architectures [102–110] in InSb/Al NW networks or can alternatively be fabricated lithographically in two-dimensional InAs/Al heterostructures [27]. Consequently, it may be foundational for future experiments aimed at a controlled manipulation of MBSs.

3.2 Model

We consider a system of two parallel Rashba NWs labeled by $\tau = 1, \bar{1}$, which are positioned along the x direction and coupled to one another via an s-wave SC, see Fig. 3.1(a). The kinetic part of the Hamiltonian is given by

$$H_0 = \sum_{\tau,\sigma} \int \mathrm{d}x \; \Psi^\dagger_{\tau\sigma} \left(-\frac{\hbar^2 \partial_x^2}{2m} - \mu_\tau \right) \Psi_{\tau\sigma'}. \tag{3.1}$$

Here, $\Psi_{\tau\sigma}(x)$ denotes the annihilation operator of an electron with mass m and spin $\sigma/2 = \pm 1/2$ at position x in the τ-wire and μ_τ is the chemical potential in the τ-wire. The Rashba SOI field $\boldsymbol{\alpha}_\tau = \alpha_\tau \hat{z}$ in the τ-wire is of strength α_τ and points along the z direction,

$$H_{so} = i \sum_{\tau,\sigma,\sigma'} \alpha_\tau \int \mathrm{d}x \; \Psi^\dagger_{\tau\sigma} \left(\sigma_z\right)_{\sigma\sigma'} \partial_x \Psi_{\tau\sigma'}, \tag{3.2}$$

where $\sigma_{x,y,z}$ are Pauli matrices acting in spin space. We assume that $\alpha_{\bar{1}} \geq \alpha_1 > 0$. The chemical potentials in both NWs are tuned to the crossing point of the spin-polarized bands, $\mu_\tau = 0$. (We will address the important case when $\mu_\tau \neq 0$ below.) The electron bulk spectrum of $H_0 + H_{so}$ is given by $E_{\tau\sigma}(k) = \hbar^2 (k - \sigma k_{so,\tau})^2/2m - E_{so,\tau}$, where $k_{so,\tau} = m\alpha_\tau/\hbar^2$ is the SOI wavevector and $E_{so,\tau} = \hbar^2 k_{so,\tau}^2/2m$ the SOI energy in the τ-wire, see Fig. 3.1(b). Applying an external magnetic field $\boldsymbol{B} = B\hat{x}$ of magnitude B parallel to the NWs induces a Zeeman splitting described by

$$H_Z = \sum_{\tau,\sigma,\sigma'} \Delta_{Z\tau} \int \mathrm{d}x \; \Psi^\dagger_{\tau\sigma} (\sigma_x)_{\sigma\sigma'} \Psi_{\tau\sigma'}, \tag{3.3}$$

where $\Delta_{Z\tau} = g_\tau \mu_B B/2$ is the Zeeman splitting in the τ-wire, with g_τ the corresponding g-factor and μ_B the Bohr magneton. Assuming that the NWs are effectively one-dimensional, orbital magnetic field effects are neglected.

Superconductivity is induced in the NWs through a tunnel coupling with an s-wave SC. The tunneling of both electrons of a Cooper pair into the same NW is described by

$$H_d = \sum_{\tau,\sigma,\sigma'} \frac{\Delta_\tau}{2} \int \mathrm{d}x \left[\Psi_{\tau\sigma} (i\sigma_y)_{\sigma\sigma'} \Psi_{\tau\sigma'} + \text{H.c.} \right], \tag{3.4}$$

where $\Delta_\tau > 0$ is the pairing potential of the induced direct superconductivity in NW τ. Additionally, we allow for crossed-Andreev pairing where a Cooper pair splits and one electron tunnels into one NW and its partner into the other NW; this process is described by

$$H_c = \frac{\Delta_c}{2} \sum_{\tau,\sigma,\sigma'} \int \mathrm{d}x \left[\Psi_{\tau\sigma}(i\sigma_y)_{\sigma\sigma'}\Psi_{\bar{\tau}\sigma'} + \text{H.c.}\right], \tag{3.5}$$

where $\Delta_c > 0$ is the induced crossed-Andreev pairing potential. The total Hamiltonian is given by $H = H_0 + H_{so} + H_Z + H_d + H_c$. In the Supplemental Material (SM) [111] we provide microscopic expressions for Δ_τ and Δ_c for the special case of weak tunnel coupling between the NWs and the SC, $\gamma \ll \Delta_{sc}$, where γ is the energy scale of the NW-SC tunnel coupling and Δ_{sc} is the superconducting order parameter of the s-wave SC. There, we also show that the ratio $\sqrt{\Delta_1\Delta_{\bar{1}}}/\Delta_c$ can be tuned by varying the NW separation d but always satisfies $\sqrt{\Delta_1\Delta_{\bar{1}}}/\Delta_c > 1$ in the absence of strong electron-electron interactions [101, 111]. For our discussions in the main part, we focus on the experimentally most relevant regime, $|E_{so,1} - E_{so,\bar{1}}| \gg \Delta_{Z\tau}, \Delta_\tau, \Delta_c \gg |\Delta_1 - \Delta_{\bar{1}}|, |\Delta_{Z1} - \Delta_{Z\bar{1}}|$, corresponding to the limit of strong and different SOI energies and the differences in the proximity gaps and Zeeman energies being the smallest energy scales in the system. This allows us to replace $\Delta_\tau, \Delta_{Z\tau} \to \Delta_d, \Delta_Z$, and to compensate the effects of interwire tunneling, $H_\Gamma = -\Gamma \sum_{\tau,\sigma} \int \mathrm{d}x [\Psi^\dagger_{\tau\sigma}(x)\Psi_{\bar{\tau}\sigma}(x) + \text{H.c.}]$ with tunneling strength $\Gamma > 0$, by tuning the NW chemical potentials to an appropriate *sweet spot*, see the stability analysis below and the SM [111]. Notably, without tuning the chemical potentials, interwire tunneling is substantial compared to the crossed-Andreev pairing [111], $\Delta_c/\Gamma = \tanh(d/\xi_{sc}) < 1$ with ξ_{sc} the coherence length of the s-wave SC, and pushes the topological threshold to significantly higher magnetic fields, and not much is gained. For that reason, the low-field topological threshold did not emerge in previous studies [76].

3.3 Topological phase diagram

First, we resolve the topological phase diagram of our model. We note that for $\Delta_Z > 0$ ($\Delta_Z = 0$) the Hamiltonian H is placed in symmetry class BDI (DIII) with a $\mathbb{Z}$ ($\mathbb{Z}_2$) topological invariant [111, 112]. We begin by linearizing the Hamiltonian $H_0 + H_{so}$ around its Fermi points at $k = 0$ and $k = \pm 2k_{so,\tau}$ and consider the effects of magnetic field and superconductivity perturbatively, see the SM [111]. When $|E_{so,1} - E_{so,\bar{1}}| \gg$

Δ_c, the crossed-Andreev pairing couples only the interior branches, see Fig. 3.1(b). We find that the spectrum is gapless at $k = 0$ provided

$$\Delta_c^2 = (\Delta_d \pm \Delta_Z)^2. \tag{3.6}$$

There is no gap closing at finite-momentum for $|E_{so,1} - E_{so,\bar{1}}| \gg \Delta_Z, \Delta_d, \Delta_c$.

Based on Eq. (4.6), we are now in the position to determine the topological phases themselves, see Fig. 3.2. When $\Delta_Z = 0$ and $\Delta_c > \Delta_d$ the system is a time-reversal symmetric topological superconductor and hosts a Kramers pair of MBSs at each end [32]. For $\Delta_Z = 0$ and all remaining values of Δ_c it is a trivial superconductor. Since the number of MBSs is a topological invariant, it cannot change without closing the energy gap. Consequently, for $\Delta_c > \Delta_d + \Delta_Z$ the system must be in a topological phase with two MBSs at each end, while for $\Delta_d - \Delta_Z > \Delta_c$ it must be in a trivial phase. Moreover, for $\Delta_c = 0$ and $\Delta_Z > \Delta_d$ each NW independently hosts a pair of MBSs at its ends [3,4]. From the same reasoning as above we conclude that the system must therefore also exhibit a topological phase with two MBSs at each end for $\Delta_Z - \Delta_d > \Delta_c$. Finally, from an explicit calculation of the MBS wavefunctions, we find that the system hosts one MBS on each end for $\Delta_d + \Delta_Z > \Delta_c > |\Delta_d - \Delta_Z|$.

We now discuss this one-MBS phase in more detail. There are three remarkable aspects: (1) For any finite crossed-Andreev pairing strength Δ_c, the one-MBS phase occurs even for Zeeman splittings smaller than the direct pairing strength, $\Delta_Z < \Delta_d$. Notably, for $\Delta_c = \Delta_d$ an infinitesimal magnetic field can drive the system into the one-MBS phase. This behavior originates from the destructive interference of direct and crossed-Andreev pairing, which lowers the topological threshold to $\Delta_Z = \Delta_d - \Delta_c$. (2) The one-MBS phase is realized for $\Delta_c < \Delta_d$. This fact ensures that the phase can also be achieved in a noninteracting system which, consequently, constitutes a powerful advantage over systems at strictly zero field which host Kramers pairs of MBSs. The latter usually rely on the presence of strong electron-electron interactions that are difficult to control experimentally [32, 77, 99, 100]. Also, the definition of a topological qubit in time-reversal invariant topological superconductors is potentially problematic as it requires additional symmetry conditions [113, 114]. Compared to that, the one-MBS phase allows for the standard definition of a topological qubit for topological superconductors without time-reversal symmetry. (3) The one-MBS phase exists in the limit of strong SOI, which ensures sufficiently short localization length and immediate accessibility with current experimental technology. The weak

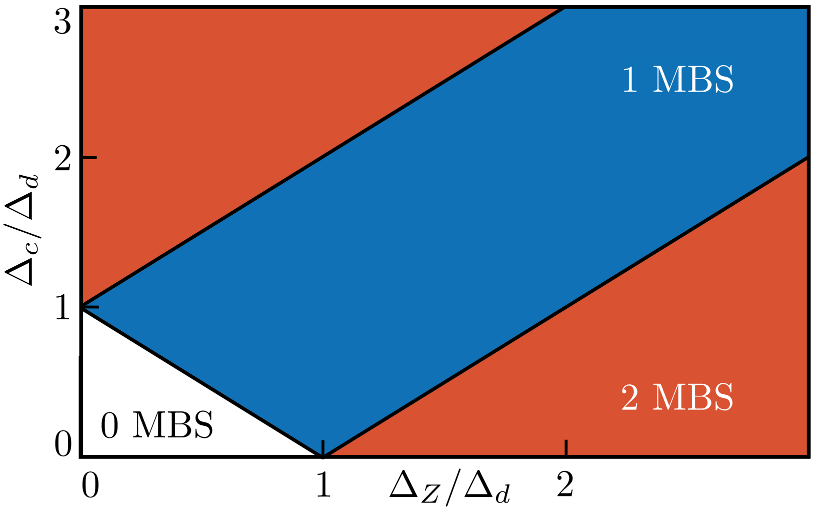

Figure 3.2: (Color online) Topological phase diagram as a function of the Zeeman splitting Δ_Z and the strength of the induced crossed-Andreev pairing Δ_c for the regime $|E_{so,1}-E_{so,\bar{1}}| \gg \Delta_{Z\tau}, \Delta_\tau, \Delta_c \gg |\Delta_1-\Delta_{\bar{1}}|, |\Delta_{Z1}-\Delta_{Z\bar{1}}|$. There are two topological phases hosting one MBS (blue) and two MBSs (red) at each end. The trivial phase (white) does not host any MBSs. To take advantage of the low-field topological threshold, the setup shown in Fig. 3.1(a) should be operated in the one-MBS phase for $\Delta_d + \Delta_Z > \Delta_c > |\Delta_d - \Delta_Z|$.

SOI limit [76] is experimentally less feasible, as it leads to large localization lengths of the MBSs requiring ultra-long NWs.

3.4 Localization lengths

We continue the discussion of the one-MBS phase by computing the localization lengths of the MBS wavefunctions. We assume that the NW length is much longer than the MBS localization lengths, so that MBSs at opposite ends do not overlap [87, 88, 115]. The MBS wavefunctions then correspond to zero energy eigenstates of the Hamiltonian H and can be determined independently for each end, see the SM [111].

We find that the MBS wavefunctions are characterized by the localization lengths determined by the two branches of the spectrum [31]. The localization lengths corresponding to the exterior (e) branches at $k = \pm k_{F\tau} = \pm 2k_{so,\tau}$ of the spectrum are given by the superconducting coherence lengths, $\xi_{e\tau} = \hbar \upsilon_{F\tau}/\Delta_d$, where $\upsilon_{F\tau} = \hbar k_{so,\tau}/m$ is the Fermi velocity in NW τ. The localization length due to the interior (i) branch of the spectrum is given by

$$\xi_i = 2\hbar \upsilon_{F1}\upsilon_{F\bar{1}}\Big[(\upsilon_{F1}+\upsilon_{F\bar{1}})(\Delta_Z-\Delta_d) + \sqrt{\left[(\upsilon_{F1}-\upsilon_{F\bar{1}})(\Delta_Z-\Delta_d)\right]^2+4\upsilon_{F1}\upsilon_{F\bar{1}}\Delta_c^2}\Big]^{-1}. \tag{3.7}$$

The total localization length is given by $\xi = \max\{\xi_i, \xi_{e\tau}\}$.

We now want to compare the MBS localization length in the double NW setup to the one in the standard setup of a single Rashba NW coupled to an s-wave SC and subjected to a magnetic field along the NW axis [3,4]. Assuming that the NW chemical potential is tuned to the crossing point of the spin-polarized bands of the Rashba spectrum, this single NW setup hosts a MBS at each end provided $\Delta_Z > \Delta_d$. The MBS localization length is $\xi' = \max\{\hbar\upsilon_F/(\Delta_Z-\Delta_d), \hbar\upsilon_F/\Delta_d\}$, where υ_F is the Fermi velocity in the NW [31]. In general, we find that the MBS localization length of the double NW setup is always shorter than that in the single NW setup for a fixed Zeeman splitting, $\xi \leq \xi'$ when $\Delta_c > 0$. To give numerical estimates, we choose typical experimental values for semiconducting NWs, $\Delta_d = 0.1$ meV, $g = 2$, and $\upsilon_{F1} = \upsilon_F = 1.5 \times 10^4$ m/s and $\upsilon_{F\bar{1}} = 2.5 \times 10^4$ m/s. Furthermore, we take $\Delta_Z = 0.13$ meV for the Zeeman splitting which corresponds to a field strength of ~ 2.2 T. For the MBS localization length in the single NW setup we find $\xi' \sim 330$ nm. In contrast, the double NW setup with a modest strength of crossed-Andreev pairing $\Delta_c = 0.08$ meV yields a reduction of the MBS localization length to $\xi \sim 160$ nm. Inversely, a localization length of $\xi \sim 330$ nm which is comparable to the single NW case is achieved already for a Zeeman splitting of $\Delta_Z = 0.27$ meV corresponding to a field strength of ~ 1 T. The double NW setup thus allows for MBS localization lengths that are comparable to the single NW setup despite a significant reduction of the magnetic field strength by ~ 1.2 T.

3.5 Stability analysis

Next, we study the stability of the one-MBS phase with respect to interwire tunneling and rotations of the SOI vector away from the directions specified in Fig. 3.1. First, we show that the effects of interwire tunneling on the low-field topological threshold can be compensated by tuning the NW chemical potentials μ_τ to an appropriate sweet spot and we estimate

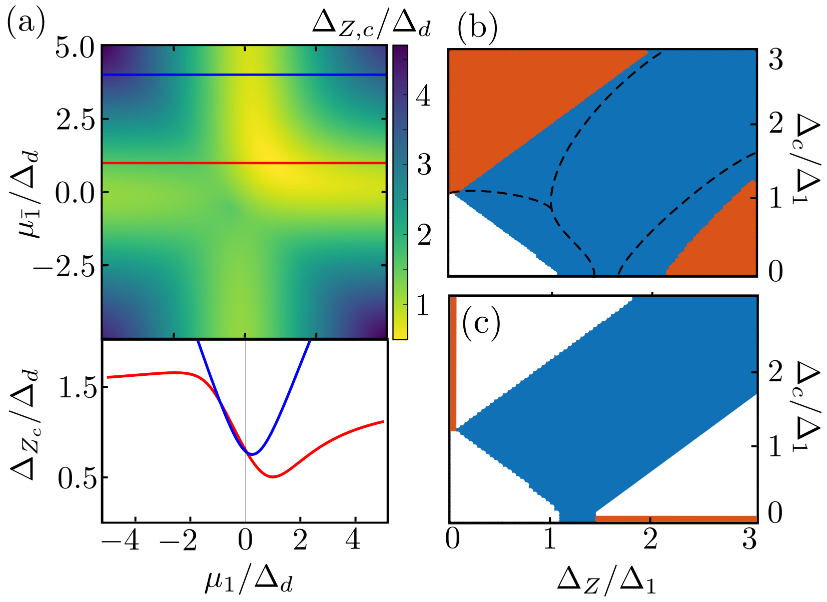

Figure 3.3: (Color online) (a) Top panel: Color-scale plot of the topological threshold $\Delta_{Z,c}/\Delta_d$ for the one-MBS phase as a function of μ_τ/Δ_d for $\Delta_c/\Delta_d = 0.5$, $\Gamma/\Delta_d = 1$. Bottom panel: $\Delta_{Z,c}/\Delta_d$ as a function of μ_1/Δ_d for $\mu_{\bar{1}} = \Gamma$ (red) and $\mu_{\bar{1}}/\Delta_d = 4$ (blue). The topological threshold $\Delta_{Z,c}$ exhibits a global minimum for $\mu_\tau = \Gamma$. (b) Topological phase diagram as a function of Δ_Z/Δ_1 and Δ_c/Δ_1 (obtained from a tight-binding diagonalization of 800 sites per NW) for finite interwire tunneling. We have $E_{so,1}/\Delta_1 = 6.25$, $E_{so,\bar{1}}/\Delta_1 = 12.25$, $\Delta_{\bar{1}}/\Delta_1 = 1.3$, $\Gamma/\Delta_1 = 1$, $\mu_1 = \mu_{\bar{1}} = \Gamma$. Colors are the same as in Fig. 3.2. Black dashed lines denote the approximate phase boundaries for $\mu_\tau = 0$. For $\mu_1 = \mu_{\bar{1}} = \Gamma$ the one-MBS phase itself and also its phase boundary to the trivial phase remains stable. In contrast, for $\mu_\tau = 0$, the topological threshold seperating the trivial and one-MBS phase is pushed to higher magnetic fields. (c) Same phase diagram as in (b) but with the two SOI vectors not being parallel to each other but still orthogonal to the magnetic field. We take $\mu_\tau = 0$, $\Gamma = 0$ and $\theta = \pi/6$ for the relative angle between the SOI vectors. Unlike the one-MBS phase, the two-MBS phases are unstable against rotations of the SOI direction.

the precision of this tuning. For general μ_τ and finite interwire tunneling, we find that the low-field topological threshold from the trivial to the one-MBS phase occurs at the critical Zeeman splitting

$$\begin{aligned}\Delta_{Z,c}^2 = \Big[&2(\Delta_d^2 + \Delta_c^2 + \Gamma^2) + \mu_1^2 + \mu_{\bar{1}}^2 \\ &- \Big(\left[4\Delta_d\Delta_c\right]^2 + \left[4\Delta_c^2 + (\mu_1 + \mu_{\bar{1}})^2\right]\left[\mu_1 - \mu_{\bar{1}}\right]^2 \\ &\quad + 4\Gamma\left[\mu_1 + \mu_{\bar{1}}\right]\left[4\Delta_d\Delta_c + \Gamma(\mu_1 + \mu_{\bar{1}})\right]\Big)^{1/2}\Big]\Big/2. \end{aligned} \tag{3.8}$$

The critical Zeeman splitting is minimized to $\Delta_{Z,c} = \Delta_d - \Delta_c$ at the sweet spot $\mu_\tau = \Gamma$. For $|\mu_\tau| > \Gamma$, the critical Zeeman splitting increases and approaches $\Delta_{Z,c}^2 = \Delta_d^2 + \mu_\tau^2$ when $|\mu_{\bar{\tau}}| \gg |\mu_\tau|$, see Fig. 3.3(a) and Fig. 3.4 in the SM. To tune the chemical potentials to the desired sweet spot, we fix $\mu_{\bar{1}}$ and determine $\Delta_{Z,c}$ as a function of μ_1 (e.g. by the emergence of a zero-bias conductance peak). This procedure is repeated for different values of $\mu_{\bar{1}}$. The case $\mu_\tau = \Gamma$ is achieved for the global minimum of $\Delta_{Z,c}$ as a function of μ_1 and $\mu_{\bar{1}}$. The required precision of this tuning is determined by the width of $\Delta_{Z,c}$ as a function of μ_τ, which is on the scale of Δ_c. Importantly, without this tuning the lowering of the topological threshold between the trivial and one-MBS phase does not occur [76] as the phase boundary separating the one- and two-MBSs phases shifts to larger magnetic fields, see Fig. 3.3(b). In the SM we show that the described compensation is still possible in the regime of low Zeeman splittings for $\Delta_\tau \sim |\Delta_1 - \Delta_{\bar{1}}|$ but requires an asymmetric tuning of the chemical potentials.

Second, we address the case when the SOI vectors in the two NWs are not parallel but still orthogonal to the magnetic field vector. We replace $H \to H - i\sum_{\tau,\sigma,\sigma'} \alpha'_\tau \int \mathrm{d}x\ \Psi^\dagger_{\tau\sigma} \left(\sigma_y\right)_{\sigma\sigma'} \partial_x \Psi_{\tau\sigma'}$ and set $\alpha_1 = \alpha$, $\alpha'_1 = 0$, $\alpha_{\bar{1}} = \tilde{\alpha}\cos\theta$, $\alpha'_{\bar{1}} = \tilde{\alpha}\sin\theta$. The new Hamiltonian is in symmetry class D with a $\mathbb{Z}_2$ topological invariant [111, 112] and a tight-binding diagonalization reveals a stable one-MBS phase and unstable two-MBSs phases that turn trivial for $\sin\theta \neq 0$, see Fig. 3.3(c).

Finally, we have also verified by a numerical tight-binding diagonalization as above that the one-MBS phase is stable against Gaussian disorder with mean $\langle\mu_\tau\rangle = 0$ and a standard deviation that is smaller than the gap.

3.6 Conclusions

We have shown that in a double NW setup the destructive interference of direct and crossed-Andreev pairing significantly reduces the topological threshold compared to the standard single NW setups [3, 4]. Moreover, we have demonstrated that the resulting MBSs exhibit localization lengths that can be shorter than those of the standard single NW setups. Consequently, they represent ideal candidates for future experiments on quantum information processing with MBSs.

3.A Microscopic model of the proximity effect

In this first section of the Supplemental Material, we provide a microscopic derivation of the system parameters of our model Hamiltonian $H = H_0 + H_{so} + H_Z + H_d + H_c + H_\Gamma$ presented in the main text for a weak tunnel coupling between the NWs and the SC, following methods similar to those found in Refs. [101, 116]. We assume that the NWs are of infinite length, so that the momentum k_x in the x direction is conserved. The momentum-space representation of the bare Hamiltonian of the NWs is given by

$$H_0 + H_{so} + H_Z = \sum_{\tau,\sigma,\sigma'} \int \frac{dk_x}{2\pi}\, \Psi^\dagger_{\tau\sigma}(k_x)\left(\xi_\tau - \alpha_\tau k_x \sigma_z + \Delta_{Z\tau}\sigma_x\right)_{\sigma\sigma'} \Psi_{\tau\sigma'}(k_x), \tag{3.9}$$

where we have introduced the single-particle dispersion in the absence of SOI and magnetic field, $\xi_\tau = k_x^2/2m - \mu_\tau$. The Pauli matrices $\sigma_{x,y,z}$ are acting spin space. The NWs are separated by an s-wave SC of finite width d. We describe the SC by the Hamiltonian

$$\begin{aligned} H_{sc} = &\sum_\sigma \int \frac{dk_x}{2\pi} \int_0^d dz \left[\Psi^\dagger_{sc,\sigma}(k_x,z)\left(-\frac{\partial_z^2}{2m_{sc}} + \frac{k_x^2}{2m_{sc}} - \mu_{sc}\right)\Psi_{sc,\sigma}(k_x,z)\right] \\ &+ \frac{\Delta_{sc}}{2}\sum_{\sigma,\sigma'} \int \frac{dk_x}{2\pi} \int_0^d dz \left[\Psi^\dagger_{sc,\sigma}(k_x,z)\,(i\sigma_y)_{\sigma\sigma'}\,\Psi_{sc,\sigma'}(-k_x,z) + \text{H.c.}\right], \end{aligned} \tag{3.10}$$

where m_{sc} and μ_{sc} are the effective mass and chemical potential of the SC, respectively, and Δ_{sc} is the superconducting pairing potential. Notably, we neglect the Zeeman splitting due to the applied in-plane field on the superconductor; this is a good approximation at weak magnetic fields if the Zeeman splitting of the superconductor is much smaller than its bulk gap. We also allow for electrons to tunnel between SC and NW, assuming that this process preserves both spin and momentum,

$$H_t = -\sum_{\tau,\sigma} \int \frac{dk_x}{2\pi}\, t_\tau \left[\Psi^\dagger_{\tau\sigma}(k_x, z_\tau)\Psi_{sc,\sigma}(k_x, z_\tau) + \text{H.c.}\right], \tag{3.11}$$

where t_τ is a nanowire-dependent tunneling amplitude and z_τ denotes the position of τ-wire ($z_1 = 0$ and $z_{\bar{1}} = d$).

The total Hamiltonian can be diagonalized by introducing a Bogoliubov transformation. The resulting Bogoliubov-de Gennes (BdG) equations are given by

$$\begin{aligned}
&\sum_{\sigma'} \left[(\xi_\tau - \alpha_\tau k_x \sigma_z + \Delta_{Z\tau}\sigma_x)_{\sigma\sigma'} u_{\tau\sigma'}(k_x) - t_\tau u_{sc,\sigma}(k_x, z_\tau)\right] = E u_{\tau\sigma}(k_x),\\
&\sum_{\sigma'} \left[-\left(\xi_\tau - \alpha_\tau k_x \sigma_z + \Delta_{Z\tau}\sigma_x\right)_{\sigma'\sigma} + t_\tau v_{sc,\sigma}(k_x, z_\tau)\right] = E v_{\tau\sigma}(k_x),\\
&\sum_{\tau,\sigma'} \Bigg[\left(-\frac{\partial_z^2}{2m_{sc}} + \frac{k_x^2}{2m_{sc}} - \mu_{sc}\right) u_{sc,\sigma}(k_x, z) + i\Delta_{sc}(\sigma_y)_{\sigma\sigma'} v_{sc,\sigma'}(-k_x, z)\\
&\qquad - t_\tau \delta(z - z_\tau) u_{\tau\sigma}(k_x)\Bigg] = E u_{sc,\sigma}(k_x, z),\\
&\sum_{\tau,\sigma'} \Bigg[\left(\frac{\partial_z^2}{2m_{sc}} - \frac{k_x^2}{2m_{sc}} + \mu_{sc}\right) v_{sc,\sigma}(k_x, z) - i\Delta_{sc}(\sigma_y)_{\sigma\sigma'} u_{sc,\sigma'}(-k_x, z)\\
&\qquad + t_\tau \delta(z - z_\tau) v_{\tau\sigma}(k_x)\Bigg] = E v_{sc,\sigma}(k_x, z).
\end{aligned} \tag{3.12}$$

Here, $u_{\tau[sc]\sigma}(v_{\tau[sc]\sigma})$ is the wave function describing an electron (hole) of spin σ in the τ-wire (in the SC). Inside the SC (*i.e.*, for $0 < z < d$), we must solve the BdG equations for a conventional s-wave SC:

$$\left[\left(-\frac{\partial_z^2}{2m_{sc}} + \frac{k_x^2}{2m_{sc}} - \mu_{sc}\right)\eta_z - \Delta_{sc}\eta_y\sigma_y\right]\psi_{sc}(k_x, z) = E\psi_{sc}(k_x, z), \tag{3.13}$$

where $\psi_{sc}(k_x, z) = [u_{sc,\uparrow}(k_x, z), u_{sc,\downarrow}(k_x, z), v_{sc,\uparrow}(-k_x, z), v_{sc,\downarrow}(-k_x, z)]^T$ is a spinor wave function. Solving independently in the left ($z < z_w$), middle ($z_w < z < d - z_w$), and right ($z > z_w$) regions, the wave function can be expressed as

$$\begin{aligned}
\psi_l(z < z_w) &= c_1\chi_{e,\uparrow}\sin(p_+z) + c_2\chi_{e,\downarrow}\sin(p_+z) \\
&\quad + c_3\chi_{h,\uparrow}\sin(p_-z) + c_4\chi_{h,\downarrow}\sin(p_-z), \\
\psi_m(z_w < z < d - z_w) &= c_5\chi_{e,\uparrow}e^{ip_+z} + c_6\chi_{e,\downarrow}e^{ip_+z} + c_7\chi_{e,\uparrow}e^{-ip_+z} \\
&\quad + c_8\chi_{e,\downarrow}e^{-ip_+x} + c_9\chi_{h,\uparrow}e^{ip_-z} + c_{10}\chi_{h,\downarrow}e^{ip_-z} \\
&\quad + c_{11}\chi_{h,\uparrow}e^{-ip_-z} + c_{12}\chi_{h,\downarrow}e^{-ip_-z}, \\
\psi_r(z > z_w) &= c_{13}\chi_{e,\uparrow}\sin[p_+(d-z)] + c_{14}\chi_{e,\downarrow}\sin[p_+(d-z)] \\
&\quad + c_{15}\chi_{h,\uparrow}\sin[p_-(d-z)] + c_{16}\chi_{h,\downarrow}\sin[p_-(d-z)]
\end{aligned} \tag{3.14}$$

where $p_\pm^2 = 2m_{sc}(\mu_{sc} \pm i\Omega) - k_x^2$, with $\Omega^2 = \Delta_{sc}^2 - E^2$. The spinors are defined as $\chi_{e,\uparrow} = (u_0, 0, 0, v_0)^T$, $\chi_{e,\downarrow} = (0, u_0, -v_0, 0)^T$, $\chi_{h,\uparrow} = (0, -v_0, u_0, 0)^T$, and $\chi_{h,\downarrow} = (v_0, 0, 0, u_0)^T$, where u_0 and v_0 are the BCS coherence factors,

$$u_0(v_0) = \sqrt{\frac{1}{2}\left(1 \pm \frac{i\Omega}{E}\right)}. \tag{3.15}$$

The nanowires enter only through the boundary conditions. These boundary conditions, which must be imposed at $z = z_\tau$ (vanishing boundary conditions at $z = 0$ and $z = d$ are accounted for already), are given by

$$\begin{aligned}
&\psi_l(z_1) = \psi_m(z_1), \\
&\psi_r(z_{\bar{1}}) = \psi_m(z_{\bar{1}}), \\
&[\partial_z\psi_m(z_1) - \partial_x\psi_l(z_1)]/k_F = 2\gamma_1\eta_z G_1^R(E, k_x)\psi_l(z_1), \\
&[\partial_z\psi_m(z_{\bar{1}}) - \partial_x\psi_r(z_{\bar{1}})]/k_F = 2\gamma_{\bar{1}}\eta_z G_{\bar{1}}^R(E, k_x)\psi_l(z_{\bar{1}}),
\end{aligned} \tag{3.16}$$

where $G_\tau^R(E, k_x) = (E - \xi_\tau\eta_z + \alpha_\tau k_x\sigma_z - \Delta_{Z\tau}\eta_z\sigma_x + i0^+)^{-1}$ is the retarded Green's function of the τ-wire in the absence of tunneling. The boundary conditions Eq. (3.16) can be rearranged into the form $Mc = 0$, where M is a 16×16-matrix and c is a 16-component vector of unknown coefficients. The excitation spectrum of the junction is determined by solving the equation $\det M = 0$ for $E(k_x)$.

We now map the exact BdG solution to the effective pairing model in the limit of weak coupling. We adopt the following approximations: First, we assume that the chemical potential of the SC is the largest energy scale of the problem ($\mu_{sc} \gg E_{so}, \Delta_{Z\tau}, \Delta_{sc}, \mu_\tau$). This allows us to approximate

$$p_\pm = \sqrt{2m_{sc}(\mu_{sc} \pm i\Omega) - k_x^2} \approx k_{F,sc} \pm i\Omega/v_{F,sc}, \tag{3.17}$$

where $k_{F,sc} = \sqrt{2m_{sc}\mu_{sc}}$ and $v_{F,sc} = k_{F,sc}/m_{sc}$ are the Fermi momentum and velocity of the SC, respectively. When differentiating the wave function [on the left-hand side of Eq. (3.16)], we approximate $p_{\pm} = k_{F,sc}$; however, in the exponentials [entering through $\psi_{sc}(k_x, d)$], we keep $p_{\pm} = k_{F,sc} \pm i\Omega/v_{F,sc}$ (this gives the exponentially growing/decaying parts of the wave function). The weak-tunneling limit is assumed by taking $\gamma_\tau \ll \Delta_{sc}$, where γ_τ is a nanowire-dependent tunneling energy scale given by $\gamma_\tau = t_\tau^2/v_{F,sc}$. In this limit, the relevant pairing energies are small ($E \ll \Delta_{sc}$) and we can expand the coherence factors as

$$u_0(v_0) = \left(\frac{1 \pm i}{2}\right)\frac{\Delta_{sc}}{E}. \tag{3.18}$$

However, even with these simplifications, the matrix M [defined below Eq. (**??**)] is too complicated to be displayed explicitly here. Also due to the complicated nature of the matrix M, we can only evaluate $\det M$ numerically; this means that the energy spectrum $E(k_x, \mu_\tau, \alpha_\tau, \Delta_{Z\tau}, \gamma_\tau, d)$ must be effectively "guessed" to be mapped out over all of parameter space (i.e., it would be very computationally expensive to numerically map out the spectrum as function of all parameters of the problem). Luckily, it is actually quite straightforward to guess the correct spectrum.

The superconductor induces four effective terms in the Hamiltonian of the NWs. Induced pairing terms are of direct type,

$$H_d = \sum_\tau \Delta_\tau \int \frac{dk_x}{2\pi}\left[\Psi^\dagger_{\tau 1}(k_x)\Psi^\dagger_{\tau\bar{1}}(-k_x) + \text{H.c.}\right], \tag{3.19}$$

and crossed-Andreev type,

$$H_c = \Delta_c \sum_\tau \int \frac{dk_x}{2\pi}\left[\Psi^\dagger_{\tau 1}(k_x)\Psi^\dagger_{\bar{\tau}\bar{1}}(-k_x) + \text{H.c.}\right]. \tag{3.20}$$

In addition, the superconductor induces single-particle couplings, which again can be of direct type,

$$H_{\delta\mu} = -\sum_{\tau,\sigma} \delta\mu_\tau \int \frac{dk_x}{2\pi}\left[\Psi^\dagger_{\tau\sigma}(k_x)\Psi_{\tau\sigma}(k_x) + \text{H.c.}\right], \tag{3.21}$$

and of interwire type,

$$H_\Gamma = -\Gamma \sum_{\tau,\sigma} \int \frac{dk_x}{2\pi}\left[\Psi^\dagger_{\tau\sigma}(k_x)\Psi_{\bar{\tau}\sigma}(k_x) + \text{H.c.}\right]. \tag{3.22}$$

With these proximity-induced terms, we propose to describe the nanowires with an effective Hamiltonian of the form

$$H = \frac{1}{2}\int \frac{dk_x}{2\pi}\Phi^\dagger(k_x)\mathcal{H}_{\text{eff}}(k_x)\Phi(k_x), \tag{3.23}$$

where $\Phi = (\Psi_{11}, \Psi_{1\bar{1}}, \Psi^\dagger_{11}, \Psi^\dagger_{1\bar{1}}, \Psi_{\bar{1}1}, \Psi_{\bar{1}\bar{1}}, \Psi^\dagger_{\bar{1}1}, \Psi^\dagger_{\bar{1}\bar{1}})^T$ and the effective Hamiltonian density $\hat{\mathcal{H}}_{\text{eff}}$ is given by

$$\begin{aligned}\mathcal{H}(k_x) = {} & \tilde{\xi}_1\left(\frac{1+\tau_z}{2}\right)\eta_z + \tilde{\xi}_{\bar{1}}\left(\frac{1-\tau_z}{2}\right)\eta_z \\ & - \alpha_1 k_x\left(\frac{1+\tau_z}{2}\right)\sigma_z - \alpha_{\bar{1}} k_x\left(\frac{1-\tau_z}{2}\right)\sigma_z \\ & + \Delta_{Z1}\left(\frac{1+\tau_z}{2}\right)\eta_z\sigma_x + \Delta_{Z\bar{1}}\left(\frac{1-\tau_z}{2}\right)\eta_z\sigma_x - \Delta_c\tau_x\eta_y\sigma_y - \Gamma\tau_x\eta_z \\ & - \Delta_1\left(\frac{1+\tau_z}{2}\right)\eta_y\sigma_y - \Delta_{\bar{1}}\left(\frac{1-\tau_z}{2}\right)\eta_y\sigma_y\end{aligned} \tag{3.24}$$

with $\tilde{\xi}_\tau = k_x^2/2m - \mu_\tau - \delta\mu_\tau$ and the Pauli matrices $\tau_{x,y,z}$, $\eta_{x,y,z}$, $\sigma_{x,y,z}$ acting in nanowire, particle-hole and spin-space, respectively. In the special case when $\Delta_{Z\tau} = 0$, the Hamiltonian obeys both time-reversal and particle-hole symmetry with operators $U_T = \sigma_y$, $U_P = \eta_x$, and transformations $U_T^\dagger\mathcal{H}^*(k_x)U_T = \mathcal{H}(-k_x)$, $U_P^\dagger\mathcal{H}^*(k_x)U_P = -\mathcal{H}(-k_x)$, respectively. Furthermore, $U_T^*U_T = -1$, $U_P^*U_P = 1$. Hence, for $\Delta_{Z\tau} = 0$ the Hamiltonian is placed in the DIII symmetry class with a $\mathbb{Z}_2$ topological invariant [112]. In general, the Hamiltonian also exhibits an effective time-reversal symmetry described by $U_T' = \eta_z\sigma_x$ with $(U_T')^2 = 1$. Therefore, for $\Delta_{Z\tau} \neq 0$ the Hamiltonian is placed in the symmetry class BDI with a $\mathbb{Z}$ topological invariant [112]. However, we note that the effective time-reversal symmetry U_T' is unstable when the SOI vectors are not parallel but still orthogonal to the magnetic field vector,

$$k_x\alpha\left(\frac{1+\tau_z}{2}\right)\sigma_z + k_x\tilde{\alpha}\left(\frac{1-\tau_z}{2}\right)\left[\cos(\theta)\sigma_z + \sin(\theta)\eta_z\sigma_y\right], \tag{3.25}$$

where $\theta \in [0, 2\pi)$ is the relative angle between the SOI vectors. Moreover, the effective time-reversal symmetry U_T' is also unstable if we allow for a magnetic field vector component that is aligned with one of the SOI vectors,

$$\Delta_{Z1}\left(\frac{1+\tau_z}{2}\right)\eta_z\sigma_x + \Delta_{Z\bar{1}}\left(\frac{1-\tau_z}{2}\right)\eta_z\left[\cos(\phi)\sigma_x + \sin(\phi)\sigma_z\right]. \tag{3.26}$$

with $\phi \in [0, 2\pi)$. In the presence of either one of these perturbations with $\sin(\theta) \neq 0$ or $\sin(\phi) \neq 0$, the Hamiltonian is in the symmetry class D with a $\mathbb{Z}_2$ topological invariant [112].

The effective parameters Δ_τ, Δ_c, $\delta\mu_\tau$, and Γ were determined as functions of the tunneling strength γ_τ and wire separation d in the absence of spin-orbit coupling and Zeeman splitting in Ref. [101]. They are given by ($\xi_{sc} = v_{F,sc}/\Delta_{sc}$ is the superconducting coherence length)

$$\begin{aligned}
\Delta_\tau &= \frac{2\gamma_\tau \sinh(2d/\xi_{sc})}{\cosh(2d/\xi_s) - \cos(2k_F d)}, \\
\Delta_c &= \frac{4\sqrt{\gamma_1\gamma_{\bar{1}}}\sinh(d/\xi_{sc})\cos(k_F d)}{\cosh(2d/\xi_{sc}) - \cos(2k_F d)}, \\
\delta\mu_\tau &= -\frac{2\gamma_\tau \sin(2k_F d)}{\cosh(2d/\xi_{sc}) - \cos(2k_F d)}, \\
\Gamma &= -\frac{4\sqrt{\gamma_1\gamma_{\bar{1}}}\cosh(d/\xi_{sc})\sin(k_F d)}{\cosh(2d/\xi_{sc}) - \cos(2k_F d)}.
\end{aligned} \tag{3.27}$$

Because the effective proximity-induced parameters should depend only on properties of the superconductor and the tunneling amplitude, let us make the ansatz that all four of the proximity-induced effective parameters given in Eq. (3.27) remain unchanged when spin-orbit coupling and a Zeeman splitting are added to the nanowires. That is, we substitute Eq. (3.27) to describe the effective parameters of Eq. (3.24). We then find that if we substitute the energy eigenvalues E of Eq. (3.24) into the boundary conditions Eq. (3.16), these choices of E ensure that $\det M = 0$; this means that the eigenvalues of the effective Hamiltonian (3.24) correspond to the energy spectrum obtained by solving the BdG equations.

3.B Energy spectrum in the strong spin-orbit interaction regime

In this second section of the Supplemental Material, we compute the bulk energy spectrum of the model $H = H_0 + H_{so} + H_Z + H_d + H_c$ proposed in the main text [32,76,117]. Additionally, we will determine the gapless points of the spectrum which potentially correspond to topological phase boundaries. We assume the regime of strong SOI, $E_{so,\tau} \gg \Delta_Z, \Delta_\tau, \Delta_c$, and that the deviations in the proximity-induced gaps are the smallest energy scale [32, 117], $\Delta_\tau \gg |\Delta_1 - \Delta_{\bar{1}}|$ and $\Delta_{Z\tau} \gg |\Delta_{Z1} - \Delta_{\bar{Z}1}|$. This allows us to set $\Delta_d = \Delta_\tau$, $\Delta_Z = \Delta_{Z\tau}$ and to neglect the effects of interwire tunneling as they can always be compensated by an appropriate adjustment of the nanowire chemical potentials.

We begin by expanding the electron operator according to [118, 119]

$$\Psi_{\tau\sigma}(x) = R_{\tau\sigma}(x)e^{i\frac{(\sigma+1)}{2}k_{F\tau}x} + L_{\tau\sigma}(x)e^{i\frac{(\sigma-1)}{2}k_{F\tau}x}, \tag{3.28}$$

where $R_{\tau\sigma}(x)$ and $L_{\tau\sigma}(x)$ are slowly varying right and left moving fields with spin $\sigma/2$ in the τ-wire. Furthermore, we recall that $k_{F\tau} = 2k_{so,\tau}$. Next, we distinguish between three regimes.

Strongly detuned SOI energies

The first case corresponds to strongly detuned nanowire SOI energies, $|E_{so,1} - E_{so,\bar{1}}| \gg \Delta_Z, \Delta_d, \Delta_c$. In this case the crossed-Andreev pairing couples the two nanowires only at $k = 0$. The Hamiltonian is given by $H = (1/2)\int \mathrm{d}x\Psi^\dagger(x)\mathcal{H}(x)\Psi(x)$ with the Hamiltonian density

$$\begin{aligned}\mathcal{H}(x) = \hbar v_{F1}\hat{k}(1+\tau_z)\rho_z/2 + \hbar v_{F\bar{1}}\hat{k}(1-\tau_z)\rho_z/2 \\ + \Delta_Z\eta_z(\sigma_x\rho_x + \sigma_y\rho_y)/2 \\ + \Delta_c\tau_x\eta_y(\sigma_x\rho_y - \sigma_y\rho_x)/2 + \Delta_d\eta_y\sigma_y\rho_x\end{aligned} \tag{3.29}$$

and the basis Ψ=(R_{11}, L_{11}, $R_{1\bar{1}}$, $L_{1\bar{1}}$, $R^\dagger_{11}$, $L^\dagger_{11}$, $R^\dagger_{1\bar{1}}$, $L^\dagger_{1\bar{1}}$, $R_{\bar{1}\bar{1}}$, $L_{\bar{1}1}$, $R_{\bar{1}\bar{1}}$, $L_{\bar{1}\bar{1}}$, $R^\dagger_{\bar{1}\bar{1}}$, $L^\dagger_{\bar{1}1}$, $R^\dagger_{\bar{1}\bar{1}}$, $L^\dagger_{\bar{1}\bar{1}}$). The Pauli matrices $\tau_{x,y,z}$, $\eta_{x,y,z}$, $\sigma_{x,y,z}$, $\rho_{x,y,z}$ act in nanowire, electron-hole, spin and right-left mover space respectively. Furthermore, $\hat{k} = -i\partial_x$ denotes the momentum operator whose eigenvalues are k and measured with respect to the Fermi points at $0, \pm k_{F\tau} = \pm 2k_{so,\tau}$ and $v_{F\tau} = \hbar k_{so,\tau}/m$ is the Fermi velocity in the τ-wire.

We find that the bulk energy spectrum is given by

$$\begin{aligned}&E_\tau^2 = (\hbar v_{F\tau}k)^2 + \Delta_d^2, \\ &E_{\pm\pm}^2 = \frac{1}{2}\Bigg[\hbar^2\left(v_{F1}^2 + v_{F\bar{1}}^2\right)k^2 + 2\left(\Delta_d \pm \Delta_Z\right)^2 + 2\Delta_c^2 \\ &\qquad \pm\sqrt{4\Delta_c^2\left(\hbar^2\left[v_{F1} - v_{F\bar{1}}\right]^2 k^2 + 4\left[\Delta_d \pm \Delta_Z\right]^2\right) + \hbar^4\left(v_{F1}^2 - v_{F\bar{1}}^2\right)^2 k^4}\,\Bigg],\end{aligned} \tag{3.30}$$

where the first (second) equation corresponds to exterior (interior) branch of the spectrum. We find that the spectrum is gapless at $k = 0$ provided $\Delta_c = |\Delta_d \pm \Delta_Z|$. There exist no gapless closing points for $k \neq 0$.

Weakly detuned SOI energies

The second case corresponds to weakly detuned nanowire SOI energies, $|E_{so,1} - E_{so,\bar{1}}| \ll \Delta_Z, \Delta_d, \Delta_c$. In this limit, we neglect the difference in spin-orbit energies, $\upsilon_F = \upsilon_{F1} = \upsilon_{F\bar{1}}$. The crossed-Andreev pairing now couples the two nanowires both at $k = 0$ and $k = \pm k_F = \pm 2k_{so}$. The Hamiltonian density is given by

$$\mathcal{H}(x) = \hbar\upsilon_F \hat{k}\rho_z + \Delta_Z\eta_z(\sigma_x\rho_x + \sigma_y\rho_y)/2 - \Delta_c\tau_x\eta_y\sigma_y\rho_x + \Delta_d\eta_y\sigma_y\rho_x,$$

and the bulk spectrum is modified to

$$\begin{aligned} E_{\pm}^2 &= (\hbar\upsilon_F k)^2 + (\Delta_d \pm \Delta_c)^2, \\ E_{\pm\pm}^2 &= (\hbar\upsilon_F k)^2 + \left(\Delta_c \pm |\Delta_d \pm \Delta_Z|\right)^2, \end{aligned} \tag{3.31}$$

where the first (second) equation corresponds to exterior (interior) branch of the spectrum. Besides the gap closing at $k = 0$ when $\Delta_c = |\Delta_d \pm \Delta_Z|$, we find an additional gap closing at $k = \pm k_F = 2k_{so}$ when $\Delta_c = \Delta_d$. For $\Delta_Z = 0$ this gap closing does not correspond to a topological phase transition because the SOI interaction can be removed by a gauge transformation. For $\Delta_Z > 0$ we also find from a numerical tight-binding diagonalization that the number of MBS is unchanged across the gap closing line $\Delta_c = \Delta_d$, see also Fig. 3.6(b).

Intermediate regime

The last case corresponds to the intermediate regime, when $|E_{so,1} - E_{so,\bar{1}}| \sim \Delta_Z, \Delta_d, \Delta_c$. To determine the gapless points of the spectrum, we consider for this case the full quadratic Hamiltonian given by $H = (1/2)\int \mathrm{d}x\ \Phi^\dagger(x)\mathcal{H}(x)\Phi(x)$ with Hamiltonian density

$$\begin{aligned} \mathcal{H}(x) = {} & \hbar^2\hat{k}^2\eta_z/2m - \alpha_1\hat{k}(1+\tau_z)\sigma_z/2 - \alpha_{\bar{1}}\hat{k}(1-\tau_z)\sigma_z/2 \\ & + \Delta_Z\eta_z\sigma_x - \Delta_d\eta_y\sigma_y - \Delta_c\tau_x\eta_y\sigma_y \end{aligned} \tag{3.32}$$

and basis $\Phi = (\Psi_{11}, \Psi_{1\bar{1}}, \Psi_{11}^\dagger, \Psi_{1\bar{1}}^\dagger, \Psi_{\bar{1}1}, \Psi_{\bar{1}\bar{1}}, \Psi_{\bar{1}1}^\dagger, \Psi_{\bar{1}\bar{1}}^\dagger)$. We focus on the gap closing points at finite momentum, because the zero momentum gap closing points are not affected by the SOI. Furthermore, because a finite magnetic field cannot open an energy gap at finite momentum in the regime of strong SOI, we can restrict ourselves to the case when $\Delta_Z = 0$. Our findings will be equally valid for the case when $\Delta_Z \neq 0$. First, we determine the bulk energy spectrum,

$$\begin{aligned}
&E^2_{\pm\pm}(\Delta_Z = 0)\\
&= \left(\frac{\hbar^2 k^2}{2m}\right)^2 + \frac{k^2(\alpha_1^2 + \alpha_{\bar{1}}^2)}{2} + \Delta_d^2 + \Delta_c^2 \pm k(\alpha_1 + \alpha_{\bar{1}})\left(\frac{\hbar^2 k^2}{2m}\right)\\
&\pm \sqrt{\left(k[\alpha_1 - \alpha_{\bar{1}}]\left[\frac{k(\alpha_1 + \alpha_{\bar{1}})}{2} - \frac{\hbar^2 k^2}{2m}\right]\right)^2 + \Delta_c^2\left(k^2[\alpha_1 - \alpha_{\bar{1}}]^2 + 4\Delta_d^2\right)}
\end{aligned} \quad . \tag{3.33}$$

Next, we find that the spectrum is gapless provided that

$$\begin{aligned}
\Delta_c^2 = \Delta_d^2 &- \left(\frac{\hbar^2 k^2}{2m}\right)^2 - k^2 \alpha_1 \alpha_{\bar{1}} + \left(\frac{\hbar^2 k^2}{2m}\right) k(\alpha_1 + \alpha_{\bar{1}})\\
&\pm i\Delta_d \left[2\left(\frac{\hbar^2 k^2}{2m}\right) - k(\alpha_{\bar{1}} + \alpha_1)\right].
\end{aligned} \tag{3.34}$$

The spectrum is also gapless for the same condition, but with $k \to -k$. Because $\Delta_c > 0$, we need to require that

$$2\left(\frac{\hbar^2 k^2}{2m}\right) - k(\alpha_{\bar{1}} + \alpha_1) = 0. \tag{3.35}$$

Solving this expression (and the corresponding one with $k \to -k$) for k, yields the two gap-closing points

$$k^* = \pm \frac{2m}{\hbar^2}\left(\frac{\alpha_{\bar{1}} + \alpha_1}{2}\right). \tag{3.36}$$

Inserting this result back into Eq. (3.34), we find the gap-closing condition for $k \neq 0$,

$$\Delta_c = \Delta_c^* \equiv \Delta_d \sqrt{1 + 4\left(\frac{E_{so,1} - E_{so,\bar{1}}}{\Delta_d}\right)^2}. \tag{3.37}$$

We note that $\Delta_c^* \geq \Delta_d$, so that the gap closing occurs for larger values of the strength of the crossed-Andreev pairing as compared to the regime when $|E_{so,1} - E_{so,\bar{1}}| \ll \Delta_Z, \Delta_d, \Delta_c$. Additionally, we emphasize once more that the result in Eq. (3.37) is valid also for $\Delta_Z \neq 0$ in the limit of strong SOI. Finally, we point out that the topological phase diagram for the regime $|E_{so,1} - E_{so,\bar{1}}| \sim \Delta_Z, \Delta_d, \Delta_c$ is given in Fig. 3.5(b).

3.C Majorana bound state wavefunctions in the strong spin-orbit interaction regime

In this third section of the Supplemental Material, we compute the zero-energy MBS wavefunctions of the model $H = H_0 + H_{so} + H_Z + H_d + H_c$. As in the last section and the main text, we assume the regime of strong SOI, $E_{so,\tau} \gg \Delta_Z, \Delta_\tau, \Delta_c$, and that the fluctuations in the proximity-induced gaps are the smallest energy scale, $\Delta_\tau \gg |\Delta_1 - \Delta_{\bar{1}}|$ and $\Delta_{Z\tau} \gg |\Delta_{Z1} - \Delta_{\bar{Z}1}|$. This allows us to once again set $\Delta_d = \Delta_\tau$, $\Delta_Z = \Delta_{Z\tau}$ and to neglect the effects of interwire tunneling as they can always be compensated by an appropriate adjustment of the nanowire chemical potentials.

We begin by assuming that the nanowire length is much longer than the localization length of the MBSs. This means that the MBSs at opposite ends of the system do not overlap and can hence be treated independently. Next, we choose the origin of our coordinate system so that one of the boundaries of the system is located at $x = 0$ and focus on this boundary when computing the wavefunctions. We discuss two regimes:

Strongly detuned SOI energies

The first regime corresponds to strongly detuned nanowire SOI energies, $|E_{so,1} - E_{so,\bar{1}}| \gg \Delta_Z, \Delta_d, \Delta_c$. Without loss of generality, we choose $\alpha_{\bar{1}} > \alpha_1$. For $\Delta_d + \Delta_Z > \Delta_c > |\Delta_d - \Delta_Z|$, we find a single MBS given by $\gamma = \sum_\tau \int \mathrm{d}x \; \phi_\tau(x) \cdot \Phi_\tau(x)$ where $\Phi_\tau^T = (\Psi_{\tau 1}, \Psi_{\tau \bar{1}}, \Psi_{\tau 1}^\dagger, \Psi_{\tau \bar{1}}^\dagger)$ is the electron spinor and $\phi_\tau = (\phi_{\tau 1}, \phi_{\tau \bar{1}}, \phi_{\tau 1}^*, \phi_{\tau \bar{1}}^*)$ the wavefunction vector in the τ-wire. The latter is (up to normalization) given by

$$\begin{aligned} &\phi_{\tau\sigma}(x) \\ &= i e^{i\pi(1-\sigma)/4} \left(e^{-x/\xi_{e\tau} - i\sigma k_{F\tau} x} - e^{-x/\xi_i} \right) \left[\frac{1+\tau}{2} + \left(\frac{1-\tau}{2} \right) \right. \\ &\left. \times \frac{\sqrt{4\Delta_c^2 \upsilon_{F1} \upsilon_{F\bar{1}} + (\Delta_d - \Delta_Z)^2 (\upsilon_{F1} - \upsilon_{F\bar{1}})^2} + (\Delta_d - \Delta_Z)(\upsilon_{F\bar{1}} - \upsilon_{F1})}{2\Delta_c \upsilon_{F\bar{1}}} \right], \end{aligned} \tag{3.38}$$

with the localization lengths corresponding to the interior (i) and exterior (e) branches of the spectrum given by

$$\xi_i = \frac{2\hbar \upsilon_{F1}\upsilon_{F\bar{1}}}{\sqrt{4\Delta_c^2 \upsilon_{F1}\upsilon_{F\bar{1}} + \left(\Delta_d - \Delta_Z\right)^2 \left(\upsilon_{F1} - \upsilon_{F\bar{1}}\right)^2} + \left(\Delta_Z - \Delta_d\right)\left(\upsilon_{F1} + \upsilon_{F\bar{1}}\right)}. \tag{3.39}$$

For $\Delta_Z > \Delta_d$ and $\Delta_c < \Delta_Z - \Delta_d$, we find two MBSs given by $\gamma = \sum_\tau \int \mathrm{d}x\ \phi_\tau(x) \cdot \Phi_\tau(x)$ and $\gamma' = \sum_\tau \int \mathrm{d}x\ \phi'_\tau(x) \cdot \Phi_\tau(x)$ where the wavefunction vector $\phi'_\tau = (\phi'_{\tau 1}, \phi'_{\tau\bar{1}}, (\phi'_{\tau 1})^*, (\phi'_{\tau\bar{1}})^*)$ is (up to normalization) given by

$$\begin{aligned} &\phi'_{\tau\sigma}(x) \\ &= i e^{i\pi(1-\sigma)/4} \left(e^{-x/\xi_{e\tau} - i\sigma k_{F\tau} x} - e^{-x/\xi'_i}\right) \left[\frac{\tau - 1}{2} + \left(\frac{1+\tau}{2}\right)\right. \\ &\times \left.\frac{\sqrt{4\Delta_c^2 \upsilon_{F1}\upsilon_{F\bar{1}} + \left(\Delta_d - \Delta_Z\right)^2 \left(\upsilon_{F1} - \upsilon_{F\bar{1}}\right)^2} + \left(\Delta_Z - \Delta_d\right)\left(\upsilon_{F1} - \upsilon_{F\bar{1}}\right)}{2\Delta_c \upsilon_{F1}}\right], \end{aligned} \tag{3.40}$$

with the localization length

$$\xi'_i = \frac{2\hbar \upsilon_{F1}\upsilon_{F\bar{1}}}{\left(\Delta_Z - \Delta_d\right)\left(\upsilon_{F1} + \upsilon_{F\bar{1}}\right) - \sqrt{4\Delta_c^2 \upsilon_{F1}\upsilon_{F\bar{1}} + \left(\Delta_d - \Delta_Z\right)^2 \left(\upsilon_{F1} - \upsilon_{F\bar{1}}\right)^2}}. \tag{3.41}$$

For $\Delta_c > \Delta_d + \Delta_Z$, we again find two MBSs. They are given by $\gamma = \sum_\tau \int \mathrm{d}x\ \phi_\tau(x) \cdot \Phi_\tau(x)$ and $\gamma'' = \sum_\tau \int \mathrm{d}x\ \phi''_\tau(x) \cdot \Phi_\tau(x)$, where the wavefunction vector $\phi''_\tau = (\phi''_{\tau 1}, \phi''_{\tau\bar{1}}, (\phi''_{\tau 1})^*, (\phi''_{\tau\bar{1}})^*)$ is (up to normalization) given by

$$\begin{aligned} &\phi''_{\tau\sigma}(x) \\ &= e^{i\pi(\sigma-1)/4} \left(e^{-x/\xi_{e\tau} - i\sigma k_{F\tau} x} - e^{-x/\xi''_i}\right) \left[\frac{1 - \tau}{2} + \left(\frac{1+\tau}{2}\right)\right. \\ &\times \left.\frac{\sqrt{4\Delta_c^2 \upsilon_{F1}\upsilon_{F\bar{1}} + \left(\Delta_d + \Delta_Z\right)^2 \left(\upsilon_{F1} - \upsilon_{F\bar{1}}\right)^2} + \left(\Delta_d + \Delta_Z\right)\left(\upsilon_{F1} - \upsilon_{F\bar{1}}\right)}{2\Delta_c \upsilon_{F1}}\right], \end{aligned} \tag{3.42}$$

with the localization length

$$\xi_i'' = \frac{2\hbar \upsilon_{F1}\upsilon_{F\bar{1}}}{\sqrt{4\Delta_c^2 \upsilon_{F1}\upsilon_{F\bar{1}} + \left(\Delta_d + \Delta_Z\right)^2 \left(\upsilon_{F1} - \upsilon_{F\bar{1}}\right)^2} - \left(\Delta_d + \Delta_Z\right)\left(\upsilon_{F1} + \upsilon_{F\bar{1}}\right)}. \tag{3.43}$$

We point out that the found MBSs are orthogonal to each other and correspond to independent solutions of the Hamiltonian, because $\sum_\tau \phi_\tau(x) \cdot \phi'_\tau(x) = 0$ and $\sum_\tau \phi_\tau(x) \cdot \phi''_\tau(x) = 0$. We also note that the remaining parameter regimes which we did not discuss here correspond to topologically trivial phases.

Weakly detuned SOI energies

The second regime corresponds to weakly detuned nanowire SOI energies, $|E_{so,1} - E_{so,\bar{1}}| \ll \Delta_Z, \Delta_d, \Delta_c$. For simplicity, we assume that $E_{so,1} = E_{so,\bar{1}}$. For $\Delta_d + \Delta_Z > \Delta_c > |\Delta_d - \Delta_Z|$ and $\Delta_c \neq \Delta_d$, we find a single MBS given by $\gamma = \sum_\tau \int \mathrm{d}x\ \phi_\tau(x) \cdot \Phi_\tau(x)$ with the wavefunction vector $\phi_\tau = (\phi_{\tau 1}, \phi_{\tau\bar{1}}, \phi^*_{\tau 1}, \phi^*_{\tau\bar{1}})$ in the τ-wire given (up to normalization) by

$$\phi_{\tau\sigma}(x) = i e^{i\pi(1-\sigma)/4}\left(e^{-x/\xi_e - i\sigma k_F x} - e^{-x/\xi_i}\right) \tag{3.44}$$

and the localization lengths corresponding to the interior (i) and exterior (e) branches of the spectrum

$$\xi_i = \begin{cases} \frac{\hbar\upsilon_F}{\Delta_Z - (\Delta_c - \Delta_d)} & \text{if } \Delta_c > \Delta_d \\ \frac{\hbar\upsilon_F}{\Delta_Z - (\Delta_d - \Delta_c)} & \text{if } \Delta_c < \Delta_d \end{cases}, \quad \xi_e = \begin{cases} \frac{\hbar\upsilon_F}{\Delta_c - \Delta_d} & \text{if } \Delta_c > \Delta_d \\ \frac{\hbar\upsilon_F}{\Delta_d - \Delta_c} & \text{if } \Delta_c < \Delta_d. \end{cases} \tag{3.45}$$

For $\Delta_c < |\Delta_d - \Delta_Z|$, $\Delta_Z > \Delta_d$ and $\Delta_c \neq \Delta_d$ we find two MBSs given by $\gamma = \sum_\tau \int \mathrm{d}x\ \phi_\tau(x) \cdot \Phi_\tau(x)$ and $\gamma' = \sum_\tau \int \mathrm{d}x\ \phi'_\tau(x) \cdot \Phi_\tau(x)$ where the wavefunction vector $\phi'_\tau = (\phi'_{\tau 1}, \phi'_{\tau\bar{1}}, (\phi'_{\tau 1})^*, (\phi'_{\tau\bar{1}})^*)$ is (up to normalization) given by

$$\phi'_{\tau\sigma}(x) = i\tau e^{i\pi(1-\sigma)/4}\left(e^{-x/\xi'_e - i\sigma k_F x} - e^{-x/\xi'_i}\right), \tag{3.46}$$

with the localization lengths

$$\xi'_i = \frac{\hbar\upsilon_F}{\Delta_Z - (\Delta_c + \Delta_d)}, \qquad \xi'_e = \frac{2\hbar\upsilon_F}{\Delta_c + \Delta_d}. \tag{3.47}$$

We point out that the solutions for the two-MBS phase are independent, because $\phi_\tau(x) \cdot \phi'_\tau(x) = 0$. The parameter regimes which were not discussed correspond to topologically trivial phases.

3.D Interwire tunneling

In this fourth section of the Supplemental Material, we study the effects of tunneling between NWs in the model which we presented in the main text. These interwire tunneling processes are described by

$$H_\Gamma = -\Gamma \sum_{\tau,\sigma} \int \mathrm{d}x \left[\Psi^\dagger_{\tau\sigma}(x)\Psi_{\bar\tau\sigma}(x) + \text{H.c.} \right], \tag{3.48}$$

where $\Gamma > 0$ is a spin-independent tunneling amplitude. The full Hamiltonian of our system in then given by $H = H_0 + H_{so} + H_Z + H_d + H_c + H_\Gamma$. In this section, we will analytically show that: (1) The effects of interwire tunneling on the topological phase transition between the trivial and the one-MBS phase can always be compensated by an appropriate adjustment of the nanowire chemical potentials when $\Delta_{Z\tau}, \Delta_\tau \gg |\Delta_1 - \Delta_{\bar 1}|, |\Delta_{Z1} - \Delta_{Z\bar 1}|$. For low Zeeman splittings, $\Delta_{Z\tau} \ll \Delta_\tau$, this compensation is possible even if $\Delta_{Z\tau} \sim |\Delta_{Z1} - \Delta_{Z\bar 1}|$ and $\Delta_\tau \sim |\Delta_1 - \Delta_{\bar 1}|$. (2) The latter adjustment of the nanowire chemical potentials expands the one-MBS phase by pushing the topological threshold from the one-MBS into the two-MBS phase to higher Zeeman splittings.

We first discuss the limit when $\Delta_{Z\tau}, \Delta_\tau \gg |\Delta_1 - \Delta_{\bar 1}|, |\Delta_{Z1} - \Delta_{Z\bar 1}|$. As a starting point, we set $\Delta_Z = \Delta_{Z\tau}$, $\Delta_d = \Delta_\tau$ and redisplay the full Hamiltonian in the presence of interwire tunneling, $H = \int \mathrm{d}x\ \Psi^\dagger(x)\mathcal{H}(x)\Psi(x)/2$ with $\Psi^\dagger = (\Psi^\dagger_{11}, \Psi^\dagger_{1\bar 1}, \Psi_{11}, \Psi_{1\bar 1}, \Psi^\dagger_{\bar 1 1}, \Psi^\dagger_{\bar 1\bar 1}, \Psi_{\bar 1 1}, \Psi_{\bar 1\bar 1})$ and the Hamiltonian density

$$\mathcal{H}(x) = \left(\frac{\hbar^2 \hat k^2}{2m} - \mu \right) \eta_z - \alpha \hat k \sigma_z + \Delta_Z \eta_z \sigma_x - \Delta_d \eta_y \sigma_y - \Delta_c \tau_x \eta_y \sigma_y - \Gamma \tau_x \eta_z. \tag{3.49}$$

The Pauli matrices $\sigma_{x,y,z}$, $\tau_{x,y,z}$, and $\eta_{x,y,z}$ act in spin, nanowire and electron-hole space, respectively. Because we are solely interested in the modification of the zero-momentum gap closing condition $\Delta_c^2 = (\Delta_d \pm \Delta_Z)$ for finite interwire tunneling, we have also set $\alpha = \alpha_1 = \alpha_{\bar 1}$. Our model can now be mapped onto a model of effectively two decoupled topological NWs. To see this, we introduce the basis

$$\widetilde\Psi^\dagger_\lambda = (\Psi^\dagger_{\bar 1 1} + \lambda\Psi^\dagger_{11}, \Psi^\dagger_{\bar 1\bar 1} + \lambda\Psi^\dagger_{1\bar 1}, \Psi_{\bar 1 1} + \lambda\Psi_{11}, \Psi_{\bar 1\bar 1} + \lambda\Psi_{1\bar 1})/\sqrt{2}. \tag{3.50}$$

We will interpret $\lambda = \pm 1$ as an effective nanowire index that (together with the spin index) labels the energy bands of the system in the absence of superconductivity and magnetic fields fields, $\Delta_d = \Delta_c = \Delta_Z = 0$. We choose $\mu = \Gamma$. In this new basis the Hamiltonian density can then be rewritten as $H = -\sum_\lambda \int \mathrm{d}x\, \widetilde{\Psi}^\dagger_\lambda(x)\widetilde{\mathcal{H}}_\lambda(x)\widetilde{\Psi}_\lambda(x)/2$ with

$$\widetilde{\mathcal{H}}_\lambda(x) = \left(\frac{\hbar^2\hat{k}^2}{2m} - \mu_{\text{eff},\lambda}\right)\eta_z - \lambda\alpha\hat{k}\sigma_z + \Delta_Z\eta_z\sigma_x - \lambda\Delta_{\text{eff},\lambda}\eta_y\sigma_y \tag{3.51}$$

where we have introduced the effective chemical potentials $\mu_{\text{eff},1} = 0$ and $\mu_{\text{eff},\bar{1}} = 2\Gamma$ as well as the effective pairing potentials $\Delta_{\text{eff},1} = \Delta_d - \Delta_c$ and $\Delta_{\text{eff},\bar{1}} = \Delta_d + \Delta_c$. This is precisely the Hamiltonian of two decoupled topological NWs labeled by the effective nanowire index λ. Thus, the system hosts one MBS at each end for low magnetic fields when

$$\Delta_Z^2 > \Delta_{\text{eff},1}^2 + \mu_{\text{eff},1}^2 = (\Delta_d - \Delta_c)^2 \tag{3.52}$$

and two MBSs at each end for large magnetic fields when

$$\Delta_Z^2 > \Delta_{\text{eff},\bar{1}}^2 + \mu_{\text{eff},\bar{1}}^2 = (\Delta_d + \Delta_c)^2 + (2\Gamma)^2. \tag{3.53}$$

Consequently, by an appropriate adjustment of the nanowire chemical potentials (for example by an external gate voltage), we still observe the proposed one-MBS phase for low magnetic fields. Also, the one-MBS phase now even extends to significantly stronger fields. Moreover, without a proper tuning of the chemical potentials, $|\mu| \gg \Gamma$, the topological threshold is shifted to higher magnetic fields and not much is gained, see also Fig. 3.4(a) and (b).

Next, we comment on the case when $\Delta_\tau \sim |\Delta_1 - \Delta_{\bar{1}}|$. In this case the choice

$$\mu_1 = \Gamma\sqrt{\frac{\Delta_1}{\Delta_{\bar{1}}}} \quad \text{and} \quad \mu_{\bar{1}} = \Gamma\sqrt{\frac{\Delta_{\bar{1}}}{\Delta_1}} \tag{3.54}$$

ensures that the effects of interwire tunneling can still be compensated provided $\Delta_{Z\tau} \ll \Delta_\tau$. However, we note that the topological phase transition from the trivial to the one-MBS phase at $\Delta_c = 0$ is renormalized to

$$\begin{aligned}&\Delta_{Z,c}^2\\ &=\frac{1}{2}\left[\Delta_1^2+\Delta_{\bar{1}}^2+\Gamma^2\left(2+\frac{\Delta_1}{\Delta_{\bar{1}}}+\frac{\Delta_{\bar{1}}}{\Delta_1}\right)\right.\\ &\left.-\frac{\sqrt{\left(\Delta_1\Delta_{\bar{1}}\left[\Delta_1^2+\Delta_{\bar{1}}^2\right]+\Gamma^2\left[\Delta_1+\Delta_{\bar{1}}\right]^2\right)^2-4\Delta_1^3\Delta_{\bar{1}}^3\left(\Delta_1\Delta_{\bar{1}}+4\Gamma^2\right)}}{\Delta_1\Delta_{\bar{1}}}\right]\geq 0.\end{aligned} \tag{3.55}$$

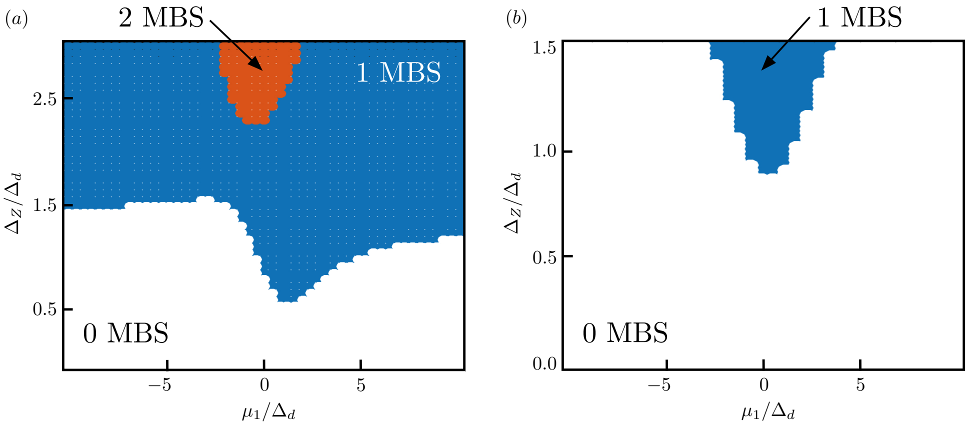

Figure 3.4: (a) Topological phase diagram as a function of Δ_Z/Δ_d and μ_1/Δ_d (obtained from a tight-binding diagonalization of 800 sites per NW) for finite interwire tunneling, $\Gamma/\Delta_d = 1$. We have set $E_{so,\tau}/\Delta_d = 6.25$, $\Delta_c/\Delta_d = 0.5$ and $\mu_{\bar{1}}/\Delta_d = 1$. Colors are the same as in Fig. 3.2 of the main text. We see that without tuning the chemical potentials to the sweet spot $\mu_\tau = \Gamma$ the topological threshold $\Delta_{Z,c}$ is shifted to significantly higher magnetic fields and not much is gained in a double NW setup compared to single NWs. (b) Same topological phase diagram as in (a) but for $\mu_{\bar{1}}/\Delta_d = 4$. Once more, we see that without the tuning to the sweet spot $\mu_\tau = \Gamma$ no low-field topological threshold is observed.

3.E Numerical results

In this final section, we study the tight-binding model which corresponds to the continuum model presented in the main text [84,87,115]. The tight-binding Hamiltonian is given by

$$\begin{aligned} H = \Bigg[\sum_{\tau} \Big(\sum_{j=1}^{N} \tilde{\psi}^{\dagger}_{\tau,j} [-\mu_\tau \eta_z + \Delta_\tau \eta_x + \Delta_{Z\tau} \sigma_x] \tilde{\psi}_{\tau,j} \\ + \sum_{j=1}^{N-1} \tilde{\psi}^{\dagger}_{\tau,j+1} [-t - i\alpha_\tau \sigma_z]\, \eta_z \tilde{\psi}_{\tau,j} + \mathrm{H.c.} \Big) \Bigg] + \sum_{j=1}^{N} \tilde{\psi}^{\dagger}_{\bar{1},j}\, (\Delta_c \eta_x)\, \tilde{\psi}_{1,j} + \mathrm{H.c.}, \end{aligned} \tag{3.56}$$

where N is the number of lattice sites per wire and furthermore $\tilde{\psi}_{\tau,j} = (\psi^{\dagger}_{\tau,j,\uparrow}, \psi^{\dagger}_{\tau,j,\downarrow}, \psi_{\tau,j,\downarrow}, -\psi_{\tau,j,\uparrow})$ is the electron spinor at site j in the τ-wire with $\psi_{\tau,j,\sigma}$ the annihilation operator of a spin σ electron at site j in the τ-wire. Moreover, μ_τ, Δ_τ, α_τ, $\Delta_{Z\tau}$ are the chemical potentials, direct pairing strengths, SOI strengths and Zeeman splittings in wire τ, respectively. Finally, Δ_c is the strength of the crossed-Andreev pairing, t is the hopping amplitude and the Pauli matrices $\sigma_{x,y,z}$ ($\eta_{x,y,z}$) act in spin (particle-hole) space.

Topological phase diagram

First, we perform a numerical diagonalization to obtain the topological phase diagram for the regime of weakly detuned SOI energies, $|E_{so,1} - E_{so,\bar{1}}| \ll \Delta_{Z\tau}, \Delta_\tau, \Delta_c$, and for the intermediate regime, $|E_{so,1} - E_{so,\bar{1}}| \sim \Delta_{Z\tau}, \Delta_\tau, \Delta_c$. The results are shown in Fig. 3.5. In the limit of weakly detuned SOI energies, we find that the two-MBS phase which for $|E_{so,1} - E_{so,\bar{1}}| \gg \Delta_{Z\tau}, \Delta_\tau, \Delta_c$ with $\Delta_d = \Delta_\tau$, $\Delta_Z = \Delta_{Z\tau}$ appeared when $\Delta_c > \Delta_d + \Delta_Z$, completely turns into a topologically trivial phase, see Fig. 3.5(a). Compared to that, in the intermediate regime, we find that the same two-MBS phase turns into a trivial phase once $\Delta_c > \Delta_c^*$ where Δ_c^* was defined in Eq. (3.37), see Fig. 3.5(b).

Stability Analysis

Second, we analyze the stability of the one-MBS phase against different perturbations.

Misalignments of the magnetic fields. First, we discuss rotations of the magnetic field in the $x - z$ plane for the regime of strongly detuned SOI energies, $|E_{so,1} - E_{so,\bar{1}}| \gg \Delta_{Z\tau}, \Delta_\tau, \Delta_c$. We replace our tight-binding

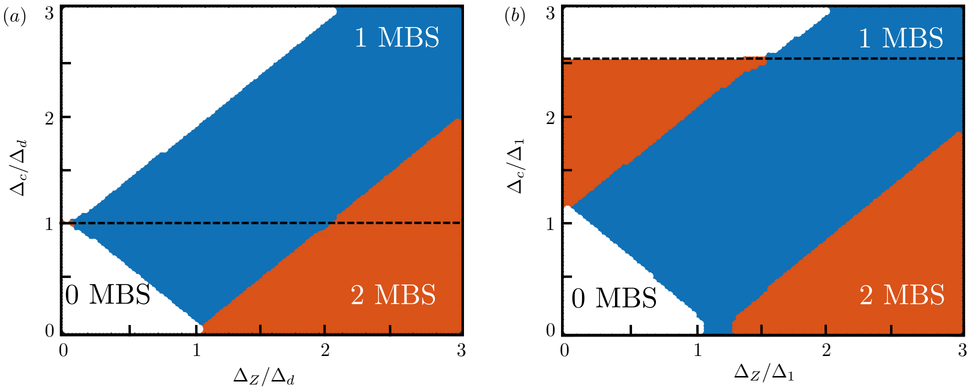

Figure 3.5: (a) Topological phase diagram as a function of Δ_Z/Δ_d and Δ_c/Δ_d for the regime of weakly detuned SOI energies, $|E_{so,1} - E_{so,\bar{1}}| \ll \Delta_{Z\tau}, \Delta_\tau, \Delta_c$. The color coding scheme is the same as in Fig. 3.2 in the main text. The dashed black line denotes a gap closing at finite momentum. We have chosen $E_{so,\tau}/\Delta_d = 2$ and $\mu_1 = \mu_{\bar{1}} = 0$. The two-MBS phase which appeared for $\Delta_c > \Delta_d + \Delta_Z$ when $|E_{so,1} - E_{so,\bar{1}}| \gg \Delta_{Z\tau}, \Delta_\tau, \Delta_c$ turns into a trivial phase. All other topological phases remain unchanged. (b) Topological phase diagram as a function of Δ_Z/Δ_1 and Δ_c/Δ_1 for the regime, $|E_{so,1} - E_{so,\bar{1}}| \sim \Delta_{Z\tau}, \Delta_\tau, \Delta_c$. We have chosen $E_{so,1}/\Delta_1 = 2$,$E_{so,\bar{1}}/\Delta_1 = 4.5$, $\mu_1 = \mu_{\bar{1}} = 0$, $\Delta_{\bar{1}}/\Delta_1 = 1.3$. We note that both two-MBS phases disappear for $\Delta_c > \Delta_c^*$, see Eq. (3.37).

Hamiltonian according to

$$H \to H + \sum_\tau \sum_{j=1}^{N} \tilde{\psi}^\dagger_{\tau,j} \left(\Delta'_{Z\tau}\sigma_z\right) \tilde{\psi}_{\tau,j}, \tag{3.57}$$

and set $\Delta_{Z1} = 0, \Delta'_{Z1} = \Delta_Z$ for the 1-wire and $\Delta_{Z\bar{1}} = \Delta_Z \cos(\phi), \Delta'_{Z\bar{1}} = \Delta_Z \sin(\phi)$ for the $\bar{1}$-wire where $\phi \in [0, 2\pi)$ is the angle of the magnetic field acting on the $\bar{1}$-wire with respect to the x axis in the $x - z$ plane. For $\sin(\phi) \neq 0$, this places the setup in symmetry class D with a $\mathbb{Z}_2$ topological invariant [112]. From a numerical tight-binding diagonalization, we find that the one-MBS phase remains stable, while the two-MBS phases turn into trivial phases for $\sin(\phi) \neq 0$, see Fig. 3.6(a). Additionally, we observe that the one-MBS phase expands to larger magnetic fields.

Misalignments of the SOI vectors. The case of misaligned SOI vectors in the two wires was discussed in the main text. To obtain the topological phase diagram shown in Fig. 3.3(c) in the main text, we modify our tight-binding Hamiltonian according to

$$H \to H + i \sum_{\tau} \sum_{j=1}^{N} \tilde{\psi}^{\dagger}_{\tau,j+1}\, \alpha'_{\tau} \sigma_y \eta_z \tilde{\psi}_{\tau,j}, \tag{3.58}$$

and set $\alpha_1 = \alpha$, $\alpha'_1 = 0$ for the 1-wire and $\alpha_{\bar{1}} = \tilde{\alpha}\cos(\theta)$, $\alpha'_{\bar{1}} = \tilde{\alpha}\sin(\theta)$ for the $\bar{1}$-wire with θ being the angle of the SOI vector in the $\bar{1}$-wire relative to the z-axis in the yz-plane. As a result, we confirm that the one-MBS phase remains stable against misalignments of the SOI vectors. In contrast to that, the two-MBS phase is unstable except special line $\Delta_Z = 0$, where time-reversal symmetry guarantees the presence of Kramers doublets [32,69,70,73,76,85,117,120–122,152]. If $\Delta_Z \neq 0$, the two MFs localized at the same end are protected from hybridization by some additional symmetry. However, as noticed above such effective time-reversal symmetries are not stable against general perturbations [123–126], resulting in lifting of the degeneracy of two zero-energy bound states.

Interwire tunneling. Lastly, we provide additional information on our analysis for the case of finite interwire tunneling presented in the main text. In this case, the tight-binding Hamiltonian is modified according to

$$H \to H + \sum_{j=1}^{N} \tilde{\psi}^{\dagger}_{2,j} (-\Gamma \eta_z) \tilde{\psi}_{1,j} + \text{H.c.}, \tag{3.59}$$

where $\Gamma > 0$ is the spin-independent tunneling amplitude. As discussed in the previous section, we find that the effects of interwire tunneling on the topological phase transition separating the trivial and one-MBS phase can be completely compensated by setting $\mu_\tau = \Gamma$. Without this tuning the topological threshold separating the trivial and one-MBS phase is pushed to significantly larger magnetic fields, see see Fig. 3.6(b).

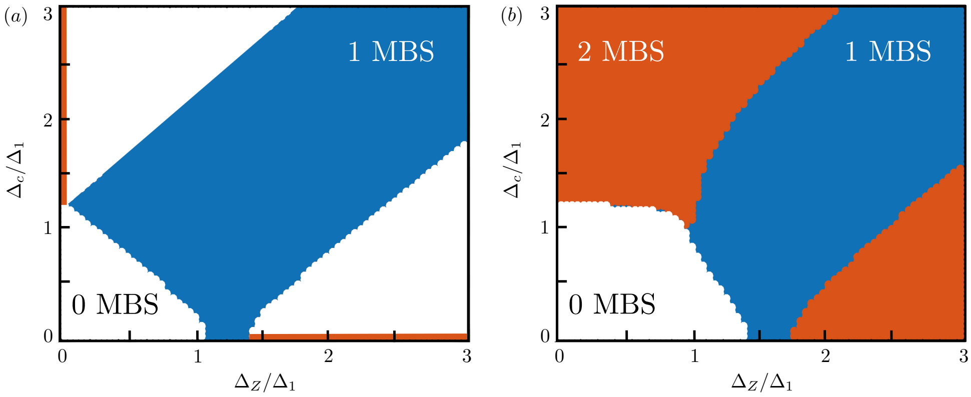

Figure 3.6: (a) Topological phase diagram as a function of Δ_Z/Δ_1 and Δ_c/Δ_1 for the regime of strongly detuned SOI energies, $|E_{so,1} - E_{so,\bar{1}}| \gg \Delta_{Z\tau}, \Delta_\tau, \Delta_c$, and a rotation of the magnetic field in the $\bar{1}$-wire by $\phi = 0.2$. The color coding scheme is the same as in Fig. 3.2 in the main text. We have chosen $E_{so,1}/\Delta_1 = 6.25$, $E_{so,\bar{1}}/\Delta_1 = 12.25$, $N = 800$, $\Delta_{\bar{1}}/\Delta_1 = 1.3$, $\mu_1 = 0$ and $\mu_{\bar{1}} = 0$. While the one-MBS remains stable, the two-MBS phases are unstable against rotations of the magnetic field with $\sin(\phi) \neq 0$. (b) Same topological phase diagram as in (a) but with finite interwire tunneling, $\Gamma/\Delta_1 = 1$. Moreover, we also set $\phi = 0$ and $\mu_\tau = 0$. Consequently, the effects of interwire tunneling are [unlike in Fig. 3.3(b) of the main text] not compensated and the topological threshold from the trivial to the one-MBS phase is pushed to substantially higher magnetic fields. Thus, to get the maximum advantage of the double nanowire setup, it is crucial to compensate for these shifts due to interwire tunneling.

Part II

New probes for topological superconductivity

CHAPTER 4

Detecting Topological Superconductivity with φ_0 Josephson Junctions

Adapted from:
Constantin Schrade, Silas Hoffman, and Daniel Loss,
"Detecting Topological Superconductivity with φ_0 Josephson Junctions",
Phys. Rev. B **95**, 195421 (2017).

The recent experimental discovery of φ_0 Josephson junctions by Szombati *et al.* [26], characterized by a finite phase offset in the supercurrent, requires the same ingredients as topological superconductors, which suggests a profound connection between these two distinct phenomena. Here, we show that a quantum dot φ_0 Josephson junction can serve as a new qualitative indicator for topological superconductivity: Microscopically, we find that the phase shift in a junction of $s-$wave superconductors is due to the spin-orbit induced mixing of singly occupied states on the quantum dot, while for a topological superconductor junction it is due to singlet-triplet mixing. Because of this important difference, when the spin-orbit vector of the quantum dot and the external Zeeman field are orthogonal, the s-wave superconductors form a π Josephson junction while the topological superconductors have a finite offset φ_0 by which topological superconductivity can be distinguished from conventional superconductivity. Our prediction can be immediately tested in nanowire systems currently used for Majorana fermion experiments and thus offers a new and realistic approach for detecting topological bound states.

4.1 Introduction

Non-abelian anyons are the building blocks of topological quantum computers [128]. The simplest realization of non-abelian anyons are Majorana bound states (MBSs) in topological superconductors (TSs) [129]. Such a TS can be induced by an s-wave superconductor (SC) in systems of nanowires with spin-orbit interaction (SOI) subject to a Zeeman field [3, 4, 6, 31], in chains of magnetic atoms [10, 12, 90, 91] and in topological insulators [2, 46–48, 130, 131]. However, providing experimental evidence for the existence of this new phase of matter has remained a major challenge.

Here we present a new qualitative indicator of MBS based on φ_0 Josephson junctions (φ_0JJs). In φ_0JJs the Josephson current is offset by a finite phase, φ_0, so that a finite supercurrent flows even when the phase difference between the superconducting leads and the magnetic flux enclosed by the Josephson junction (JJ) vanishes. Such φ_0JJs have been discussed in systems based on unconventional superconductors [132–136], ferromagnets [138–141], quantum point contacts [142], topological insulators [143], nanowires [84, 144, 145], diffusive systems [146, 147] and in Josephson junctions with alternating critical current density [148]. Recently, the connection between φ_0JJs based on nanowires and TSs has been discussed and a quantitative enhancement of the anomalous current was predicted for the topological phase [149]. Most relevant for the present work, the emergence of a φ_0JJ was theoretically predicted [24,25,150] in a system of a quantum dot (QD) with SOI subject to a Zeeman field when coupled to s-wave superconducting leads and observed in recent experiments [26]. Interestingly, the ingredients for observing a φ_0JJ in this type of system largely overlap with those required to generate MBSs. Therefore, it is expected that φ_0JJ can provide a novel platform for detecting the effects of topological superconductivity.

In this work, we focus on two models for φ_0JJs based on QDs which, compared to previous studies [24, 25, 150], are in the singlet-triplet anticrossing regime. In the first model, two s-wave SCs are tunnel coupled via a two-orbital QD with SOI and subject to a Zeeman field, see Fig. 4.1(a), wherein we find a finite phase shift caused by the SOI-induced mixing of singly occupied states of the QD. In the second model, replacing the two s-wave SCs by two TSs, see Fig. 4.1(b), we again find a finite phase shift which results from the singlet-triplet mixing of the doubly occupied QD states. When the spin-orbit vector $\mathbf{\Omega}_{\mathrm{D}}$ and the magnetic field are orthogonal, the system is invariant under a composition of time reversal and mirroring in the plane perpendicular to $\mathbf{\Omega}_{\mathrm{D}}$, under which the superconducting phase goes to opposite itself; because the energy must be invariant under this symmetry, there can be no terms that are odd in the superconducting phase difference in the Hamiltonian and thus no non-trivial phase offset [139, 151]. However, the MBSs in the TS leads are not time-reversal invariant and thus transform nontrivially under the above transformations. Consequently, we anticipate a nonzero phase shift for this case. Indeed, we show that the phase shift φ_0 is equal to π for the s-wave superconducting leads [45], while $\varphi_0 \neq 0, \pi$ for the TSs leads (unlike [39, 152]), which can, consequently, be used as a new qualitative indicator of MBSs.

4.2 Josephson junction models

Our starting point for both of the JJ models outlined above is the Hamiltonian

$$H_\nu = H_{\mathrm{D}} + H_{\nu,\mathrm{L}} + H_{\nu,\mathrm{t}}\,, \tag{4.1}$$

where $\nu = \mathrm{S}, \mathrm{TS}$ corresponds to the model with s-wave SC leads and TS leads, respectively. The first term in this expression $H_{\mathrm{D}} = H_0 + H_{\mathrm{Z}} + H_{\mathrm{SOI}}$ is the Hamiltonian of an isolated QD. Here, $H_0 = (V_g + \delta/2)\, n_a + (V_g - \delta/2)\, n_b + U/2 \sum_\tau n_\tau(n_\tau - 1) + U_{ab} n_a n_b$ describes a QD with two orbitals $\tau = a, b$ at energy difference $\delta > 0$ with respect to a gate voltage V_g. The particle number operator of orbital τ is $n_\tau = \sum_s d^\dagger_{\tau s} d_{\tau s}$ with $d_{\tau s}$ the electron annihilation operator with spin $s = \uparrow, \downarrow$ quantized along the z axis in orbital τ. The intraorbital (interorbital) Coulomb interaction strength is U (U_{ab}). Furthermore, $H_{\mathrm{Z}} = -g\mu_B B \sum_\tau (d^\dagger_{\tau\uparrow} d_{\tau\uparrow} - d^\dagger_{\tau\downarrow} d_{\tau\downarrow})/2$ describes a Zeeman field $\boldsymbol{B}$ along the z axis of magnitude $B = |\boldsymbol{B}|$ with g the electron g-factor and μ_B the Bohr magneton. Lastly, $H_{\mathrm{SOI}} = i\mathbf{\Omega}_{\mathrm{D}}/2 \cdot \sum_{s,s'} (d^\dagger_{bs} \boldsymbol{\sigma}_{ss'} d_{as'} - \mathrm{H.c.})$ describes the SOI on the QD, where $\mathbf{\Omega}_{\mathrm{D}} = \Omega_{\mathrm{D}}(\sin\theta, 0, \cos\theta)$, in which $\Omega_{\mathrm{D}} \neq 0$, $\theta \in [0, \pi]$ is the angle of the SOI vector with respect to the Zeeman field, and $\boldsymbol{\sigma}$ is the vector of Pauli matrices.

The second term in Eq. (4.1) describes the isolated superconducting leads. For the first model, $H_{\mathrm{S,L}} = \sum_{\eta,\mathbf{k}\sigma} E_{\mathbf{k}} \gamma^\dagger_{\eta,\mathbf{k}\sigma} \gamma_{\eta,\mathbf{k}\sigma}$, where $\gamma_{\eta,\mathbf{k}\sigma}$ is the quasiparticle annihilation operator in SC $\eta = 1, 2$ with momentum $\mathbf{k}$, pseudospin $\sigma = \Uparrow, \Downarrow$, and energy $E_{\mathbf{k}} = \sqrt{\xi_{\mathbf{k}}^2 + \Delta^2}$ with Δ the superconducting gap and $\xi_{\mathbf{k}}$ the single-electron dispersion relation in the normal metal state. The non-degenerate ground state of the s-wave superconductors, $|0_\eta\rangle$, is defined so that $\gamma_{\eta,\mathbf{k}\sigma}|0_\eta\rangle = 0$. For the second model, we assume that the localization length of the MBS wavefunctions is much smaller than the length of TSs. We also neglect contributions of bulk quasiparticles which is valid for energies much smaller than the energy gap. Consequently the MBSs are at zero energy and $H_{\text{TS,L}} = 0$. Hence, the ground state of the TS leads is four-fold degenerate which, upon choosing a fixed parity subspace, becomes two-fold degenerate. In the following, we consider the odd parity subspace, however, the results for the even parity ground state subspace are identical. Finally, if the localization length of the MBS wavefunction is comparable to the length of the TSs, a finite energy splitting between the MBS in the same TS is induced, $H_{\text{TS,L}} \neq 0$. However, within the perturbation theory appraoch carried out in the next section, this energy splitting only modifies the energy denominators in the effective Hamiltonian and can be neglected when it is small on the energy scale of the separation between the TS chemical potentials and the QD energy levels [107].

The last term in Eq. (4.1) describes the tunnel coupling between the superconducting leads and the QD. For the first model, it is given by

$$H_{\text{S,t}} = \sum_{\eta\tau} \sum_{\mathbf{k}s} t_{\eta\tau} e^{i\varphi_\eta/2}\, c^\dagger_{\eta,\mathbf{k}s} d_{\tau s} + \text{H.c.}\,, \tag{4.2}$$

with $c_{\eta,\mathbf{k}s}$ being the annihilation operator of an electron with momentum k and spin s in SC η [153]. It is related to the quasiparticle operators by $c_{\eta,\mathbf{k}\uparrow} = u_{\mathbf{k}}\gamma_{\eta,\mathbf{k}\Uparrow} + v_{\mathbf{k}}\gamma^\dagger_{\eta,-\mathbf{k}\Downarrow}$ and $c_{\eta,-\mathbf{k}\downarrow} = u_{\mathbf{k}}\gamma_{\eta,-\mathbf{k}\Downarrow} - v_{\mathbf{k}}\gamma^\dagger_{\eta,\mathbf{k}\Uparrow}$ with coherence factors $u_{\mathbf{k}} = (1/\sqrt{2})\sqrt{1 + \xi_{\mathbf{k}}/E_{\mathbf{k}}}$ and $v_{\mathbf{k}} = (1/\sqrt{2})\sqrt{1 - \xi_{\mathbf{k}}/E_{\mathbf{k}}}$. The tunneling Hamiltonian also contains the superconducting phase φ_η of SC η and real, spin and momentum-independent tunneling amplitudes $t_{\eta\tau}$. The more general case of spin-dependent tunneling amplitudes does not alter our results (see also Appendix 4.B and 4.C). For the second model, the coupling of the TSs and the QD is given by

$$H_{\text{TS,t}} = \sum_{\eta\tau} \sum_{s} t_{\eta\tau} e^{i\varphi_\eta/2}\, \Gamma_\eta d_{\tau s} + \text{H.c.}\,, \tag{4.3}$$

with Γ_η being the MBS in TS η which is spatially closest to the QD [105, 154, 155]. We assume that its partner Γ'_η at the opposite end of the TS

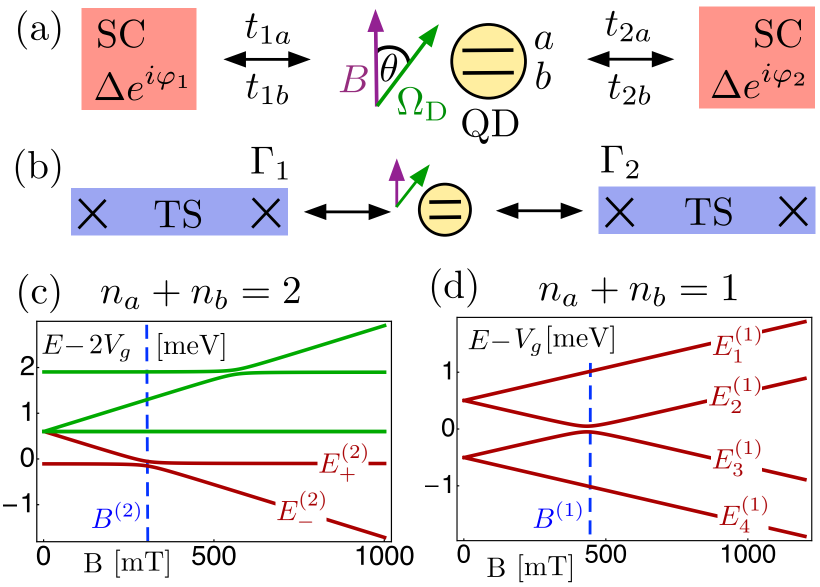
(a)
SC
$\Delta e^{i\varphi_1}$
t_{1a}
t_{1b}
B
θ
Ω_D
a
b
QD
t_{2a}
t_{2b}
SC
$\Delta e^{i\varphi_2}$
(b)
Γ_1
TS
Γ_2
TS
(c) $n_a + n_b = 2$
$E-2V_g$ [meV]
2
1
0
−1
$B^{(2)}$
$E_+^{(2)}$
$E_-^{(2)}$
0
B [mT]
500
1000
(d) $n_a + n_b = 1$
$E-V_g$ [meV]
1
0
−1
$E_1^{(1)}$
$E_2^{(1)}$
$E_3^{(1)}$
$E_4^{(1)}$
$B^{(1)}$
0
B [mT]
500
1000

Figure 4.1: Setups for φ_0JJs. (a) Two s-wave SCs (red) are tunnel coupled via a QD (yellow) with two orbitals a and b. The QD is subject to an external magnetic field $\boldsymbol{B}$ at some relative angle θ to its SOI $\boldsymbol{\Omega}_\mathrm{D}$. (b) Same visual encodings. The SCs are replaced by two TSs (blue). The QD now couples to the two inner MBS (crosses) $\Gamma_{1,2}$ of the TSs. (c) Spectrum of the bare QD as a function of B for the double occupancy sector. Red bands contribute to our effective description, green bands do not. We have chosen $\delta = 1$ meV, $g = 40$, $U = 0.9$ meV and $U_{ab} = 0.6$ meV, $\Omega_\mathrm{D} = 0.1$ meV, so that $B^{(2)} = 302$ mT. (d) Same as (c) but for the single occupancy sector with $B^{(1)} = 432$mT.

does not couple to the QD. However, they form non-local fermionic operators $C_1 = (\Gamma_1' + i\Gamma_1)/2$ and $C_2 = (\Gamma_2 + i\Gamma_2')/2$. Additionally, we assume temperatures that are smaller than the superconducting gap Δ and the separation between the MBS and the next finite-energy Andreev bound state Δ', $k_B T \ll \Delta, \Delta'$.

We now proceed with a discussion of H_D in the regime of $\delta > U > U_{AB} \gg |\Omega_\mathrm{D}|$ common to typical experiments [26]. First, we address the case of a doubly occupied dot, $n_a + n_b = 2$. For $\Omega_\mathrm{D} = 0$, the spectrum consists of three singlet (triplet) bands which are constant (split) as a function of the Zeeman field. As experimentally observed in [156], for finite Ω_D and θ, the singlet and triplet bands anticross, see Fig. 4.1(c). In all following discussions, we operate the QD in the regime close to the anticrossing of the singlet $|S\rangle = d^\dagger_{b\uparrow} d^\dagger_{b\downarrow} |0_\mathrm{D}\rangle$ and the triplet $|T\rangle = d^\dagger_{a\uparrow} d^\dagger_{b\uparrow} |0_\mathrm{D}\rangle$ which occurs at the Zeeman field $B^{(2)} = (\delta - U + U_{ab})/g\mu_B$. Here, $|0_\mathrm{D}\rangle$ is the vacuum state on the dot. The effective Hamiltonian, valid to lowest order in Ω_D, which acts in the two-level subspace spanned by $|S\rangle$ and $|T\rangle$ is $H^{(2)}_\mathrm{ST} = (2V_g - \delta + U) |S\rangle\langle S| + (2V_g + U_{ab} - g\mu_B B) |T\rangle\langle T| + [i\Omega_\mathrm{D} \sin(\theta)/2 \, |T\rangle\langle S| + \mathrm{H.c.}]$. The spectrum of $H^{(2)}_\mathrm{ST}$ is given by $E^{(2)}_\pm$ with corresponding orthonormal eigenstates

$$\left| E^{(2)}_\pm \right\rangle = iS_\pm |S\rangle + T_\pm |T\rangle . \tag{4.4}$$

Here, $S_\pm, T_\pm$ are real functions of the system parameters, see also Appendix 4.A .

Second, we discuss the case of a singly occupied dot, $n_a + n_b = 1$. For $\Omega_\mathrm{D} = 0$, the energy levels for opposite spins split as a function of the Zeeman field. For finite Ω_D and θ, an energy gap opens up at the crossing point $B^{(1)} = \delta/g\mu_B$ of the spin-up band in orbital a and the spin-down band in orbital b, see Fig. 4.1(d). We will denote the four eigenvalues of the singly occupied sector by $E^{(1)}_\lambda$ for $\lambda = 1, ..., 4$. The corresponding orthonormal eigenstates are given by

$$|E^{(1)}_\lambda\rangle = \sum_s \left(iA_{\lambda s} d^\dagger_{as} + B_{\lambda s} d^\dagger_{bs} \right) |0_\mathrm{D}\rangle . \tag{4.5}$$

Here, $A_{\lambda s}$, $B_{\lambda s}$ are real functions of the system parameters, see also Appendix 4.A. The relative imaginary unit in both Eq. (4.4) and Eq. (4.5) is due to the SOI. We adjust the filling and the gate voltage of the QD, so that its ground state is given by $E^{(2)}_-$ while its first excited states are given by $E^{(2)}_+$ and $E^{(1)}_\lambda$ for some fixed λ. The seperation between $E^{(2)}_-$ to the states $E^{(1)}_{\lambda'}$ with $\lambda' \neq \lambda$ is assumed to be large, $|E^{(1)}_{\lambda'} - E^{(2)}_-| \gg E^{(1)}_\lambda - E^{(2)}_-$. Finally, the remaining occupancy sectors of the QD, whose energies are much larger than the QD-lead coupling, are not relevant for our results and are hence omitted.

4.3 Detecting topological superconductivity.

In order to calculate the superconducting current, we tune the chemical potential of the superconductors close to the $E^{(2)}_-$ level. We require for the SC JJ that $\pi\nu_F t_{\eta\tau} t_{\eta'\tau'} \ll E^{(1)}_\lambda - E^{(2)}_-, |\Omega_\mathrm{D}| \sin(\theta), \Delta$ with ν_F the normal-state density of states of the leads at the Fermi energy and for the TS JJ that $t_{\eta\tau} \ll E^{(1)}_\lambda - E^{(2)}_-, |\Omega_\mathrm{D}| \sin(\theta)$, so that in both cases the states $E^{(2)}_+$

and $E_\lambda^{(1)}$ on the QD serve as virtual tunneling states. Our approach is valid for angles $\theta \in [\theta_c, \pi - \theta_c]$ where θ_c is a critical angle determined by the conditions above, see also Appendix 4.D . Furthermore, we work in a temperature regime of $k_B T \ll E_\lambda^{(1)} - E_-^{(2)}, |\Omega_\text{D}| \sin(\theta)$. The effective tunneling Hamiltonian $H_\text{S,t}$ ($H_\text{TS,t}$) valid up to fourth (second) order in the tunneling amplitudes acting on the ground state of the isolated dot and s-wave (odd parity) ground state of the uncoupled leads is

$$H_{\nu,\text{t}}^\text{eff} = \left(E_\nu^0 \cos\varphi_\nu + E_\nu^a \sin\varphi_\nu\right) T_\nu + \widetilde{E}_\nu, \tag{4.6}$$

with $\varphi_\text{S} = 2\varphi_\text{TS} = \varphi_1 - \varphi_2$ and $T_\text{S} = 1$, $T_\text{TS} = C_1^\dagger C_2 + \text{H.c.} = i\Gamma_2\Gamma_1$ [107]. The first term in Eq. (4.6) arises due to Cooper pair (non-local fermion) tunneling across the (TS) SC JJ. The second term is an energy offset, due to processes for which there is no such transport. At zero temperature, the Josephson current, defined by $I_\nu = 2e\partial_\varphi E_{\nu,\text{GS}}/\hbar$ with $E_{\nu,\text{GS}}$ the ground state energy of the coupled system, is given by

$$I_\nu = -I_\nu^c \sin(\varphi_\nu - \varphi_\nu^0), \quad \varphi_\nu^0 = \arctan(E_\nu^a/E_\nu^0), \tag{4.7}$$

where the critical current is $I_\nu^c = 2\kappa_\nu e\sqrt{(E_\nu^0)^2 + (E_\nu^a)^2}\text{sgn}(E_\nu^0)/\hbar$. Because in the TS case the ground state is a function of φ, the sign of the Josephson energy also depends on the phase difference: $\kappa_\text{TS} = -1/2$ when $-E_\text{TS}^0 \cos\varphi_\text{TS} - E_\text{TS}^a \sin\varphi_\nu + \widetilde{E}_\text{TS}$ is the ground state energy and $\kappa_\text{TS} = 1/2$ otherwise. In the SC case the ground state is independent of φ and therefore $\kappa_\text{S} = 1$. Notice that there is a finite phase shift only when $E_\nu^a \neq 0$. For the SC JJ the coefficients in Eq. (4.6) are given by,

$$\begin{aligned} E_\text{S}^0 &= g_\text{S} t_{1b} t_{2b} B_{\lambda\uparrow}^2 \left(A_{\lambda\uparrow}^2 t_{1b} t_{2b} + B_{\lambda\uparrow}^2 t_{1a} t_{2a}\right), \\ E_\text{S}^a &= g_\text{S} t_{1b} t_{2b} A_{\lambda\uparrow} B_{\lambda\uparrow}^3 \left(t_{1a} t_{2b} - t_{1b} t_{2a}\right). \end{aligned} \tag{4.8}$$

The prefactor $g_\text{S} > 0$, which is not relevant for the phase shift φ_S^0, includes the coherence factors and energy denominators picked up in the perturbation theory, see also Appendix 4.B. The SC JJ exhibits in general a finite phase shift, when $t_{1a}t_{2b} - t_{1b}t_{2a} \neq 0$. For $\varphi_S = 0$, the sign of the supercurrent is determined by $\text{sgn}(t_{1a}t_{2b} - t_{1b}t_{2a})$ and $\text{sgn}(A_{\lambda\uparrow}B_{\lambda\uparrow}) \propto \text{sgn}(\Omega_\text{D})$. The origin of the phase shift in the SC JJ is the superposition of singly occupied QD orbitals. Depending on the virtual state, an electron tunnels with amplitude proportional $\propto iA_{\lambda\uparrow}B_{\lambda\uparrow}$ when switching orbitals on the dot or $\propto (B_{\lambda\uparrow})^2$ or $\propto (A_{\lambda\uparrow})^2$ if the orbital is constant. Thus, Cooper pairs are tunneling with amplitude E_S^a when the former process occurs once and amplitude E^0_{S} when the process occurs an even number of times, see also Appendix 4.B.

Notably, when the relative angle between Zeeman field and SOI is $\theta = \pi/2$ the SOI only mixes opposite spins in different orbitals so that $A_{\lambda\uparrow} = B_{\lambda\downarrow} = 0$ for $\lambda = 1, 4$ and $A_{\lambda\downarrow} = B_{\lambda\uparrow} = 0$ for $\lambda = 2, 3$. Thus, $E^a_s = 0$ and the phase shift φ^0_{S} vanishes, see Fig. 4.2(a).

Unlike the SC JJ, the TS JJ allows for nonzero phase shift, see Fig. 4.2(a), at $\theta = \pi/2$. The coefficients in Eq. (4.6) for the TS JJ when $\lambda = 1, 4$ are given by

$$\begin{aligned} E^0_{\mathrm{TS}}(\pi/2) &= g_{\mathrm{TS}} B^2_{\lambda\uparrow} S_- T_- (t_{1b} t_{2a} - t_{1a} t_{2b}) \ , \\ E^a_{\mathrm{TS}}(\pi/2) &= -g_{\mathrm{TS}} B^2_{\lambda\uparrow} \left(S^2_- t_{1b} t_{2b} + T^2_- t_{1a} t_{2a} \right) \ , \end{aligned} \tag{4.9}$$

where the prefactor $g_{\mathrm{TS}} > 0$ includes the energy denominators of the perturbation theory, see also Appendix 4.C. In comparison to the SC JJ, the sign of the supercurrent at $\varphi_{\mathrm{TS}} = 0$ in the TS JJ is determined by parity $i\Gamma_2\Gamma_1$. If the parity fluctuates, the supercurrent exhibits fluctuations as well. So the observation of a phase shift requires sufficiently long parity life times which can be up to minutes [157]. Focusing on the case when $\lambda = 1, 4$, the processes that contribute to $E^0_{\mathrm{TS}}(\pi/2)$ in Eq. (4.9) come from virtual tunneling sequences taking a singlet to a triplet state, with amplitude $\propto iS_-T_-$, and the corresponding sequences taking a triplet to the singlet state, with an amplitude $\propto -iS_-T_-$. We emphasize that these processes are only possible due to the singlet-triplet mixing described in the previous section. When the order in which the nonlocal fermion is created or destroyed is opposite between these processes, the tunneling sequences differ in phase by $\varphi_{\mathrm{TS}} + \pi$ and acquire the same tunneling coefficients so that their sum is proportional to $\cos(\varphi_{\mathrm{TS}})$. Distinctly, $E^a_{\mathrm{TS}}(\pi/2)$ originates from sequences that take the singlet ($\propto S^2_-$) or triplet ($\propto T^2_-$) to itself. In both cases there exist two sequences that, again, differ in phase by $\varphi_{\mathrm{TS}} + \pi$ but have the same tunneling coefficients, so that their sums are $\propto \sin(\varphi_{\mathrm{TS}})$. When $B \gg B^{(2)}$ or $\lambda = 2, 3$, $E^0_{\mathrm{TS}} = 0$ and we obtain a $\varphi^0_{\mathrm{TS}} = \pi/2$ JJ for TS.

4.4 Experimental proposal

In this section, we propose an experiment similar to [26] for detecting topological superconductivity using a QD φ_0JJ. We consider a nanowire (NW) which is aligned along the x direction and proximity-coupled to an

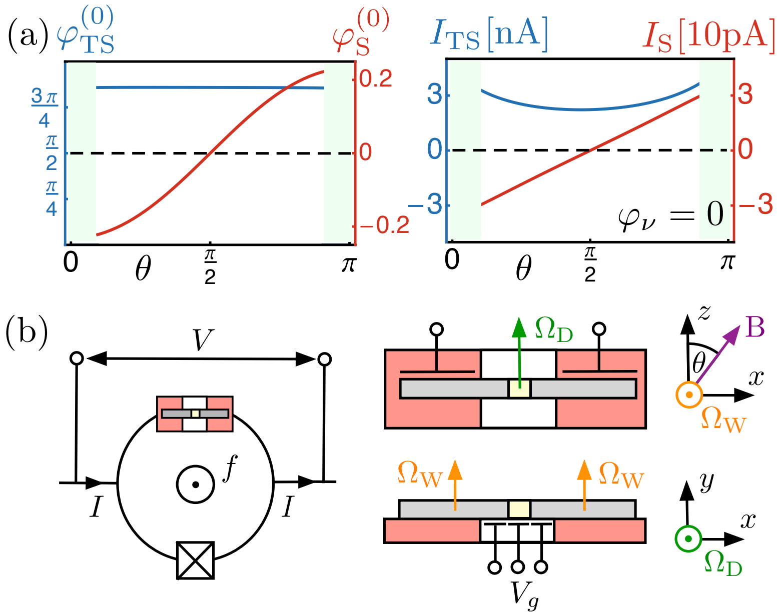

Figure 4.2: (a) Phase shift $\varphi_\nu^0(\theta)$ (left panel) and Josephson current $I_\nu(\theta)$ at $\varphi_\nu = 0$ (right panel) for $\lambda = 4$ and $\theta \in [\theta_c, \pi - \theta_c]$ with $\theta_c = 0.3$. System parameters are chosen as in Fig.4.1 with $B = B^{(2)}$, $V_g = -0.80$ meV, $t_{1a} = t_{2b} = 0.01$ meV, $t_{1b} = 0.05$ meV and $t_{2a} = 0.04$ meV. Compared to the SC JJ the phase shift (Josephson current at $\varphi_{\mathrm{S}} = 0$) is non-zero for the TS JJ. (b) Experimental proposal. Left panel: SQUID geometry of a nanowire QD JJ and a reference junction without a QD connected in parallel. The current-phase relation of the Josephson current through the QD JJ is measured with respect to the reference junction by tuning the flux f through the SQUID. Right panel: Top view (upper panel) and side view (lower panel) of the QD JJ. Local gates are applied to define the tunnel coupled QD (yellow) as a short segment in a nanowire (grey) which is proximity-coupled to an $s-$wave SC (red). Local gates are also used to orient the dot SOI $\mathbf{\Omega}_{\mathrm{D}}$ (green) and wire SOI $\mathbf{\Omega}_{\mathrm{W}}$ (orange) respectively. To measure $\varphi_\nu^0(\theta)$ and $I_\nu(\theta)$, a magnetic field $\mathbf{B}$ is rotated in the plane parallel to the SC film.

$s-$wave SC, see Fig. 4.2(b). By using local bottom-gates, we form a tunnel coupled QD as a short slice in the wire. The electric field produced by the gates points along the y direction, so that the dot SOI $\mathbf{\Omega}_{\mathrm{D}}$ points along the z direction. Furthermore, we contact the wire segments with back-gates that generate electric fields along the z direction and consequently induce a wire SOI $\mathbf{\Omega}_{\mathrm{W}}$ that points along the y direction. We also apply an external magnetic field **B** that can be rotated in the xz plane. Alternatively, the external magnetic field **B** is kept fixed and the sample is rotated. Finally, we connect the resulting QD JJ to a reference junction without a QD forming a SQUID geometry. By tuning the flux f through the SQUID, the current-phase relation of the QD JJ and consequently the anomalous phase shift can be measured with respect to the reference junction.

Our proposed experiment proceeds in three steps:

(1) Initialization. We adjust the size of the QD so that the singlet-triplet anticrossing occurs for a field close to the topological phase transition, $g\mu_B B^* = \sqrt{\Delta^2 + \mu^2}$ with the chemical potential of the NW leads, μ, tuned to $E_-^{(2)}$. Moreover, we adjust the gate voltage V_g and filling of the QD so that its ground state is given by $E_-^{(2)}$, while its first excited states are $E_+^{(2)}$ and $E_4^{(1)}$.

(2) Trivial phase. We consider the regime of a weak Zeeman field, $B < B^*$. The NW chemical potential is placed well above the magnetic field gap. In this limit, the SOI correction to the NW dispersion is irrelevant. Also, the effect of the Zeeman field on the NW leads is negligible, as it is well below the field B^* [15]. Hence, the QD JJ is described by the effective tunneling Hamiltonian $H^{\mathrm{eff}}_{\mathrm{S},t}$. We expect not to observe an anomalous phase shift when the magnetic field **B** and the dot SOI $\mathbf{\Omega}_{\mathrm{D}}$ are orthogonal, $\varphi^0_S(\theta = \pi/2) = 0$.

(3) Topological phase. The setup is tuned to the topological phase by increasing the magnitude of the Zeeman field so that $B > B^*$. The NW chemical potential is tuned inside the magnetic field gap. A MBS emerges at the NW boundaries and the QD JJ is described by the effective tunneling Hamiltonian $H^{\mathrm{eff}}_{\mathrm{TS},t}$. We expect to observe a change in the phase shift of the Josephson current from $\varphi^0_S(\pi/2) = 0$ to some $\varphi^0_{TS}(\pi/2) \neq 0$. The proposed setup also allows us to measure the phase shift dependence on the relative angle θ between **B** and $\mathbf{\Omega}_{\mathrm{D}}$ by rotating **B** in the xz plane. We note that the MBS are unaffected by this rotation because dot SOI $\mathbf{\Omega}_{\mathrm{D}}$ and the wire SOI $\mathbf{\Omega}_{\mathrm{W}}$ are always orthogonal [6]. Notably, for typical system parameters of a nanowire QD JJs, we find that, at zero

phase difference between the leads, $|I_{\mathrm{S}}| \approx 10$pA while $|I_{\mathrm{TS}}| \approx 1$nA, which corresponds to an increase by two orders of magnitude.

Finally, we remark that for a well-defined Josephson current, we consider only regions with sizable energy gap, *i.e.* deep inside the trivial or topological phase. In particular, at the phase boundary, the MBS delocalize and our effective theory breaks down. In general, we expect the behavior of the phase shift to be non-universal across the topological phase transition.

4.5 Conclusions

We have introduced a new qualitative indicator for the detection of topological superconductivity based on a QD φ_0JJ. We found that for this setup the trivial SCs always form a πJJ while the TSs can form a φ_0JJ with $\varphi_0 \neq 0, \pi$. This change in phase shift is accompanied by a significant increase in the magnitude of the critical current. These observation can be probed by simple modifications of recent experimental setups in nanowire QD JJs [26].

4.A A Quantum dot with spin orbit interaction in a Zeeman field

This first section of the appendix provides a more detailed discussion of the model for an isolated QD with SOI subject to an external Zeeman field as given by H_{D} in the main text. The Hilbert space of the system is spanned by the occupation number states

$$|n_{a\uparrow}, n_{a\downarrow}, n_{b\uparrow}, n_{b\downarrow}\rangle = (d^\dagger_{a\uparrow})^{n_{a\uparrow}} (d^\dagger_{a\downarrow})^{n_{a\downarrow}} (d^\dagger_{b\uparrow})^{n_{b\uparrow}} (d^\dagger_{b\downarrow})^{n_{b\downarrow}} |0_{\mathrm{D}}\rangle\,, \tag{4.10}$$

where $n_{\tau s} \in \{0, 1\}$ is the occupation number of an electron with spin s in orbital τ. Since the total number of electrons on the QD is conserved, we can adress each sector with fixed total occupation number separately.

Double occupancy sector

We start with an analysis of the double occupancy sector. A basis is given by the singlet states

$$|1,1,0,0\rangle\,, \quad |S\rangle = |0,0,1,1\rangle\,, \quad (|1,0,0,1\rangle - |0,1,1,0\rangle)/\sqrt{2}\,, \tag{4.11}$$

and the triplet states

$$|T\rangle = |1,0,1,0\rangle\,, \quad (|1,0,0,1\rangle + |0,1,1,0\rangle)\,/\sqrt{2}\,, \quad |0,1,0,1\rangle\,. \tag{4.12}$$

Representing $H_{\rm D}$ in terms of these basis states we find that

$$H_{\rm D}^{(2)} = \tag{4.13}$$

$$\left[\begin{array}{ccc} 2V_g+\delta+U & 0 & 0 \\ 0 & 2V_g-\delta+U & 0 \\ 0 & 0 & 2V_g+U_{ab} \\ i\Omega\sin(\theta)/2 & i\Omega\sin(\theta)/2 & 0 \\ -i\Omega\cos(\theta)/\sqrt{2} & -i\Omega\cos(\theta)/\sqrt{2} & 0 \\ -i\Omega\sin(\theta)/2 & -i\Omega\sin(\theta)/2 & 0 \end{array}\right. \cdots$$

$$\cdots \left.\begin{array}{ccc} -i\Omega\sin(\theta)/2 & i\Omega\cos(\theta)/\sqrt{2} & i\Omega\sin(\theta)/2 \\ -i\Omega\sin(\theta)/2 & i\Omega\cos(\theta)/\sqrt{2} & i\Omega\sin(\theta)/2 \\ 0 & 0 & 0 \\ 2V_g+U_{ab}-g\mu_B B & 0 & 0 \\ 0 & 2V_g+U_{ab} & 0 \\ 0 & 0 & 2V_g+U_{ab}+g\mu_B B \end{array}\right]$$

Here, the top left 3×3 block acts on the singlet subspace, while the bottom right 3×3 block acts on the triplet subspace and the off-diagonal blocks contain the SOI which couples the singlet to the triplet subspace. The spectrum of $H_{\rm D}^{(2)}$ is depicted in Fig. 4.1(c) of the main text. The effective Hamiltonian, valid to lowest order in Ω, which acts in the two-level subspace spanned by $|S\rangle$ and $|T\rangle$ is

$$H_{\rm ST}^{(2)} = \begin{bmatrix} 2V_g-\delta+U & -i\Omega\sin(\theta)/2 \\ i\Omega\sin(\theta)/2 & 2V_g+U_{ab}-g\mu_B B \end{bmatrix}\,. \tag{4.14}$$

It contains the bare energies of the singlet $|S\rangle$ and the triplet $|T\rangle$ on its diagonal. The SOI interaction then couples these levels via the off-diagonal terms. The spectrum of $H_{\rm ST}^{(2)}$ is given by

$$\begin{aligned} E_\pm^{(2)} &= 2V_g + [(U+U_{ab}-g\mu_B B-\delta)/2] \\ &\quad \pm \sqrt{[(U-U_{ab}+g\mu_B B-\delta)/2]^2 + (\Omega\sin(\theta)/2)^2}\,. \end{aligned} \tag{4.15}$$

We see that the effect of the SOI is the opening of an energy gap at the crossing point of the bare singlet and triplet energy levels. In terms of the angle between the Zeeman field and the SOI axis, the gap is maximal when $\theta = \pi/2$ and vanishes when $\theta = 0$. The eigenstates of $H^{(2)}_{\mathrm{ST}}$ are

$$\left|E^{(2)}_{\pm}\right\rangle = \begin{pmatrix} iS_{\pm} \\ T_{\pm} \end{pmatrix} \quad \Leftrightarrow \quad \left|E^{(2)}_{\pm}\right\rangle = iS_{\pm}\left|S\right\rangle + T_{\pm}\left|T\right\rangle , \tag{4.16}$$

where the coefficients are given by

$$\begin{aligned} T_{\pm} &= \pm\frac{1}{\sqrt{2}}\sqrt{1 \mp \frac{U - U_{ab} + g\mu_B B - \delta}{\sqrt{(U - U_{ab} + g\mu_B B - \delta)^2 + (\Omega\sin\theta)^2}}} , \\ S_{-} &= -\mathrm{sgn}(\Omega)T_{+} \quad S_{+} = \mathrm{sgn}(\Omega)T_{-} . \end{aligned} \tag{4.17}$$

The mixing of the singlet and the triplet is minimal when $\Omega = 0$ or $\theta = 0$ and it is maximal when $\theta = \pi/2$.

Single occupancy sector

We next discuss the single occupancy sector of the QD which is spanned by the basis states

$$\left|1,0,0,0\right\rangle , \quad \left|0,1,0,0\right\rangle , \quad \left|0,0,1,0\right\rangle , \quad \left|0,0,0,1\right\rangle . \tag{4.18}$$

The matrix representation of H_{D} in terms of these basis states is given by

$$H^{(1)}_{\mathrm{D}} = \tag{4.19}$$
$$\frac{1}{2}\begin{bmatrix} 2V_g - \delta - g\mu_B B & 0 & i\Omega\cos\theta & i\Omega\sin\theta \\ 0 & 2V_g - \delta + g\mu_B B & i\Omega\sin\theta & -i\Omega\cos\theta \\ -i\Omega\cos\theta & -i\Omega\sin\theta & 2V_g + \delta - g\mu_B B & 0 \\ -i\Omega\sin\theta & i\Omega\cos\theta & 0 & 2V_g + \delta + g\mu_B B \end{bmatrix} .$$

Here, the top left 2×2 block acts on the subspace of orbital b, while the bottom right 2×2 block acts on the subspace of orbital a. The off-diagonal blocks contain the SOI which couples the a orbital to the b orbital. The spectrum of $H^{(1)}_{\mathrm{D}}$ is depicted in Fig. 4.1(d) of the main text and is given by

$$\begin{aligned} E^{(1)}_{\lambda} &= V_g + \frac{1}{2}\left(\delta_{\lambda1} + \delta_{\lambda2} - \delta_{\lambda3} - \delta_{\lambda4}\right) \\ &\times \sqrt{(\Omega\sin\theta)^2 + \left(g\mu_B B + (\delta_{\lambda1} - \delta_{\lambda2} - \delta_{\lambda3} + \delta_{\lambda4})\sqrt{\delta^2 + (\Omega\cos\theta)^2}\right)^2} . \end{aligned} \tag{4.20}$$

Here, $\delta_{\lambda\lambda'}$ for $\lambda, \lambda' = 1, ..., 4$, is the Kronecker delta. The eigenstates of $H_{\mathrm{D}}^{(1)}$ are of the form

$$\left|E_\lambda^{(1)}\right\rangle = \begin{pmatrix} B_{\lambda\uparrow} \\ B_{\lambda\downarrow} \\ iA_{\lambda\uparrow} \\ iA_{\lambda\downarrow} \end{pmatrix} \quad \Leftrightarrow \quad |E_\lambda^{(1)}\rangle = \sum_s \left(iA_{\lambda s} d_{as}^\dagger + B_{\lambda s} d_{bs}^\dagger \right) |0_{\mathrm{D}}\rangle \,. \tag{4.21}$$

We now determine the coefficients $A_{\lambda s}$ and $B_{\lambda s}$ for the different relative angles θ between Zeeman field and SOI axis.

Zeeman field and SOI axis are orthogonal ($\theta = \pi/2$)

For $\theta = \pi/2$, the SOI is proportional to σ^x so that we expect the eigenstates of $H_{\mathrm{D}}^{(1)}$ to be linear combinations of opposite spins in different orbitals. Indeed, we find that the only coefficients which are non-zero are given by

$$\begin{aligned} B_{1\uparrow} &= A_{4\downarrow} = \frac{1}{\sqrt{2}} \sqrt{1 - \frac{g\mu_B B + \delta}{\sqrt{(g\mu_B B + \delta)^2 + \Omega^2}}} \,, \\ B_{4\uparrow} &= -A_{1\downarrow} = \frac{\mathrm{sgn}(\Omega)}{\sqrt{2}} \sqrt{1 + \frac{g\mu_B B + \delta}{\sqrt{(g\mu_B B + \delta)^2 + \Omega^2}}} \,, \\ A_{3\uparrow} &= -B_{2\downarrow} = \frac{1}{\sqrt{2}} \sqrt{1 + \frac{g\mu_B B - \delta}{\sqrt{(g\mu_B B - \delta)^2 + \Omega^2}}} \,, \\ A_{2\uparrow} &= B_{3\downarrow} = \frac{\mathrm{sgn}(\Omega)}{\sqrt{2}} \sqrt{1 - \frac{g\mu_B B - \delta}{\sqrt{(g\mu_B B - \delta)^2 + \Omega^2}}} \,. \end{aligned} \tag{4.22}$$

The remaining coefficients are vanishing, $B_{1\downarrow} = A_{1\uparrow} = A_{2\downarrow} = B_{2\uparrow} = A_{3\downarrow} = B_{3\uparrow} = B_{4\downarrow} = A_{4\uparrow} = 0$.

Zeeman field and SOI axis are parallel ($\theta = 0, \pi$)

In the case of $\theta = 0, \pi$, the SOI is proportional to σ^z. Consequently, we expect the eigenstates of $H_{\mathrm{D}}^{(2)}$ to be mixtures of same spins in different orbitals. For $\theta = 0$, we find that the non-vanishing coefficients are given by

$$\begin{aligned} B_{1\downarrow} = A_{2\downarrow} = -B_{3\uparrow} = A_{4\uparrow} &= \frac{\mathrm{sgn}(\Omega)}{\sqrt{2}}\sqrt{1 - \frac{\delta}{\sqrt{\Omega^2+\delta^2}}}\,, \\ A_{1\downarrow} = -B_{2\downarrow} = A_{3\uparrow} = B_{4\uparrow} &= \frac{1}{\sqrt{2}}\sqrt{1 + \frac{\delta}{\sqrt{\Omega^2+\delta^2}}}\,. \end{aligned} \tag{4.23}$$

The remaining coefficients are all zero, $B_{1\uparrow} = A_{1\uparrow} = A_{2\uparrow} = B_{2\uparrow} = A_{3\downarrow} = B_{3\downarrow} = B_{4\downarrow} = A_{4\downarrow} = 0$. For $\theta = \pi$, we find find that

$$\begin{aligned} B_{1\downarrow} = A_{2\downarrow} = -B_{3\uparrow} = A_{4\uparrow} &= -\frac{\mathrm{sgn}(\Omega)}{\sqrt{2}}\sqrt{1 - \frac{\delta}{\sqrt{\Omega^2+\delta^2}}}\,, \\ A_{1\downarrow} = -B_{2\downarrow} = A_{3\uparrow} = B_{4\uparrow} &= \frac{1}{\sqrt{2}}\sqrt{1 + \frac{\delta}{\sqrt{\Omega^2+\delta^2}}}\,. \end{aligned} \tag{4.24}$$

As before, the remaining coefficients vanish, $B_{1\uparrow} = A_{1\uparrow} = A_{2\uparrow} = B_{2\uparrow} = A_{3\downarrow} = B_{3\downarrow} = B_{4\downarrow} = A_{4\downarrow} = 0$.

Zeeman field and SOI axis are non-orthogonal and non-parallel ($\theta \neq 0,\ \pi/2,\ \pi$)

We assume that $\Omega \neq 0$; for $\Omega = 0$ we note that $H_{\mathrm{D}}^{(1)}$ is already diagonal. When $\theta \neq 0,\ \pi/2,\ \pi$, the SOI is proportional to both σ^x and σ^z. This means that the SOI mixes states of all spin species in all orbitals. We find that the components of the respective eigenstates are given by

$$\begin{aligned}
B_{1\uparrow} &= \frac{1}{N_1}\frac{g\mu_B B + \sqrt{\delta^2 + (\Omega\cos\theta)^2} - \sqrt{\left(g\mu_B B + \sqrt{\delta^2 + (\Omega\cos\theta)^2}\right)^2 + (\Omega\sin\theta)^2}}{\Omega\sin\theta}, \\
B_{2\uparrow} &= \frac{1}{N_2}\frac{g\mu_B B - \sqrt{\delta^2 - (\Omega\cos\theta)^2} - \sqrt{\left(g\mu_B B - \sqrt{\delta^2 + (\Omega\cos\theta)^2}\right)^2 + (\Omega\sin\theta)^2}}{\Omega\sin\theta}, \\
B_{3\uparrow} &= \frac{1}{N_3}\frac{g\mu_B B - \sqrt{\delta^2 - (\Omega\cos\theta)^2} + \sqrt{\left(g\mu_B B - \sqrt{\delta^2 + (\Omega\cos\theta)^2}\right)^2 + (\Omega\sin\theta)^2}}{\Omega\sin\theta}, \\
B_{4\uparrow} &= \frac{1}{N_4}\frac{g\mu_B B + \sqrt{\delta^2 + (\Omega\cos\theta)^2} + \sqrt{\left(g\mu_B B + \sqrt{\delta^2 + (\Omega\cos\theta)^2}\right)^2 + (\Omega\sin\theta)^2}}{\Omega\sin\theta}, \\
B_{1\downarrow} &= \frac{1}{N_1}\frac{\Omega\cos\theta}{\delta + \sqrt{\delta^2 + (\Omega\cos\theta)^2}} \quad , \quad B_{4\downarrow} = \frac{1}{N_4}\frac{\Omega\cos\theta}{\delta + \sqrt{\delta^2 + (\Omega\cos\theta)^2}} \\
B_{2\downarrow} &= \frac{1}{N_2}\frac{\Omega\cos\theta}{\delta - \sqrt{\delta^2 + (\Omega\cos\theta)^2}} \quad , \quad B_{3\downarrow} = \frac{1}{N_3}\frac{\Omega\cos\theta}{\delta - \sqrt{\delta^2 + (\Omega\cos\theta)^2}} \\
A_{\lambda\uparrow} &= \frac{1}{N_\lambda}B_{\lambda\uparrow}B_{\lambda\downarrow} \quad , \quad A_{\lambda\downarrow} = \frac{1}{N_\lambda},
\end{aligned} \tag{4.25}$$

where N_λ is a normalization factors which we choose so that the condition $\sqrt{A_{\lambda\uparrow}^2 + A_{\lambda\downarrow}^2 + B_{\lambda\uparrow}^2 + B_{\lambda\downarrow}^2} = 1$ is satisfied. The normalization also ensures that when $\theta \to 0, \pi/2, \pi$ the expressions above reproduce the the corresponding limiting cases.

4.B An s-wave Superconductor φ_0 Josephson junction

This second section of the appendix gives a more detailed discussion of the SC JJ described by H_S in the main text.

Effective tunneling Hamiltonian

We begin with a derivation of the effective tunneling Hamiltonian $H_{\text{S,t}}^{\text{eff}}$. Compared to the main text, we allow for a slightly more general tunneling Hamiltonian with spin-dependent tunneling amplitudes,

$$H_{\text{S,t}} = \sum_{\eta\tau} \sum_{\mathbf{k}s} t_{\eta\tau s} e^{i\varphi_\eta/2} \, c_{\eta,\mathbf{k}s}^\dagger d_{\tau s} + \text{H.c.} \tag{4.26}$$

Because it is only the relative phase between the two superconductors which is a physical quantity, we assume that $\varphi_2 = 0$ while $\varphi_1 \equiv \varphi$. We now briefly discuss the different tunneling processes which can occur in the system. Therefore, we rewrite $H_{\text{S,t}}$ in terms of the quasiparticle operators,

$$\begin{aligned} H_{\text{S,t}} = {} & \\ \sum_\tau \sum_{\mathbf{k}} & t_{1\tau\uparrow} e^{i\varphi/2} u_{\mathbf{k}} \gamma_{1,\mathbf{k}\Uparrow}^\dagger d_{\tau\uparrow} + t_{1\tau\uparrow} e^{i\varphi/2} v_{\mathbf{k}} \gamma_{1,\mathbf{k}\Downarrow} d_{\tau\uparrow} + t_{2\tau\uparrow} u_{\mathbf{k}} \gamma_{2,\mathbf{k}\Uparrow}^\dagger d_{\tau\uparrow} \\ & + t_{2\tau\uparrow} v_{\mathbf{k}} \gamma_{2,\mathbf{k}\Downarrow} d_{\tau\uparrow} + t_{1\tau\downarrow} e^{i\varphi/2} u_{\mathbf{k}} \gamma_{1,\mathbf{k}\Downarrow}^\dagger d_{\tau\downarrow} - t_{1\tau\downarrow} e^{i\varphi/2} v_{\mathbf{k}} \gamma_{1,\mathbf{k}\Uparrow} d_{\tau\downarrow} \\ & + t_{2\tau\downarrow} u_{\mathbf{k}} \gamma_{2,\mathbf{k}\Downarrow}^\dagger d_{\tau\downarrow} - t_{2\tau\downarrow} v_{\mathbf{k}} \gamma_{2,\mathbf{k}\Uparrow} d_{\tau\downarrow} + \text{H.c.}, \end{aligned} \tag{4.27}$$

where we have assumed that $\xi_{\mathbf{k}} = \xi_{-\mathbf{k}}$. We see that there are two types of tunneling processes: On the one hand, there are processes in which we destroy an electron on the dot and create a quasiparticle on one of the SC leads (or vice versa). Here, electrons and quasiparticles carry the same type of spin or pseudospin. On the other hand, there are processes in which we use the superconducting condensate to simultaneously create (or destroy) an electron on the dot and a quasiparticle on the SC leads. In this case, electron and quasiparticle always carry the opposite type of spin or pseudospin. Because of our convention for the superconducting phases, whenever we destroy (create) an electron on the dot and destroy or create a quasiparticle on SC $\eta = 1$ we pick up a phase of $e^{i\varphi/2}$ ($e^{-i\varphi/2}$) during the tunneling process.

We now derive the effective tunneling Hamiltonian $H_{\text{S,t}}^{\text{eff}}$ using the projection method [158]. Up to fourth order in the tunneling amplitudes we find that

$$\begin{aligned} H_{\text{S,t}}^{\text{eff}} = {} & P_{\text{S}} H_{\text{S,t}} (E_-^{(2)} - H_{\text{D}} - H_{\text{S,L}})^{-1} (1 - P_{\text{S}}) H_{\text{S,t}} \, P_{\text{S}} \\ & + P_{\text{S}} \, H_{\text{S,t}} \left[(E_-^{(2)} - H_{\text{D}} - H_{\text{SC,L}})^{-1} (1 - P_{\text{S}}) H_{\text{S,t}} \right]^3 \, P_{\text{S}}, \end{aligned} \tag{4.28}$$

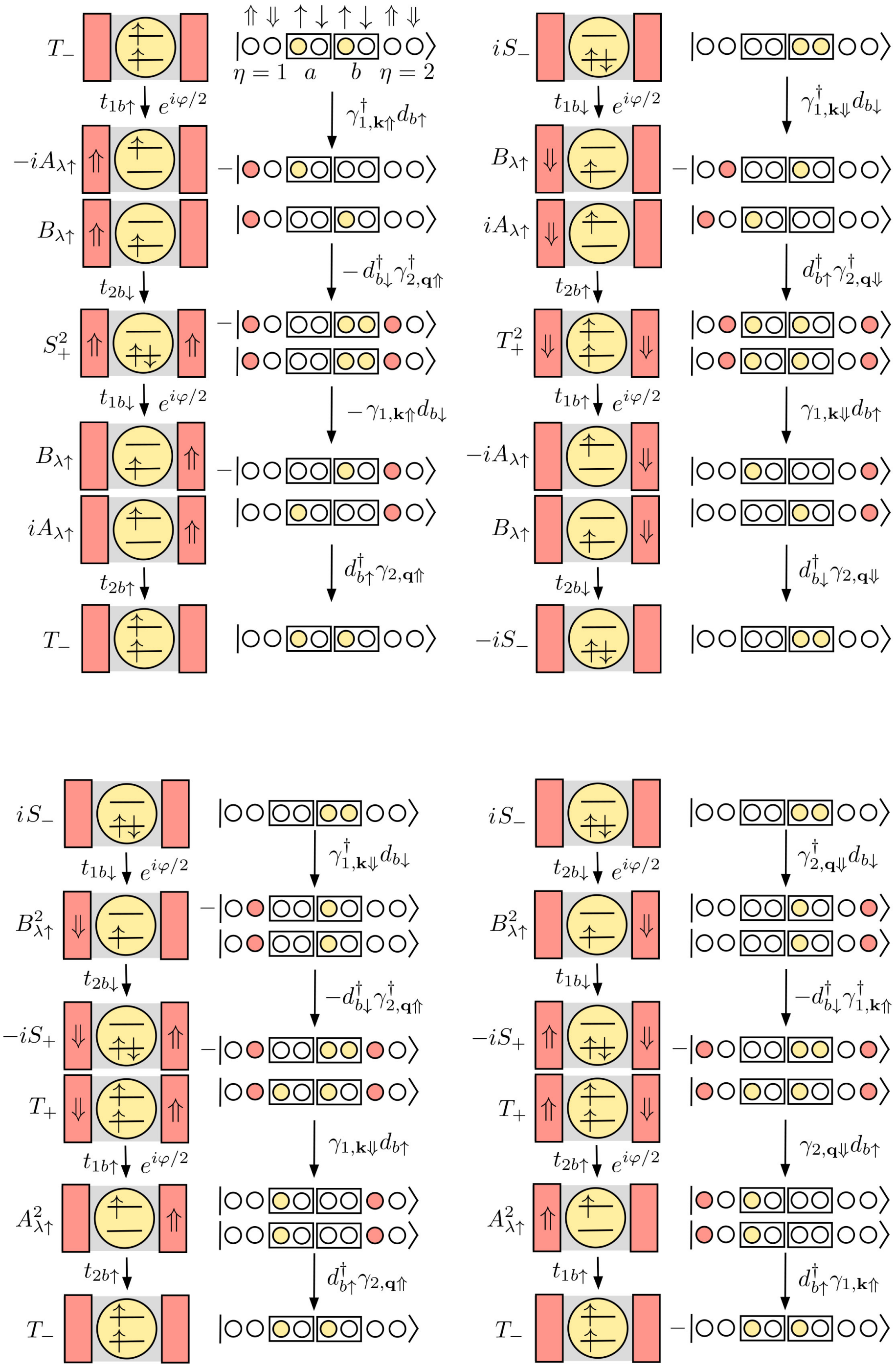
T_-
$\Uparrow\ \Downarrow\ \uparrow\ \downarrow\ \uparrow\ \downarrow\ \Uparrow\ \Downarrow$
$\eta=1$ a b $\eta=2$
$t_{1b\uparrow}$ $e^{i\varphi/2}$
$\gamma^\dagger_{1,\mathbf{k}\Uparrow} d_{b\uparrow}$
$-iA_{\lambda\uparrow}$
$B_{\lambda\uparrow}$
$t_{2b\downarrow}$
$-d^\dagger_{b\downarrow}\gamma^\dagger_{2,\mathbf{q}\Uparrow}$
S^2_+
$t_{1b\downarrow}$ $e^{i\varphi/2}$
$-\gamma_{1,\mathbf{k}\Uparrow} d_{b\downarrow}$
$B_{\lambda\uparrow}$
$iA_{\lambda\uparrow}$
$t_{2b\uparrow}$
$d^\dagger_{b\uparrow}\gamma_{2,\mathbf{q}\Uparrow}$
T_-
iS_-
$t_{1b\downarrow}$ $e^{i\varphi/2}$
$\gamma^\dagger_{1,\mathbf{k}\Downarrow} d_{b\downarrow}$
$B_{\lambda\uparrow}$
$iA_{\lambda\uparrow}$
$t_{2b\uparrow}$
$d^\dagger_{b\uparrow}\gamma^\dagger_{2,\mathbf{q}\Downarrow}$
T^2_+
$t_{1b\uparrow}$ $e^{i\varphi/2}$
$\gamma_{1,\mathbf{k}\Downarrow} d_{b\uparrow}$
$-iA_{\lambda\uparrow}$
$B_{\lambda\uparrow}$
$t_{2b\downarrow}$
$d^\dagger_{b\downarrow}\gamma_{2,\mathbf{q}\Downarrow}$
$-iS_-$
iS_-
$t_{1b\downarrow}$ $e^{i\varphi/2}$
$\gamma^\dagger_{1,\mathbf{k}\Downarrow} d_{b\downarrow}$
$B^2_{\lambda\uparrow}$
$t_{2b\downarrow}$
$-d^\dagger_{b\downarrow}\gamma^\dagger_{2,\mathbf{q}\Uparrow}$
$-iS_+$
T_+
$t_{1b\uparrow}$ $e^{i\varphi/2}$
$\gamma_{1,\mathbf{k}\Downarrow} d_{b\uparrow}$
$A^2_{\lambda\uparrow}$
$t_{2b\uparrow}$
$d^\dagger_{b\uparrow}\gamma_{2,\mathbf{q}\Uparrow}$
T_-
iS_-
$t_{2b\downarrow}$ $e^{i\varphi/2}$
$\gamma^\dagger_{2,\mathbf{q}\Downarrow} d_{b\downarrow}$
$B^2_{\lambda\uparrow}$
$t_{1b\downarrow}$
$-d^\dagger_{b\downarrow}\gamma^\dagger_{1,\mathbf{k}\Uparrow}$
$-iS_+$
T_+
$t_{2b\uparrow}$ $e^{i\varphi/2}$
$\gamma_{2,\mathbf{q}\Downarrow} d_{b\uparrow}$
$A^2_{\lambda\uparrow}$
$t_{1b\uparrow}$
$d^\dagger_{b\uparrow}\gamma_{1,\mathbf{k}\Uparrow}$
T_-

Figure 4.3: Tunneling sequences (up to hermitian conjugation) of the SC JJ for contributions $\propto \cos\varphi_\mathrm{S}$. We use the basis $|n_{1\mathbf{k}\Uparrow}, n_{1\mathbf{k}\Downarrow}, n_{a\uparrow}, n_{a\downarrow}, n_{b\uparrow}, n_{b\downarrow}, n_{2\mathbf{q}\Uparrow}, n_{2\mathbf{q}\Downarrow}\rangle = (\gamma^\dagger_{1\mathbf{k}\Uparrow})^{n_{1\mathbf{k}\Uparrow}}(\gamma^\dagger_{1\mathbf{k}\Downarrow})^{n_{1\mathbf{k}\Downarrow}}(d^\dagger_{a\uparrow})^{n_{a\uparrow}}(d^\dagger_{a\downarrow})^{n_{a\downarrow}}(d^\dagger_{b\uparrow})^{n_{b\uparrow}}(d^\dagger_{b\downarrow})^{n_{b\downarrow}}(\gamma^\dagger_{2\mathbf{q}\Uparrow})^{n_{2\mathbf{q}\Uparrow}}(\gamma^\dagger_{2\mathbf{q}\Downarrow})^{n_{2\mathbf{q}\Downarrow}}|0_1, 0_\mathrm{D}, 0_2\rangle$. Filled (empty) dots are used to visually represent a filled (an empty) level.

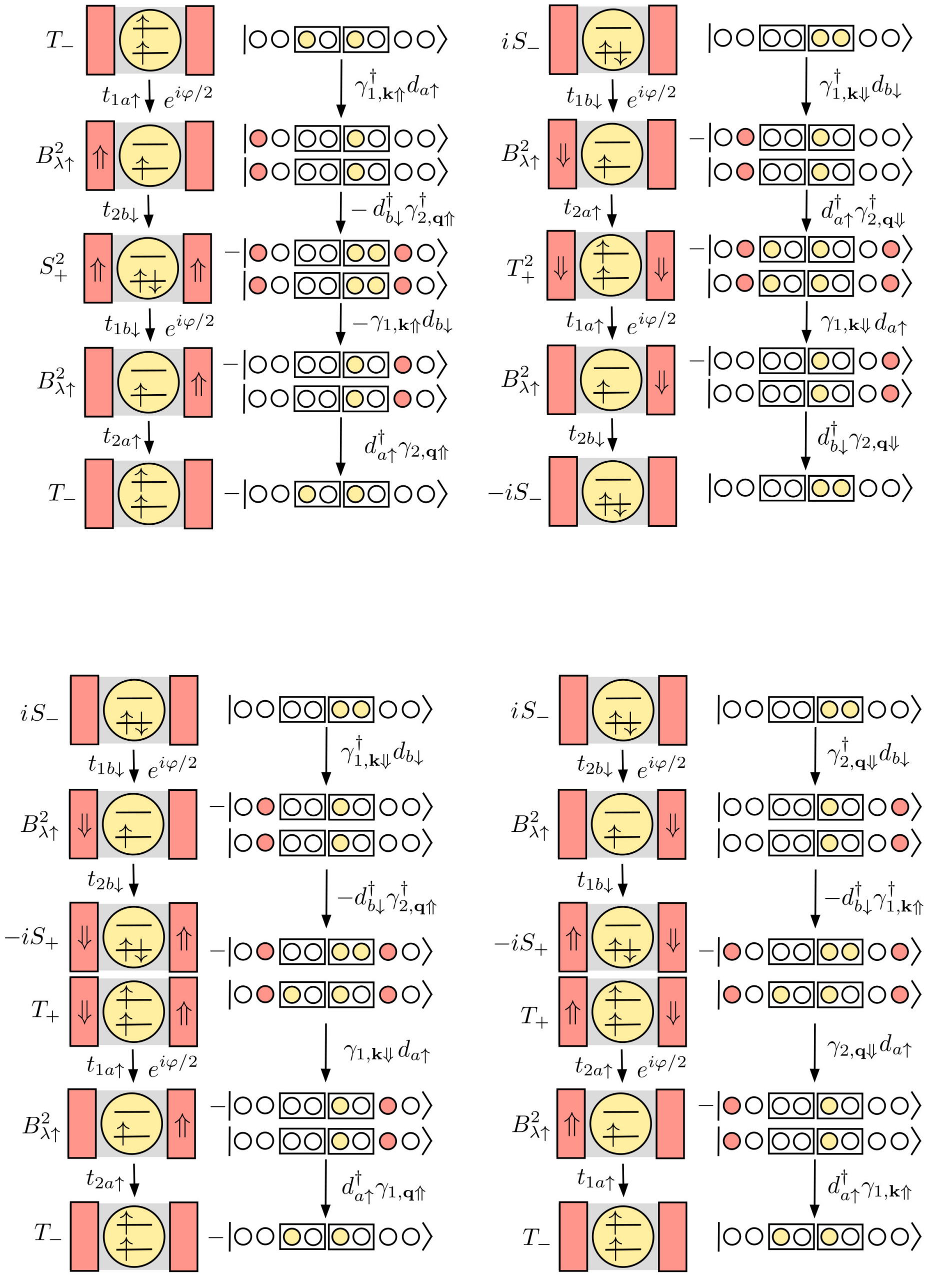
T_-
$t_{1a\uparrow}$ $e^{i\varphi/2}$
$\gamma^\dagger_{1,\mathbf{k}\Uparrow} d_{a\uparrow}$
$B^2_{\lambda\uparrow}$
$t_{2b\downarrow}$
$-\,d^\dagger_{b\downarrow}\gamma^\dagger_{2,\mathbf{q}\Uparrow}$
S^2_+
$t_{1b\downarrow}$ $e^{i\varphi/2}$
$-\gamma_{1,\mathbf{k}\Uparrow} d_{b\downarrow}$
$B^2_{\lambda\uparrow}$
$t_{2a\uparrow}$
$d^\dagger_{a\uparrow}\gamma_{2,\mathbf{q}\Uparrow}$
T_-
iS_-
$t_{1b\downarrow}$ $e^{i\varphi/2}$
$\gamma^\dagger_{1,\mathbf{k}\Downarrow} d_{b\downarrow}$
$B^2_{\lambda\uparrow}$
$t_{2a\uparrow}$
$d^\dagger_{a\uparrow}\gamma^\dagger_{2,\mathbf{q}\Downarrow}$
T^2_+
$t_{1a\uparrow}$ $e^{i\varphi/2}$
$\gamma_{1,\mathbf{k}\Downarrow} d_{a\uparrow}$
$B^2_{\lambda\uparrow}$
$t_{2b\downarrow}$
$d^\dagger_{b\downarrow}\gamma_{2,\mathbf{q}\Downarrow}$
$-iS_-$
iS_-
$t_{1b\downarrow}$ $e^{i\varphi/2}$
$\gamma^\dagger_{1,\mathbf{k}\Downarrow} d_{b\downarrow}$
$B^2_{\lambda\uparrow}$
$t_{2b\downarrow}$
$-d^\dagger_{b\downarrow}\gamma^\dagger_{2,\mathbf{q}\Uparrow}$
$-iS_+$
T_+
$t_{1a\uparrow}$ $e^{i\varphi/2}$
$\gamma_{1,\mathbf{k}\Downarrow} d_{a\uparrow}$
$B^2_{\lambda\uparrow}$
$t_{2a\uparrow}$
$d^\dagger_{a\uparrow}\gamma_{1,\mathbf{q}\Uparrow}$
T_-
iS_-
$t_{2b\downarrow}$ $e^{i\varphi/2}$
$\gamma^\dagger_{2,\mathbf{q}\Downarrow} d_{b\downarrow}$
$B^2_{\lambda\uparrow}$
$t_{1b\downarrow}$
$-d^\dagger_{b\downarrow}\gamma^\dagger_{1,\mathbf{k}\Uparrow}$
$-iS_+$
T_+
$t_{2a\uparrow}$ $e^{i\varphi/2}$
$\gamma_{2,\mathbf{q}\Downarrow} d_{a\uparrow}$
$B^2_{\lambda\uparrow}$
$t_{1a\uparrow}$
$d^\dagger_{a\uparrow}\gamma_{1,\mathbf{k}\Uparrow}$
T_-

Figure 4.3: Continued.

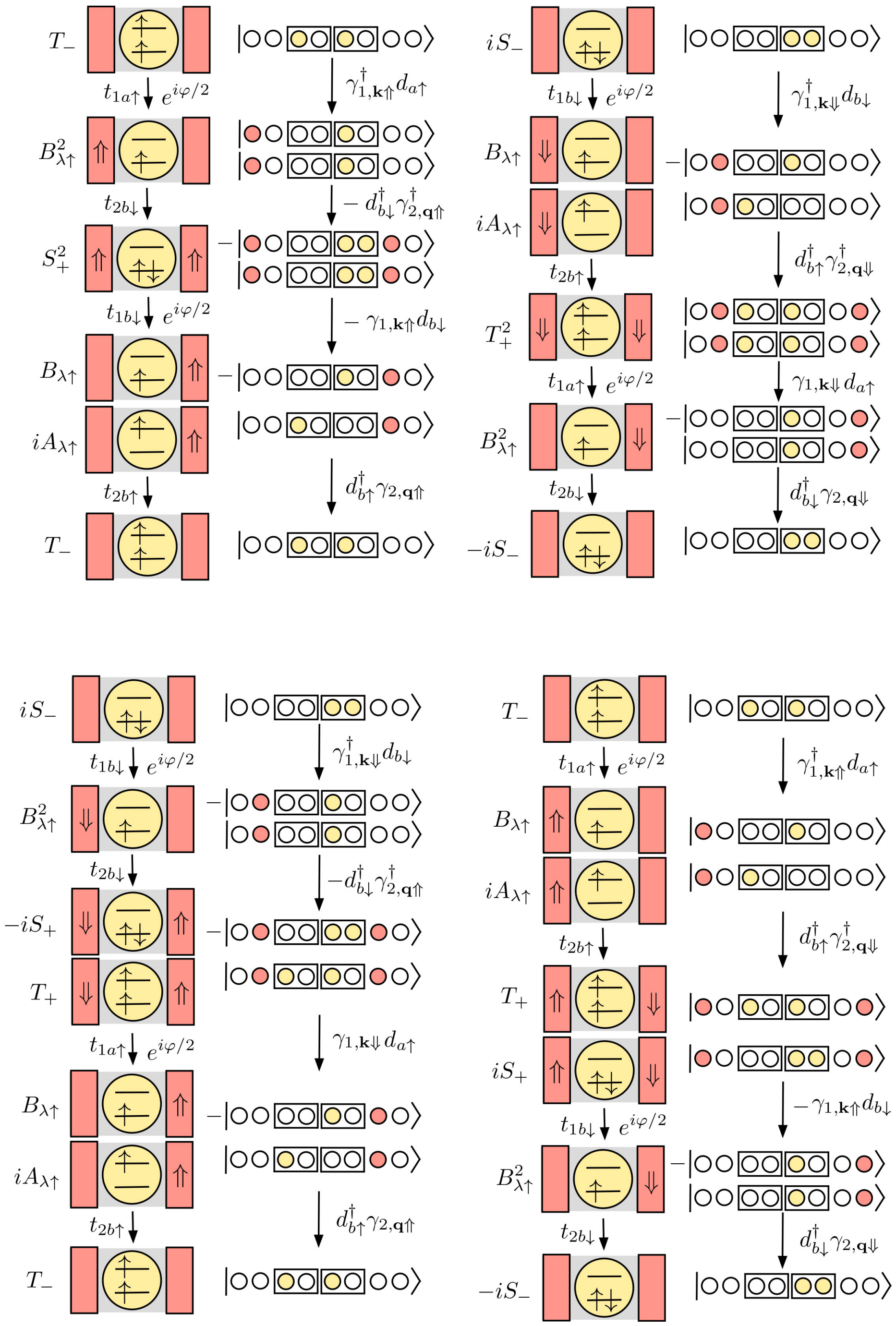
T_-
$t_{1a\uparrow}$ $e^{i\varphi/2}$
$\gamma^\dagger_{1,\mathbf{k}\Uparrow} d_{a\uparrow}$
$B^2_{\lambda\uparrow}$
$t_{2b\downarrow}$
$-\, d^\dagger_{b\downarrow}\gamma^\dagger_{2,\mathbf{q}\Uparrow}$
S^2_+
$t_{1b\downarrow}$ $e^{i\varphi/2}$
$-\,\gamma_{1,\mathbf{k}\Uparrow} d_{b\downarrow}$
$B_{\lambda\uparrow}$
$iA_{\lambda\uparrow}$
$t_{2b\uparrow}$
$d^\dagger_{b\uparrow}\gamma_{2,\mathbf{q}\Uparrow}$
T_-
iS_-
$t_{1b\downarrow}$ $e^{i\varphi/2}$
$\gamma^\dagger_{1,\mathbf{k}\Downarrow} d_{b\downarrow}$
$B_{\lambda\uparrow}$
$iA_{\lambda\uparrow}$
$t_{2b\uparrow}$
$d^\dagger_{b\uparrow}\gamma^\dagger_{2,\mathbf{q}\Downarrow}$
T^2_+
$t_{1a\uparrow}$ $e^{i\varphi/2}$
$\gamma_{1,\mathbf{k}\Downarrow} d_{a\uparrow}$
$B^2_{\lambda\uparrow}$
$t_{2b\downarrow}$
$d^\dagger_{b\downarrow}\gamma_{2,\mathbf{q}\Downarrow}$
$-iS_-$
iS_-
$t_{1b\downarrow}$ $e^{i\varphi/2}$
$\gamma^\dagger_{1,\mathbf{k}\Downarrow} d_{b\downarrow}$
$B^2_{\lambda\uparrow}$
$t_{2b\downarrow}$
$-d^\dagger_{b\downarrow}\gamma^\dagger_{2,\mathbf{q}\Uparrow}$
$-iS_+$
T_+
$t_{1a\uparrow}$ $e^{i\varphi/2}$
$\gamma_{1,\mathbf{k}\Downarrow} d_{a\uparrow}$
$B_{\lambda\uparrow}$
$iA_{\lambda\uparrow}$
$t_{2b\uparrow}$
$d^\dagger_{b\uparrow}\gamma_{2,\mathbf{q}\Uparrow}$
T_-
T_-
$t_{1a\uparrow}$ $e^{i\varphi/2}$
$\gamma^\dagger_{1,\mathbf{k}\Uparrow} d_{a\uparrow}$
$B_{\lambda\uparrow}$
$iA_{\lambda\uparrow}$
$t_{2b\uparrow}$
$d^\dagger_{b\uparrow}\gamma^\dagger_{2,\mathbf{q}\Downarrow}$
T_+
iS_+
$t_{1b\downarrow}$ $e^{i\varphi/2}$
$-\,\gamma_{1,\mathbf{k}\Uparrow} d_{b\downarrow}$
$B^2_{\lambda\uparrow}$
$t_{2b\downarrow}$
$d^\dagger_{b\downarrow}\gamma_{2,\mathbf{q}\Downarrow}$
$-iS_-$

Figure 4.4: Same as Fig. 4.3 but for contributions $\propto \sin\varphi_{\mathrm{S}}$ to the effective Hamiltonian of the SC JJ.

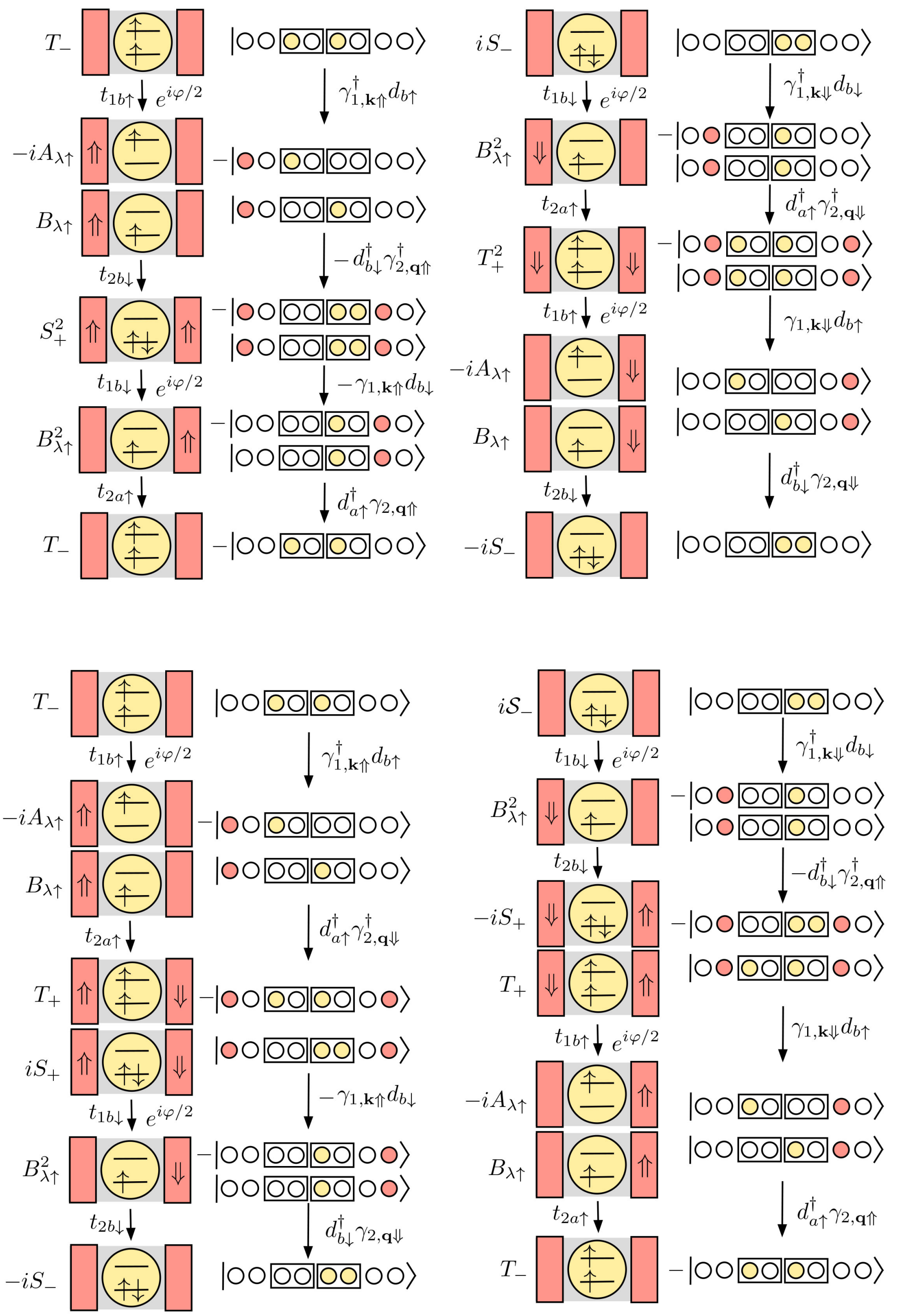
T_-
$t_{1b\uparrow}$ $e^{i\varphi/2}$
$\gamma^\dagger_{1,\mathbf{k}\Uparrow}d_{b\uparrow}$
$-iA_{\lambda\uparrow}$
$B_{\lambda\uparrow}$
$t_{2b\downarrow}$
$-d^\dagger_{b\downarrow}\gamma^\dagger_{2,\mathbf{q}\Uparrow}$
S^2_+
$t_{1b\downarrow}$ $e^{i\varphi/2}$
$-\gamma_{1,\mathbf{k}\Uparrow}d_{b\downarrow}$
$B^2_{\lambda\uparrow}$
$t_{2a\uparrow}$
$d^\dagger_{a\uparrow}\gamma_{2,\mathbf{q}\Uparrow}$
T_-
iS_-
$t_{1b\downarrow}$ $e^{i\varphi/2}$
$\gamma^\dagger_{1,\mathbf{k}\Downarrow}d_{b\downarrow}$
$B^2_{\lambda\uparrow}$
$t_{2a\uparrow}$
$d^\dagger_{a\uparrow}\gamma^\dagger_{2,\mathbf{q}\Downarrow}$
T^2_+
$t_{1b\uparrow}$ $e^{i\varphi/2}$
$\gamma_{1,\mathbf{k}\Downarrow}d_{b\uparrow}$
$-iA_{\lambda\uparrow}$
$B_{\lambda\uparrow}$
$t_{2b\downarrow}$
$d^\dagger_{b\downarrow}\gamma_{2,\mathbf{q}\Downarrow}$
$-iS_-$
T_-
$t_{1b\uparrow}$ $e^{i\varphi/2}$
$\gamma^\dagger_{1,\mathbf{k}\Uparrow}d_{b\uparrow}$
$-iA_{\lambda\uparrow}$
$B_{\lambda\uparrow}$
$t_{2a\uparrow}$
$d^\dagger_{a\uparrow}\gamma^\dagger_{2,\mathbf{q}\Downarrow}$
T_+
iS_+
$t_{1b\downarrow}$ $e^{i\varphi/2}$
$-\gamma_{1,\mathbf{k}\Uparrow}d_{b\downarrow}$
$B^2_{\lambda\uparrow}$
$t_{2b\downarrow}$
$d^\dagger_{b\downarrow}\gamma_{2,\mathbf{q}\Downarrow}$
$-iS_-$
iS_-
$t_{1b\downarrow}$ $e^{i\varphi/2}$
$\gamma^\dagger_{1,\mathbf{k}\Downarrow}d_{b\downarrow}$
$B^2_{\lambda\uparrow}$
$t_{2b\downarrow}$
$-d^\dagger_{b\downarrow}\gamma^\dagger_{2,\mathbf{q}\Uparrow}$
$-iS_+$
T_+
$t_{1b\uparrow}$ $e^{i\varphi/2}$
$\gamma_{1,\mathbf{k}\Downarrow}d_{b\uparrow}$
$-iA_{\lambda\uparrow}$
$B_{\lambda\uparrow}$
$t_{2a\uparrow}$
$d^\dagger_{a\uparrow}\gamma_{2,\mathbf{q}\Uparrow}$
T_-

Figure 4.4: Continued.

where $P_{\mathrm{S}} = |0_1, E_-^{(2)}, 0_2\rangle\langle 0_1, E_-^{(2)}, 0_2|$ is the projector on the $E_-^{(2)}$ state on the dot and the ground states of the SC leads. It acts within the reduced Hilbert space of the states $E_\pm^{(2)}, E_\lambda^{(1)}$ on the dot and the full Hilbert space of the SC leads. Evaluating Eq. (4.28) yields an expression as given by Eq. (6) in the main text with $\nu = \mathrm{S}$ and

$$\begin{aligned} E_{\mathrm{S}}^0 &= g_{\mathrm{S}} t_{1b\downarrow} t_{2b\downarrow} B_{\lambda\uparrow}^2 \left(A_{\lambda\uparrow}^2 t_{1b\uparrow} t_{2b\uparrow} + B_{\lambda\uparrow}^2 t_{1a\uparrow} t_{2a\uparrow}\right) \\ E_{\mathrm{S}}^a &= g_{\mathrm{S}} t_{1b\downarrow} t_{2b\downarrow} A_{\lambda\uparrow} B_{\lambda\uparrow}^3 \left(t_{1a\uparrow} t_{2b\uparrow} - t_{1b\uparrow} t_{2a\uparrow}\right). \end{aligned} \tag{4.29}$$

We point out that unlike Eq. (8) in the main text, this results holds also for spin-dependent tunneling amplitudes. The coupling constant is given by

$$\begin{aligned} &g_{\mathrm{S}} = \\ &2\sum_{\mathbf{k},\mathbf{q}} \frac{u_{\mathbf{k}} u_{\mathbf{q}} v_{\mathbf{k}} v_{\mathbf{q}}}{(E_\lambda^{(1)} + E_{\mathbf{q}} - E_-^{(2)})(E_+^{(2)} + E_{\mathbf{k}} + E_{\mathbf{q}} - E_-^{(2)})(E_\lambda^{(1)} + E_{\mathbf{k}} - E_-^{(2)})} > 0. \end{aligned} \tag{4.30}$$

We give a complete table of the tunneling sequences (up to hermitian conjugation) contributing to the Cooper pair transport in Fig. 4.3 and Fig. 4.4. Here, we note that the sum of the processes in each row of Fig. 4.3 and Fig. 4.4 is $\propto (S_+ T_- - S_- T_+)^2$. This factor is unity because the states $E_\pm^{(2)}$ are orthonormal, see Eq. (4.17). This explains why the singlet-triplet mixing does not enter the effective tunneling Hamiltonian. We omit the presentation of $\widetilde{E}_{\mathrm{S}}$ since it is not relevant to compute the Josephson current. The phase shifts $\varphi_{\mathrm{S}}^0(\theta)$ and Josephson currents $I_{\mathrm{S}}(\theta)$ at $\varphi_{\mathrm{S}} = 0$ are plotted in Fig. 4.9.

Finally, we highlight that it is sufficient to consider a parabolic normal state dispersion for the topologically trivial superconducting phase, *i.e.* to neglect the effects of SOI. To see this, recall that in the topologically superconducting phase of the nanowires the chemical potential needs to be carefully tuned inside of the gap opened by the magnetic field while for typical experiments in the trivial superconducting phase the chemical potential lies well above the gap opened by the magnetic field. In the latter case, the small linear correction of the SOI to the parabolic dispersion of the nanowire becomes practically irrelevant. Hence, we do not expect that the SOI axis in the wire has any measurable effect on the anomalous phase offset in the trivial superconducting phase of the wire, *i.e.* we expect a trivial phase offset in the case when Zeeman field and SOI axis on the dot are orthogonal. This also means that a wire SOI axis that is misaligned with respect to the dot SOI axis will not effect the phase shift

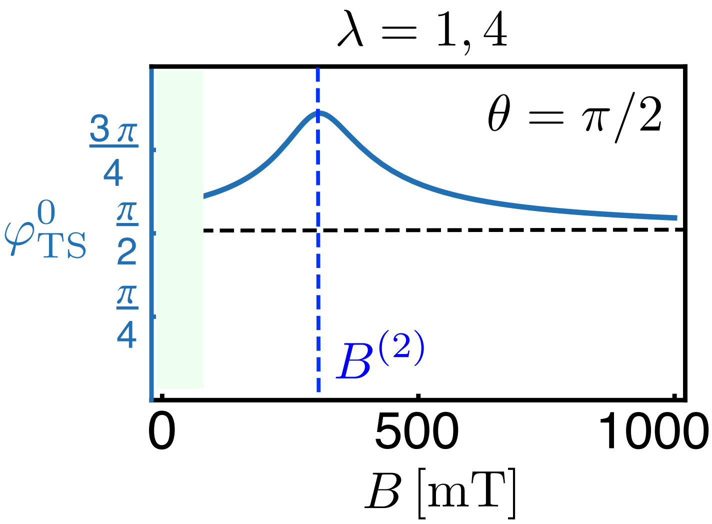

Figure 4.5: Phase shift φ^0_{TS} as a function of the magnitude of the external magnetic field B at $\theta = \pi/2$ for $\lambda = 1, 4$. For $\lambda = 2, 3$ the phase shift is independent of B and given by $\varphi^0_{\mathrm{TS}} = \pi/2$. For the SC JJ we do not observe a phase shift when $\theta = \pi/2$, $\varphi^0_{\mathrm{S}} = 0$. We see that the phase shift is peaked at $B = B^{(2)}$ when the singlet triplet mixing is maximal and it saturates at $\pi/2$ when $B \gg B^{(2)}$. Note however that our perturbative approach is not valid when $B \ll B^{(2)}$, because additional energy levels would have to be taken into account.

of the supercurrent. This argument was also verified by recent experiments, see Ref. [26], which were carried out in the trivial superconducting phase at around 100-200mT. In these experiments the gates applied to the quantum dot inevitably cause its SOI axis to deviate from the intrinsic wire SOI axis, while at the same time no non-trivial phase offset was measured when Zeeman field and dot SOI axis are orthogonal.

4.C A Topological Superconductor φ_0 Josephson junction

Effective tunneling Hamiltonian

We devote this third part of the appendix to the derivation and discussion of the effective tunneling Hamiltonian $H^{\text{eff}}_{\text{TS,t}}$ for the TS JJ. Here, the lowest order contribution comes at t^2. This is, roughly, due to the remarkable property of MBSs being their own antiparticle: it takes two steps in a sequence of intermediate states to transfer a non-local fermion from the left to the right TS (or vice versa) and to return to the ground state of the quantum dot. This will ensure an enhancement in critical current, for sufficiently small tunneling, and a 4π periodicity of the supercurrent as a function of the phase difference. Also we note that our arguments apply to the effective Hamiltonian containing amplitudes, while a real transport process would be described eventually by probabilities (amplitudes squared).

We now begin with derivation of the effective Hamiltonian for the TS JJ. In general, the tunnel coupling between the SC leads and the QD is described by the tunneling Hamiltonian,

$$H_{\text{t}} = \sum_{\eta}\sum_{s}\int \mathrm{d}x\,\mathrm{d}x'\,\tilde{t}_{\eta s}(x,x')\,e^{i\varphi_\eta/2}\Psi^{\dagger}_{\eta s}(x)d_s(x') + \text{H.c.} \tag{4.31}$$

Here, $\Psi^{\dagger}_{\eta s}(x)$ is the creation operator of an electron with spin s at position x in SC lead η and $d_s(x')$ is the annihilation of an electron with spin s at position x' in the QD. Furthermore, $\tilde{t}_{\eta\tau s}(x,x')$ is the tunneling matrix element. If the leads are topological superconducting leads, we can rewrite the electron operators in the TSs in terms of quasiparticle operators [154],

$$\Psi^{\dagger}_{\eta s}(x) = \psi_{\eta s}(x)\Gamma_\eta + \psi'_{\eta s}(x)\Gamma'_\eta + ... \tag{4.32}$$

Here, as in the main text, Γ_η is the zero-energy MBS which is localized at the boundary of the TS η that is spatially closest to the QD, while Γ'_η is the zero-energy MBS that is localized at the opposite end. The corresponding MBS wavefunctions are given by $\psi_\eta(x)$ and $\psi'_\eta(x)$, respectively. Moreover, "+..." refers to the contributions of finite-energy quasiparticles, which we neglect as we are interested only in energies much smaller than the energy gap. Similarly, assuming for simplicity that the QD consists of only two orbitals a and b, we can expand the electron operator in the QD according to

$$d_s(x') = \sum_{\tau=a,b} \xi_{\tau s}(x') d_{\tau s}, \tag{4.33}$$

where $d_{\tau s}$ is the annihilation operator of an electron with spin s in orbital τ of the QD and $\xi_{\tau s}(x')$ is the corresponding wavefunction. Now, we insert the expansions given in Eq. (4.32) and Eq. (4.33) into Eq. (4.31). Assuming that the wavefunctions of the MBSs Γ'_η have zero overlap with the QD wavefunctions, this yields the tunneling Hamiltonian given in Eq. (3) of the main text,

$$H_{\text{t}} \rightarrow H_{\text{TS,t}} = \sum_{\eta\tau} \sum_{s} t_{\eta\tau s} e^{i\varphi_\eta/2}\, \Gamma_\eta d_{\tau s} + \text{H.c.}\,, \tag{4.34}$$

where we have defined new tunneling amplitudes

$$t_{\eta\tau s} = \int \mathrm{d}x\, \mathrm{d}x'\, \tilde{t}_{\eta s}(x,x') \psi_{\eta s}(x) \xi_{\tau s}(x'). \tag{4.35}$$

For simplicity, we will assume that the tunneling ampitudes $t_{\eta\tau s}$ are real. We now derive an effective Hamiltonian considering the tunneling amplitudes as small perturbations. Once more, we emphasize that the lowest order processes which contribute to the Josephson current are of second order in the tunneling amplitudes. In particular these processes do not mix the total fermion parity of the TS leads. Because of that, we focus on the odd parity subspace of the TSs. The results for the even parity subspace of the TSs are identical. The effective tunneling Hamiltonian up to second order in the tunneling amplitudes is given by,

$$H^{\text{eff}}_{\text{TS,t}} = P_{\text{TS}} H_{\text{TS,t}} (E^{(2)}_- - H_{\text{D}} - H_{\text{TS,L}})^{-1} (1 - P_{\text{TS}}) H_{\text{TS,t}}\, P_{\text{TS}}, \tag{4.36}$$

where $P_{\text{TS}} = |1_1, E^{(2)}_-, 0_2\rangle\langle 1_1, E^{(2)}_-, 0_2| + |0_1, E^{(2)}_-, 1_2\rangle\langle 0_1, E^{(2)}_-, 1_2|$ is the projector on the $E^{(2)}_-$ state on the dot and the ground states of the TS leads. It acts within the reduced Hilbert space of the states $E^{(2)}_\pm, E^{(1)}_\lambda$ on the dot and the odd parity ground state subspace of the TS leads. In particular, 0_η (1_η) denotes the ground state in which the non-local fermionic mode in TS η is unoccupied (occupied). When evaluating Eq. (4.36) we find that the result is of the form as given in the main text by Eq. (6) with $\nu =$ TS

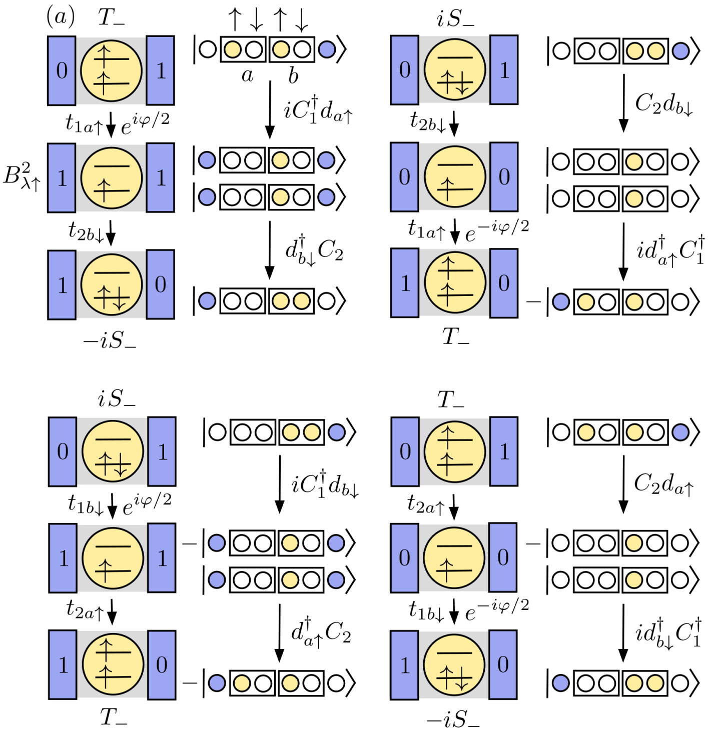
(a)
T_-
$\uparrow \downarrow \uparrow \downarrow$
a
b
$iC_1^\dagger d_{a\uparrow}$
$t_{1a\uparrow}$
$e^{i\varphi/2}$
$B_{\lambda\uparrow}^2$
$t_{2b\downarrow}$
$d_{b\downarrow}^\dagger C_2$
$-iS_-$
iS_-
$C_2 d_{b\downarrow}$
$t_{2b\downarrow}$
$t_{1a\uparrow}$
$e^{-i\varphi/2}$
$id_{a\uparrow}^\dagger C_1^\dagger$
T_-
iS_-
$iC_1^\dagger d_{b\downarrow}$
$t_{1b\downarrow}$
$e^{i\varphi/2}$
$t_{2a\uparrow}$
$d_{a\uparrow}^\dagger C_2$
T_-
T_-
$C_2 d_{a\uparrow}$
$t_{2a\uparrow}$
$t_{1b\downarrow}$
$e^{-i\varphi/2}$
$id_{b\downarrow}^\dagger C_1^\dagger$
$-iS_-$
0
1
$-$

Figure 4.6: Tunneling sequences of the TS JJ for $\theta = \pi/2$. We use the basis $|n_1, n_{a\uparrow}, n_{a\downarrow}, n_{b\uparrow}, n_{b\downarrow}, n_2\rangle = (C_1^\dagger)^{n_1}(d_{a\uparrow}^\dagger)^{n_{a\uparrow}}(d_{a\downarrow}^\dagger)^{n_{a\downarrow}}(d_{b\uparrow}^\dagger)^{n_{b\uparrow}}(d_{b\downarrow}^\dagger)^{n_{b\downarrow}}(C_2^\dagger)^{n_2}|0_1, 0_\mathrm{D}, 0_2\rangle$. Filled (empty) dots are used to visually represent a filled (an empty) level. (a) Tunneling sequences that give contributions $\propto \cos(\varphi_\mathrm{TS})$. (b) Tunneling sequences that give contributions $\propto \sin(\varphi_\mathrm{TS})$.

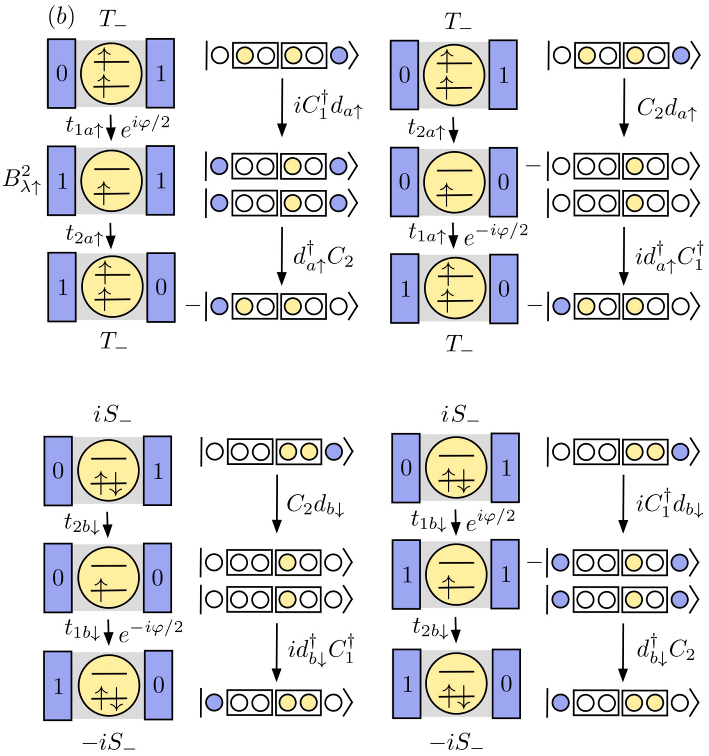
(b)
T_-
$iC_1^\dagger d_{a\uparrow}$
$t_{1a\uparrow}$ $e^{i\varphi/2}$
$B^2_{\lambda\uparrow}$
$t_{2a\uparrow}$
$d^\dagger_{a\uparrow}C_2$
$C_2 d_{a\uparrow}$
$t_{2a\uparrow}$
$t_{1a\uparrow}$ $e^{-i\varphi/2}$
$id^\dagger_{a\uparrow}C_1^\dagger$
iS_-
$C_2 d_{b\downarrow}$
$t_{2b\downarrow}$
$t_{1b\downarrow}$ $e^{-i\varphi/2}$
$id^\dagger_{b\downarrow}C_1^\dagger$
$-iS_-$
$iC_1^\dagger d_{b\downarrow}$
$t_{1b\downarrow}$ $e^{i\varphi/2}$
$t_{2b\downarrow}$
$d^\dagger_{b\downarrow}C_2$
0
1
−

Figure 4.6: Continued.

and

$$\begin{aligned}
E^0_{\text{TS}} &= g_{\text{TS}}\left[B_{\lambda\uparrow}T_-\left(A_{\lambda\uparrow}T_- + B_{\lambda\downarrow}S_-\right)\left(t_{1a\uparrow}t_{2b\uparrow} - t_{1b\uparrow}t_{2a\uparrow}\right)\right. \\
&\qquad \left. + B^2_{\lambda\uparrow}S_-T_-\left(t_{1b\downarrow}t_{2a\uparrow} - t_{1a\uparrow}t_{2b\downarrow}\right)\right] \\
E^a_{\text{TS}} &= -g_{\text{TS}}\left[\left(A_{\lambda\uparrow}T_- + B_{\lambda\downarrow}S_-\right)^2 t_{1b\uparrow}t_{2b\uparrow} + B^2_{\lambda\uparrow}\left(S^2_- t_{1b\downarrow}t_{2b\downarrow} + T^2_- t_{1a\uparrow}t_{2a\uparrow}\right)\right. \\
&\qquad \left. - B_{\lambda\uparrow}S_-\left(A_{\lambda\uparrow}T_- + B_{\lambda\downarrow}S_-\right)\left(t_{1b\uparrow}t_{2b\downarrow} + t_{1b\downarrow}t_{2b\uparrow}\right)\right],
\end{aligned} \tag{4.37}$$

where we have introduced the coefficient

$$g_{\text{TS}} = \frac{2}{E^{(1)}_\lambda - E^{(2)}_-} > 0. \tag{4.38}$$

There are also processes which do not transport a non-local fermion across the JJ and thus lead to a contribution $\widetilde{E}_{\text{TS}}$ which is independent of the superconducting phase difference. In these processes each TS interacts seperately with the QD. In particular this means that the action of the effective tunneling Hamiltonian on the two odd parity ground states of the TS is identical. Consequently, this contribution is proportional to the identity operator and is not relevant when computing the zero-temperature Josephson current. For the case when $\theta = \pi/2$ we have listed all the intermediate tunneling sequences which contribute to the Josephson current in Fig. 4.6. The phase shift $\varphi^0_{\text{TS}}(\theta = \pi/2)$ for $\lambda = 1, 4$ is plotted as a function of the external Zeeman field in Fig. 4.5. The phase shifts $\varphi^0_{\text{TS}}(\theta)$ and Josephson currents $I_{\text{TS}}(\theta)$ at $\varphi_{\text{TS}} = 0$ are plotted in Fig. 4.9.

Lastly, one might think that also finite energy quasiparticles contribute to the effective Hamiltonian. This is indeed true. However, the finite energy quasiparticle sequences of intermediate states which contribute to the Josephson current are of fourth order in the tunneling amplitudes and suppressed by the superconducting gap. Compared to that the Majorana bound state contributions are of second order in tunneling amplitudes. For this reason, we neglect finite energy quasiparticle contributions for the TS-Dot-TS junction when working in the weak tunnel coupling limit.

4.D Critical angle

The effective Hamiltonians for the SC JJ and the TS JJ are valid in the weak tunnel coupling limit. For the SC JJ this limit is defined by

$$\pi\nu_F t_{\eta\tau}t_{\eta'\tau'} \ll E^{(1)}_\lambda - E^{(2)}_-, \Omega\sin(\theta), \Delta \tag{4.39}$$

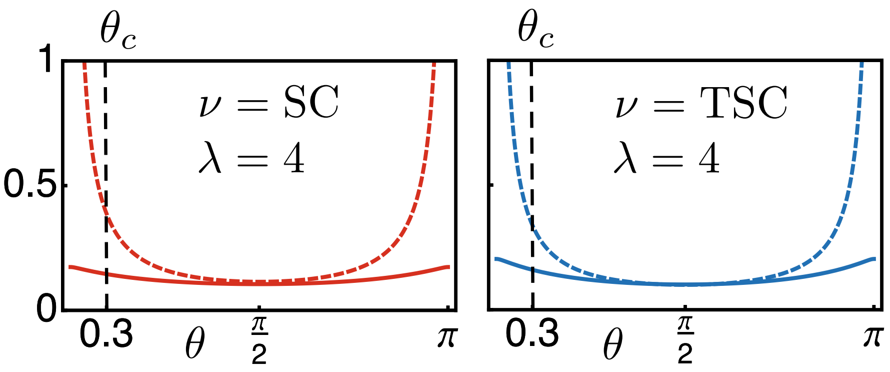

Figure 4.7: Estimate of the critical angle θ_c when $\lambda = 4$ by analyzing the conditions for the weak coupling limit as a function of θ. The system parameters are chosen as in the main text and appendix. In the left panel we plot $\pi\nu_F t^2/(\Omega\sin\theta)$ (red dashed) and $\pi\nu_F t^2/|E_4^{(1)} - E_-^{(2)}|$ (red solid). In the right panel we plot $t/(\Omega\sin\theta)$ (blue dashed) and $t/|E_4^{(1)} - E_-^{(2)}|$ (blue solid). We find that $\theta_c = 0.3$. This choice of critical angle also works for $\lambda = 1, 2, 3$.

and for the TS JJ by

$$t_{\eta\tau} \ll E_\lambda^{(1)} - E_-^{(2)}, \Omega\sin(\theta). \tag{4.40}$$

These conditions fix a critical angle $\theta_c > 0$ so that our perturbative approach is valid when $\theta \in [\theta_c, \pi - \theta_c]$. In this section we want to determine this critical angle for the system parameters which we have chosen in Fig. 4.2 of the main text. To get a sense of scales, we consider an InAs nanowire QD JJ with SC leads of length $L = 1$ μm. We assume that the effective mass of the electrons in the wire is given by $m = 0.05m_e$ where m_e is the bare electron mass. Furthermore, we expect that the Fermi energy of the leads is given by $E_F = 0.1$ meV and the induced superconducting gap by $\Delta = 0.1$ meV. The density of states at the Fermi level of the nanowires in the normal metal state is given by $\nu_F = \frac{L}{\pi}\sqrt{\frac{2m}{\hbar^2}}\frac{1}{\sqrt{E_F}}$. For the order of magnitude of the tunnel coupling between dot and leads we assume that $t = 0.01$ meV. Furthermore, we fix V_g so that $E_\lambda^{(1)}(\pi/2) - E_-^{(2)}(\pi/2) \approx 0.1$ meV. This means that depending on the choice of λ we have that $(V_g|_{\lambda=1}, V_g|_{\lambda=2}, V_g|_{\lambda=4}, V_g|_{\lambda=4}) = (0.89 \text{ meV}, 0.20 \text{ meV}, -0.12 \text{ meV}, -0.80 \text{ meV})$. We can now graphically

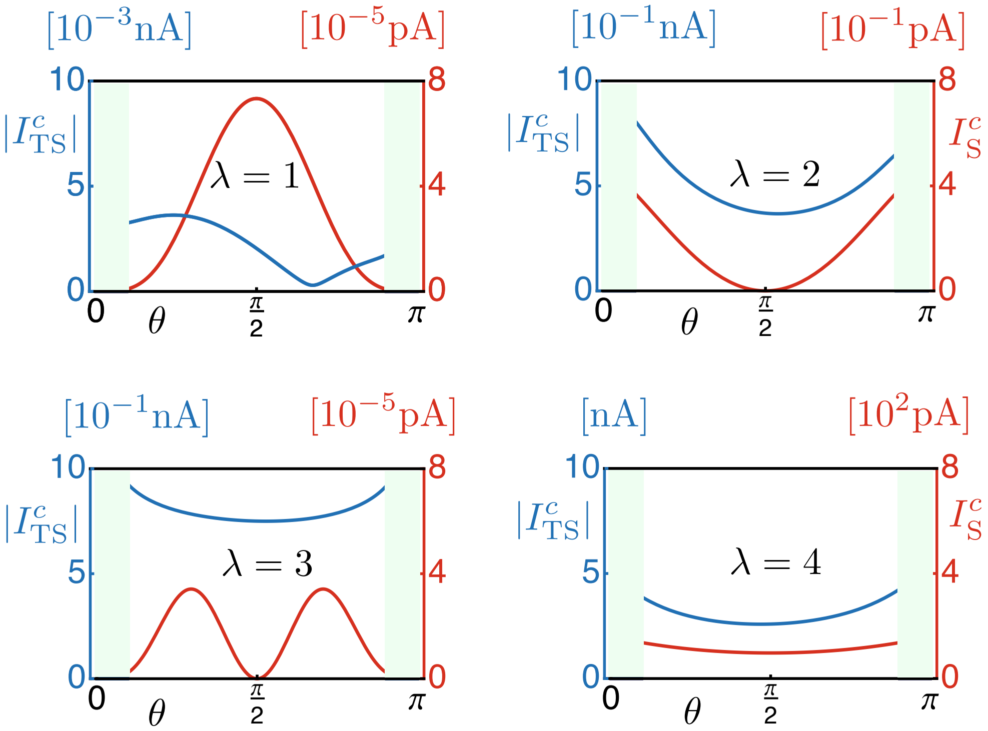

Figure 4.8: Magnitude of the critical current $|I^c_\nu(\theta)|$ for different choices of λ. The system parameters are chosen as in the main text and appendix.

find an estimate for θ_c, see Fig. 4.7. A choice of critical angle that works for all λ is given by $\theta_c = 0.3$.

4.E Critical currents

Critical current of the SC JJ

In this section of appendix we compute the critical current $I_{\text{S},c}$. First, we need to find an approximate value for the coefficient g_{S}. To this end, we notice that it can be rewritten as

$$
\begin{aligned}
g_{\mathrm{S}} = \frac{\Delta^2}{2} \int_{-\hbar\omega_c}^{\hbar\omega_c} \nu(E_1)\,\mathrm{d}E_1 \int_{-\hbar\omega_c}^{\hbar\omega_c} \nu(E_2)\,\mathrm{d}E_2 \Big(\sqrt{E_1^2+\Delta^2}\sqrt{E_2^2+\Delta^2}\Big)^{-1} \\
\times \Bigg(\Big[(E^{(1)}_{\lambda_0} - E^{(2)}_{-}) + \sqrt{E_1^2+\Delta^2}\Big] \Big[(E^{(1)}_{\lambda_0} - E^{(2)}_{-}) + \sqrt{E_2^2+\Delta^2}\Big] \\
\Big[(E^{(2)}_{+} - E^{(2)}_{-}) + \sqrt{E_1^2+\Delta^2} + \sqrt{E_2^2+\Delta^2}\Big] \Bigg)^{-1}
\end{aligned}
\tag{4.41}
$$

where $\nu(E) = \sum_{\mathbf{k}} \delta(E - E_{\mathbf{k}})$ is the density of state of the leads in the normal state at energy E and ω_c is a cut-off frequency which is typically of the order of the Debye frequency of the crystal. For simplicity, we now assume that $\nu(E) \approx \nu_F$ for $|E| \geq \Delta$ and $\nu(E) = 0$ for $|E| < \Delta$. This yields

$$
\begin{aligned}
g_{\mathrm{S}} \approx \frac{(\Delta\nu_F)^2}{2} \Big(\int_{-\hbar\omega_c}^{-\Delta} \mathrm{d}E_1 + \int_{\Delta}^{\hbar\omega_c} \mathrm{d}E_1\Big) \Big(\int_{-\hbar\omega_c}^{-\Delta} \mathrm{d}E_2 + \int_{\Delta}^{\hbar\omega_c} \mathrm{d}E_2\Big) \\
\times \Big(\sqrt{E_1^2+\Delta^2}\sqrt{E_2^2+\Delta^2}\Big)^{-1} \\
\times \Bigg(\Big[(E^{(1)}_{\lambda_0} - E^{(2)}_{-}) + \sqrt{E_1^2+\Delta^2}\Big] \Big[(E^{(1)}_{\lambda_0} - E^{(2)}_{-}) + \sqrt{E_2^2+\Delta^2}\Big] \\
\Big[(E^{(2)}_{+} - E^{(2)}_{-}) + \sqrt{E_1^2+\Delta^2} + \sqrt{E_2^2+\Delta^2}\Big] \Bigg)^{-1}.
\end{aligned}
\tag{4.42}
$$

Defining $\xi_{\pm} = (E^{(1)}_{\lambda} - E^{(2)}_{\pm})/\Delta$ allows us to rewrite this expression as

$$
g_{\mathrm{S}} \approx \frac{4\alpha}{\pi^2} \frac{mL^2}{\hbar^2 \Delta E_F}.
\tag{4.43}
$$

where we have introduced the dimensionless factor

$$
\begin{aligned}
\alpha = \int_1^{\infty} \mathrm{d}x \int_1^{\infty} \mathrm{d}y \, \Big(\sqrt{1+x^2}\sqrt{1+y^2}\Big)^{-1} \qquad (4.44) \\
\times \Big[\Big(\sqrt{1+x^2} + \sqrt{1+y^2} + \xi_- - \xi_+\Big) \Big(\sqrt{1+x^2} + \xi_-\Big) \Big(\sqrt{1+y^2} + \xi_-\Big) \Big]^{-1}
\end{aligned}
$$

and we have assumed that $\hbar\omega_c \gg \Delta$ which ensures that the Cooper potential of the BCS theory is a good approximation to the actual electron pairing potential. We note that α is a function of the relative orientation of SOI axis and Zeeman field, $\alpha = \alpha(\theta)$. For the system parameters chosen in the main text we find that $\alpha \approx 10^{-1}$. In total the critical current is then given by

$$I_{\rm S}^c \approx \frac{8\alpha}{\pi^2}\frac{meL^2}{\hbar^3\Delta E_F}\sqrt{(E_{\rm S}^0)^2+(E_{\rm S}^a)^2}\,{\rm sgn}(E_{\rm S}^0). \tag{4.45}$$

We have plotted $I_{\rm S}^c(\theta)$ in Fig. 4.8. For the case when $\theta = \pi/2$ and $\lambda = 2, 3$ we have $I_{\rm S}^c = 0$ because $B_{2(3)\uparrow} = 0$. Moreover, there exists a significant difference in magnitude of the critical currents for the cases when $\lambda = 1, 4$ which are most relevant for our experimental proposal in the main text. We can understand this because $I_{{\rm S},c}|_{\lambda=1} \,/\, I_{{\rm S},c}|_{\lambda=4} \propto (B_{1\uparrow}/B_{4\uparrow})^4 \approx 10^{-6}$: The virtual state $E_1^{(1)}$ only contains a small amount of $B_{1\uparrow}$ due to the SOI, while $E_4^{(1)}$ consists mostly of $B_{4\uparrow}$, hence $B_{4\uparrow} \gg B_{1\uparrow}$. The conclusion is that the absence or presence of a phase shift can most easily be measured when virtual tunneling occurs via the $E_4^{(1)}$ state.

Critical current of the TS JJ

For the TS JJ we find that the critical current is given by

$$I_{\rm TS}^c = \frac{4\kappa_{\rm TS}e}{\hbar(E_{\lambda_0}^{(1)} - E_-^{(2)})}\sqrt{(E_{\rm TS}^0)^2+(E_{\rm TS}^a)^2}\,{\rm sgn}(E_{\rm TS}^0). \tag{4.46}$$

We plot $I_{\rm TS}^c(\theta)$ in Fig. 4.8. Again we see a significant difference in magnitude when comparing the most relevant cases of $\lambda = 1$ and $\lambda = 4$. This can be explained in the same way as for the SC JJ. However, this time we have for example at $\theta = \pi/2$, $I_{{\rm TS},c}|_{\lambda=1} \,/\, I_{{\rm TS},c}|_{\lambda=4} \propto (B_{1\uparrow}/B_{4\uparrow})^2 \approx 10^{-3}$.

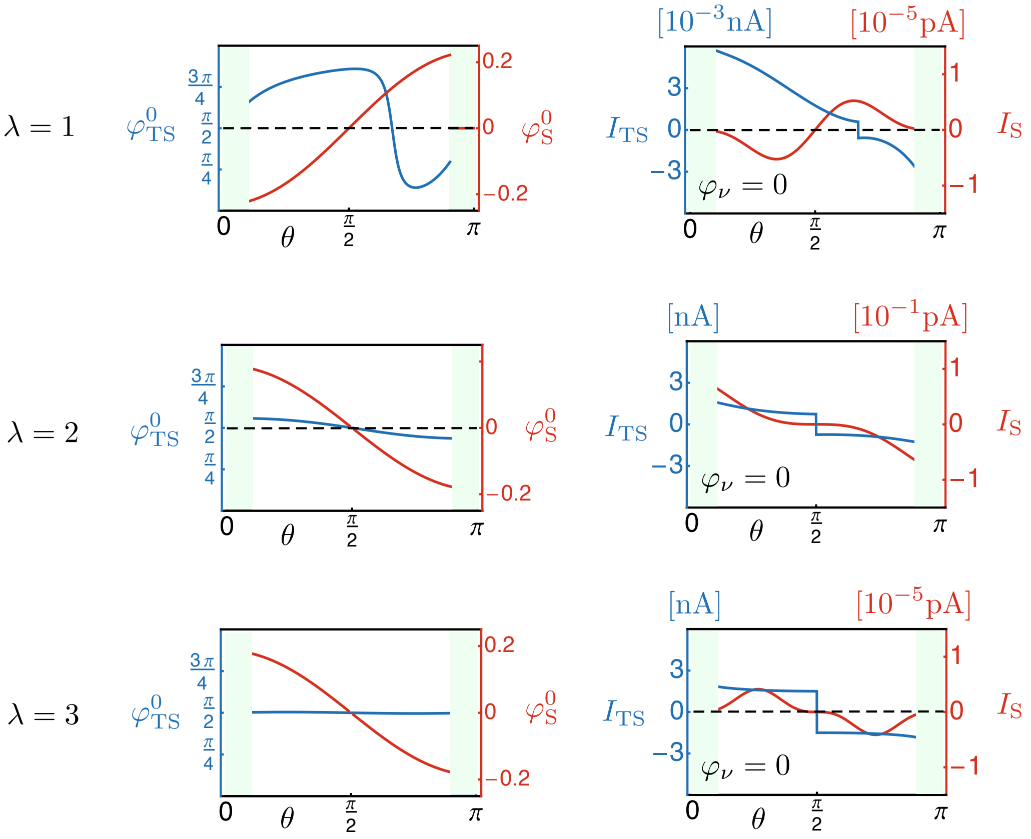

Figure 4.9: Phase shift $\varphi^0_\nu(\theta)$ (top row) and Josephson current $I_\nu(\theta)$ at $\varphi_{\mathrm{S}} = 0$ (bottom row) for $\lambda = 1, 2, 3$. The system parameters are chosen as in the main text. The jumps in the Josephson current $I_{\mathrm{TS}}(\theta)$ correspond to a change of the ground state of the junction.

Part III

Spin-Majorana hybrid qubits and scalability

CHAPTER 5

Universal Quantum Computation with Hybrid Spin-Majorana Qubits

Adapted from:
Silas Hoffman, Constantin Schrade, Jelena Klinovaja, Daniel Loss,
"Universal Quantum Computation with Hybrid Spin-Majorana Qubits",
Phys. Rev. B **94**, 045316 (2016).

We theoretically propose a set of universal quantum gates acting on a hybrid qubit formed by coupling a quantum dot spin qubit and Majorana fermion qubit. First, we consider a quantum dot tunnel-coupled to two topological superconductors. The effective spin-Majorana exchange facilitates a hybrid CNOT gate for which either qubit can be the control or target. The second setup is a modular scalable network of topological superconductors and quantum dots. As a result of the exchange interaction between adjacent spin qubits, a CNOT gate is implemented that acts on neighboring Majorana qubits, and eliminates the necessity of interqubit braiding. In both setups the spin-Majorana exchange interaction allows for a phase gate, acting on either the spin or the Majorana qubit, and for a SWAP or hybrid SWAP gate which is sufficient for universal quantum computation without projective measurements.

5.1 Introduction

Quantum dots are promising, scalable, settings to store and manipulate quantum information using spin states [159,160]. However, the quantum data stored is susceptible to decoherence by the environment wherein quantum information is lost [161].

An alternative proposal to such traditional quantum bits are topological quantum computers [128] which make use of degenerate ground states of topological matter, whose edge states obey non-Abelian statistics upon exchange [162], to encode qubits. The information stored in these nonlocal degrees of freedom are tolerant to local system noise and can be manipulated by braiding [164–167]. There are several proposed realizations of such topological qubits [128], the most successful one to date being those composed of Majorana fermions (MFs) due to their immediate experimental accessibility [6–8, 10, 12, 168–170]. Several theoretical setups to realize MFs have been proposed: semiconducting - superconducting nanowires [3,4], topological insulators [2], topological superconductors (TSCs) [171], and magnetic adatoms on top of s-wave superconductors [5,89–91,172]. However, MFs do not generate a universal set of topological gate operations necessary for quantum computation [173,174].

The additional non-topological gates needed to achieve universality with MF qubits can be implemented by fusing anyons [173], using magnetic flux [177], or quantum information transfer with spins in quantum dots [176, 178]. The principle drawback of these schemes is twofold: (1) after preparing the system state, a projective measurement must be made, which should be perfect [173] and which is typically time intensive [160]; (2) braiding between two topological qubits is required to perform universal quantum computation, which necessitates a long distance topologically nontrivial interaction between them. Scalable networks of qubits have been proposed by using MFs as elements of plaquettes for surface codes [103–105], such schemes, however, do not take advantage of the MF braid statistics. In this work using a hybrid qubit composed of a coupled spin and MF qubit [Fig. 5.1(a)], we can coherently transfer information between the qubit components, thereby keeping the gate operation time on MF qubits potentially as short as possible. Furthermore, when the spins on two such hybrid qubits are allowed to interact, universal quantum computation can be achieved by applying gate operations directly to MF qubits using fixed spin qubits as a control for the interaction, thus eliminating the need for large tunnel-connected wire networks.

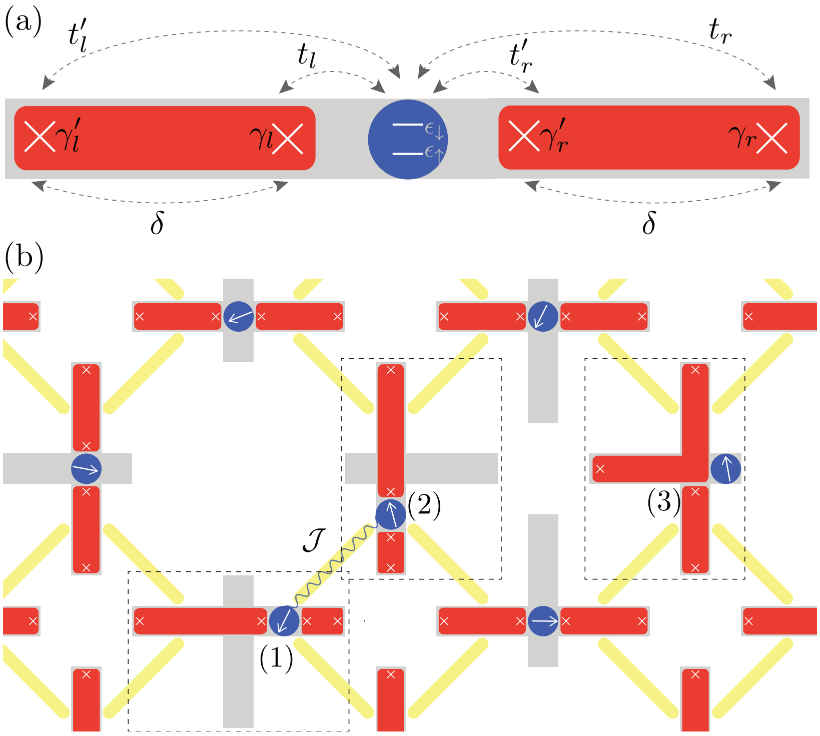

Figure 5.1: (a) Setup of two TSCs (red bars) furnishing two MFs (X's) on the left TSC, γ'_l and γ_l, and two MFs on the right TSC, γ'_r and γ_r in contact with a nontopological SC (grey); the MFs on each TSC can overlap causing a splitting δ. Between the two TSCs is a quantum dot (blue disc) with two single electron levels of up, $\epsilon_\uparrow$, and down, $\epsilon_\downarrow$, spin. The MFs are coupled to the dot through the tunneling elements t_ν and t'_ν where ν labels the right (r) and left (l) TSCs. (b) MaSH network of TSCs where a grid of hybrid qubits (red and grey crosses) are long-distance coupled by tunably connecting the spin-1/2 quantum dots, with strength $\mathcal{J}$, via floating gates (solid yellow lines), *e.g.* hybrid qubit (1) is coupled to hybrid qubit (2). Braiding of MFs utilizes the T-junctions of the TSCs on each hybrid qubit; for instance hybrid qubit (3). Note that the T-junctions are isolated units without tunnel-connection to each other.

Making use of such a coupling, we propose a scalable modular network of Majorana and spin hybrid (MaSH) qubits [Fig. 5.1(b)].

In the following, we derive the effective coupling between the spin and MF qubits which is used to perform a phase gate on the MF qubit and a SWAP gate between the spin and MF qubits. Extending the system to a network of MaSH qubits, long-distance coupled by the spins, we demonstrate the necessary operations to obtain universal quantum computing. Because MFs can be realized in many different setups, we have considered a rather general coupling between spin and MF qubits which provides a proof of principle for a wide class of physical systems.

5.2 Setup

We consider a single level quantum dot placed between two topological superconductors [Fig. 5.1(a)], which can be realized as any of the previously mentioned setups. The chemical potential and Coloumb repulsion, U, on the dot are assumed to be tuned to favor single occupancy (or more generally a spin-1/2 groundstate). The two opposite spin levels of the dot $\epsilon_{\uparrow/\downarrow}$ are non-degenerate in the presence of a magnetic field. The Hamiltonian of the quantum dot is

$$H_D = \sum_{\sigma=\uparrow,\downarrow} (\epsilon_\sigma d_\sigma^\dagger d_\sigma + U n_\sigma n_{\bar{\sigma}}/2)\,, \tag{5.1}$$

where $d_\sigma^\dagger$ (d_σ) creates (annihilates) an electron with spin σ and $n_\sigma = d_\sigma^\dagger d_\sigma$. The right ($r$) and left ($l$) TSCs, modeled as a Kitaev chain [1], are tuned to the topological regime, furnishing MFs at opposite ends. As the separation between MFs can be comparable with the MF localization length, we include a phenomenological splitting of δ between MFs in the same TSC but neglect splitting between MFs on opposite TSCs [87,88]. Neglecting also quasiparticle excitations [179–181] , we consider the MF states on the TSC, which is a good approximation when the tunneling is much smaller than the superconducting gap; the Hamiltonian of the TSC is

$$H_M = \sum_{\nu=r,l} i\delta\gamma'_\nu\gamma_\nu\,, \tag{5.2}$$

where γ'_ν (γ_ν) is the MF at the left (right) end of the νth TSC and we have set the chemical potential of the superconductors to zero.

The overlap of the electron wavefunctions on the dot and MF wavefunctions in the TSC is described by the tunneling Hamiltonian [1,182],

$$H_T = \sum_{\sigma,\nu} d_\sigma^\dagger (it'_\nu\gamma'_\nu + t_\nu\gamma_\nu) + \text{H.c.}\,, \tag{5.3}$$

where t'_ν (t_ν) is the matrix element for an electron on the dot tunneling into the left (right) MF in the νth TSC . We assume our Kitaev chains to have a single spin species oriented perpendicular to the axis of quantization on the dot and the tunneling elements to be spin independent. A spin dependent tunneling, or equivalently choosing a different axis of spin polarization on the TSC, changes the direction of the effective magnetic field on the dot [183], which should not qualitatively affect our results.

Each pair of MFs in the TSCs are conveniently described as a single Dirac fermion $f_\nu = (\gamma'_\nu + i\gamma_\nu)/2$; the MF and tunneling Hamiltonians are rewritten as

$$\begin{aligned} H_M &= \sum_\nu \delta(2f^\dagger_\nu f_\nu - 1)\,, \\ H_T &= \sum_{\sigma,\nu} it^*_{\nu-} f^\dagger_\nu d_\sigma - it^*_{\nu+} f_\nu d_\sigma + \text{H.c.}\,, \end{aligned} \tag{5.4}$$

respectively, where $t_{\nu\pm} = t_\nu \pm t'_\nu$. The value of $f^\dagger_\nu f_\nu = 0, 1$ determines the parity of the νth TSC, which can be even or odd, respectively. The total parity of the MF qubit is defined as the sum of the parities of the TSCs modulo two. The terms proportional to $t_{\nu+}$ ($t^*_{\nu+}$) correspond to removing (adding) a Cooper pair from the condensate and adding (removing) one electron to the dot and one to the νth TSC; the terms proportional to $t_{\nu-}$ or $t^*_{\nu-}$ correspond to the transfer of electrons between the dot and the νth TSC [182]. The full model Hamiltonian of our hybrid qubit system is $H = H_D + H_M + H_T$.

5.3 Effective Hamiltonian

If the coupling between the dot and the TSCs is weak compared to the difference in energies of the dot electrons and MFs, we obtain an effective Hamiltonian $\mathcal{H}_T = \mathcal{H}_s + \mathcal{H}_o + \mathcal{H}_e$ by applying a Schrieffer-Wolff transformation [83, 154, 184, 185] to H (see also Appendix 5.A),

$$\begin{aligned} \mathcal{H}_s &= \sum_{\sigma,\nu} \left(\frac{|t_{\nu-}|^2}{\epsilon_\sigma - 2\delta} f_\nu f^\dagger_\nu + \frac{|t_{\nu+}|^2}{\epsilon_\sigma + 2\delta} f^\dagger_\nu f_\nu \right) \mathcal{B}_\sigma \\ \mathcal{H}_o &= \sum_{\sigma,\nu} \left(\frac{t^*_{\bar\nu-} t_{\nu-}}{\epsilon_\sigma - 2\delta} f_\nu f^\dagger_{\bar\nu} + \frac{t^*_{\bar\nu+} t_{\nu+}}{\epsilon_\sigma + 2\delta} f^\dagger_\nu f_{\bar\nu} \right) \mathcal{B}_\sigma \\ \mathcal{H}_e &= -\sum_{\sigma,\nu} t^*_{\bar\nu-} t_{\nu+} \left(\frac{\mathcal{A}_\sigma}{\epsilon_\sigma - 2\delta} + \frac{\mathcal{A}^\dagger_\sigma}{\epsilon_\sigma + 2\delta} \right) f^\dagger_\nu f^\dagger_{\bar\nu} + \text{H.c.} \end{aligned} \tag{5.5}$$

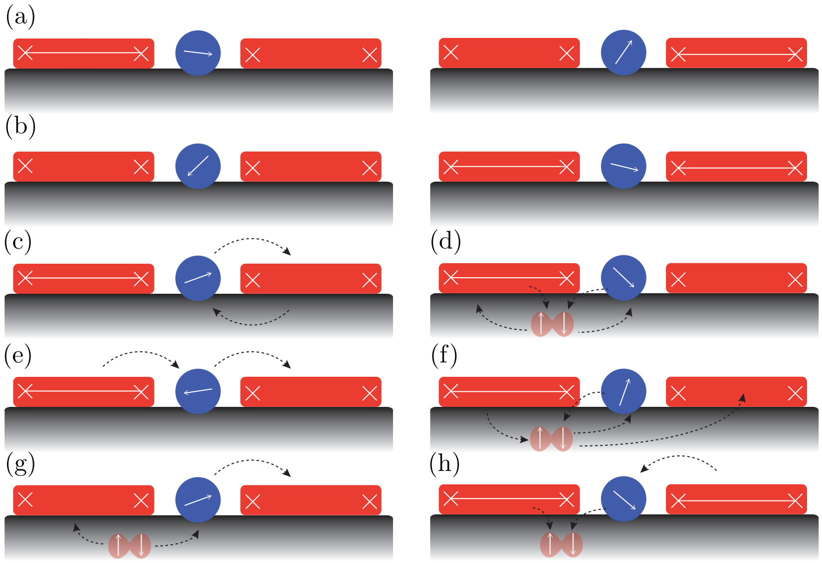

Figure 5.2: Schematic of the MF qubit formed by a left and right TSC (red bars) tunnel coupled by a quantum dot (blue disc) with spin-1/2 groundstate and some of the processes that result from the coupling between spin and MF qubit dictated by $\mathcal{H}_T$. The odd parity of the TSCs is indicated by a straight line (white) between the MFs (white crosses), *i.e.*, $f_\nu^\dagger f_\nu = 1$. The four MF states give rise to two types of MF qubits: (a) The degenerate odd parity states of the MF qubit (even total system parity) with one fermion on the left TSC (left panel) and one on the right TSC (right panel); (b) The degenerate even parity states of the MF qubit (odd total system parity) with no fermions on either TSC (left panel) and with one fermion on each TSC (right panel). (c-d) The virtual processes described by $\mathcal{H}_s$; the remaining undepicted processes are similar but take place on the one, three, and four total electron state. (e-f) The transfer of an electron from one TSC to the other due to $\mathcal{H}_o$. (g-h) The processes determined by $\mathcal{H}_e$ that map the system between the two states in the even parity sector of the MF qubit. The other processes resulting from $\mathcal{H}_o$ and $\mathcal{H}_e$ are obtained by exchanging the right and left TSCs (or initial and final states) in panels (c-h).

We have taken U the largest energy scale, *i.e.*, $U \to \infty$, and defined the operators $\mathcal{A}_\sigma = n_\sigma + d_{\bar{\sigma}}^\dagger d_\sigma$ and $\mathcal{B}_\sigma = \mathcal{A}_\sigma + \mathcal{A}_\sigma^\dagger$. In this limit, the dot is always singly-occupied which fixes the MF qubit to be in an even- [Fig.5.2(a)] or odd-parity [Fig.5.2(b)] subspace of the full Hilbert space. Here, $\mathcal{H}_s$ results from hopping between the dot and a single TSC. The term proportional to $|t_{\nu-}|^2$ corresponds to the process of the electron on the dot hopping to the νth TSC then back to the dot [Fig. 5.2(c)], while the term proportional to $|t_{\nu+}|^2$ corresponds to the process of the electron on the dot combining with the electron on the νth TSC into a Cooper pair, and breaking a Cooper pair adding one electron to the dot and one to the same TSC [Fig. 5.2(d)]; both processes can happen in either parity subspace. The Hamiltonian $\mathcal{H}_o$ ($\mathcal{H}_e$) results from hopping between the dot and both TSCs, which couple states in the odd (even) parity subspace exclusively. The term proportional to $t^*_{\bar{\nu}-}t_{\nu-}$ corresponds to transferring an electron from the dot to the even parity TSC then from the odd parity TSC to the quantum dot [Fig. 5.2(e)]. The condensing of the electron on the dot and with the electron from the odd parity TSC into a Cooper pair and then breaking apart a Cooper pair, putting one electron on the opposite TSC and the other electron on the dot [Fig. 5.2(f)], is described by $t^*_{\bar{\nu}+}t_{\nu+}$. The term proportional to $t^*_{\bar{\nu}-}t_{\nu+}$ acts on the zero total electron state by transferring the dot electron to the νth TSC then taking two electrons from the condensate, filling the state in the latter TSC and transferring the other onto the dot [Fig. 5.2(g)]. The latter term, $t^*_{\bar{\nu}+}t_{\nu-}$, acting on the three total electron state, condenses the dot electron with one of the TSC electrons while the other TSC electron tunnels onto the dot [Fig. 5.2(h)].

In order to create a MF qubit, one must have a superposition of same parity states. In the two TSC system, we restrict to the even total parity or odd MF qubit parity subspace, *i.e.*, one electron on the dot and one electron on either the right ($|r\rangle = f_r^\dagger|0\rangle$) or left ($|l\rangle = f_l^\dagger|0\rangle$) TSC with $|0\rangle$ being the vacuum. In first quantized notation, the effective Hamiltonian is

$$\mathcal{H}_T = \sum_{\kappa,\lambda=0,\ldots,3} J_{\kappa\lambda}\sigma_\kappa\eta_\lambda \,, \tag{5.6}$$

where σ_κ (η_λ) act on the spin of the dot (odd parity sector of TCSs defined such that $\eta_3|r\rangle = +|r\rangle$ and $\eta_3|l\rangle = -|l\rangle$). For κ (λ) $\in \{1,2,3\}$ these are the standard Pauli matrices, while σ_0 (η_0) is the identity matrix. The anisotropic exchange constant $J_{\kappa\lambda}$ is a function of δ, ϵ_σ, and $t_{\nu\pm}$ (Appendix 5.B).

5.4 Quantum gates

In general, when the interaction between qubits is entangling, *i.e.*, $J_{\kappa\lambda} \neq 0$ for $\kappa\,,\lambda \neq 0$, a SWAP gate between the qubits can be implemented. However, a simple setup that yields a so-called hybrid SWAP (hSWAP) gate

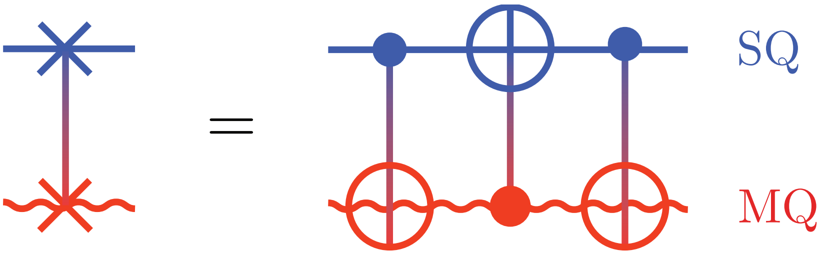

Figure 5.3: Schematic of the hybrid swap (hSWAP) gate obtained as follows: apply the hCNOT gate using, say, the spin qubit (SQ) as the control and the MF qubit (MQ) as the target qubit, apply the hCNOT gate reversing the roles of the qubits, apply the hCNOT gate with the control and target qubits as in the first operation. Starting with the initial state $|x, y\rangle$ such that $x,\ y \in \{0,\ 1\}$, where we identify 0 (1) with the $|{\downarrow}\rangle$ $(|{\uparrow}\rangle)$ and $|l\rangle$ $(|r\rangle)$ state of the spin and MF qubit, respectively, applying the pictured gate sequence one obtains $|x, y\rangle \rightarrow (-1)^x|x, y \oplus x\rangle \rightarrow (-1)^y|y, y \oplus x\rangle \rightarrow |y, x\rangle$; this results in coherent swap of states between the spin and MF qubit.

(Fig. 5.3) consists of two semi-infinite TSCs with no magnetic field on the dot. The first condition implies that the outer MF wave functions do not overlap with that of the inner MFs ($\delta = 0$) or the quantum dot ($t_l' = t_r = 0$), while the second implies the spin states on the dot are degenerate, $\epsilon_\uparrow = \epsilon_\downarrow = \epsilon_0$, for which $\mathcal{H}_T$ becomes $(1 + \sigma_1)\left[(|t_r'|^2 + |t_l|^2) + 2\text{Re}(t_r' t_l^*)\eta_1\right]/\epsilon_0$. When $t_l = t_r' = t$, $\mathcal{H}_T$ further reduces to [159, 186] (see Appendix 5.B)

$$\mathcal{H}_{\text{hCP}} = 2|t|^2(1 + \sigma_1)(1 + \eta_1)/\epsilon_0\,, \tag{5.7}$$

which can be used to perform a hybrid controlled phase (hCP) gate [187]. Although in the following we focus on the manipulation of the MF qubit using the spin qubit, owing to the symmetry of the Hamiltonian between spin and MF operations, *i.e.*, under the exchange $\sigma_1 \leftrightarrow \eta_1$, one could equally use the MF qubit to manipulate the spin qubit.

After a single-qubit unitary rotation by a Hadamard gate, which can be implemented by applying a magnetic field to the spin qubit and by braiding [173] MFs [Fig. 5.4(a)], $\mathcal{H}_{\text{hCP}}$ transforms into

$$\mathcal{H}^{ij}_{\text{hCNOT}} = 2|t|^2(1 + \sigma_i)(1 + \eta_j)/\epsilon_0\,, \tag{5.8}$$

where $(i, j) = (1, 3)$ or $(3, 1)$. Pulsing the coupling t between the dot and TSCs for the duration τ so that $\int^\tau \mathcal{H}^{ij}_{\text{hCNOT}} = \pi(1 + \sigma_i)(1 + \eta_j)/4$, one obtains the hybrid CNOT (hCNOT) gate,

$$U^{ij}_{\text{hCNOT}} = (1 - \sigma_i - \eta_j - \sigma_i \eta_j)/2\,, \tag{5.9}$$

(see Appendix 5.C) from which an hSWAP gate can be coded as $U_{\text{hSWAP}} = U^{31}_{\text{hCNOT}} U^{13}_{\text{hCNOT}} U^{31}_{\text{hCNOT}}$. Applying the hSWAP gate to the two qubits exchanges the relative weights of the up and down spin states of the spin qubit with the right and left parity states of the MF qubit (Fig. 5.3), respectively. To implement a $\pi/8$ gate, one may hSWAP the quantum state of the MF qubit onto the spin qubit, perform a $\pi/8$ gate on the spin qubit, and hSWAP the states back; this requires no preparation or projective measurement. Alternatively, one can fix the spin qubit by a magnetic field along the z axis and pulse $\mathcal{H}^{13}_{\text{CNOT}}$. This generates a phase gate for any value of phase according to the duration of the pulse [Fig. 5.4(b)]. These three gates are sufficient for universal quantum computation of the hybrid qubit. We note that, according to Eq. (5.7), the lower bound on operation time of this gate is of the order $\hbar\epsilon_0/|t|^2$ which can be quite small even within the limits of validity of our Schrieffer-Wolff transformation.

5.5 MaSH network

We consider a network of MaSH qubits formed by crossing one TSC in the topological phase with one in the trivial phase and defining the spin-1/2 quantum dots at their intersection [Fig. 5.1(b)]. The MaSH qubit elements are connected via floating gates [188] whose ends are placed off center from quantum dots. One can perform braiding of MFs by first moving the quantum dot to an unused topologically trivial arm of the hybrid qubit so it does not participate in the operation then performing braiding as usual [29]: move (as a concrete example) the left TSC to the other topologically trivially arm, shifting the right (left) TSC to where the left (right) was and finally returning the quantum dot to the position between the two. Because the coupling of quantum dots through floating gates is very sensitive to the relative position of the two [188], the hybrid qubits are engaged when the spin qubit components are near the respective edges of the connective floating gate. This induces an isotropic interaction given by $\mathcal{J}\boldsymbol{\sigma}^{(i)} \cdot \boldsymbol{\sigma}^{(j)}$, where (i, j) refers to two neighboring hybrid qubits, say $i = 1$ and $j = 2$. If $\mathcal{J} \gg |t|$, there is an effective interaction between the MF qubits modulated by the relative direction of the spin qubits,

$$\mathcal{H}_{MQ}^{(12)} = \frac{|t|^4}{\epsilon_0^2 \mathcal{J}} \left[\sigma_2^{(1)}\sigma_2^{(2)} + \sigma_3^{(1)}\sigma_3^{(2)}\right]\left[1 - \eta_1^{(1)}\eta_1^{(2)}\right] . \tag{5.10}$$

Fixing the direction of the spin qubits along the z axis and applying $\mathcal{H}^{(12)}$ for a specified time (see Appendix 5.D), one obtains the gate $U_{MQ}^{(12)} = \exp[i\pi(1-\eta_1^{(1)}\eta_1^{(2)})/4]$, which directly couples the two MF qubits. A CNOT gate [Fig. 5.4(c)], using MF qubit (1) as the target and qubit (2) as the control, can be implemented using the sequence

$$U_{\text{CNOT}}^{(12)} = H^{(2)} U_{MQ}^{(12)} H^{(1)} H^{(2)} R^{(1)} R^{(2)} H^{(1)}, \tag{5.11}$$

where $H^{(i)}$ and $R^{(i)}$ are the Hadamard and $(-\pi/4)$-phase gates, respectively, acting on the ith MF qubit (see Appendix 5.C). Therefore, using this CNOT gate, the Hadamard and $\pi/8$ gate in the MaSH setup, one can implement the necessary gates to realize universal quantum computation by fixing the spin qubits as a control and storing all quantum information in the MF qubits. As noted before, owing to the symmetry of the setup, the role of the spin and the MF qubits can be interchanged and the MF qubits can be used as control qubits.

One may also use the spin qubit to read out parity of the MF qubit by applying the hSWAP gate and measuring the spin on the dot. Alternatively, one can prepare the system so the initial state of the spin qubit is spin up and the MF qubit is in a superposition of eigenvalues of η_1, $|i\rangle = |\uparrow\rangle(\alpha|+\rangle + \beta|-\rangle)$ where $\eta_1|\pm\rangle = \pm|\pm\rangle = (|r\rangle \pm |l\rangle)/\sqrt{2}$. Rewriting the effective exchange Hamiltonian in terms of projection operators, $\mathcal{P}_\pm = (1 \pm \eta_1)/2$, we find that Eq. (1) becomes

$$(1+\sigma_1)\left[(|t_r'|^2 + |t_l|^2) + 2\text{Re}t_r' t_l^* \left(\mathcal{P}_+ - \mathcal{P}_-\right)\right]/\epsilon_0 \tag{5.12}$$

after taking $\delta = t_l' = t_r = 0$ and $\epsilon_\uparrow = \epsilon_\downarrow = \epsilon_0$. The time evolved initial state is

$$\begin{aligned} |i(\tau)\rangle &= [\alpha e^{i\omega_+\tau}\cos(\omega_+\tau)|+\rangle + \beta e^{i\omega_-\tau}\cos(\omega_-\tau)|-\rangle]\,|\uparrow\rangle \\ &+ i[\alpha e^{i\omega_+\tau}\sin(\omega_+\tau)|+\rangle + \beta e^{i\omega_-\tau}\sin(\omega_-\tau)|-\rangle]|\downarrow\rangle , \end{aligned} \tag{5.13}$$

where $\omega_\pm = |t_r' \pm t_l|^2/\hbar\epsilon_0$. In the simplest case when $t_r' = t_l = t$, the probability to find the spin in the down state is $\mathbb{P}(|\downarrow\rangle) = |\alpha|^2 \sin^2(4|t|^2\tau/\hbar\epsilon_0)$ and the probability to find the spin in the up state is $\mathbb{P}(|\uparrow\rangle) = 1 - \mathbb{P}(|\downarrow\rangle)$. Coupling the spin and MF qubit for a time $\pi\hbar\epsilon_0/8|t|^2$, the probability for the quantum dot to be in a spin up (down) state is equal to probability of finding the initial system in the $|-\rangle$ ($|+\rangle$) state, from which one can deduce the superposition of MF parity states.

Finally, this network can serve as a platform for the surface code with the well-known error threshold of 1.1% [189, 190]. For this we assess the fidelities of our gates and show that they can be made to satisfy this threshold by tuning the tunneling amplitude t and dot level energy ϵ_0 appropriately. Indeed, since $\mathcal{H}_T$ in eq. (5.6) differs from the exact $\mathcal{H}_T^{exact}$ by a term of order $|t|^4/\epsilon_0^3$, to leading order in our small expansion parameter t/ϵ_0, the hCNOT gate constructed from the full Hamiltonian, $U'^{ij}_{\text{hCNOT}} = \exp[i\tau(\mathcal{H}^{ij}_{\text{hCNOT}} + \hat{\varepsilon})/\hbar]$, is not an exact hCNOT-gate, where $\hat{\varepsilon} \sim |t|^4/\epsilon_0^3$ is the leading order correction term. Because τ is of order $\hbar\epsilon_0/|t|^2$, we may expand in $\hat{\varepsilon}$ to find $U'^{ij}_{\text{hCNOT}} \approx U^{ij}_{\text{hCNOT}}(1 + i\int_0^\tau d\tau'\hat{\varepsilon}(\tau')/\hbar)$, where $\hat{\varepsilon}(\tau) = U^{ij\dagger}_{\text{hCNOT}}\hat{\varepsilon}U^{ij}_{\text{hCNOT}}$. The fidelity of an hCNOT-gate is [188]

$$\begin{aligned} F(U'^{ij}_{\text{hCNOT}}) &= \min_{\nu,\sigma} |\langle\nu\sigma|U^{ij\dagger}_{\text{hCNOT}}U'^{ij}_{\text{hCNOT}}|\nu\sigma\rangle|^2 \\ &\approx 1 - \frac{2}{\hbar}\max_{\nu,\sigma}\{\int_0^\tau d\tau'\text{Im}\langle\nu\sigma|U^{ij\dagger}_{\text{hCNOT}}\hat{\varepsilon}(\tau')|\nu\sigma\rangle\}\,, \end{aligned} \tag{5.14}$$

where the minimum (maximum) is taken over $\nu = r, l$ and $\sigma = \uparrow, \downarrow$. Thus, the increase in infidelity $1 - F$ is of order $\tau\hat{\varepsilon}/\hbar \sim |t|^2/\epsilon_0^2$ which can be made controllably small as to satisfy the surface code error threshold, *i.e.*, $1 - F \leq 1.1\%$. Similarly, we can bound the infidelity for the $\pi/8$ and $U^{(12)}_{\text{CNOT}}$ gates below 1.1% by tuning the ratio $|t|^2/\epsilon_0^2$ sufficiently small.

5.6 Outlook and conclusions

Although there are several systems in which our setup could be implemented, perhaps the most natural scenario is in nanowires because (1) signatures of MFs in nanowires with proximity-induced superconductivity were identified experimentally [6–8, 23, 168–170]; (2) single electron quantum dots and electrical implementation of single qubit quantum gates were realized in semiconducting nanowires [156, 191, 192] also on top of superconductors [23, 26, 193].

For a single hybrid qubit setup, we envision one nanowire on top of a conventional s-wave superconductor in which one electrically tunes the left and right ends of the wire into the topological regime while a quantum dot is electrically defined between them. The length of the topological section in the wires can be changed, thereby independently controlling the overlap between the MFs (δ). Similarly, one may set the

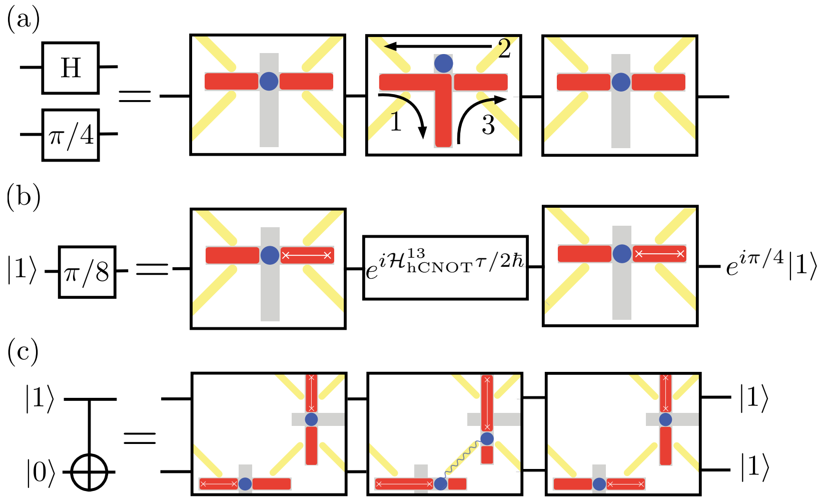

Figure 5.4: Implementation of the necessary gates for universal quantum computation: (a) Hadamard and $\pi/4$ phase gate as a result of braiding, (b) $\pi/8$ phase gate obtained by coupling the MF qubit and the fixed spin qubit, and (c) CNOT gate obtained through an effective coupling of two MF qubits facilitated by a long-range interaction between the corresponding spin qubits.

size of the quantum dot so that the Coulomb repulsion is large as well as applying a gate voltage to ensure the dot is in a spin-1/2 groundstate and fix the dot energy level (ϵ_σ) relative to the chemical potential of the wires. One can likewise control the tunneling between quantum dot and wire (t_ν and t'_ν) by either adjusting the distance between the two or tuning the barrier height that separates them. To assemble a MaSH network, one composes individual hybrid qubits from two crossed nanowires then connects them with floating gates. Voltage controls, in addition to the previously mentioned tunneling elements, braiding operations and the position of the quantum dot and thus the effective coupling between spin qubits ($\mathcal{J}$).

By coupling spin and Majorana qubits, we have constructed the necessary gates for universal quantum computation of spin-Majorana hybrid qubits. Forming a MaSH network, a universal set of gates can be implemented directly on the MF qubits while using the spin qubits only as a control. Thanks to the modular nature of this setup and the construction of the CNOT gate, it is unnecessary to engineer a large scale coherent network of TSCs. The necessary experimental techniques to realize a single spin-MF hybrid qubit or a network of such qubits are available.

Our results demonstrate that one can harness universal quantum computation from both single and multiple element spin-MF hybrid qubit systems.

5.A Effective Hamiltonian

In this section we perform a Schrieffer-Wolff transformation on the tunneling Hamiltonian beginning with a Hamiltonian that couples two Kitaev chains to a quantum dot,

$$
\begin{aligned}
&H = H_M + H_D + H_T \,, \\
&H_M = i\sum_{\nu} \delta_\nu \gamma'_\nu \gamma_\nu \,, \\
&H_D = \sum_{\sigma} \epsilon_\sigma d^\dagger_\sigma d_\sigma + U n_\sigma n_{\bar{\sigma}}/2 \,, \\
&H_T = \sum_{\sigma,\nu} d^\dagger_\sigma (it'_\nu \gamma'_\nu + t_\nu \gamma_\nu) + (t^*_\nu \gamma_\nu - it'^*_\nu \gamma'_\nu) d_\sigma \,,
\end{aligned}
\tag{5.15}
$$

where ν labels the left (l) and right (r) chains. We rewrite the Majorana fermions as $f_\nu = (\gamma'_\nu + i\gamma_\nu)/2$ so that $f^\dagger_\nu f_\nu = (1 + i\gamma'_\nu \gamma_\nu)/2$ and $i\delta_\nu \gamma'_\nu \gamma_{R\nu} = \delta_\nu (2 f^\dagger_\nu f_\nu - 1)$. The logical values of the qubit are written in terms of the parity of the left and right TSCs.

Writing $\gamma'_\nu = f_\nu + f^\dagger_\nu$ and $\gamma_\nu = (f_\nu - f^\dagger_\nu)/i$ the tunneling Hamiltonian is transformed into

$$
\begin{aligned}
H_T &= \sum_{\sigma\nu} d^\dagger_\sigma [it_\nu (f_\nu + f^\dagger_\nu) - it'_\nu (f_\nu - f^\dagger_\nu)] + [-it'^*_\nu (f_\nu - f^\dagger_\nu) - it^*_{L\nu}(f_\nu + f^\dagger_\nu)] d_\sigma \\
&= \sum_{\sigma\nu} i(t'^*_\nu - t^*_\nu) f^\dagger_\nu d_\sigma - i(t'^*_\nu + t^*_\nu) f_\nu d_\sigma + i(t_\nu - t'_\nu) d^\dagger_\sigma f_\nu + i(t'_\nu + t_\nu) d^\dagger_\sigma f^\dagger_\nu \\
&= \sum_{\sigma\nu} it^*_{\nu-} f^\dagger_\nu d_\sigma - it^*_{\nu+} f_\nu d_\sigma - it_{\nu-} d^\dagger_\sigma f_\nu + it_{\nu+} d^\dagger_\sigma f^\dagger_\nu \,,
\end{aligned}
\tag{5.16}
$$

where $t_{\nu\pm} = t'_\nu \pm t_\nu$. Using a Schrieffer-Wolff transformation, one may show that the operators $A_\nu - A^\dagger_\nu$ and $B_\nu - B^\dagger_\nu$ eliminate the tunneling Hamiltonian, $H_T = -[A_\nu - A^\dagger_\nu + B_\nu - B^\dagger_\nu, H_M + H_D]$, to first order in $t_{\nu\pm}$

where

$$\begin{aligned} A_\nu &= i(t^*_\nu - t'^*_\nu)\sum_\sigma \left[\frac{1}{\epsilon_\sigma - 2\delta_\nu} - \frac{U n_{\bar\sigma}}{(\epsilon_\sigma - 2\delta_\nu)(\epsilon_\sigma + U - 2\delta_\nu)}\right] f^\dagger_\nu d_\sigma \\ &= -it^*_{\nu-}\sum_\sigma \left[\frac{1}{\epsilon_\sigma - 2\delta_\nu} - \frac{U n_{\bar\sigma}}{(\epsilon_\sigma - 2\delta_\nu)(\epsilon_\sigma + U - 2\delta_\nu)}\right] f^\dagger_\nu d_\sigma\,, \\ B_\nu &= i(t^*_\nu + t'^*_\nu)\sum_\sigma \left[\frac{1}{\epsilon_\sigma + 2\delta_\nu} - \frac{U n_{\bar\sigma}}{(\epsilon_\sigma + 2\delta_\nu)(\epsilon_\sigma + U + 2\delta_\nu)}\right] f_\nu d_\sigma \\ &= it^*_{\nu+}\sum_\sigma \left[\frac{1}{\epsilon_\sigma + 2\delta_\nu} - \frac{U n_{\bar\sigma}}{(\epsilon_\sigma + 2\delta_\nu)(\epsilon_\sigma + U + 2\delta_\nu)}\right] f_\nu d_\sigma\,. \end{aligned} \tag{5.17}$$

We must now calculate $[A_\nu, H_T]$ and $[B_\nu, H_T]$. The following commutation relations will be useful

$$\begin{aligned} [f^\dagger_\nu d_\rho, H_T] &= i\sum_{\sigma\mu}[f^\dagger_\nu d_\rho, t^*_{-\mu} f^\dagger_\mu d_\sigma - t^*_{+\mu} f_\mu d_\sigma - t_{-\mu} d^\dagger_\sigma f_\mu + t_{+\mu} d^\dagger_\sigma f^\dagger_\mu] \\ &= i\sum_{\sigma\mu} \delta_{\mu\nu} t^*_{+\mu} d_\rho d_\sigma - t_{-\mu}(\delta_{\rho\sigma} f^\dagger_\nu f_\mu - \delta_{\nu\mu} d^\dagger_\sigma d_\rho) + t_{+\mu}\delta_{\rho\sigma} f^\dagger_\nu f^\dagger_\mu\,, \\ [f_\nu d_\rho, H_T] &= i\sum_{\sigma\mu}[f_\nu d_\rho, t^*_{-\mu} f^\dagger_\mu d_\sigma - t^*_{+\mu} f_\mu d_\sigma - t_{-\mu} d^\dagger_\sigma f_\mu + t_{+\mu} d^\dagger_\sigma f^\dagger_\mu] \\ &= i\sum_{\sigma\mu} -t^*_{-\mu}\delta_{\mu\nu} d_\rho d_\sigma - t_{-\mu}\delta_{\rho\sigma} f_\nu f_\mu + t_{+\mu}(\delta_{\rho\sigma} f_\nu f^\dagger_\mu - \delta_{\mu\nu} d^\dagger_\sigma d_\rho)\,. \end{aligned} \tag{5.18}$$

Note that $[U n_{\bar\rho} f^\dagger_\nu d_\rho, H_T] = U n_{\bar\rho}[f^\dagger_\nu d_\rho, H_T] + [U n_{\bar\rho}, H_T] f^\dagger_\nu d_\rho$ and

$$\begin{aligned} [n_{\bar\rho}, H_T] &= i\sum_{\sigma\nu}[n_{\bar\rho}, t^*_{\nu-} f^\dagger_\nu d_\sigma - t^*_{\nu+} f_\nu d_\sigma - t_{\nu-} d^\dagger_\sigma f_\nu + t_{\nu+} d^\dagger_\sigma f^\dagger_\nu] \\ &= i\sum_{\sigma\nu} t^*_{\nu-}\delta_{\bar\rho\sigma} d_{\bar\rho} f^\dagger_\nu - t^*_{\nu+}\delta_{\bar\rho\sigma} d_{\bar\rho} f_\nu - t_{\nu-}\delta_{\bar\rho\sigma} d^\dagger_\sigma f_\nu + t_{\nu+}\delta_{\bar\rho\sigma} d^\dagger_\sigma f^\dagger_\nu\,. \end{aligned} \tag{5.19}$$

Taking the large on-site charging limit, $U \to \infty$, we find

$$\begin{aligned}
\sum_{\nu}[A_\nu, H_T] &= -i\sum_{\rho\nu} t^*_{\nu-}\Bigg[\left(\frac{1}{\epsilon_\rho - 2\delta_\nu} - \frac{n_{\bar\rho}}{\epsilon_\rho - 2\delta_\nu}\right)[f^\dagger_\nu d_\rho, H_T] \\
&\qquad - \frac{[n_{\bar\rho}, H_T] f^\dagger_\nu d_\rho}{\epsilon_\rho - 2\delta_\nu}\Bigg] \\
&= -i\sum_{\rho\nu} \frac{t^*_{\nu-}}{\epsilon_\rho - 2\delta_\nu}\left[n_\rho[f^\dagger_\nu d_\rho, H_T] - [n_{\bar\rho}, H_T] f^\dagger_\nu d_\rho\right] \\
&= \sum_{\sigma\rho\mu\nu} \frac{t^*_{\nu-}}{\epsilon_\rho - 2\delta_\nu} \\
&\times \big[n_\rho(t^*_{+\mu}\delta_{\mu\nu}d_\rho d_\sigma - t_{-\mu}(\delta_{\rho\sigma}f^\dagger_\nu f_\mu - \delta_{\mu\nu}d^\dagger_\sigma d_\rho) + t_{+\mu}\delta_{\rho\sigma}f^\dagger_\nu f^\dagger_\mu) \\
&-(t^*_{-\mu}\delta_{\bar\rho\sigma}d_{\bar\rho}f^\dagger_\mu - t^*_{+\mu}\delta_{\bar\rho\sigma}d_{\bar\rho}f_\mu - t_{-\mu}\delta_{\bar\rho\sigma}d^\dagger_\sigma f_\mu + t_{+\mu}\delta_{\bar\rho\sigma}d^\dagger_\sigma f^\dagger_\mu)f^\dagger_\nu d_\rho\big]\ , \\
\sum_{\nu}[B_\nu, H_T] &= i\sum_{\rho\nu} t^*_{\nu+}\Bigg[\left(\frac{1}{\epsilon_\rho + 2\delta_\nu} - \frac{n_{\bar\rho}}{\epsilon_\rho + 2\delta_\nu}\right)[f_\nu d_\rho, H_T] \\
&\qquad - \frac{[n_{\bar\rho}, H_T] f_\nu d_\rho}{\epsilon_\rho + 2\delta_\nu}\Bigg] \\
&= i\sum_{\rho\nu} \frac{t^*_{\nu+}}{\epsilon_\rho + 2\delta_\nu}\left[n_\rho[f_\nu d_\rho, H_T] - [n_{\bar\rho}, H_T] f_\nu d_\rho\right] \\
&= -\sum_{\sigma\rho\mu\nu} \frac{t^*_{\nu+}}{\epsilon_\rho + 2\delta_\nu} \\
&\times \Big[n_\rho(-t^*_{-\mu}\delta_{\mu\nu}d_\rho d_\sigma - t_{-\mu}\delta_{\rho\sigma}f_\nu f_\mu + t_{+\mu}(\delta_{\rho\sigma}f_\nu f^\dagger_\mu - \delta_{\mu\nu}d^\dagger_\sigma d_\rho)) \\
&- (t^*_{-\mu}\delta_{\bar\rho\sigma}d_{\bar\rho}f^\dagger_\mu - t^*_{+\mu}\delta_{\bar\rho\sigma}d_{\bar\rho}f_\mu - t_{-\mu}\delta_{\bar\rho\sigma}d^\dagger_\sigma f_\mu + t_{+\mu}\delta_{\bar\rho\sigma}d^\dagger_\sigma f^\dagger_\mu)f_\nu d_\rho\Big]\,.
\end{aligned} \tag{5.20}$$

Notice that, for $\hat{O} = f^\dagger_\nu,\ f_\nu$, $n_\rho[\hat{O}d_\rho, H_T] = -n_\rho H_T \hat{O} d_\rho$. The only term that survives from H_T is proportional to $d^\dagger_\rho$ so that this term has no spin flip processes:

$$\begin{aligned}
&- n_\rho H_T f^\dagger_\nu d_\rho \\
&\quad = i(t_{-\mu}n_\rho d^\dagger_\rho f_\mu - t_{+\mu}d^\dagger_\rho f^\dagger_\mu)f^\dagger_\nu d_\rho = i(t_{-\mu}f_\mu f^\dagger_\nu - t_{+\mu}f^\dagger_\mu f^\dagger_\nu)n_\rho\,, \\
&- n_\rho H_T f_\nu d_\rho \\
&\quad = -i(-t_{+\mu}n_\rho d^\dagger_\rho f^\dagger_\mu + t_{-\mu}d^\dagger_\rho f_\mu)f_\nu d_\rho = -i(-t_{+\mu}f^\dagger_\mu f_\nu + t_{-\mu}f_\mu f_\nu)n_\rho\,.
\end{aligned} \tag{5.21}$$

Therefore, these terms do not involve spin flips and

$$\begin{aligned}
\sum_{\nu}[A_\nu, H_T] &= -i\sum_{\rho\nu} t^*_{\nu-}\left[\left(\frac{1}{\epsilon_\rho-2\delta_\nu}-\frac{n_{\bar\rho}}{\epsilon_\rho-2\delta_\nu}\right)[f^\dagger_\nu d_\rho, H_T]-\frac{[n_{\bar\rho}, H_T]f^\dagger_\nu d_\rho}{\epsilon_\rho-2\delta_\nu}\right] \\
&= -i\sum_{\rho\nu}\frac{t^*_{\nu-}}{\epsilon_\rho-2\delta_\nu}\left[n_\rho[f^\dagger_\nu d_\rho, H_T]-[n_{\bar\rho}, H_T]f^\dagger_\nu d_\rho\right] \\
&= \sum_{\sigma\rho\mu\nu}\frac{t^*_{\nu-}}{\epsilon_\rho-2\delta_\nu} \\
&\quad\times\Big[(t_{-\mu}f_\mu f^\dagger_\nu - t_{+\mu}f^\dagger_\mu f^\dagger_\nu)\delta_{\sigma\rho}n_\rho-(t^*_{-\mu}\delta_{\bar\rho\sigma}d_{\bar\rho}f^\dagger_\mu \\
&\qquad - t^*_{+\mu}\delta_{\bar\rho\sigma}d_{\bar\rho}f_\mu - t_{-\mu}\delta_{\bar\rho\sigma}d^\dagger_\sigma f_\mu + t_{+\mu}\delta_{\bar\rho\sigma}d^\dagger_\sigma f^\dagger_\mu)f^\dagger_\nu d_\rho\Big] \\
&= \sum_{\sigma\rho\mu\nu}\frac{t^*_{\nu-}}{\epsilon_\rho-2\delta_\nu}\Big[t_{-\mu}\delta_{\sigma\rho}n_\rho f_\mu f^\dagger_\nu - t_{+\mu}\delta_{\sigma\rho}n_\rho f^\dagger_\mu f^\dagger_\nu \\
&\qquad - (-t_{-\mu}\delta_{\bar\rho\sigma}d^\dagger_\sigma f_\mu + t_{+\mu}\delta_{\bar\rho\sigma}d^\dagger_\sigma f^\dagger_\mu)f^\dagger_\nu d_\rho\Big]\,, \\
\sum_{\nu}[B_\nu, H_T] &= i\sum_{\rho\nu} t^*_{\nu+}\left[\left(\frac{1}{\epsilon_\rho+2\delta_\nu}-\frac{n_{\bar\rho}}{\epsilon_\rho+2\delta_\nu}\right)[f_\nu d_\rho, H_T]-\frac{[n_{\bar\rho}, H_T]f_\nu d_\rho}{\epsilon_\rho+2\delta_\nu}\right] \\
&= i\sum_{\rho\nu}\frac{t^*_{\nu+}}{\epsilon_\rho+2\delta_\nu}\left[n_\rho[f_\nu d_\rho, H_T]-[n_{\bar\rho}, H_T]f_\nu d_\rho\right] \\
&= -\sum_{\sigma\rho\mu\nu}\frac{t^*_{\nu+}}{\epsilon_\rho+2\delta_\nu} \\
&\quad\times[-t_{+\mu}\delta_{\sigma\rho}n_\rho f^\dagger_\mu f_\nu + t_{-\mu}\delta_{\sigma\rho}n_\rho f_\mu f_\nu \\
&\qquad - (t^*_{-\mu}\delta_{\bar\rho\sigma}d_{\bar\rho}f^\dagger_\mu - t^*_{+\mu}\delta_{\bar\rho\sigma}d_{\bar\rho}f_\mu - t_{-\mu}\delta_{\bar\rho\sigma}d^\dagger_\sigma f_\mu + t_{+\mu}\delta_{\bar\rho\sigma}d^\dagger_\sigma f^\dagger_\mu)f_\nu d_\rho] \\
&= -\sum_{\sigma\rho\mu\nu}\frac{t^*_{\nu+}}{\epsilon_\rho+2\delta_\nu} \\
&\quad\times\Big[-t_{+\mu}\delta_{\sigma\rho}n_\rho f^\dagger_\mu f_\nu + t_{-\mu}\delta_{\sigma\rho}n_\rho f_\mu f_\nu \\
&\qquad - (-t_{-\mu}\delta_{\bar\rho\sigma}d^\dagger_\sigma f_\mu + t_{+\mu}\delta_{\bar\rho\sigma}d^\dagger_\sigma f^\dagger_\mu)f_\nu d_\rho\Big]\,.
\end{aligned} \tag{5.22}$$

Let us consider processes when only one TSC is involved in then tunneling, $\mu = \nu$ [Fig. 2(a), (b)]:

$$\begin{aligned}
\sum_{\nu}[A_\nu, H_T] &= \sum_{\sigma\rho\mu\nu} \frac{t^*_{\nu-}}{\epsilon_\rho - 2\delta_\nu}\Big[t_{-\mu}\delta_{\sigma\rho}n_\rho f_\mu f^\dagger_\nu - (t^*_{-\mu}\delta_{\bar\rho\sigma}d_{\bar\rho}f^\dagger_\mu - t^*_{+\mu}\delta_{\bar\rho\sigma}d_{\bar\rho}f_\mu \\
&\qquad - t_{-\mu}\delta_{\bar\rho\sigma}d^\dagger_\sigma f_\mu + t_{+\mu}\delta_{\bar\rho\sigma}d^\dagger_\sigma f^\dagger_\mu)f^\dagger_\nu d_\rho\Big] \\
&= \sum_{\rho\nu} \frac{t^*_-}{\epsilon_\rho - 2\delta_\nu}\left[t_- n_\rho f_\nu f^\dagger_\nu - (-t^*_+ d_{\bar\rho}f_\nu - t_- d^\dagger_{\bar\rho}f_\nu)f^\dagger_\nu d_\rho\right] \\
&= \sum_{\rho\nu} \frac{t^*_-}{\epsilon_\rho - 2\delta}\left[t_- n_\rho f_\nu f^\dagger_\nu + t_- d^\dagger_{\bar\rho}f_\nu f^\dagger_\nu d_\rho\right] \\
\sum_{\nu}[B_\nu, H_T] &= -\sum_{\sigma\rho\mu\nu} \frac{t^*_{\nu+}}{\epsilon_\rho + 2\delta_\nu}\Big[- t_{+\mu}\delta_{\sigma\rho}n_\rho f^\dagger_\mu f_\nu - (t^*_{-\mu}\delta_{\bar\rho\sigma}d_{\bar\rho}f^\dagger_\mu - t^*_{+\mu}\delta_{\bar\rho\sigma}d_{\bar\rho}f_\mu \\
&\qquad - t_{-\mu}\delta_{\bar\rho\sigma}d^\dagger_\sigma f_\mu + t_{+\mu}\delta_{\bar\rho\sigma}d^\dagger_\sigma f^\dagger_\mu)f_\nu d_\rho\Big] \\
&= -\sum_{\rho\nu} \frac{t^*_+}{\epsilon_\rho + 2\delta}\left[-t_+ n_\rho f^\dagger_\nu f_\nu - (t^*_- d_{\bar\rho}f^\dagger_\nu + t_+ d^\dagger_{\bar\rho}f^\dagger_\nu)f_\nu d_\rho\right] \\
&= \sum_{\rho\nu} \frac{t^*_+}{\epsilon_\rho + 2\delta}\left[t_+ n_\rho f^\dagger_\nu f_\nu + t_+ d^\dagger_{\bar\rho}f^\dagger_\nu f_\nu d_\rho\right] , \qquad (5.23)
\end{aligned}$$

where the final inequalities for each term is due to the single occupancy of the dot. Summing these together, with their Hermitian conjugate, we get

$$\mathcal{H}_s = \sum_{\rho\nu}\left(\frac{|t_{\nu+}|^2}{\epsilon_\rho + 2\delta_\nu}f^\dagger_\nu f_\nu + \frac{|t_{\nu-}|^2}{\epsilon_\rho - 2\delta_\nu}f_\nu f^\dagger_\nu\right)\left(2n_\rho + d^\dagger_{\bar\rho}d_\rho + d^\dagger_\rho d_{\bar\rho}\right) . \qquad (5.24)$$

Processes involving multiple TSCs, $\mu = \bar{\nu}$, are calculated from

$$\begin{aligned}
\sum_{\nu}[A_\nu, H_T] &= \sum_{\sigma\rho\mu\nu} \frac{t^*_{\nu-}}{\epsilon_\rho - 2\delta_\nu} \Big[t_{-\mu}\delta_{\sigma\rho} n_\rho f_\mu f^\dagger_\nu - t_{+\mu}\delta_{\sigma\rho} n_\rho f^\dagger_\mu f^\dagger_\nu \\
&\quad - (t^*_{-\mu}\delta_{\bar{\rho}\sigma} d_{\bar{\rho}} f^\dagger_\mu - t^*_{+\mu}\delta_{\bar{\rho}\sigma} d_{\bar{\rho}} f_\mu - t_{-\mu}\delta_{\bar{\rho}\sigma} d^\dagger_\sigma f_\mu + t_{+\mu}\delta_{\bar{\rho}\sigma} d^\dagger_\sigma f^\dagger_\mu) f^\dagger_\nu d_\rho \Big] \\
&= \sum_{\sigma\rho\mu\nu} \frac{t^*_{\nu-}}{\epsilon_\rho - 2\delta_\nu} \Big[t_{-\mu}\delta_{\sigma\rho} n_\rho f_\mu f^\dagger_\nu - t_{+\mu}\delta_{\sigma\rho} n_\rho f^\dagger_\mu f^\dagger_\nu \\
&\quad - (-t_{-\mu}\delta_{\bar{\rho}\sigma} d^\dagger_\sigma f_\mu + t_{+\mu}\delta_{\bar{\rho}\sigma} d^\dagger_\sigma f^\dagger_\mu) f^\dagger_\nu d_\rho \Big] , \\
\sum_{\nu}[B_\nu, H_T] &= -\sum_{\sigma\rho\mu\nu} \frac{t^*_{\nu+}}{\epsilon_\rho + 2\delta_\nu} \Big[- t_{+\mu}\delta_{\sigma\rho} n_\rho f^\dagger_\mu f_\nu + t_{-\mu}\delta_{\sigma\rho} n_\rho f_\mu f_\nu \\
&\quad - (t^*_{-\mu}\delta_{\bar{\rho}\sigma} d_{\bar{\rho}} f^\dagger_\mu - t^*_{+\mu}\delta_{\bar{\rho}\sigma} d_{\bar{\rho}} f_\mu - t_{-\mu}\delta_{\bar{\rho}\sigma} d^\dagger_\sigma f_\mu + t_{+\mu}\delta_{\bar{\rho}\sigma} d^\dagger_\sigma f^\dagger_\mu) f_\nu d_\rho \Big] \\
&= -\sum_{\sigma\rho\mu\nu} \frac{t^*_{\nu+}}{\epsilon_\rho + 2\delta_\nu} \Big[- t_{+\mu}\delta_{\sigma\rho} n_\rho f^\dagger_\mu f_\nu + t_{-\mu}\delta_{\sigma\rho} n_\rho f_\mu f_\nu \\
&\quad - (-t_{-\mu}\delta_{\bar{\rho}\sigma} d^\dagger_\sigma f_\mu + t_{+\mu}\delta_{\bar{\rho}\sigma} d^\dagger_\sigma f^\dagger_\mu) f_\nu d_\rho \Big] . \qquad (5.25)
\end{aligned}$$

Because we will have to add the Hermitian conjugates of these terms, notice that

$$\begin{aligned}
\left[\sum_{\rho\nu} \frac{t^*_{\bar{\nu}-}}{\epsilon_\rho - 2\delta_{\bar{\nu}}} t_{\nu-} n_\rho f_\nu f^\dagger_{\bar{\nu}}\right]^\dagger &= \sum_{\rho\nu} \frac{t^*_{\bar{\nu}-}}{\epsilon_\rho - 2\delta_\nu} t_{\nu-} n_\rho f_\nu f^\dagger_{\bar{\nu}} , \\
\left[\sum_{\rho\nu} \frac{t^*_{\bar{\nu}+}}{\epsilon_\rho + 2\delta_{\bar{\nu}}} t_{\nu+} n_\rho f^\dagger_\nu f_{\bar{\nu}}\right]^\dagger &= \sum_{\rho\nu} \frac{t^*_{\bar{\nu}+}}{\epsilon_\rho + 2\delta_\nu} t_{\nu+} n_\rho f^\dagger_\nu f_{\bar{\nu}} , \\
\left[\sum_{\rho\nu} \frac{t^*_{\bar{\nu}-}}{\epsilon_\rho - 2\delta_{\bar{\nu}}} t_{\nu-} d^\dagger_{\bar{\rho}} d_\rho f_\nu f^\dagger_{\bar{\nu}}\right]^\dagger &= \sum_{\rho\nu} \frac{t^*_{\bar{\nu}-}}{\epsilon_{\bar{\rho}} - 2\delta_\nu} t_{\nu-} d^\dagger_{\bar{\rho}} d_\rho f_\nu f^\dagger_{\bar{\nu}} , \\
\left[\sum_{\rho\nu} \frac{t^*_{\bar{\nu}+}}{\epsilon_\rho + 2\delta_{\bar{\nu}}} t_{\nu+} d^\dagger_{\bar{\rho}} d_\rho f^\dagger_\nu f_{\bar{\nu}}\right]^\dagger &= \sum_{\rho\nu} \frac{t^*_{\bar{\nu}+}}{\epsilon_{\bar{\rho}} + 2\delta_\nu} t_{\nu+} d^\dagger_{\bar{\rho}} d_\rho f^\dagger_\nu f_{\bar{\nu}} , \qquad (5.26)
\end{aligned}$$

so that the contribution from the transfer of the fermions [Fig. 2(c), (d)] is

$$
\begin{aligned}
\mathcal{H}_o = \sum_{\rho\nu} & \Bigg[\left(\frac{1}{\epsilon_\rho - 2\delta_{\bar{\nu}}} + \frac{1}{\epsilon_\rho - 2\delta_\nu} \right) t_{\nu-} t^*_{\bar{\nu}-} f_\nu f^\dagger_{\bar{\nu}} \\
& + \left(\frac{1}{\epsilon_\rho + 2\delta_{\bar{\nu}}} + \frac{1}{\epsilon_\rho + 2\delta_\nu} \right) t_{\nu+} t^*_{\bar{\nu}+} f^\dagger_\nu f_{\bar{\nu}} \Bigg] n_\rho \\
& + \Bigg[\left(\frac{1}{\epsilon_\rho - 2\delta_{\bar{\nu}}} + \frac{1}{\epsilon_{\bar{\rho}} - 2\delta_\nu} \right) t^*_{\bar{\nu}-} t_{\nu-} f_\nu f^\dagger_{\bar{\nu}} \\
& + \left(\frac{1}{\epsilon_\rho + 2\delta_{\bar{\nu}}} + \frac{1}{\epsilon_{\bar{\rho}} + 2\delta_\nu} \right) t^*_{\bar{\nu}+} t_{\nu+} f^\dagger_\nu f_{\bar{\nu}} \Bigg] d^\dagger_{\bar{\rho}} d_\rho \\
= \sum_{\rho\nu} & \left(\frac{n_\rho + d^\dagger_{\bar{\rho}} d_\rho}{\epsilon_\rho - 2\delta_{\bar{\nu}}} + \frac{n_\rho + d^\dagger_\rho d_{\bar{\rho}}}{\epsilon_\rho - 2\delta_\nu} \right) t^*_{\bar{\nu}-} t_{\nu-} f_\nu f^\dagger_{\bar{\nu}} \\
& + \left(\frac{n_\rho + d^\dagger_{\bar{\rho}} d_\rho}{\epsilon_\rho + 2\delta_{\bar{\nu}}} + \frac{n_\rho + d^\dagger_\rho d_{\bar{\rho}}}{\epsilon_\rho + 2\delta_\nu} \right) t^*_{\bar{\nu}+} t_{\nu+} f^\dagger_\nu f_{\bar{\nu}} \,. \qquad (5.27)
\end{aligned}
$$

Next notice that

$$
\begin{aligned}
\left(-\sum_{\rho\nu} \frac{t^*_{\bar{\nu}-} t_{\nu+}}{\epsilon_\rho - 2\delta_{\bar{\nu}}} d^\dagger_{\bar{\rho}} f^\dagger_\nu f^\dagger_{\bar{\nu}} d_\rho \right)^\dagger &= -\sum_{\rho\nu} \frac{t^*_{\bar{\nu}+} t_{\nu-}}{\epsilon_{\bar{\rho}} - 2\delta_\nu} d^\dagger_{\bar{\rho}} f_\nu f_{\bar{\nu}} d_\rho \,, \\
\left(-\sum_{\rho\nu} \frac{t^*_{\bar{\nu}+} t_{\nu-}}{\epsilon_\rho + 2\delta_{\bar{\nu}}} d^\dagger_{\bar{\rho}} f_\nu f_{\bar{\nu}} d_\rho \right)^\dagger &= -\sum_{\rho\nu} \frac{t^*_{\bar{\nu}-} t_{\nu+}}{\epsilon_{\bar{\rho}} + 2\delta_\nu} d^\dagger_{\bar{\rho}} f^\dagger_\nu f^\dagger_{\bar{\nu}} d_\rho \,, \qquad (5.28)
\end{aligned}
$$

so that terms acting the even parity sector [Fig. 2(e), (f)] are

$$
\begin{aligned}
\mathcal{H}_e = -\Bigg[\sum_{\rho\nu} t^*_{\bar{\nu}+} t_{\nu-} & \left(\frac{n_\rho + d^\dagger_{\bar{\rho}} d_\rho}{\epsilon_\rho + 2\delta_{\bar{\nu}}} + \frac{n_\rho + d^\dagger_\rho d_{\bar{\rho}}}{\epsilon_\rho - 2\delta_\nu} \right) f_\nu f_{\bar{\nu}} \\
+ t^*_{\bar{\nu}-} t_{\nu+} & \left(\frac{n_\rho + d^\dagger_{\bar{\rho}} d_\rho}{\epsilon_\rho - 2\delta_{\bar{\nu}}} + \frac{n_\rho + d^\dagger_\rho d_{\bar{\rho}}}{\epsilon_\rho + 2\delta_\nu} \right) f^\dagger_\nu f^\dagger_{\bar{\nu}} \Bigg]. \qquad (5.29)
\end{aligned}
$$

Summing up the results we have the tunneling Hamiltonian to second order in $t_{\nu\pm}$:

$$\begin{aligned}
\mathcal{H}_T &= \mathcal{H}_s + \mathcal{H}_e + \mathcal{H}_o\,,\\
\mathcal{H}_s &= \sum_{\sigma\nu}\left(\frac{|t_{\nu+}|^2}{\epsilon_\sigma + 2\delta_\nu} f_\nu^\dagger f_\nu + \frac{|t_{\nu-}|^2}{\epsilon_\sigma - 2\delta_\nu} f_\nu f_\nu^\dagger\right)\left(2n_\sigma + d_{\bar\sigma}^\dagger d_\sigma + d_\sigma^\dagger d_{\bar\sigma}\right)\,,\\
\mathcal{H}_o &= \left[\sum_{\sigma\nu}\left(\frac{n_\sigma + d_{\bar\sigma}^\dagger d_\sigma}{\epsilon_\sigma - 2\delta_{\bar\nu}} + \frac{n_\sigma + d_\sigma^\dagger d_{\bar\sigma}}{\epsilon_\sigma - 2\delta_\nu}\right) t_{\bar\nu-}^* t_{\nu-} f_\nu f_{\bar\nu}^\dagger\right.\\
&\qquad\left. + \left(\frac{n_\sigma + d_{\bar\sigma}^\dagger d_\sigma}{\epsilon_\sigma + 2\delta_{\bar\nu}} + \frac{n_\sigma + d_\sigma^\dagger d_{\bar\sigma}}{\epsilon_\sigma + 2\delta_\nu}\right) t_{\bar\nu+}^* t_{\nu+} f_\nu^\dagger f_{\bar\nu}\right],\\
\mathcal{H}_e &= -\left[\sum_{\sigma\nu} t_{\bar\nu+}^* t_{\nu-}\left(\frac{n_\sigma + d_{\bar\sigma}^\dagger d_\sigma}{\epsilon_\sigma + 2\delta_{\bar\nu}} + \frac{n_\sigma + d_\sigma^\dagger d_{\bar\sigma}}{\epsilon_\sigma - 2\delta_\nu}\right) f_\nu f_{\bar\nu}\right.\\
&\qquad\left. + t_{\bar\nu-}^* t_{\nu+}\left(\frac{n_\sigma + d_{\bar\sigma}^\dagger d_\sigma}{\epsilon_\sigma - 2\delta_{\bar\nu}} + \frac{n_\sigma + d_\sigma^\dagger d_{\bar\sigma}}{\epsilon_\sigma + 2\delta_\nu}\right) f_\nu^\dagger f_{\bar\nu}^\dagger\right]. \qquad (5.30)
\end{aligned}$$

When the splitting is equal in both TSCs $\delta_\nu = \delta$, we obtain Eq. (1) in the main text,

$$\begin{aligned}
\mathcal{H}_T &= \mathcal{H}_s + \mathcal{H}_o + \mathcal{H}_e\,,\\
\mathcal{H}_s &= \sum_{\sigma,\nu}\left(\frac{|t_{\nu-}|^2}{\epsilon_\sigma - 2\delta} f_\nu f_\nu^\dagger + \frac{|t_{\nu+}|^2}{\epsilon_\sigma + 2\delta} f_\nu^\dagger f_\nu\right)\left(2n_\sigma + d_{\bar\sigma}^\dagger d_\sigma + d_\sigma^\dagger d_{\bar\sigma}\right)\,,\\
\mathcal{H}_o &= \sum_{\sigma,\nu}\left(\frac{t_{\bar\nu-}^* t_{\nu-}}{\epsilon_\sigma - 2\delta} f_\nu f_{\bar\nu}^\dagger + \frac{t_{\bar\nu+}^* t_{\nu+}}{\epsilon_\sigma + 2\delta} f_\nu^\dagger f_{\bar\nu}\right)(2n_\sigma + d_{\bar\sigma}^\dagger d_\sigma + d_\sigma^\dagger d_{\bar\sigma})\,,\\
\mathcal{H}_e &= -\left[\sum_{\sigma,\nu} t_{\bar\nu-}^* t_{\nu+}\left(\frac{n_\sigma + d_{\bar\sigma}^\dagger d_\sigma}{\epsilon_\sigma - 2\delta} + \frac{n_\sigma + d_\sigma^\dagger d_{\bar\sigma}}{\epsilon_\sigma + 2\delta}\right) f_\nu^\dagger f_{\bar\nu}^\dagger\right.\\
&\qquad\left. + t_{\bar\nu+}^* t_{\nu-}\left(\frac{n_\sigma + d_{\bar\sigma}^\dagger d_\sigma}{\epsilon_\sigma + 2\delta} + \frac{n_\sigma + d_\sigma^\dagger d_{\bar\sigma}}{\epsilon_\sigma - 2\delta}\right) f_\nu f_{\bar\nu}\right]. \qquad (5.31)
\end{aligned}$$

5.B Full exchange Hamiltonian

The full interaction between the MF qubit and the spin qubit can be written down as the exchange Hamiltonian

$$\mathcal{H}_T = \sum_{\kappa,\lambda=0,\ldots,3} J_{\kappa\lambda}\sigma_\kappa\eta_\lambda\,, \qquad (5.32)$$

in which

$$J_{\kappa\lambda} = \begin{pmatrix} B_1 & B_2 & B_3 & B_4 \\ B_1 & B_2 & B_3 & B_4 \\ 0 & 0 & 0 & 0 \\ B_5 & B_6 & B_7 & B_8 \end{pmatrix} , \tag{5.33}$$

where

$$\begin{aligned}
B_1 &= (\mathcal{C}_{++} + \mathcal{C}_{-+})(\Gamma_{+r} + \Gamma_{+l}) + (\mathcal{C}_{+-} + \mathcal{C}_{--})(\Gamma_{-r} + \Gamma_{-l}) \,, \\
B_2 &= (\mathcal{C}_{++} + \mathcal{C}_{-+})(\tilde{\Gamma}_{+r} + \tilde{\Gamma}_{+l}) - (\mathcal{C}_{+-} + \mathcal{C}_{--})(\tilde{\Gamma}_{-r} + \tilde{\Gamma}_{-l}) \,, \\
B_3 &= i \left[(\mathcal{C}_{++} + \mathcal{C}_{-+})(\tilde{\Gamma}_{+r} - \tilde{\Gamma}_{+l}) + (\mathcal{C}_{+-} + \mathcal{C}_{--})(\tilde{\Gamma}_{-r} - \tilde{\Gamma}_{-l}) \right] \,, \\
B_4 &= (\mathcal{C}_{++} + \mathcal{C}_{-+})(\Gamma_{+r} - \Gamma_{+l}) - (\mathcal{C}_{+-} + \mathcal{C}_{--})(\Gamma_{-r} - \Gamma_{-l}) \,, \\
B_5 &= (\mathcal{C}_{++} - \mathcal{C}_{-+})(\Gamma_{+r} + \Gamma_{+l}) + (\mathcal{C}_{+-} - \mathcal{C}_{--})(\Gamma_{-r} + \Gamma_{-l}) \,, \\
B_6 &= (\mathcal{C}_{++} - \mathcal{C}_{-+})(\tilde{\Gamma}_{+r} + \tilde{\Gamma}_{+l}) - (\mathcal{C}_{+-} - \mathcal{C}_{--})(\tilde{\Gamma}_{-r} + \tilde{\Gamma}_{-l}) \,, \\
B_7 &= i \left[(\mathcal{C}_{++} - \mathcal{C}_{-+})(\tilde{\Gamma}_{+r} - \tilde{\Gamma}_{+l}) + (\mathcal{C}_{+-} - \mathcal{C}_{--})(\tilde{\Gamma}_{-r} - \tilde{\Gamma}_{-l}) \right] \,, \\
B_8 &= (\mathcal{C}_{++} - \mathcal{C}_{-+})(\Gamma_{+r} - \Gamma_{+l}) - (\mathcal{C}_{+-} - \mathcal{C}_{--})(\Gamma_{-r} - \Gamma_{-l}) \,.
\end{aligned} \tag{5.34}$$

Here, $\Gamma_{\pm\nu} = |t_{\nu\pm}|^2$ and $\tilde{\Gamma}_{\pm\nu} = t^*_{\pm\bar{\nu}} t_{\nu\pm}$ and $\mathcal{C}_{\sigma\rho} = 1/(\epsilon_\sigma + 2\rho\delta)$ or, with a σ and ρ independent denominator,

$$\begin{aligned}
\mathcal{C}_{\sigma\rho} = & \frac{(\epsilon_0 - 2\rho\delta)(\epsilon_0^2 + \Delta^2 - 4\delta^2) - 2\epsilon_0\Delta^2}{[(\epsilon_0 - \Delta)^2 - 4\delta^2][(\epsilon_0 + \Delta)^2 - 4\delta^2]} \\
& + \frac{\sigma\Delta[2\epsilon_0(\epsilon_0 - 2\rho\delta) - (\epsilon_0^2 + \Delta^2 - 4\delta^2)]}{[(\epsilon_0 - \Delta)^2 - 4\delta^2][(\epsilon_0 + \Delta)^2 - 4\delta^2]} \,,
\end{aligned} \tag{5.35}$$

where we have written $\epsilon_\sigma = \epsilon_0 + \sigma\Delta$.

We consider the limit that the length of the TSCs is infinite and the dot is placed between them, so that $t'_l = t_r = 0$ and $\delta = 0$, thus $t_{\pm r} = \pm t'_r$ and $t_{\pm l} = t_l$. When the difference in phase between t'_r and t_l is ϕ, we find that $\Gamma_{\pm r} = |t'_r|^2$, $\Gamma_{\pm l} = |t_l|^2$, $\Gamma_{\pm r} = \pm t'_r t_l e^{i\phi}$, and $\Gamma_{\pm l} = \pm t'_r t_l e^{-i\phi}$. The exchange interaction becomes

$$\begin{aligned}
B_1 &= \mathcal{D}^+(|t'_r|^2 + t_l^2)\,, \\
B_2 &= 2\mathcal{D}^+ t'_r t_l \cos\phi \\
B_3 &= 0\,, \\
B_4 &= 0\,, \\
B_5 &= \mathcal{D}^-(|t'_r|^2 + t_l^2)\,, \\
B_6 &= 2\mathcal{D}^- t'_r t_l \cos\phi\,, \\
B_7 &= 0\,, \\
B_8 &= 0\,,
\end{aligned} \tag{5.36}$$

where

$$\begin{aligned}
\mathcal{D}^+ &= \mathcal{C}_{++} + \mathcal{C}_{+-} + \mathcal{C}_{-+} + \mathcal{C}_{-+} = \frac{\epsilon_0}{\epsilon_0^2 - \Delta^2}\,, \\
\mathcal{D}^- &= \mathcal{C}_{++} + \mathcal{C}_{+-} - \mathcal{C}_{-+} - \mathcal{C}_{-+} = \frac{\Delta}{\epsilon_0^2 - \Delta^2}\,.
\end{aligned} \tag{5.37}$$

When $\Delta = 0$ and $t'_r = t_l = t$, this reduces to Eq. (2) in the main text.

5.C Hybrid CNOT gate

Let us introduce the hCP gate $U'_{\text{hCP}} = \exp[i\pi(1-\sigma_3)(1-\eta_3)/4] = (1 + \sigma_3 + \eta_3 - \sigma_3\eta_3)/2$ and relate it to the one used in the main text, $U_{\text{hCP}} = \exp[i\pi(1+\sigma_3)(1+\eta_3)/4] = (1 - \sigma_3 - \eta_3 - \sigma_3\eta_3)/2$. Note that U'_{hCP} reduces to the 'canonical form' of the conditional phase gate for identical qubit types. Next, we note that $U'_{\text{hCP}} = U_{\text{hCP}} R_{SQ}(-\pi) R_{MQ}(-\pi)$, where $R_{SQ}(\phi) = \exp[i\phi\sigma_3/2]$ and $R_{MQ}(\phi) = \exp[i\phi\eta_3/2]$ are the phase gates on the spin and MF qubit, respectively. Then, we get the corresponding hybrid CNOT gate $U'^{31}_{\text{hCNOT}} = (1 + \sigma_3 + \eta_1 - \sigma_3\eta_1)/2$ from U'_{hCP} by a Hadamard operation $H_{MQ} = (\eta_1 + \eta_3)/\sqrt{2}$ (which takes η_3 into η_1), $U'^{31}_{\text{hCNOT}} = H_{MQ} U'_{\text{hCP}} H_{MQ}$, and thus

$$\begin{aligned}
U'^{31}_{\text{hCNOT}} &= H_{MQ} U'_{\text{hCP}} R_{SQ}(-\pi) R_{MQ}(-\pi) H_{MQ} \\
&= U^{31}_{\text{hCNOT}} R_{SQ}(-\pi) H_{MQ} R_{MQ}(-\pi) H_{MQ},
\end{aligned} \tag{5.38}$$

where $U^{31}_{\text{hCNOT}} = (1 - \sigma_3 - \eta_1 - \sigma_3\eta_1)/2$ (used in the main text). Thus, we can get the 'canonical form' of the CNOT gate, U'^{31}_{hCNOT}, from U^{31}_{hCNOT} by simple single-qubit unitary operations. And similarly for U^{13}_{hCNOT}. Note that the phase gate $R_{MQ}(-\pi)$ can be obtained by braiding since it is the square of the $\pi/4$ phase gate.

5.D Effective interaction between Majorana fermion qubits

In this section we derive an effective Hamiltonian for the interaction of neighboring hybrid qubits, labeled (1) and (2), in a MaSH network [Fig. 1(b)]. We assume that adjacent spin qubits couple via an isotropic exchange interaction of the form

$$\mathcal{H}_{SQ}^{(12)} = \mathcal{J}\left[\sigma_1^{(1)}\sigma_1^{(2)} + \sigma_2^{(1)}\sigma_2^{(2)} + \sigma_3^{(1)}\sigma_3^{(2)}\right] \tag{5.39}$$

and that the MF qubits couple to the spin qubits via

$$\mathcal{H}_{\text{hCP}} = \frac{2|t|^2}{\epsilon_0}\left[1 + \sigma_1^{(1)} + \eta_1^{(1)} + \sigma_1^{(1)}\eta_1^{(1)} + \sigma_1^{(2)} + \eta_1^{(2)} + \sigma_1^{(2)}\eta_1^{(2)}\right], \tag{5.40}$$

according to Eq. (2) in the main text. When $\mathcal{J} \gg 2|t|^2/\epsilon_0$, we can make a Schrieffer-Wolff transformation on $\mathcal{H}_{SQ}^{(12)}$, using $\mathcal{H}_{\text{hCP}}$ as a perturbation, which gives an effective coupling between two hybrid qubits up to second order in $|t|^2/\epsilon_0$,

$$\mathcal{H}_{HQ}^{(12)} = \mathcal{H}_{SQ}^{(12)} + \mathcal{H}_{MQ}^{(12)}, \tag{5.41}$$

where

$$\mathcal{H}_{MQ}^{(12)} = -\lim_{\varepsilon\to 0^+}\frac{i}{2\hbar}\int_0^\infty \mathrm{d}\tau\, e^{-\varepsilon\tau}\left[\mathcal{H}_{\text{hCP}}(\tau), \mathcal{H}_{\text{hCP}}\right]. \tag{5.42}$$

Here, $\mathcal{H}_{\text{hCP}}(\tau)$ is the time-evolution of $\mathcal{H}_{\text{hCP}}$ under the unperturbed Hamiltonian $\mathcal{H}_{SQ}^{(12)}$,

$$\begin{aligned}
\mathcal{H}_{\text{hCP}}(\tau) &= e^{i\mathcal{H}_{SQ}^{(12)}\tau/\hbar}\mathcal{H}_{\text{hCP}}e^{-i\mathcal{H}_{SQ}^{(12)}\tau/\hbar} \\
&= \left[e^{i\omega_{\mathcal{J}}\sigma_1^{(1)}\sigma_1^{(2)}\tau}e^{i\omega_{\mathcal{J}}\sigma_2^{(1)}\sigma_2^{(2)}\tau}e^{i\omega_{\mathcal{J}}\sigma_3^{(1)}\sigma_3^{(2)}\tau}\right] \\
&\quad\times \mathcal{H}_{\text{hCP}}\left[e^{-i\omega_{\mathcal{J}}\sigma_1^{(1)}\sigma_1^{(2)}\tau}e^{-i\omega_{\mathcal{J}}\sigma_2^{(1)}\sigma_2^{(2)}\tau}e^{-i\omega_{\mathcal{J}}\sigma_3^{(1)}\sigma_3^{(2)}\tau}\right] \\
&= \frac{2|t|^2}{\epsilon_0}\Big\{1 + \eta_1^{(1)} + \eta_1^{(2)} \\
&\quad + e^{2i\omega_{\mathcal{J}}\sigma_2^{(1)}\sigma_2^{(2)}\tau}e^{2i\omega_{\mathcal{J}}\sigma_3^{(1)}\sigma_3^{(2)}\tau}\left[\sigma_1^{(1)} + \sigma_1^{(1)}\eta_1^{(1)} + \sigma_1^{(2)} + \sigma_1^{(2)}\eta_1^{(2)}\right]\Big\},
\end{aligned} \tag{5.43}$$

with $\omega_{\mathcal{J}} = \mathcal{J}/\hbar$. Evaluating the commutator in Eq. (5.42)

$$\begin{aligned}
\left[\mathcal{H}_{\text{hCP}}(\tau), \mathcal{H}_{\text{hCP}}\right] &= 4i\left(\frac{2|t|^2}{\epsilon_0}\right)^2\cos(2\omega_{\mathcal{J}}\tau)\sin(2\omega_{\mathcal{J}}\tau) \\
&\quad\times\left[\sigma_2^{(1)}\sigma_2^{(2)} + \sigma_3^{(1)}\sigma_3^{(2)}\right]\left[1 - \eta_1^{(1)}\eta_1^{(2)}\right]
\end{aligned} \tag{5.44}$$

and using the integral

$$\lim_{\varepsilon\to0^+}\int_0^\infty \mathrm{d}\tau\; e^{-\varepsilon\tau}\sin(2\omega_{\mathcal{J}}\tau)\cos(2\omega_{\mathcal{J}}\tau)=\frac{1}{8\omega_{\mathcal{J}}}\,, \tag{5.45}$$

we find

$$\mathcal{H}_{MQ}^{(12)}=\frac{|t|^4}{\epsilon_0^2\mathcal{J}}\left[\sigma_2^{(1)}\sigma_2^{(2)}+\sigma_3^{(1)}\sigma_3^{(2)}\right]\left[1-\eta_1^{(1)}\eta_1^{(2)}\right]\,, \tag{5.46}$$

an effective exchange coupling between adjacent MF qubits which is modulated by the corresponding spin qubits. Applying this interaction for a time $\tau_{MF}=\pi\hbar\epsilon_0\mathcal{J}/|t|^4$, we obtain the gate $U_{MQ}^{(12)}=\exp[i\pi(1-\eta_1^{(1)}\eta_1^{(2)})/4]$.

5.E Inner-outer Majorana basis

Instead of forming Dirac fermions in the same TSC, one can instead form a full fermion from the MFs closest together (inner fermion) and a fermion from the MFs furthest apart (outer fermion),

$$\begin{aligned} g_r &= (\gamma_r'+i\gamma_l)/2\,,\\ g_l &= (\gamma_l'+i\gamma_r)/2\,, \end{aligned} \tag{5.47}$$

respectively. The MFs are, in turn, written as

$$\begin{aligned} \gamma_\nu' &= g_\nu+g_\nu^\dagger\,,\\ \gamma_\nu &= (g_{\bar\nu}-g_{\bar\nu}^\dagger)/i\,. \end{aligned} \tag{5.48}$$

The tunneling Hamiltonian can then be written as

$$\begin{aligned} \tilde{H}_T &= \sum_{\sigma,\nu} it_\nu d_\sigma^\dagger(g_\nu+g_\nu^\dagger)-it_\nu' d_\sigma^\dagger(g_{\bar\nu}-g_{\bar\nu}^\dagger)-it_\nu'^*(g_{\bar\nu}-g_{\bar\nu}^\dagger)d_\sigma-it_\nu^*(g_\nu+g_\nu^\dagger)d_\sigma\\ &= \sum_{\sigma,\nu} id_\sigma^\dagger[(t_\nu-t_{R\bar\nu})g_\nu+(t_\nu+t_{\bar\nu}')g_\nu^\dagger]-i[(t_\nu^*+t_{\bar\nu}'^*)g_\nu+(t_\nu^*-t_{\bar\nu}'^*)g_\nu^\dagger]d_\sigma\\ &= \sum_{\sigma,\nu} -i\tilde{t}_{\nu-}d_\sigma^\dagger g_\nu+i\tilde{t}_{\nu-}^*g_\nu^\dagger d_\sigma+i\tilde{t}_{\nu+}d_\sigma^\dagger g_\nu^\dagger-i\tilde{t}_{\nu+}^*g_\nu d_\sigma\,, \end{aligned} \tag{5.49}$$

where we have defined $\tilde{t}_{\nu-}=t_{\bar\nu}'-t_\nu$ and $\tilde{t}_{\nu+}=t_\nu+t_{\bar\nu}'$. Furthermore, we redefine the MF coupling in the TSC so that $\tilde{H}_M=\sum_\nu\tilde{\delta}_\nu(2g_\nu^\dagger g_\nu-1)$ where $\tilde{\delta}_r$ ($\tilde{\delta}_l$) now parameterizes the overlap between the inner (outer)

MFs. With this redefinition, we see that the transformed Hamiltonian is, term by term, identical to Eq. (2). Upon performing the same Schrieffer-Wolff transformation we find

$$\begin{aligned}
\tilde{\mathcal{H}}_T &= \tilde{\mathcal{H}}_s + \tilde{\mathcal{H}}_e + \tilde{\mathcal{H}}_o \,, \\
\tilde{\mathcal{H}}_s &= \sum_{\sigma,\nu} \left(\frac{|\tilde{t}_{\nu+}|^2}{\epsilon_\sigma + 2\tilde{\delta}_\nu} g_\nu^\dagger g_\nu + \frac{|\tilde{t}_{\nu-}|^2}{\epsilon_\sigma - 2\tilde{\delta}_\nu} g_\nu g_\nu^\dagger \right) \left(2n_\sigma + d_{\bar\sigma}^\dagger d_\sigma + d_\sigma^\dagger d_{\bar\sigma} \right) \,, \\
\tilde{\mathcal{H}}_o &= \sum_{\sigma,\nu} \Bigg[\left(\frac{n_\sigma + d_{\bar\sigma}^\dagger d_\sigma}{\epsilon_\sigma - 2\tilde{\delta}_{\bar\nu}} + \frac{n_\sigma + d_\sigma^\dagger d_{\bar\sigma}}{\epsilon_\sigma - 2\tilde{\delta}_\nu} \right) \tilde{t}_{\bar\nu -}^* \tilde{t}_{\nu -} g_\nu g_{\bar\nu}^\dagger \\
&\quad + \left(\frac{n_\sigma + d_{\bar\sigma}^\dagger d_\sigma}{\epsilon_\sigma + 2\tilde{\delta}_{\bar\nu}} + \frac{n_\sigma + d_\sigma^\dagger d_{\bar\sigma}}{\epsilon_\sigma + 2\tilde{\delta}_\nu} \right) \tilde{t}_{\bar\nu +}^* \tilde{t}_{\nu +} g_\nu^\dagger g_{\bar\nu} \Bigg] \,, \\
\tilde{\mathcal{H}}_e &= -\Bigg[\sum_{\sigma,\nu} \tilde{t}_{\bar\nu +}^* \tilde{t}_{\nu -} \left(\frac{n_\sigma + d_{\bar\sigma}^\dagger d_\sigma}{\epsilon_\sigma + 2\tilde{\delta}_{\bar\nu}} + \frac{n_\sigma + d_\sigma^\dagger d_{\bar\sigma}}{\epsilon_\sigma - 2\tilde{\delta}_\nu} \right) g_\nu g_{\bar\nu} \\
&\quad + \tilde{t}_{\bar\nu -}^* \tilde{t}_{\nu +} \left(\frac{n_\sigma + d_{\bar\sigma}^\dagger d_\sigma}{\epsilon_\sigma - 2\tilde{\delta}_{\bar\nu}} + \frac{n_\sigma + d_\sigma^\dagger d_{\bar\sigma}}{\epsilon_\sigma + 2\tilde{\delta}_\nu} \right) g_\nu^\dagger g_{\bar\nu}^\dagger \Bigg] \,. \qquad (5.50)
\end{aligned}$$

When the outer MFs are totally uncoupled to the system, $t_r = t_l' = 0$, then $t_{l\pm} = 0$ so that

$$\left(\frac{|\tilde{t}_{r+}|^2}{\epsilon_\sigma + 2\tilde{\delta}_r} g_r^\dagger g_r + \frac{|\tilde{t}_{r-}|^2}{\epsilon_\sigma - 2\tilde{\delta}_r} g_r g_r^\dagger \right) \left(2n_\sigma + d_{\bar\sigma}^\dagger d_\sigma + d_\sigma^\dagger d_{\bar\sigma} \right) \,. \qquad (5.51)$$

One can immediately see that the effective magnetic field is, in general, different when the state is occupied versus unoccupied.

One can use this basis as more transparent construction of parity. When the MFs on the same topological superconductor are well separated, $\delta = t_l' = t_r = 0$, the tunneling Hamiltonian in the new basis is given by $2\left(|\tilde{t}_{r+}|^2 g_r^\dagger g_r + |\tilde{t}_{r-}|^2 g_r g_r^\dagger\right)(1+\sigma_1)/\epsilon_0$. When the parity of the junction between the TSCs is one (zero), i.e. the complex fermion state formed by the inner MFs is occupied (unoccupied), there is an effective magnetic field on the dot proportional to $|\tilde{t}_{r-}|^2/\epsilon_0$ ($|\tilde{t}_{r+}|^2/\epsilon_0$). The Rabi oscillations between the spin up and down eigenstates, which can be detected, are therefore sensitive to the parity of the junction between two TSCs. The parity can be measured because the MF qubit is in a fixed parity subspace, i.e. if the fermion is not shared by the nearest MFs then the it must be shared between the outer MFs. If the parity is unrestricted, one must measure both MFs on both the left and right TSCs to determine the state of the MF qubit.

Bibliography

[1] A.Y. Kitaev, Physics-Uspekhi **44**, 131 (2001).

[2] L. Fu and C. L. Kane, Phys. Rev. Lett. **100**, 096407 (2008).

[3] R. M. Lutchyn, J. D. Sau, and S. Das Sarma, Phys. Rev. Lett. **105**, 077001 (2010).

[4] Y. Oreg, G. Refael, and F. von Oppen, Phys. Rev. Lett. **105**, 177002 (2010).

[5] J. Klinovaja, P. Stano, A. Yazdani, and D. Loss, Phys. Rev. Lett. **111**, 186805 (2013).

[6] V. Mourik, K. Zuo, S. M. Frolov, S. R. Plissard, E. Bakkers, and L. P. Kouwenhoven, Science **336**, 1003 (2012).

[7] A. Das, Y. Ronen, Y. Most, Y. Oreg, M. Heiblum, and H. Shtrikman, Nat. Phys. **8**, 887 (2012).

[8] L. P. Rokhinson, X. Liu, and J. K. Furdyna, Nat. Phys. **8**, 795 (2012).

[9] H. O. H. Deng, P. Caroff, H. Q. Xu, and C. M. Marcus, Phys. Rev. B **87**, 241401 (2013).

[10] S. Nadj-Perge, I. K. Drozdov, J. Li, H. Chen, S. Jeon, J. Seo, A. H. MacDonald, B. A. Bernevig, and A. Yazdani, Science **346**, 602 (2014).

[11] M. Ruby, F. Pientka, Y. Peng, F. v. Oppen, B. W. Heinrich, and K. J. Franke, Phys. Rev. Lett. **115**, 197204 (2015).

[12] R. Pawlak, M. Kisiel, J. Klinovaja, T. Meier, S. Kawai, T. Glatzel, D. Loss, and E. Meyer, npj Quantum Information **2**, 16035 (2016).

[13] W. Chang, S. M. Albrecht, T. S. Jespersen, F. Kuemmeth, P. Krogstrup, J. Nygøard, and C. M. Marcus, Nat Nano **10**, 232 (2014).

[14] H. Zhang, Ö. Gül, S. Conesa-Boj, K. Zuo, V. Mourik, F. K. de Vries, J. van Veen, D. J. van Woerkom, M. P. Nowak, M. Wimmer, D. Car, S. Plissard, E. P. A. M. Bakkers, M. Quintero-Prez, S. Goswami, K. Watanabe, T. Taniguchi, and L. P. Kouwenhoven, arXiv:1603.04069.

[15] Ö. Gül, H. Zhang, F. K. de Vries, J. van Veen, K. Zuo, V. Mourik, S. Conesa-Boj, M. P. Nowak, D. J. van Woerkom, M. Quintero-Pérez, M. C. Cassidy, A. Geresdi, S. Kölling, D. Car, S. R. Plissard, E. P. A. M. Bakkers, and L. P. Kouwenhoven, arXiv:1702.02578.

[16] M. T. Deng, S. Vaitiekenas, E. B. Hansen, J. Danon, M. Leijnse, K. Flensberg, J. Nygøard, P. Krogstrup, and C. M. Marcus, Science **354**, 1557 (2016).

[17] J. Chen, P. Yu, J. Stenger, M. Hocevar, D. Car, S. R. Plissard, E. P. Bakkers, T. D. Stanescu, and S. M. Frolov, arXiv:1610.04555.

[18] S. Sasaki, S. De Franceschi, J. Elzerman, W. Van der Wiel, M. Eto, S. Tarucha, and L. Kouwenhoven, Nature (London) **405**, 764 (2000).

[19] D. I. Pikulin, J. P. Dahlhaus, M. Wimmer, H. Schomerus, and C. W. J. Beenakker, New J.Phys. **14**, 125011 (2012).

[20] G. Kells, D. Meidan, and P. W. Brouwer, Phys. Rev. B **86**, 100503 (2012).

[21] J. Liu, A. C. Potter, K. T. Law, and P. A. Lee, Phys. Rev. Lett. **109**, 267002 (2012).

[22] D. Bagrets and A. Altland, Phys. Rev. Lett. **109**, 227005 (2012).

[23] E. J. Lee, X. Jiang, R. Aguado, G. Katsaros, C. M. Lieber, and S. De Franceschi, Phys. Rev. Lett. **109**, 186802 (2012).

[24] A. Zazunov, R. Egger, T. Jonckheere, and T. Martin, Phys. Rev. Lett. **103**, 147004 (2009).

[25] A. Brunetti, A. Zazunov, A. Kundu, and R. Egger, Phys. Rev. B **88**, 144515 (2013).

[26] D. B. Szombati, S. Nadj-Perge, D. Car, S. R. Plissard, E. P. A. M. Bakkers, and L. P. Kouwenhoven, Nat. Phys. **12**, 568 (2016).

[27] H. J. Suominen, M. Kjaergaard, A. R. Hamilton, J. Shabani, C. J. Palmstrøm, C. M. Marcus, and F. Nichele, arXiv:1703.03699.

[28] D. A. Ivanov, Phys. Rev. Lett., **86**, 268 (2001).

[29] J. Alicea, Y. Oreg, G. Refael, F. von Oppen, and M. P. A. Fisher, Nature Phys. **7**, 412 (2011).

[30] M. Greiter, *Mapping of parent Hamiltonians: from Abelian and non-Abelian quantum Hall states to exact models of critical spin chains* (Springer, 2011).

[31] J. Klinovaja and D. Loss, Phys. Rev. B **86**, 085408 (2012).

[32] J. Klinovaja and D. Loss, Phys. Rev. B **90**, 045118 (2014).

[33] L. G. Aslamazov, and A. I. Larkin, 1969, Pis?ma Zh. Eksp. Teor. Fiz. textbf9, 150 [JETP Lett. **9**, 87 (1969)].

[34] I. O. Kulik and A. N. Omelyanchuk, 1977, Fiz. Nizk. Temp. 3, **945** [Sov. J. Low Temp. Phys. **3**, 459 (1977)].

[35] C. W. J. Beenakker and H. van Houten, Phys. Rev. Lett. **66**, 3056 (1991).

[36] N. Kopnin, *Theory of Nonequilibrium Superconductivity (International Series of Monographs on Physics)* (Oxford Science Publications, 2009).

[37] I. O. Kulik, Pis'ma Zh. Eksp. Teor. Fiz. **49**, 1211 (1966) [JETP Lett. **22**, 841 (1966)].

[38] L. N. Bulaevskii, V. V. Kuzii, and A. A. Sobyanin, Pis'ma Zh. Eksp. Teor. Fiz. **25**, 314 (1977) [JETP Lett. **25**, 290 (1977)].

[39] B. I. Spivak and S. A. Kivelson, Phys. Rev. B **43**, 3740 (1991).

[40] J. Alicea, Rep. Prog. Phys. **75**, 076501 (2012).

[41] A. A. Golubov, M. Yu. Kupriyanov, and E. Il'ichev, Rev. Mod. Phys. **76**, 411 (2004).

[42] O. Vavra, S. Gazi, D. S. Golubovic, I. Vavra, J. Derer, J. Verbeeck, G. Van Tendeloo, and V. V. Moshchalkov, Phys. Rev. B **74**, 020502(R) (2006).

[43] A. I. Buzdin, L. N. Bulaevskii, and S. V. Panyukov, Pis'ma Zh. Eksp. Teor. Fiz. **35**, 147 (1982) [JETP Lett. **35**, 487 (1982)].

[44] V. V. Ryazanov, V. A. Oboznov, A. Yu. Rusanov, A. V. Veretennikov, A. A. Golubov, and J.Aarts, Phys. Rev. Lett. **86**, 2427 (2001).

[45] J. A. van Dam, Y. V. Nazarov, E. P. A. M. Bakkers, and L. P. Kouwenhoven, Nature (London) **442**, 667 (2006).

[46] S. Hart, H. Ren, T. Wagner, P. Leubner, M. Muhlbauer, C. Brune, H. Buhmann, L. Molenkamp, and A. Yacoby, Nature Physics **10**, 638 (2014).

[47] V. S. Pribiag, A. J. A. Beukman, F. Qu, M. C. Cassidy, C. Charpentier, W. Wegscheider, and L. P. Kouwenhoven, Nature Nanotechnology **10**, 593 (2015).

[48] J. Wiedenmann, E. Bocquillon, R. S. Deacon, S. Hartinger, T. M. Klapwijk, L. Maier, C. Ames, C. Brüne, K. Ishibashi, S. Tarucha, H. Buhmann, and L. W. Molenkamp, Nat. Commun. **7**, 10303 (2016).

[49] M. Z. Hasan and C. L. Kane, Rev. Mod. Phys. **82**, 3045 (2010).

[50] X.-L. Qi and S.-C. Zhang, Rev. Mod. Phys. **83**, 1057 (2011).

[51] G. Tkachov and E. M. Hankiewicz, Phys. Status Solidi B **250**, 215 (2013).

[52] B. A. Volkov and O. A. Pankratov, Pis'ma Zh. Eksp. Teor. Fiz. **42**, 145 (1985) [JETP Lett. **42**, 178 (1985)].

[53] O. A. Pankratov, S. V. Pakhomov, and B. A. Volkov, Solid State Commun. **61**, 93 (1987).

[54] B. A. Bernevig, T. L. Hughes, S.-C. Zhang, Science **314**, 1757 (2006).

[55] M. König, S. Wiedmann, C. Brune, A. Roth, H. Buhmann, L. W. Molenkamp, X.-L. Qi, and S.-C. Zhang, Science **318**, 766 (2007).

[56] A. Roth, C. Brune, H. Buhmann, L. W. Molenkamp, J. Maciejko, X.-L. Qi, and S.-C. Zhang, Science **325**, 294 (2009).

[57] K. C. Nowack, E. M. Spanton, M. Baenninger, M. König, J. R. Kirtley, B. Kalisky, C. Ames, P. Leubner, C. Brune, H. Buhmann, L. W. Molenkamp, D. Goldhaber-Gordon, and K. A. Moler, Nature Materials **12**, 787 (2013).

[58] J. Linder, Y. Tanaka, T. Yokoyama, A. Sudbø, and N. Nagaosa, Phys. Rev. B **81**, 184525 (2010).

[59] F. Crepin and B. Trauzettel, Phys. Rev. Lett. **112**, 077002 (2014).

[60] F. Crepin, B. Trauzettel, and F. Dolcini, Phys. Rev. B **89**, 205115 (2014).

[61] G. Tkachov, P. Burset, B. Trauzettel, and E. M. Hankiewicz, Phys. Rev. B **92**, 045408 (2015).

[62] A. G. Lebed, Pis'ma Zh. Eksp. Teor. Fiz. **43**, 137 (1986) [JETP Lett. **43**, 174 (1986)].

[63] C. L. Kane, R. Mukhopadhyay, and T. C. Lubensky, Phys. Rev. Lett. **88**, 036401 (2002).

[64] J. Klinovaja and D. Loss, Phys. Rev. Lett. **111**, 196401 (2013).

[65] J. C. Y. Teo and C. L. Kane, Phys. Rev. B **89**, 085101 (2014).

[66] J. Klinovaja and D. Loss, Eur. Phys. J. B **87**, 171 (2014).

[67] J. Klinovaja and Y. Tserkovnyak, Phys. Rev. B **90**, 115426 (2014).

[68] J. Klinovaja, Y. Tserkovnyak, and D. Loss, Phys. Rev. B **91**, 085426 (2015).

[69] C. L. M. Wong and K. T. Law, Phys. Rev. B **86**, 184516 (2012).

[70] S. Nakosai, J. C. Budich, Y. Tanaka, B. Trauzettel, and N. Nagaosa, Phys. Rev. Lett. **110**, 117002 (2013).

[71] X.-J. Liu, C. L. M. Wong, and K. T. Law, Phys. Rev. X **4**, 021018 (2014).

[72] E. Dumitrescu, J. D. Sau, and S. Tewari, Phys. Rev. B **90**, 245438 (2014).

[73] F. Zhang, C. L. Kane, and E. J. Mele, Phys. Rev. Lett. **111**, 056402 (2013).

[74] A. Keselman, L. Fu, A. Stern, and E. Berg, Phys. Rev. Lett. **111**, 116402 (2013).

[75] A. Haim, A. Keselman, E. Berg, and Y. Oreg, Phys. Rev. B **89**, 220504 (2014).

[76] E. Gaidamauskas, J. Paaske, and K. Flensberg, Phys. Rev. Lett. **112**, 126402 (2014).

[77] J. Klinovaja, A. Yacoby, and D. Loss, Phys. Rev. B **90**, 155447 (2014).

[78] C.-X. Liu and B. Trauzettel, Phys Rev B **83**, 220510(R) (2011).

[79] N. Kopnin, Theory of Nonequilibrium Superconductivity, (Oxford University Press, Oxford, 2001).

[80] V. M. Galitski and A. I. Larkin, Phys. Rev. B **66**, 064526 (2002).

[81] C.-Z. Chang, W. Zhao, D. Y. Kim, H. Zhang, B. A. Assaf, D. Heiman, S.-C. Zhang, C. Liu, M. H. W. Chan, and J. S. Moodera, Nature Materials **14**, 473 (2015).

[82] M. Li, C.-Z. Chang, L. Wu, J. Tao, W. Zhao, M. H. W. Chan, J. S. Moodera, J. Li, and Y. Zhu, Phys. Rev. Lett. **114**, 146802 (2015).

[83] J. R. Schrieffer and P. A. Wolff, Phys. Rev. **149**, 491 (1966).

[84] J. Klinovaja and D. Loss, Eur. Phys. J. B **88**, 62 (2015).

[85] J. Klinovaja and D. Loss, Phys. Rev. B **92**, 121410(R) (2015).

[86] See the Supplemental Material (SM) for more details such as the spectrum, explicit MF wave functions, and phase diagram.

[87] D. Rainis, L. Trifunovic, J. Klinovaja, and D. Loss, Phys. Rev. B **87**, 024515 (2013).

[88] A. A. Zyuzin, D. Rainis, J. Klinovaja, and D. Loss. Phys. Rev. Lett. **111**, 056802 (2013).

[89] B. Braunecker and P. Simon, Phys. Rev. Lett. **111**, 147202 (2013).

[90] F. Pientka, L. I. Glazman, and F. von Oppen, Phys. Rev. B **88**, 155420 (2013).

[91] S. Nadj-Perge, I. K. Drozdov, B. A. Bernevig, and A. Yazdani, Phys. Rev. B **88**, 020407(R) (2013).

[92] S. Takei, B. M. Fregoso, H.-Y. Hui, A. M. Lobos, and S. Das Sarma, Phys. Rev. Lett. **110**, 186803 (2013).

[93] T. D. Stanescu, R. M. Lutchyn, and S. Das Sarma, Phys. Rev. B **90**, 085302 (2014).

[94] T. D. Stanescu and S. Das Sarma, arXiv:1702.03976.

[95] C. R. Reeg and D. L. Maslov, arXiv:1702.05046.

[96] P. Recher and D. Loss, Phys. Rev. B **65**, 165327 (2002).

[97] C. Bena, S. Vishveshwara, L. Balents, and M. P. A. Fisher, Phys. Rev. Lett. **89**, 037901 (2002).

[98] K. Sato, D. Loss, and Y. Tserkovnyak, Phys. Rev. B **85**, 235433 (2012).

[99] A. Haim, E. Berg, K. Flensberg, and Y. Oreg, Phys. Rev. B **94**, 161110 (2016).

[100] A. Haim, K. Wölms, E. Berg, Y. Oreg, and K. Flensberg, Phys. Rev. B **94**, 115124 (2016).

[101] C. R. Reeg, J. Klinovaja, and D. Loss, arXiv:1701.07107.

[102] S. Bravyi, B. Leemhuis, and B. M. Terhal, New J.Phys. **12**, 083039 (2010).

[103] S. Vijay, T. H. Hsieh, and L. Fu, Phys. Rev. X **5**, 041038 (2015).

[104] S. Vijay and L. Fu, Phys. Scr. **2016**, 014002.

[105] L. A. Landau, S. Plugge, E. Sela, A. Altland, S. M. Albrecht, and R. Egger, Phys. Rev. Lett. **116**, 050501 (2016).

[106] S. Plugge, L. A. Landau, E. Sela, A. Altland, K. Flensberg, and R. Egger Phys. Rev. B **94**, 174514 (2016).

[107] S. Hoffman, C. Schrade, J. Klinovaja, and D. Loss Phys. Rev. B **94**, 045316 (2016).

[108] S. Vijay and L. Fu, Phys. Rev. B **94,** 235446 (2016).

[109] S. Plugge, A. Rasmussen, R. Egger, and K. Flensberg, New J. Phys **19**, 012001 (2017).

[110] T. Karzig, C. Knapp, R. Lutchyn, P. Bonderson, M. Hastings, C. Nayak, J. Alicea, K. Flensberg, S. Plugge, Y. Oreg, C. Marcus, M. H. Freedman, arXiv:1610.05289.

[111] In the SM, we derive the energy spectrum and the MBS wavefunctions for the model presented in the main text. We also provide more details on the topological phase diagram, study the effects of interwire tunneling, and derive a microscopic model of the proximity effect for weak NW-SC coupling.

[112] S. Ryu, A. P. Schnyder, A. Furusaki, and A. W. W. Ludwig, New J. Phys. **12**, 065010 (2010).

[113] K. Wölms, A. Stern, and K. Flensberg, Phys. Rev. Lett. **113**, 246401 (2014)

[114] K. Wölms, A. Stern, and K. Flensberg, Phys. Rev. B **93**, 045417 (2016).

[115] E. Prada, P. San-Jose, and R. Aguado, Phys. Rev. B **86**, 180503 (2012).

[116] C. R. Reeg and D. L. Maslov, Phys. Rev. B **94**, 020501(R) (2016).

[117] H. Ebisu, B. Lu, J. Klinovaja, and Y. Tanaka, Prog. Theor. Exp. Phys. 083I01 (2016).

[118] B. Braunecker, G. I. Japaridze, J. Klinovaja, and D. Loss, Phys. Rev. B **82**, 045127 (2010).

[119] J. Klinovaja, P. Stano, and D. Loss, Phys. Rev. Lett. **109**, 236801 (2012).

[120] L. Fu and C. L. Kane, Phys. Rev. Lett. **102**, 216403 (2009).

[121] S. Nakosai, Y. Tanaka, and N. Nagaosa, Phys. Rev. Lett. **108**, 147003 (2012).

[122] D. I. Pikulin, Y. Komijani, and Ian Affleck, Phys. Rev. B **93**, 205430 (2016).

[123] D. Sticlet, C. Bena, and P. Simon, Phys. Rev. B **87**, 104509 (2013).

[124] C. Hsu, P. Stano, J. Klinovaja, and D. Loss, Phys. Rev. B **92** 235435 (2015).

[125] S. Hoffman, J. Klinovaja, and D. Loss, Phys. Rev. B **93**, 165418 (2016).

[126] N. Sedlmayr, J.M. Aguiar-Hualde, and C. Bena, Phys. Rev. B **93**, 155425 (2016).

[127] W. DeGottardi, M. Thakurathi, S. Vishveshwara, and D. Sen, Phys. Rev. B **88**, 165111 (2013).

[128] C. Nayak, S. H. Simon, A. Stern, M. Freedman, and S. Das Sarma, Rev. Mod. Phys. **80**, 1083 (2008).

[129] J. Alicea, Rep. Prog. Phys. **75**, 076501 (2012).

[130] E. Bocquillon, R. S. Deacon, J. Wiedenmann, P. Leubner, T. M. Klapwijk, C. Brüne, K. Ishibashi, H. Buhmann, and L. W. Molenkamp, Nat. Nanotechnology **12**, 137 (2017).

[131] R. S. Deacon, J. Wiedenmann, E. Bocquillon, T. M. Klapwijk, P. Leubner, C. Brüne, S. Tarucha, K. Ishibashi, H. Buhmann, L. W. Molenkamp, Phys. Rev. X **7**, 021011 (2017).

[132] V.B. Geshkenbein and A.I. Larkin, Pis'ma Zh. Eksp. Teor. Fiz. **43**, 306 (1986) [JETP Lett. **43**, 395 (1986)].

[133] S. Yip, Phys. Rev. B **52**, 3087 (1995).

[134] M. Sigrist, Prog. Theor. Phys. **99**, 899 (1998).

[135] S. Kashiwaya, and Y. Tanaka, Rep. Prog. Phys. **63**, 1641 (2000).

[136] Y. Asano, Y. Tanaka, M. Sigrist, and S. Kashiwaya, Phys. Rev. B **71**, 214501 (2005).

[137] Y. Avishai and T.K. Ng, Phys. Rev. B **81**, 104501 (2010).

[138] A. Buzdin, Phys. Rev. Lett. **101**, 107005 (2008).

[139] J.-F. Liu and K. S. Chan, Phys. Rev. B **82**, 184533 (2010).

[140] E. Goldobin, D. Koelle, R. Kleiner, and R. G. Mints, Phys. Rev. Lett. **107**, 227001 (2011).

[141] H. Sickinger, A. Lipman, M. Weides, R.G. Mints, H. Kohlstedt, D. Koelle, R. Kleiner, and E. Goldobin, Phys. Rev. Lett. **109**, 107002 (2012).

[142] A. A. Reynoso, G. Usaj, C. A. Balseiro, D. Feinberg, and M. Avignon, Phys. Rev. Lett. **101**, 107001 (2008).

[143] F. Dolcini, M. Houzet, and J. S. Meyer, Phys. Rev. B **92**, 035428 (2015).

[144] T. Yokoyama, M. Eto, and Y. V. Nazarov, Phys. Rev. B **89**, 195407 (2014).

[145] G. Campagnano, P. Lucignano, D. Giuliano, and A. Tagliacozzo, J. Phys. Condens. Matter **27**, 205301 (2015).

[146] M. Alidoust and J. Linder, Phys. Rev. B **87**, 060503 (2013).

[147] F. S. Bergeret and I. V. Tokatly, Europhys. Lett. **110**, 57005 (2015).

[148] R. G. Mints, Phys. Rev. B **57**, R3221 (1998).

[149] K. N. Nesterov, M. Houzet, and J. S. Meyer, Phys. Rev. B **93**, 174502 (2016).

[150] L. Dell'Anna, A. Zazunov, R. Egger, and T. Martin, Phys. Rev. B **75**, 085305 (2007).

[151] A. Rasmussen, J. Danon, H. Suominen, F. Nichele, M. Kjaergaard, and K. Flensberg, Phys. Rev. B **93**, 155406 (2016).

[152] C. Schrade, A. A. Zyuzin, J. Klinovaja, and D. Loss, Phys. Rev. Lett. **115**, 237001 (2015).

[153] M.-S. Choi, C. Bruder, and D. Loss, Phys. Rev. B **62**, 13569 (2000).

[154] M. Lee, J.S. Lim, and R. Lopez, Phys. Rev. B **87**, 241402(R) (2013).

[155] B. Béri, Phys. Rev. Lett. **110**, 216803 (2013).

[156] C. Fasth, A. Fuhrer, L. Samuelson, V.N. Golovach, and D. Loss, Phys. Rev. Lett. **98**, 266801 (2007).

[157] D. J. van Woerkom, A. Geresdi, and L. P. Kouwenhoven, Nat. Phys. **11**, 547 (2015).

[158] A. Auerbach, *Interacting Electrons and Quantum Magnetism* (Springer-Verlag, Berlin, 1994).

[159] D. Loss and D. P. DiVincenzo, Phys. Rev. A **57**, 120 (1998).

[160] R. Hanson, L. P. Kouwenhoven, J. R. Petta, S. Tarucha, and L. M. K. Vandersypen, Rev. Mod. Phys. **79**, 1217 (2007).

[161] C. Kloeffel and D. Loss, Annu. Rev. Condens. Matter Phys. **4**, 51 (2013).

[162] G. A. Goldin, R. Meniko, and D. H. Sharp, Phys. Rev. Lett. **54**, 603 (1985).

[163] A. Y. Kitaev, Ann. Phys. **303**, 2 (2003).

[164] H. M. Freedman, A. Kitaev, and Z. Wang, Commun. Math. Phys. **227**, 587 (2002).

[165] H. M. Freedman, A. Kitaev, and Z. Wang, Commun. Math. Phys. **227**, 587 (2002).

[166] S. B. Bravyi and A. Y. Kitaev, Annals of Physics 298, **210** (2002).

[167] M. H. Freedman, A. Kitaev, M. J. Larsen, and Z. Wang, Bull. Amer. Math. Soc. (N.S.) **40**, 31 (2003).

[168] M. T. Deng, C. L. Yu, G. Y. Huang, M. Larsson, P. Caro, and H. Q. Xu, Nano Letters **12**, 6414 (2012).

[169] A. D. K. Finck, D. J. Van Harlingen, P. K. Mohseni, K. Jung, and X. Li, Phys. Rev. Lett. **110**, 126406 (2013).

[170] H. O. H. Churchill, V. Fatemi, K. Grove-Rasmussen, M. T. Deng, P. Caro, H. Q. Xu, and C. M. Marcus, Phys. Rev. B **87**, 241401 (2013).

[171] G. Volovik, JETP Letters **70**, 609 (1999).

[172] M. M. Vazifeh and M. Franz, Phys. Rev. Lett. **111**, 206802 (2013).

[173] S. Bravyi, Phys. Rev. A **73**, 042313 (2006).

[174] Here we specifically encode n topological qubits by $4n$ MFs [173] such that the parity of each qubit is conserved, in contrast to an alternative scheme where n qubits are represented by $2n + 2$ MFs [175,176].

[175] L. S. Georgiev, Phys. Rev. B **74**, 235112 (2006); A. Ahlbrecht, L. S. Georgiev, and R. F. Werner, Phys. Rev. A **79**, 032311 (2009).

[176] M. Leijnse and K. Flensberg, Phys. Rev. B **86**, 104511 (2012).

[177] T. Hyart, B. van Heck, I. C. Fulga, M. Burrello, A. R. Akhmerov, and C. W. J. Beenakker, Phys. Rev. B **88**, 035121 (2013).

[178] M. Leijnse and K. Flensberg, Phys. Rev. Lett. **107**, 210502 (2011).

[179] D. Rainis and D. Loss, Phys. Rev. B **85**, 174533 (2012).

[180] F. L. Pedrocchi and D. P. DiVincenzo, Phys. Rev. Lett. **115**, 120402 (2015).

[181] A. Hutter and J. R. Wootton, Phys. Rev. A **93**, 042327 (2016) (2015).

[182] S. Tewari, C. Zhang, S. D. Sarma, C. Nayak, and D.-H. Lee, Phys. Rev. Lett. **100**, 027001 (2008).

[183] M. Braun, J. König, and J. Martinek, Phys. Rev. B **70**, 195345 (2004).

[184] E. Vernek, P. Penteado, A. Seridonio, and J. Egues, Phys. Rev. B **89**, 165314 (2014).

[185] This Hamiltonian is valid for hybrid qubit operations when the rate of gate operations is much smaller than $|t_{\nu\pm}|^2/\hbar(\epsilon_\sigma - 2\delta)$, $t_{\nu\pm}t^*_{\bar{\nu}\pm}/\hbar(\epsilon_\sigma - 2\delta)$, and $t_{\nu\pm}t^*_{\bar{\nu}\mp}/\hbar(\epsilon_\sigma - 2\delta)$.

[186] M. A. Nielsen and I. L. Chuang, *Quantum Computation and Quantum Information* (Cambridge University Press, 2010).

[187] Alternatively, one may achieve another simple entangling Hamiltonian in the presence of a magnetic field, $\tilde{\mathcal{H}}_{\mathrm{hCP}} = -2|t|^2\sigma_3(1 + \eta_1)/(\epsilon_\uparrow - \epsilon_\downarrow)$, by tuning $\epsilon_0 = 0$, $\delta = 0$, $t'_l = t_r = 0$, and $t_l = t'_r = t$ (Appendix 5.B). This is equivalent to Eq. (5.7), up to a single a gate operation, and thus can similarly be used to implement an hSWAP gate.

[188] L. Trifunovic, O. Dial, M. Trif, J. R. Wootton, R. Abebe, A. Yacoby, and D. Loss, Phys. Rev. X **2**, 011006 (2012).

[189] R. Raussendorf and J. Harrington, Phys. Rev. Lett. **98**, 190504 (2007).

[190] D. S. Wang, A. G. Fowler, and L. C. Hollenberg, Phys. Rev. A **83**, 020302 (2011).

[191] S. Nadj-Perge, S. Frolov, E. Bakkers, and L. P. Kouwenhoven, Nature **468**, 1084 (2010).

[192] S. Nadj-Perge, V. Pribiag, J. Van den Berg, K. Zuo, S. Plissard, E. Bakkers, S. Frolov, and L. Kouwenhoven, Phys. Rev. Lett. **108**, 166801 (2012).

[193] S. De Franceschi, L. Kouwenhoven, C. Schonenberger, and W. Wernsdorfer, Nat. Nano. **5**, 703 (2010).

Constantin Schrade

Curriculum Vitae

Herrenberger Strasse 107
D-71069 Sindelfingen
☎ *+49 7031 381122*
✉ *constantin.schrade@t-online.de*

Personal Information

Name: Constantin Schrade

Adress: Herrenberger Strasse 107, D-71069 Sindelfingen, Germany

Email: constantin.schrade@t-online.de

ResearcherID: D-5062-2017

Phone: +49 7031 381122

Birth: June 13, 1989 (Boeblingen, Stuttgart)

Nationality: German

Languages: English (fluent), German (fluent), French (intermediate)

Education

University of Basel **Basel, Switzerland**
PhD in Theoretical Physics *09/2013 –07/2017*
Title of the thesis: *Majorana bound states in topological insulators and nanowires*
Supervisor: Prof. Daniel Loss

ETH Zurich **Zurich, Switzerland**
Master of Science in Physics *09/2011 – 08/2013*
Title of the thesis: *Riemannian Geometry in Statistical Physics*
Supervisor: Prof. Claudio Chamon (Boston University), Prof. Manfred Sigrist (ETH Zurich)

Boston University **Boston, USA**
Visiting Researcher *09/2012 – 01/2013*
Supervisor: Prof. Claudio Chamon

ETH Zurich **Zurich, Switzerland**
Bachelor of Science in Physics *09/2008 – 08/2011*

Employment history

University of Basel **Basel, Switzerland**
Doctoral Candidate *09/2013 –07/2017*
Supervisor: Prof. Daniel Loss

Institutional responsibilities

University of Basel **Basel, Switzerland**
IT Specialist in the Research Group of Prof. Daniel Loss *09/2016 –09/2017*

Teaching activities

University of Basel
Teaching assistant *09/2013 –06/2016*
Statistical Mechanics (Spring 2014, Spring 2015, Spring 2016)
Quantum Mechanics (Fall 2014)
Topological Quantum Computation (Fall 2015)

University of Basel **Basel, Switzerland**
Voted third best teaching assistant for a compulsory physics lecture *12/2014, 06/2015*

Prizes, awards, fellowships

The Helmut Fischer Foundation
Fellowship *09/2012*

ETH Zurich
Karolus Travel Fellowship *09/2012*

Publications

1: **Constantin Schrade**, Manisha Thakurathi, Christopher Reeg, Silas Hoffman, Jelena Klinovaja, and Daniel Loss,
Low-field Topological Threshold in Majorana Double Wire Setup,
Physical Revew B **96**, 035306 (2017).

1: **Constantin Schrade**, Silas Hoffman, and Daniel Loss,
Detecting Topological Superconductivity with φ_0 *Josephson Junctions*,
Physical Review B **95**, 195421 (2017).

2: Silas Hoffman, **Constantin Schrade**, Jelena Klinovaja, and Daniel Loss,
Universal Quantum Computation with Hybrid Spin-Majorana Qubits,
Physical Review B **93**, 075425 (2016).

3: **Constantin Schrade**, A. A. Zyuzin, Jelena Klinovaja, and Daniel Loss,
Proximity-Induced π *Josephson Junctions in Topological Insulators and Kramers Pairs of Majorana Fermions*,
Phys. Rev. Lett. **115**, 237001 (2015).

Academic presentations

1: *Low-field Topological Threshold in Majorana Double Nanowires*
"Majorana States in Condensed Matter: Towards Topological Quantum Computation" conference, Mallorca, Spain. May 14-20, 2017. Poster presentation.

2: *Majorana Tunnel Junctions*
Seminar of Professor Jagadeesh Moodera's research group, Massachusetts Institute of Technology - Department

of Physics, Cambridge, MA, USA, February 15, 2017. Talk.

3: *Majorana Tunnel Junctions*
Condensed Matter Theory Seminar, Massachusetts Institute of Technology - Department of Physics, Cambridge, MA, USA, February 14, 2017. Talk.

4: *Detecting Topological Superconductivity with* φ_0 *Josephson Junctions*
7th NCCR QSIT General Meeting, Arosa, Switzerland. February 1-3, 2017. Poster presentation.

5: *Majorana Fermions and the Josephson effect*
Quantum Science and Technologies Research Seminar, University of Basel, Basel, Switzerland. November 29, 2016. Talk.

6: *Detecting Topological Superconductivity with* φ_0 *Josephson Junctions*
"Topological States of Matter" conference, Donostia-San Sebastian, Spain. September 5-9, 2016. Poster presentation.

7: *Proximity-induced* π *Josephson Junctions in Topological Insulators*
6th NCCR QSIT General Meeting, Arosa, Switzerland. February 3-5, 2016. Poster presentation.

8: *Proximity-induced* π *Josephson Junctions in Topological Insulators*
Condensed Matter Theory Seminar, University of Basel, Basel, Switzerland, June 30, 2015. Talk.

9: *On the Relationship of Riemannian Geometry and Condensed Matter Physics*
Séminaire de l'Institut de Théorie des Phénomènes Physiques, EPF Lausanne, Lausanne, Switzerland. March, 2013. Talk.

10: *On the Relationship of Riemannian Geometry and Condensed Matter Physics*
Condensed Matter Theory Seminar, University of Basel, Basel, Switzerland. March 28, 2013. Talk.